Electromagnetic signature of human cortical dynamics during wakefulness and sleep

Nima Dehghani

Electromagnetic signature of human cortical dynamics during wakefulness and sleep

Signature électromagnétique de la dynamique corticale pendant l'éveil et le sommeil chez l'homme

Nima Dehghani

Thèse de Doctorat
en Neurosciences Computationnelles

Université Pierre et Marie Curie (UPMC)
École Doctorale Cerveau, Cognition, Comportement

Soutenue le 30 Août 2012, avec le Jury composé de:

Sonja Grün	Rapporteur
Jean-Philippe Lachaux	Rapporteur
Eric Halgren	Examinateur
Michel Le Van Quyen	Examinateur
Régis Lambert	Président du Jury
Alain Destexhe	Directeur de thèse

Laboratory of Computational Neuroscience
Unité de Neurosciences, Information et Complexité (UNIC, UPR-3293),
Centre National de la Recherche Scientifique (CNRS), Gif-sur-Yvette, France

Contents

Preface

My training as both a medical doctor and a theoretical scientist has made me very aware of the gap between diagnostic/therapeutic approaches to disease and the quantitative characterization of biological network dynamics. It is my belief that to bridge this gap, practicing medicine will and should be supplemented by automated adapting algorithms of combined anticipatory and therapeutic devices. In keeping with this belief, after completing my medical training I joined the Harvard/MIT Martinos center for Biomedical Imaging. Since then, I switched to pure research to understand the fundamentals of how different parts of a biological system interact. At Martinos and then UCSD Multimodal Imaging Lab (a joint venture between Departments of Radiology and Neuroscience) and MGH Neurology department (Cortical Physiology Lab) under the supervision of Eric Halgren, along with Syd Cash we adapted multimodal investigations to study the sleep rhythms in healthy and epileptic patients. Together, we studied the electromagnetic signature of sleep graphoelements. We continued this line of work in intracranial recordings from epileptic patients.

Subsequently, I joined Unité de Neurosciences, Information et Complexité (UNIC) at Centre national de la recherche scientifique (CNRS), to earn a PhD in theoretical and computational neuroscience under the supervision of Alain Destexhe. At CNRS, we adapted the physics of electromagnetism toward the understanding of the spectral properties of non-invasive large scale neural activity measurements. In studying invasive ensemble recordings of neural spiking and local field potentials from epileptic patients, we used concepts from statistical physics to assess self organized criticality in neural tissue. In addition, we analyzed the network properties of excitation and inhibition in micro-circuitry of the cerebral cortex in order to better understand cortical spatiotemporal dynamics.

Throughout my independent studies, I have let the questions define what I read and learn next. The questions that interest me have always been out of the jurisdiction of the reductionist view. I do believe this is a natural fruit of my initial training in medicine. It is my belief that for better understanding a complex system, one needs to quantify its characteristics at many scales. The body of work presented in this thesis, is driven by this belief. I hope to use this invaluable experience in my future investigations.

Acknowledgments

Throughout these investigation, I have immensely enjoyed working in interdisciplinary environments, collaborating with theoretical physicists, computer scientists, engineers, neuroscientists, applied mathematicians and clinicians. I feel very lucky that I have joined centers that were not limited by departmental boundaries and fostered like-minded people. I shall thank the director of UNIC, Yves Fregnac, all the senior members and administrators of this center who have created such a unique environment.

Though there are many to name, last but not least, I wish to personally acknowledge a few friends, colleagues and teachers. I am very thankful to ENP (École des Neurosciences de Paris), its directors and administrators. They generously have provided the funding during my doctoral studies [1]. I wish to extend my gratitude to fellow students at ENP, each of whom comes from a different country and has taught me more than just science. I wish to thank all the lab members. I wish to particularly thank Claude Bédard from whom I have learned a new way of looking at things. Lively discussions with Michelle Rudolph and Lyle Muller have sparked new ideas. Explorations of spiking patterns with Adrien Peyrache has been a joyful experience. Yann Zerlot's enthusiasm and Marco Brigham's relentless drive have been grand lessons for me. I wish to thank Gerald Hahn, Esin Yavuz, Sebastian Béhoret for their friendship and challenging scientific puzzles.

I would also like to thank my past advisors but now collaborators, Eric Halgren and Syd Cash who have been instrumental in my success and progress. Their patience and scientific guidance have been invaluable. I am also grateful to the jury members. It is an honor to have those whose scientific work I admire be on my thesis committee.

I have always been autonomous in defining my projects and have been lucky to have advisors who let me follow my interests. Alain Destexhe has been an exemplar advisor. In fact he was my teacher before we met as I had already read so many of his works. I feel lucky to have

[1] Research supported by through variety of grants from Centre National de la Recherche Scientifique (CNRS, France), Agence Nationale de la Recherche (ANR, France), European Community Future and Emerging Technologies program (BRAINSCALES grant FP7-269921), the National Institutes of Health (NIH grants 5R01NS062092, R01 EB009282) and DARPA (BAA05-26, Revolutionizing Prosthetics). I was supported by a fellowship from Ecole de Neurosciences de Paris (ENP).

studied under his supervision, to learn from his scientific view and experiences, and to watch his humane and gracious attitude toward his students and colleagues. His openness and constant enthusiasm have helped me to better shape my scientific path.

I am in debt to my family, specifically my parents, and *Emily* who has been infinitely kind, thoughtful and supportive throughout these years. Without them, this work would have never been.

Summary

Analyzing brain function at multiple scales is a necessary step to understand its complexities. In this thesis work, we tackled this issue at both macro and micro-scales using non-invasive and invasive recordings. We have used a series of computational techniques and correlation analyses to analyze recordings of the human brain activity during wakefulness and sleep.

In a first study, we analyzed simultaneous elecroencephalogram (EEG) and magnetoencephalogram (MEG) recordings in awake human subjects. We showed theoretically that if the medium is resistive, the frequency scaling of EEG and MEG signals should be the same at low frequencies ($<$10 Hz). To test this prediction, we analyzed the spectrum of simultaneous EEG and MEG measurements in four human subjects. In a given region, although the variability of the frequency scaling exponent was higher for MEG compared to EEG, both signals consistently scale with a different exponent. In some cases, the scaling was similar, but only when the signal-to-noise ratio of the MEG was low. Several methods of noise correction for environmental and instrumental noise were tested, and they all increased the difference between EEG and MEG scaling. We conclude that there is a significant difference in frequency scaling between EEG and MEG, which can be explained if the extracellular medium (including other layers such as dura matter and skull) is globally non-resistive. The resistive or non-resistive nature of the extracellular space in the brain is an important determinant for correctly modeling extracellular potentials.

In a second study, we analyzed the spatio-temporal dynamics of excitation and inhibition during human sleep from high-density intracranial recordings. We used high-density recordings obtained in epileptic patients and from unit recordings, we successfully separated between RS neurons (regular or bursting cells) from fast-spiking (FS) cells. The high density of the array allowing recording from large number of cells (up to 90) helped us to identify apparent monosynaptic connections, which confirmed the excitatory and inhibitory nature of RS and FS cells, thus categorized as putative pyramidal and interneurons, respectively. Using such a separation, we investigated the dynamics of correlations within each class. A marked exponential decay with distance was observed in the case of excitatory but not for inhibitory cells. Thus, our study provides, for a first time, insight on the interplay of excitation and inhibition in the human neocortex.

In a third study, we investigated dynamical signatures of complex dynamics, and self-organized activity, from intracranial recordings in cat, monkey and humans. We compared the collective dynamics of different in vivo preparations during wakefulness, slow-wave sleep and REM sleep, in cat parietal cortex (96 electrodes), monkey motor cortex (64/96 electrodes) and human temporal cortex (96 electrodes) in epileptic patients. In neuronal avalanches defined from units (up to 152 single units), the size of avalanches never clearly scaled as power-law, but rather scaled exponentially or displayed intermediate scaling. Avalanches defined from nLFPs displayed power-law scaling in double logarithmic representations, as reported previously in monkey. However, avalanche defined as positive LFP (pLFP) peaks, which are not related to neuronal firing, also displayed apparent power-law scaling. Closer examination of this scaling using the more severe cumulative distribution function (CDF) representation did not confirm power-law scaling. The same pattern was seen for cats, monkey and human, as well as for different brain states of wakefulness and sleep. We also tested other alternative distributions. While simple exponentials yielded very good fits of the avalanche dynamics, the bi-exponential distribution provided the best fit to the data. Collectively, these results show no clear evidence for power-law scaling or self-organized critical states, at the level of spiking activity or local field potential, in the awake and sleeping brain of mammals, from cat to man.

Finally, in an appendix, we provide preliminary results about the relations between excitatory and inhibitory cells with local field potentials in human sleep. The high-density intracranial recordings described above (96-electrode array) were used to analyze the differential firing of RS and FS cells during different sleep stages, devoid of interictal activity. Up to 90 simultaneously recorded units (in Layer III), and 96 local field potential (LFP) recordings, provide a good basis to characterize the dynamics of excitation and inhibition during different brain states. During slow-wave sleep (SWS, Stage III or IV), dominated by delta-wave activity, all neurons fired according to Up and Down states, in relation to slow-waves complexes in the LFP, as described previously. Both RS and FS cells were silent during the Down-states. During REM sleep and wakefulness, both types of units fired according to very irregular patterns of discharge, while the LFP or ECoG were desynchronized. In all states, FS cells fired significantly more than RS cells (about 4 to 5 times on average). These results provide a characterization of the different roles of excitation and inhibition in the different wake and sleep states in humans.

In conclusion, we have used different measurement methods, from microscopic scale (single unit activity), mesoscopic (LFP) and macroscopic (ECoG, EEG, MEG) to characterize wake and sleep states in humans (as well as cat and monkey in one study). We conclude that the brain follows complex dynamics at all scales. There is globally no evidence for self-organized critical dynamics, but the brain activity manifests other signs of self-organization, such as large-scale rhythmical activity and multiple exponential processes. We suggest that all results could be explained by the interplay of excitation and inhibition. We anticipate that coupled oscillator network models of interacting excitation and inhibition should reproduce these findings, which constitutes a challenge for future work.

Résumé

L'analyse de la fonction cérébrale à de multiples échelles est une étape nécessaire pour comprendre ses complexités. Dans ce travail de thèse, nous avons étudié cet aspect aux niveaux microscopiques et macroscopiques en utilisant des enregistrements invasifs et non-invasifs. Nous avons utilisé une série d'outils d'analyse computationnels et de corrélation pour étudier l'activité cérébrale pendant l'éveil et le sommeil.

Dans une première étude, nous avons analysé les enregistrements simultanés d'électroencéphalogramme (EEG) et magnétoencéphalogramme (MEG) dans le cerveau de sujets éveillés. Nous montrons théoriquement, que si le milieu est résistif, le comportement d'echelle en fréquence doit être le même pour les signaux EEG and MEG à basse fréquence ($<$10 Hz). Afin de tester cette prédiction, nous avons analysé le spectre d'enregistrements EEG et MEG simultanés de quatre sujets humains. Le comportement d'échelle en fréquence de l'EEG montre des variations cohérentes sur la surface du cerveau, avec des exposants en général compris entre $1/f$ et $1/f^2$; ces exposants tendent à être plus faibles dans les régions temporales et pariétales. Dans une région donnée, les exposants de la MEG ont une variabilité plus grande que pour l'EEG, mais les deux signaux ont systématiquement un exposant différent. Dans certains cas, les exposants sont proches, mais ces cas correspondent à un mauvais rapport signal/bruit pour la MEG. Plusieurs méthodes de corrections du bruit instrumental et environmental ont été testées, et dans tous les cas, ces méthodes augmentent la différence de comportement spectral entre l'EEG et la MEG. En conclusion, il y a une différence significative de comportement déchelle en fréquence entre EEG et MEG, ce qui peut être expliqué si le milieu extracellulaire (incluant d'autres couches telles que la dure-mère et le crâne) est globalement non-résistif. La nature résistive ou non-résistive du milieu extracellulaire est un déterminant important pour la modélisation des potentiels extracellulaires.

Au cours d'une seconde étude, nous avons analysé la dynamique spatio-temporelle de l'excitation et de l'inhibition pendant le sommeil à partir d'enregistrements intra-crâniens à haute densité. Ces enregistrements à haute densité permettent la séparation efficace entre cellules "regular spiking" (RS) et "fast spiking" (FS). La haute densité des électrodes permet d'obtenir des connections apparemment mono-synaptiques, et de corroborer cette séparation RS-FS avec la nature excitatrice ou inhibitrice de la connection. Cette procédure confirme

que les cellules classifiées comme FS sont toujours inhibitrices, alors que les RS sont toujours excitatrices, et donc peuvent être classifiées respectivement comme cellules pyramidales ou interneurones inhibiteurs. Finalement, nous investiguons la dynamique des corrélations au sein de chaque classe de neurone. Les corrélations entre excitateurs montrent une décroissance exponentielle avec la distance, tandis que les cellules inhibitrices restent corrélées à plus grande distance. L'amplitude des corrélations dépend de l'échelle temporelle du calcul de corrélation, mais pas la constante spatiale. Cette constante est compatible avec la taille typique des collonnes corticales chez l'homme. Ces résultats permettent, pour la première fois, de caractériser l'activité neuronale et l'interaction entre excitation et inhibition dans le neocortex humain.

Dans une troisième étude, nous avons investigué les signatures de la dynamique complexe et l'activité auto-organisée, à partir d'enregistrements intra-crâniens chez le chat, le singe et l'homme. Nous utilisons des enregistrements à haute densité dans le cortex moteur du chat (96 électrodes), le cortex moteur et prémoteur du singe et dans le cortex temporal humain (96 électrodes) de patients épileptiques. Lors d'avalanches définies à partir d'unités (jusqu'à 160 neurones), les distributions ne se comportent pas en loi de puissance, mais tendent a être exponentielles ou intermédiaires. Nous analysons également les potentiels de champ (LFPs), et en particulier les pics négatifs (nLFPs) au sein de l'ensemble délectrodes (de 96 a 128 sites, selon la configuration d'enregistrement). Dans ce cas, les avalanches définies à partir des nLFPs peuvent se comporter en loi d'échelle, comme observé précédemment chez le singe. Cependant, les avalanches définies à partir des pics positifs (pLFPs), qui ne sont pas directement reliées aux décharges des neurones, ont le même comportement. Une analyse plus détaillée en utilisant la représentation cumulée (CDF) ne confirme pas la présence de loi de puissance. Les mêmes résultats s'appliquent au chat, au singe et aux enregistrements humains, pendant différents états cérébraux d'éveil et de sommeil. Nous avons également testé des distributions alternatives, et des processus multi-exponentiels semblent expliquer les distributions obtenues, de façon optimale pour des distributions bi-exponentielles. L'ensemble de ces résultats ne montrent pas d'evidence de loi de puissance ou d'états critiques dans le cerveau éveillé ou en sommeil de différents mammifères, du chat à l'homme.

Finalement, dans un appendice, nous montrons des résultats préliminaires concernant les relations entre cellules excitatrices et inhibitrices, et les potentiels de champ locaux pendant le sommeil humain. Nous avons pu séparer les cellules entre "regular-spiking" (RS) et "fast-spiking" (FS), ce qui a été confirmé par connections monosynaptiques (voir Peyrache et al., PNAS, 2012). Nous analysons ici la décharge spécifique des cellules RS et FS pendant différents états d'éveil et de sommeil, sélectionnés sans activité interictale. Jusqu'à 92 unités enregistrées simultanément, procurent une base solide pour la caractérisation de la dynamique de l'excitation et de l'inhibition pendant ces différents états. Pendant le sommeil lent (Stade III ou IV), dominé par les ondes lentes de type delta, tous les neurones déchargent selon des états "Up" ou "Down", en relation avec les ondes lentes du LFP, comme décrit précédemment. Les cellules RS et FS sont toutes silencieuses pendant les états "Down". Pendant le sommeil REM et pendant l'éveil, les neurones déchargent de façon irrégulière alors que le LFP ou l'ECoG sont désynchronisés.

Dans tous les états les cellules FS déchargent plus que les cellules RS (4 ou 5 fois plus en moyenne). En conclusion, ces résultats procurent une caractŕisation des differents rôles de l'excitation et de l'inhibition pendant l'éveil et le sommeil chez l'homme.

En conclusion, nous avons utilisé différentes méthodes de mesure, aux échelles microscopiques (activité unitaire), mésoscopique (LFP) et macroscopiques (ECoG, EEG, MEG), pour caractériser les états de veille et sommeil chez l'homme (ainsi que chez le chat et le singe dans une étude). Nous concluons que le cerveau suit une dynamique complexe à toutes les échelles. Il n'y a pas d'évidence de dynamique auto-organisée critique, mais l'activité du cerveau manifeste d'autres signes d'auto-organisation, comme l'activité synchrone à grande distance et des processus multi-exponentiels. Nous suggérons que ces résultats peuvent être expliqués par l'interaction entre excitation et inhibition. Nous anticipons que des réseaux d'oscillateurs couplés, avec interaction entre excitation et inhibition, devraient pouvoir expliquer ces résultats. Cette perspective constitue un défi pour des études futures.

Part I

Introduction

Chapter 1

History & Instrumentation

The history of the sciences is a great fugue, in which the voices of the nations come one by one into notice.

Johann Wolfgang von Goethe

In our studies, we used large scale non-invasive and invasive recordings of the brain. The two non-invasive modalities, Electroencephalogram (EEG) and Magnetoencephalogram (MEG) are capable of registering the ongoing dynamics of the brain with millisecond accuracy. They provide a window to capture the global dynamics of the brain. Multielectrode recordings, on the other hand, give us the opportunity to zoom into the dynamics of microcircuitry of cortical columns. Below, we briefly present the instrumentation of each of these modalities. The physics of the signal obtained from these devices dictates the nature of the biophysical signature of the underlying measurements of neural computation.

1.1 Macroscale recordings

1.1.1 Electroencephalography (EEG)

1.1.1.1 Brief history of the instrumentation

The first measurements of the spontaneous electrical activity of the brain were carried out by Richard Caton (1842-1926). The initial report was only a presentation before the British Med-

ical Association in 1875. A summary of that report, later, appeared in the British Medical Journal in 1877 [1].

The following paragraph is based on the narrative of his report: ”In every brain hitherto examined, the galvanometer has indicated the existence of electric currents. The external surface of the grey matter is usually positive in relation to the surface of a section through it. Feeble currents of varying direction pass through the multiplier when the electrodes are placed on two points of the external surface of the skull. The electric currents of the grey matter appear to have a relation to its functions. When any part of the grey matter is in a state of functional activity, its electric current usually exhibits negative variation. For example, on the areas shown by Dr. Ferrier to be related to rotation of the head and to mastication, negative variation of the current was observed to occur whenever those two acts respectively were performed. Impressions through the senses were found to influence the currents of certain areas, e.g., the currents of that part of the rabbit’s brain which Dr. Ferrier has shown to be related to movements of the eyelids, were found to be markedly influenced by stimulation of the opposite retina by light. (1875)” [2].

Caton studied electrical activity of more than 40 cat’s, rabbit’s and monkey’s brains using unipolar electrodes. In some experiments, he used bi-hemispheres recordings and in the others, he placed one electrode on the cerebral cortex (or on the grey matter) and the other on the surface of the skull [2, 3]. Caton used Thompson’s galvanometer to track variations of the electrical activity; however lacking recording instruments, he amplified the waveform optically by shining a meniscus lamp on a wall. Therefore his count of these initial studies are based on personal observations. He also identified the regions associated with motor movement (of the head and eye). In his 1887 report to the Ninth International Medical Congress in Washington DC, he mentioned that variations happen across sleep and wakefulness, anesthesia, and noticed their cessation after death. He was also successful in evoking current variation through shining light into the eyes and stimulating the skin but was unable to evoke auditory responses [3]. Therefore not only was he the discoverer of EEG, but he was also the first functional topographer who discovered oscillatory, spontaneous and evoked responses.

After Caton, Danilevsky (Russia, 1852-1939) carried out spontaneous and evoked EEG recordings in animals (published in 1877). In 1890s, Adolf Beck (Poland, 1863-1939) adapted these techniques and, in EEGs from rabbit and dog, added desynchronization in visual cortex to the scientific repertoire. Later in 1908, he used a string galvanometer to achieve higher precision in his recordings. This instrument had just been introduced by Willhelm Einthoven (Netherlands, 1860-1927) for cardiac electric activity measurements. After this publication, the Austrian Academy of Science published Fleischel Von Marxov’s unpublished work on disabling the visual cortices of numerous species by cooling and chloroform, though he had not reported any oscillatory activity. In Kiev, 1912, Vladimir Vladimirovich Pravdich-Neminsky created the first photographic recordings through a combination of the galvanometer and a moving paper; in fact, he reported a very clear description of alpha and beta waves. In 1913, Beck’s advisor, Cybulski combined a camera with the galvanometer and recorded experimentally induced

seizures in dogs [3, 4].

In 1924, Hans Berger (Germany, 1873-1941) was the first to record the human electroencephalogram. In his paper ”Uber das Elektrenkephalogramm des Menschen” (On the EEG in humans), which was published in 1929, he gave full credit to Caton:

”Caton has already (1874) published experiments on the brains of dogs and apes in which bare unipolar electrodes were placed either on the cerebral cortex and the other on the surface of the skull. The currents were measured by a sensitive galvanometer. There were found distinct variations in current, which increased during sleep and with the onset of death strengthened, and after death became weaker and then completely disappeared. Caton could show that strong current variations resulted in brain from light shone into the eyes, and he speaks already of the conjecture that under the circumstances these cortical currents could be applied to localization within the cortex of the brain. (Translated by Cohen, 1959, 258)”, [2, 5, 6].

Berger used the Einthoven string galvanometer. He initially used zinc-plated needle in order to stabilize electrode and thus reduce the high level of noise. As the amplitude was very weak, he replaced his needle electrodes with lead-foiled electrodes soaked in saline [2, 3]. Berger described low-frq (low frequency) as low order and high-frq (high frequency) as high order: ”I shall subsequently designate the waves of first order as alpha waves and waves of second order as beta waves, just as i shall use E.E.G as the abbreviation for electroencephalogram and E.C.G for the electrocardiogram” [2].

Berger discovered alpha rhythm, describing its frequency at 10 cycles per second (hertz) and as a dominant oscillation during relaxation or eyes-closed condition. He found that this rhythm would disappear in the eyes-open condition and diminishes during mental effort (such as arithmetics) and the presentation of loud noises or painful stimuli [2, 3, 7]. Interestingly, his reports were unnoticed by the scientific community until 1934, when Lord Adrian (England, 1889-1977) and Matthews confirmed his basic observations recording their own brainwaves using their cathode-ray oscilloscope [2]. Both Adrien and Einthoven went on to win the Nobel prize for their work on neurons and ECG. It was the discoveries of EEG pattern dynamics during sleep by Alfred Loomis (USA, 1887-1975) in the mid1930s that attracted the attention of the scientific community to the value of EEG [7]. By the 1940s, EEG had become widespread and since then, little has changed in the basics of its instrumentation.

1.1.1.2 Apparatus and the recordings

EEG is widely used and had become a popular method for the non-invasive measurement of the global activity of the brain. Its ease of operation, low cost, non-invasiveness and high temporal resolution (in the order of millisecond) has put it ahead of the other non-invasive modalities like PET (positron emission tomography), fMRI (functional magnetic resonance imaging), MRS (magnetic resonance spectroscopy) and SPECT (Single-photon emission computed tomogra-

phy). Of the non-invasive methods, only MEG matches its temporal resolution [8–10]. In contrast, EEG has disadvantage in localization by comparison to the mentioned methods [11].

EEG recordings are done with different spatial arrangement of electrodes. These montages can have anywhere from a few to a couple hundred electrodes. Recordings can be acquired as referential, bipolar or referenced to average of electrodes [11]. EEG has clinical usage in monitoring epilepsy, anesthesia, intensive care units (ICU) and in comatose states. In research, it is widely used in cognitive neuroscience and experimental psychology. In such fields, usually the focus is on the quantification of behavior using evoked potentials (EPs), associated with sensory stimuli, or Event-related potentials (ERPs), occurring at later latencies and are more associated with endogenous brain state. ERPs, like p300 reported by [12–14] and N400 discovered by [15] could also be used in brain-computer interface (BCI) research.

One of the key conditions for such studies is that the EP or ERP has to be reliably linked to the ongoing behavior and stimuli [16]. Though, the dynamics of the underlying characteristics of magnitude, phase and coherence are the cornerstone of any conclusion obtained from EEG recordings. In chapter 2, we focus on the EEG spectral biophysics as the hallmark of these features.

1.1.2 Magnetoencephalography (MEG)

1.1.2.1 Brief history of the instrumentation

In comparison to EEG, magnetoencephalography (MEG) is a fairly new method for measuring brain dynamics. It is much more complex and far more expensive in terms of its cost and operation. However, with this price, comes powerful abilities to measure extremely weak magnetic field of the brain. The first sensitive measurements of the magnetic field of currents generated by biological tissue was done for the heart. In 1967, David Cohen built a magnetic shielded room to record from weak magnetic signals of the heart at the order of amplitudes of 10^{-8} to 10^{-7} gauss [17]. Shortly after, he also pioneered measuring the magnetic field of the brain in a multilayer magnetically shielded chamber and introduced the MEG [18]. These initial measurements were based on a million turn coil. Later, James Zimmerman invented a highly sensitive magnetometer, called ”superconducting quantum interference device” (SQUID) which is based on superconducting loops containing Josephson junctions [19]. By adapting SQUIDs, magnetoencephalography became much more sensitive to weak magnetic fields of the brain and the new age MEG was born. In that work, David Cohen measured alpha rhythm in a healthy human and also recorded the abnormal activity of an epileptic patient [20].

1.1.2.2 Apparatus and the recordings

Electrical currents in the cortex produce minute (10^{-12} Tesla) perturbation in the magnetic field outside the skull near the scalp. These changes in magnetic flux will cause current to flow in a flux transformer. This flux transformer, via an input coil is coupled to the SQUID [8, 21]. Because SQUID-sensor units operate at low temperature, they are typically housed in a thermos-like container, named a dewar, filled with liquid helium. The bottom of the dewar is shaped like a helmet and houses hundreds of SQUID-sensor units. Therefore the sensors are only a few millimeters away, on the other side of the insulating layer, from the scalp [8]. Each sensing coil samples the local magnetic field (in the case of magnetometers) or the gradient of the magnetic field (in the case of gradiometers). The sampling frequency of the full set of sensors can reach a few thousand times a second [10].

In recent years, advancements in atomic magnetometry, based on the interaction of resonant light with atomic vapor, has become an alternative to SQUIDs [10]. Also, some efforts have been made to measure the magnetic field at higher temperatures; a magnetic field sensor that combines a superconducting flux-to-field transformer with a low-noise giant magnetoresistive sensor. This type of sensor can reliably operate at temperatures up to 77 degrees of kelvin. A prototype of this design has shown the ability to successfully measure 32 fT (femto Tesla) [22].

1.1.2.3 MEG & noise

Handling noise is a major challenge in MEG. Magnetic fluctuations of the brain signal, are usually lower than 10^{-12} T (tesla), or 10^{-8} G (gauss). This is many orders of magnitude weaker than the fluctuating magnetic background. Such urban and ambient magnetic fluctuations can reach 10^{-7} T (or 10^{-3} G). Earth's steady magnetic field is in the range of 0.5x 10^{-4} T (or 0.5 G). Therefore, reliable measurements of MEG not only require a very sensitive magnetic detector (i.e. SQUID), but is also highly dependent on the proper suppression of the magnetic noise (i.e. fluctuating magnetic background) [23].

There are three major ways to suppress the magnetic noise. The first way is to record in a magnetically shielded room, which can exclude major components of the fluctuating external fields. The magnetic shielded room (MSR) is constructed with three nested enclosures. Each enclosure consists of a high-permeability magnetic layer as well as an aluminum layer. The mu-metal reduces the low frequency noise while the aluminum suppresses high-frequency noise [24]. The second way is to measure the gradient of the magnetic field instead of the field itself. To do so, some manufacturers, have developed gradiometers, which are of two types: i) planar gradiometer, consisting of two flux transformer loops within one plane but connected in opposition, ii) radial gradiometer, consisting of two co-axial flux transformer loops connected in opposition. When a background fluctuation is far from a gradiometer, its signal at the two coils is almost equal and therefore its gradient approximates zero and largely cancels. On the

other hand, fluctuations near the gradiometer have different values when reaching the coil and therefore their gradient is not canceled. The third way of noise suppression is via software processing of the MEG signals [8, 9, 23]. There are numerous ways to implement algorithms to suppress the noise. Independent Component Analysis (ICA) [25] coupled to electro-oculogram (EOG) and electrocardiogram (ECG) can be very effective in eliminating magnetic artifacts of biological origin (see [26] for an example). Another way is the signal source separation (SSS) method. Assuming that there are no magnetic sources in between the sensors and the outside of the brain, the measured signal is decomposed to two categories: i) harmonics that arise from within the sphere surrounding the head, ii) harmonics that must have arisen at a distance. By removing the external harmonics, one can achieve exclusion of the possible interference [27].

In evaluating the spectrum of the MEG, the background noise deserves meticulous attention. For dealing with this issue, we have adapted noise suppression techniques based on empty MSR recordings. Details of the methods are described in chapter 5.

1.2 Microscale recordings

1.2.1 Importance of in vivo measurements

Over the last three decades, a variety of in vitro preparations have been used in experimental neuroscience research. They range from isolated single neurons to cell cultures, brain slices, and sometimes whole brain preparations. All these techniques have high-resolution. The operator can control and directly manipulate experimental conditions. The widespread adaptation of such methods has been very valuable in that they enable us to rapidly explore processes in individual cells, synapses, and small neuronal networks and increasingly enrich the wealth of the data on the basic functioning of the neurons. However the compromise is that such data are obtained in dramatically altered in vitro preparations where the interconnections between the brain areas are severed. [28, 29]. The absence of full connectivity in most brain slices and distorted GABAergic levels create patterns of spontaneous activity that are very different from those observed in vivo situation [30].

Moreover, the in vivo high conductance state has a profound effect on the responsiveness of neurons, individually and en masse. In individual neurons, total synaptic conductance received by the neuron is larger than its leaky resting conductance. Therefore, a network of neurons, has the capacity to operate in certain states that are not properly achievable in the case of low conductance in vitro (see [31] for an extensive review of high conductance state). Intact cortical inhibitory processes and connectivity of cortico-thalamic pathways are essential elements of the oscillatory and synchronicity activity of the reciprocal thalamocortical networks [30]. Such characteristics magnify the importance of in vivo measurements for studies that, like ours, tackle the dynamics of sleep and wakefulness.

1.2.2 Extracellular in vivo measurements

Extracellular recordings are usually done by inserting high impedance microwires. Extracellular voltage measurements could be split into two components: i) a high-frequency component (usually $>$300 or 500 Hz) that contains the action potentials (spikes) of neurons and samples the activity proximal to the electrode, and ii) a low-frequency component (up to 300 or 500 Hz), called ”Local Field Potential”, which reflects the ensemble activity in the vicinity of the electrode [29].

High enough signal-to-noise ratios (SNR) for the signals coming from neurons that are in close proximity (50-100 micron) to the electrode tip enable us to measure the activity of single units. As the neurons get further and further away from the electrode (up to 150 microns), the shape of their spikes can no longer be reliably distinguished as it is masked by the noise. This type of signal is referred to as MUA (multi-unit activity). If the distance to the electrode is too far, the spiking activity is not reliably separated from noise [32, 33].

From the high-frequency component, individual spikes are detected using an amplitude threshold. Next they are sorted according to the characteristic spike waveform shape of individual neurons. This shape is mainly dictated by the morphology of the dendritic trees, as well as the distance from the electrode and the orientation of arborization relative to the electrode [34, 35]. These morphological features are then used as inputs to cluster the (or for clustering) algorithms performing the classification [36]. Many different methods of spike sorting have been proposed. Some detailed reviews solely focus on this issue [37, 38]. Based on such spike waveform features from high-density recordings, it is also possible to reliably separate the units into two categories of ”regular-spiking” (RS) and ”fast-spiking” (FS) [39–41]. In chapter 6, we show how this can be done in extracellular recordings from the human cortex.

1.2.3 Multielectrode recording of extracellular signature of neural activity

Gerstein & Clark were among the first to pioneer multiple recordings. In their experiment, they used a tungsten microelectrode with several small holes in its vinyl insulation. This electrode enabled simultaneous recording of the action potentials from multiple adjacent neurons [32]. Current acquisition systems allow the simultaneous recording of up to hundreds of channels simultaneously [29]. This opens up the fascinating opportunity to study large cell populations in order to understand how they encode sensory processing and behavior in anesthetized animals and in behaving animals. Also, in recent years, the advancement of etching and silicon probe fabrication has created the opportunity to record from chronically implanted arrays of hundreds of electrodes [42]. Multielectrode recording techniques vary in their design, ranging from ”microwires” [43], stereotrodes and tetrodes [44], to complex 3-D systems built from sili-

con [45,46]. These types of electrode arrays enable simultaneous recording of MUA, single-unit activity as well as LFP from large numbers of neurons [42].

Complex brain processes require the recruitment of large population of neurons [47]. The study of single neurons only provides a very limited scope of the whole dynamics [33, 48]. Using multielectrode arrays provides the opportunity to study connectivity patterns of close-by neurons [33, 49]. Multielectrode recordings of ensembles can act as a bridge between the activity of individual neurons and their computational orchestration toward a rich collective dynamics [50]. Expression of these higher-order brain functions is only achievable through the coordinated spatiotemporal activity patterns of distributed neuronal ensembles [51, 52]. Some studies have begun to validate such hypotheses through studies of recordings of the activity patterns in neural ensembles excited by patterned visual stimuli [53].

In our studies of the dynamics of cortical microcircuitry, we benefited from the Utah electrode arrays (known as UEA, and specifically Neuroport in human recordings). Utah multielectrode arrays have been used in visual prosthetics [53], motor prosthetic [54] or in studies of epilepsy [55, 56]. The fabrication and characteristics of these devices are described elsewhere (see [46, 57]). Their pneumatic insertion technique [58], as well as the stability of recordings [59] and their neurosurgical aspects in human patients [60] have been discussed extensively in those references. In our study, we used these types of arrays to tackle the spatiotemporal dynamics of excitation and inhibition (chapter 6), the dynamics of neural avalanches (chapter 7) and the relationship between spiking and LFP in different states (chapter 8).

Chapter 2

Biphysics

The knowledge of anything, since all things have causes, is not acquired or complete unless it is known by its causes.

Ibn Sina (Avicenna)

Computation and information processing in the brain takes shape at multiple scales. Studying the complex dynamics of the brain requires integration of information acquired at different levels of neural computation. In the last chapter, we discussed the instrumentation of large-scale non-invasive methods and invasive electrophysiological modalities. In this chapter, we describe the biophysics at these scales along with each other.

2.1 Sources of Extracellular fields

Microelectrodes wires in the extracellular space measure the voltage fluctuations at the conductive tip of the electrode. These measurements reflect the electrical field perturbations that happen within the vicinity of the electrode [34]. A variety of sources, rising from the interaction of neural elements, contribute to such fluctuations. It is the superposition of the currents and potentials produced by such sources that is studied in the field of electrophysiology. These sources originate at a multitude of positions on the excitable membrane, ranging from spine to dendrite, soma, axon or axon terminal. The different temporal nature of these sources, as well as their electrochemical composition, dictate the biophysical nature of the measured signal. The known sources include: a) synaptic activity, b) fast action potentials, c) calcium spikes , d) intrinsic currents, e) gap junctions, f) neuro-glia interaction and g) ephaptic coupling [61].

2.2 From micro-scale to meso-scale to macro-scale

Typically, the measured extracellular electrical signal is divided into the high frequency and low frequency components. The high frequency component is thought to be mainly influenced by action potentials while the low frequency component, the so-called ”local field potential (LFP)” has a much more complicated origin [62, 63]. The relationship between spike and LFP is of great interest to the neuroscience community. It is believed that spikes reflects the output of individual neural elements while LFPs serves as some sort of collective input. Therefore, in essence, spike and LFP act as the two pillars of neural network computation. Their interaction evolves as a bidirectional entity. The LFP acts as a modulator of spiking activity while the spikes leave their imprint on the oscillatory signals conveyed by LFP [62, 63]. What are the origins of these different signals? How do they coalesce in cortical computations? How do they link to the recordings at larger scales (i.e. EEG and MEG)? We evaluate these issues from theoretical considerations as below:

The assumption that transmembrane current flow is the generator of LFP, was first put forward a few decades ago by Eccles and Lorente de No [64, 65]. It has been suggested that the spatial weighted average of the synaptic transmembrane currents constitutes the biophysical origins of LFP [66]. Some have pointed that it is not the action potentials themselves but the dendritic processing of synaptic inputs that shape the local field potential [66–68]. Interestingly, there is a study that postulates the possibility of action potentials contributing to the MEG signal [69].

In contrast to the invasive recordings of extracellular potential, EEG recordings are acquired through electrodes placed at the surface of the scalp. Usually these electrodes are orders of magnitude bigger than those optimized to record local field potentials [16]. What are the generators of EEG signals? A much widely practiced assumption is that by using bigger electrodes, one scales up the volume of the recorded tissue. Therefore, by moving from micro-meso scale (LFP) toward meso-macro scale (iEEG and EEG), the nature of the signal stays the same but the measurement include a much larger population of neurons [61, 70]. In the case of LFP, complexity is a result of the evolving temporal dynamics of the spatial distribution of current sources within the conducting volume of the cortex. The conductivity and permittivity properties of the extracellular medium dictate the spatiotemporal patterns of the electric field. In this view, the constraints of filtering by the scalp is the major assumptive difference between LFP and EEG [16]. Computational studies based on the detailed morphology of neurons have proposed that these spatiotemporal LFP patterns also depend on neuronal morphologies, spatial positions of the driving synapse, as well as electrode recording positions [68].

The link between the meso-scale ”local field potential” (literally known as LFP) and the meso-macro scale ”global field potential” (i.e. iEEG or EEG) is based on the structure of the cortex. By adapting quasi-static approximation of Maxwell equations, macroscale recordings are modeled based on the mesoscopic details of the cortical organization. Cortical architecture

is arranged in laminar and columnar fashion. The laminarity of the cortex corresponds to the distribution of the incoming cortical projection from thalamic relay nuclei as well as the specialization of the output units of corticothalamic connectivity [71, 72]. Columnar modules of the cortex contain pyramidal cells in layers III, IV and V. The apical dendrite (and initial part of the axons) of these cells run in parallel and are perpendicular to the cortical sheet, while the spatial extension of their dendritic tufts binds them together to create a functional module of network of neurons [73, 74]. In the biophysical characterization of EEG, these features are chosen as the simple mesoscopic elements of the model. Each mesoscopic element is a simplified cortical minicolumn (0.03 mm) and macrocolumn scales (1 mm) with height 2-5 mm [75].

In these mesoscopic elements, post-synaptic potentials cause ionic currents to flow in the apical dendrites of parallel cortical pyramidal neurons. These currents (”impressed current”), represent the overall effects of post-synaptic potentials at layers II/III and V of the neocortex. Based on the electrical conservation law, impressed currents leave the soma and passively return through the extracellular space. This passive ohmic propagation of the ions is called ”return current” [16, 76, 77]. These return currents propagate through a conductive three-dimensional extracellular continuum [75, 76]. The potential difference of the ”return currents” at the scalp is the measured EEG signal. [75, 78, 79]. While both impressed and return currents create magnetic fields, it is mostly the intracellular longitudinal impressed currents that create measurable magnetic induction field at the MEG sensors [8, 78]. The connection between the generating current and the magnetic flux was studied in biophysically realistic computational models showing that local neural dynamics are the products of lamina-specific synaptic drive [80, 81].

In the current practice of EEG/MEG modeling, it is suggested that the vector sum of the electrical activity (within the mesoscopic elements of the cortex) can always be approximated with a current dipole [75, 78]. The post-synaptic current traveling through parallel dendritic structure and the asymmetrical arrangement of the cortical layers impose the perpendicular displacement of charges as the major component of electromagnetic signature [8, 75, 79]. It has been argued that current multipoles could properly formulate the spatially extended sources and that dipoles are not physiologically well-suited for modeling such cases [82–84]. The counter argument has been that quadrupole and higher moments can always be reduced to a combination of proximal dipoles [78]. Others have argued that single monopoles are mathematically and physically implausible entities and the description of dipoles as a gradient of monopoles is solely for mathematical convenience [77]. However, in a recent study, it was shown that this standard model is insufficient for describing the observed LFP to EEG and that monopoles are necessary for the macroscopic modeling of these signals [85]. If future investigations further confirm these findings, it becomes necessary to develop models that incorporate monopoles as an essential element of the electrical signature of neural activity [63].

2.3 Forward model and inverse solution in a volume conductor medium

Given an electromagnetic measurement, what can we say about the source generators of the observations? Conversely, if we preset the sources to a given value, can we predict the electromagnetic measurements at a point, nearby or far? These two questions belong to the general category of inverse problems and forward predictors. The first, deals with estimating the physical parameters that we cannot directly observe, while the latter uses physical parameters to predict observations. In other words, inverse solution and forward predictor are inseparable sides of the same coin. This concept was first introduced in 1929 by Viktor Hambardzumyan (1908-1996). Since then, it had been widely used in seismology, astrophysics, and of course electromagnetism. Naturally, it was adapted in studying EEG/MEG and LFPs. An essential property of inverse solutions in electromagnetism is its ill-posed property. In other words, given a set of electromagnetic measurements, there are no unique arrangement of generators; many different solutions exists for that specific set of measurements. However, as discussed above, each inverse solution is coupled with its forward predictor. A more accurate forward predictor will bring us a better approximation in the inverse modeling. Including a priori information in our inverse models, narrows down the solutions to a few possibilities instead of unlimited counts of an ill-posed situation. This type of thinking simply translates to the bioelectromagnetism as well.

The so-called ”source localization”, based on inverse solution, is geared toward identification of the sources of the measured signal throughout time. At the micro-meso scale, it refers to the reconstruction of the membrane potential fluctuations from the measured invasive extracellular recordings, i.e.,LFP/spikes (for a review see [62]). In the meso-macro scale domain, it refers to the reconstruction of the impressed currents from the EEG, MEG or combined EEG/MEG recordings (for a review see [8, 78]).

As discussed above, the accuracy of the forward predictor determines how close the solutions of the inverse problem are to reality. Here, the forward predictor equals the simulation of the field distribution for a given arrangement of current dipoles in a volume conductor medium. For the rationale behind the adaptation of dipoles as the main sources of the electromagnetic signature and the pitfalls of such assumptions see above. The main elements in forward models of Maxwell’s equations are a) spatial distribution of the sources, b) volume conductor geometry (morphological structure, detail characteristics of the tissue conductivities) c) sensor characteristics (their spatial configuration; size and material of the sensors), and d) the spatial relation between the above mentioned 3 elements. More accurate details of the forward predictor is paralleled with an improved inverse solution [8, 77, 78]. After achieving a proper forward model, adding constraints (such as temporal behavior, noise characteristics, anatomical constraints based on MRI, and a priori assumptions from other modalities) to inverse models, improves the yielded solutions [77, 86–88].

Neglecting the capacitive and inductive effect in the electromagnetic propagation will provide the opportunity to adapt linear quasi-static Maxwell equations. This approach, because of it convenience, has become the cornerstone of modeling the forward predictor for both micro-meso (LFP) and meso-macro scale (EEG/MEG) [8, 62, 76, 77, 89]. In such case, the inaccuracies in forward modeling of mesoscopic dipole currents simplifies to a few categories: a) mis-specification of the source space, b) inaccuracies in the description of the physical properties of the head (boundary shape, conductivity values of the large scale mediums), c) improper sensor configuration information and d) incorrect or inadequate information on the spatial relation of the last 3 mentioned elements [78]. In parallel, the current forward model of LFP generators relies on several assumptions: (a) Quasistatic approximation of Maxwell's equations based on the assumption that the electric and magnetic fields are decoupled [8], (b) Linearity of the extracellular medium, (c) Ohmic (resistive) medium and the assumption that the capacitive properties of the neural tissue are negligible, (d) Isotropic (scalar) extracellular conductivity, (e) Frequency-independent extracellular conductivity and (f) Homogeneous extracellular conductivity [62].

In the next few sections, we will evaluate the consequences of these assumptions, will discuss their pitfalls and provide a summary of experimental/theoretical studies which support or refute them. We will begin with a brief overview of synchrony at multiple scales followed by a discussion of the different characteristics of volume conductor.

2.4 Multiscale synchrony

he precise timing between the LFP and spikes is a fundamental characteristic of how they co-modulate each other. The correlation of LFP with synchronized slow subthreshold membrane potential oscillations does not necessitate the synchrony of spiking within that neural population [90]. Some reports have shown that even in the absence of spiking, LFP and nearby neuron membrane potential could be highly correlated [91]. Studies of spike-free LFP segments have provided evidence that some LFP-spike relationships follow millisecond precision while other do not harbor such features [92]. This is in with the notion that LFP could also reflect surplus spiking activity. In such a scenario, only a fraction of spikes could be devoted to the assembly formation among neurons [93].

The importance of synchronized activity in modeling LFP and EEG/MEG is severalfold (the word is actually severalfold, not an indication of multiple folds). First, when measured signals are correlated, there are two plausible interpretations: a) the measurements are reflective of two independent but correlated sources or b) the correlation is a byproduct of volume conduction from a distant single source and has nothing to do with a correlation at the two spatial location of electrodes [75]. It has been shown that long-scale synchrony are the signature of cognitive processing and short-scale synchronies are likely a byproduct of volume conduction. These

studies also propose an elegant method for separating volume conduction induced effects from true signal synchrony of the generators. [70, 94, 95]. Second, based on the hypothesis that the LFP and EEG are generated by summed postsynaptic potentials, for these signal to gain enough strength to be recorded, there must exist a synchronized excitation of the cortical neurons within the generating unit [64]. The non-synchronized fluctuations in the dendritic structure will cancel, and the signature at a distant electrode approximately fades to zero [77]. Therefore, the accepted view is that the generation of both LFP and EEG are dependent on the synchronized synaptic currents leading to the formation of strong enough dipoles that can be measured at the recording electrodes [16, 75]. It is because of the influence of synchrony that the size of the generating region not only depends on the detailed neuron morphology and spatial arrangement of synapses, but is also heavily influenced by the correlation in synaptic activity [96].

It has been suggested that the synchrony profile of the extracellular potentials may be different based on the recording modality. These findings originated from EEG/MEG studies of sleep spindles. In prior studies of spindles in cats, these graphoelements appear to be synchronous across the cortex and thalamus [97]. Simultaneous recording of EEG/MEG showed that, like the prior reports in cats, spindles are highly synchronous across the scalp in the electroencephalogram (EEG). However, they had had a low spatial coherence in MEG. In addition, the correlation between the MEG and EEG signature of the same graphoelements were low [26, 98]. Aside from the variability in spindle frequency and its phase across locations, MEG also manifested a pronounced variability across spindles, and early vs late segments of spindles [26, 99]. Depth and grid intracranial recordings (iEEG) further certified that, in contrast to the scalp EEG, cortical spindles show strong dissociations in their phase and amplitude. Current source density (CSD) from transcortical laminar recordings proved the existence of two patterns of spindling: a) spindles with sinks in the middle layer, b) spindles with the sink in the superficial layers [98]. The comparatively higher coherence of the superficial spindles, in light of the incoming projections from the matrix thalamocortical system to these layers [100, 101], suggested a possible sensitivity of EEG to the matrix system and its diffuse targets across wider areas of the cortex. In contrast, it seems that the MEG may be more sensitive to the focal thalamocortical core system. The scenario can be summarized as poor sensitivity of MEG (relative to EEG and due to spatiotemporal cancellation), to widespread synchronous generators along with it higher relative sensitivity to focal generators [26, 98, 102]. These findings and hypotheses were further confirmed by the experimental and computational studies of spindles [103, 104]. Moreover, it was found that in some cases spindles are only seen by MEG and when they are detected by both MEG and EEG, the oscillatory fingerprint starts earlier and last longer in the case of MEG. This study suggests that EEG spindles emerge when MEG spindles become synchronized and activate diffuse generators visible to EEG [105]. Thus, it is possible that EEG and MEG have differential sensitivity to thalamocortical core and matrix systems. This conjecture further adds to the complexity of discerning the sources of the measured multiscale signal.

2.5 Spatial reach of LFP & Electromagnetic Lead field

One of the complex features of the LFP is its spatial reach. Some investigations pointed to a possible extreme locality of LFP [106, 107]. However, the majority of other reports have provided evidence to the contrary. These studies report a much more extensive scope of LFP, horizontally or vertically, ranging from few hundred microns up to few millimeters [68, 108–111]. Recent experimental and biophysically-driven computational studies, shed light on this issue and bring them together as two sides of the same coin, in that the LFP spatial reach is not statically fixed [96, 112]. It has been shown that LFP can expand beyond its microdomain and, through volume conduction, be detected many millimeters distant to its active generator. Such volume-conducted potential may reach the surface of the cortex from deep layer generators [111, 112]. These studies show that LFPs may reflect two different modes: I) a less differentiated but more local versus ii) a more differentiated but less local mode. It is the synchrony that dictates whether the coin is flipped to reflect very local or loosely local neural population signature. In the case of uncorrelated synaptic input to a population of neurons, the measured LFP only reflects the activity within its 200 micrometer perimeter [96]. This finding is in line with the predictions of Nunez and Srinivasan which indicate that isolated stimuli which activate a very small area will invoke LFPs that have a very limited spatial reach [75]. When the synaptic currents are correlated, the activated area is larger and its spatial reach is wider.

In parallel to the spatial reach of LFP, the sensitivity patterns of the MEG and EEG sensors is known as the lead fields of the sensors. These ”lead fields” are calculated based on the implemented forward predictor. A variety of situation may lead to a microscopic or macroscopic ”silent source” for either MEG, EEG or both. These ”silent sources” do not generate any scalp potentials or extracranial magnetic fields at all [65, 78]. Therefore, comparison of MEG and EEG lead fields is not straightforward. The complexity of this comparison lies in their differential characteristics in a few main categories. First, MEG has an advantage over EEG in the insensitivity of the magnetic field to tissue conductivity differences (see section below for details). In this case, EEG is affected by MEG is not. For example, CSF will have a very minimal effect on MEG but because of its high conductivity, it amplifies EEG’s leadfield. Secondly there is an orientation selectivity/bias; this factor mainly affects MEG. In a symmetric spherical conductive volume, the radial sources are invisible to the magnetic sensor outside [8, 113]. In an analogy, MEG sensors are blind to the dipoles that are oriented perpendicular to the inner surface of the skull and thus are normal to the surface of the magnetic sensors [23, 76, 114]. One should note that because of the convolutions of the cortex, these so-called, radial dipoles may be originating from either gyri or sulci. In contrast to MEG sensors, EEG lead fields see both tangential and radial sources due to the fact that both of these sources produce return currents. [76, 114–117]. Thirdly, MEG’s relative blindness to the deep sources is caused by loss of its sensitivity to the small fluctuations in the magnetic field. Assuming that the generator is a current dipole, the sensor’s sensitivity drops proportional to distance squared between source and sensor [8, 76, 77]. Goldenholz et al have shown that MEG is more sensitive to superfi-

cial sources and EEG is more sensitive to deep sources [118]. Lastly one must consider signal cancellation due to the complex spatial configuration of the sources. In the case of both EEG and MEG, closely opposing dipole sources cancel each other. This could happen in variety of complex spatial configuration. An example is the cancellation of sources of the walls of the sulcus due to their orientation disparity. In such a case, it is possible that even tangential dipoles get canceled out and therefore do not reach the sensors [116, 119]. In addition, when distributed sources become simultaneously active, there is a chance for widespread cancellation of the sources [115,116,119]. Selective cancellation of signals due to background brain activity significantly contributes to the signal to noise ratio (SNR) of the source of interest in MEG vs. EEG [116, 118, 119]. In the light of all these complexities and individual sensors differences in their lead fields, it is always essential to record from a large number of sensors in order to deduce the information about the spatial distribution of the sources [78].

There are few of points that are worth mentioning in this section. First, the independence of the LFP spatial reach from the morphology of the neurons and the spatial distribution of the synapses [96] does not match with the concept of ”silent sources” as discussed above. Although the closed sources were defined for mesoscopic models [65], it is very likely that the complex geometry of source distribution within a microdomain of the cortex dramatically affects the eventual net electrical field and orientation magnitude. Second, if according the Riera et al. ([85]) monopoles participate in the field generation, then the lead field or spatial reach are no longer going to be solely affected as the inverse of squared distance ($1/r^2$), but rather the monopole sources attenuate much more sharply [63]. This scenario also makes the prediction of forward models more complex. Finally, in order to gain maximal information about the lead field, it may be very good to i) increase the number of sensing electrodes and ii) combine modalities from different scales; for example, simultaneous iEEG and MEG [120] or laminar electrode with grid [98].

2.6 Frequency-dependent characteristics: Low-pass filtering and its effect on frequency scaling

To begin, it is important to note that the model in [96] has certain assumptions that dictate the fate of its predictions. While this model factors out the frequency-dependence of LFP spatial reach, there is evidence that both intrinsic dendritic filtering of the LFP at the level of individual neurons [68, 121] as well as frequency dependence of the extracellular medium [122, 123] could play a significant role in imposing a frequency-dependence of LFP spatial reach, in vivo. Moreover, the linearity of the model based on its prior assumptions like passive dendrites and current-based synaptic inputs, is inconsistent with the existent knowledge of nonlinear interaction of transmembrane current and membrane potential [124, 125].

There are a few types of low-pass filterings that affect the electromagnetic signature of neural activity. Filtering effects on EEG signal is more aggressive and frequency dependence of the conductivity of the tissues within the head, acting as a temporal filter, imposes a considerable effect on the EEG [126]. The reason is because EEG is not only influenced by non-resistivity of the extracellular medium, but also must propagate through various media, such as cerebrospinal fluid (CSF), dura mater, cranium, muscle and scalp skin. By comparison, LFP is less filtered; however, it still is influenced because the signals coming from the sources must pass through the extracellular medium to reach the recording electrode [63]. These frequency filtering properties cause the action potential to have minimal contribution to the LFPs, unless the distance to the recording electrode is very small. Such investigations predict that the relative position of the neuron, with respect to the electrode, as well as the detailed morphology affect the amplitude of the extracellularly recorded spikes [35, 62, 66]. The overall effect is that signals of a high frequency nature travel minimally while low frequencies propagate more widespread pattern. The result is that the action potentials are only recorded by nearby electrodes while the LFP reflects signals coming from a larger population. Moreover, neuronal dendritic morphology also acts as an additional source of low-pass frequency filtering effect for the field potential (for both LFP and EEG). This type of filtering is mediated by the passive cable properties of the dendritic tree structure [68, 121].

1/ f spectra can be the signature of self-organized critical phenomena [127, 128]. Frequency scaling has been reported in the power spectra of EEG [129, 130], MEG [131], intrarcranial recordings (iEEG) from epileptic patients [132, 133] as well LFP from awake cats [134]. It has been suggested that neuronal activity, manifested in spiking and LFP, could be orchestrated according to a self-organized fashion [135]. Alternatively, this frequency dependence of the impedance could be a phenomenon that is caused by ionic diffusion and the filtering properties of the currents through extracellular media rather than being influenced by the dendritic low-pass filtering [63, 136]. According to this hypothesis, the observed 1/f scaling in measurements of the electrical field (LFP, iEEG and EEG) have the same origins in frequency filtering by extracellular media. This view is further supported by the consistency of the predictions of this type of filtering with the transfer function between simultaneously recorded intracellular and extracellular potentials [123].

2.7 Nonuniformity of the extracellular space and inhomogeneity of the conductive medium

The assumption of homogeneity of the extracellular medium has been widely adapted in the models of LFP and EEG [75,137]. The simplicity of the resultant constant conductivity/permittivity variable in Maxwell equations has made this assumption a popular one. Such models do not allow for the frequency-dependence of signals of extracellular origin [63]. This approach is sup-

ported by findings of an experimental study [138] which reported that the extracellular medium is purely resistive. However, these experimental findings are opposed by comprehensive studies of the conductivity in biological tissue [139–141]. For a comparison between the findings by Logothetis vs Gabrieli and the plausible pitfalls of the experimental conditions , see a recent review [63]. Moreover, it is known that at the microscale level, the structural composition of the extracellular space is highly inhomogeneous [142, 143].

Similarly, the inverse solution of the macroscale electromagnetic signal is also sensitive to the conductivities of the medium [8,77,144,145]. Although, because of the adaptation of mesoscopic current dipole elements in the case of EEG/MEG inverse solution, the conductivity issue is more limited to tissues ”en large” rather than the small elements in a cortical column. To be precise, it has been shown that cerebrospinal fluid (CSF), skull, scalp white matter and gray matter each have their own specific conductivities. For example, it was reported that CSF is much more conductive than the cellular brain tissue [146–148]. The skull itself was found to be composed of a low-conducting part named compacta and much better conducting one called spongiosa [149, 150]. Recent advancements have led to the development of numerous in vivo methods for measuring conductivities of different tissues in the head. [151–156]. It is important to point out that MEG and EEG have different conductivity profiles. Skull conductivity imposes great smearing of the EEG signal, thus reducing its spatial resolution, while MEG is largely unaffected [8, 150]. Modeling MEG, advantageously, requires a much simpler volume conductor model and fewer tissue boundaries. It has been shown that approximating the outer skull surface by an isotropic sphere or by a set of overlapping spheres seems to perform on par with more computationally demanding boundary element methods [76, 157]. The reasoning behind this model is the assumption that MEG is mostly sensitive to the impressed current (and not to the ohmic return current) and the induced magnetic field in an infinite medium is independent of the conductivity [77].

These characteristics also become crucial in cross-scale studies aiming to connect the mesoscale field potentials (iEEG) to macro-scale field potentials (EEG). It has been shown that holes in the skull affects the conductivity pattern. Therefore in simultaneous iEEG/EEG recordings, the relation between the two becomes quite complex unless such conductivity changes are taken into account. Beside invasive (simultaneous iEEG and EEG) determination of these altered conductivities [155], an indirect MR-based method (Diffusion Tensor Magnetic Resonance Imaging) has also been developed [152, 156].

2.8 Influence of tissue conductivity anisotropy

In micro-meso scale forward models, the assumptions is that conductivity in all 3 directions (of x,y,z) is equal [62]. These assumptions, as discussed before, are based on a study reporting homogeneity of conductivity in the grey matter of monkey cortex [138]. Others have shown ev-

idence of anisotropy in the rat barrel cortex [158, 159]. There is a possibility that some of these differences could be species-dependent. However, it seems that the reports by Logothetis et al are inconclusive without further quantitative analysis [159]. Moreover, in another series of studies done with great emphasis on details, strong evidence of nonhomogeneity in different tissues are provided [139–141]. (for a detailed critical evaluation of the technical aspects of these two studies and their potential shortcomings, see [63]). Additionally, , if the lack of anisotropy were to be true, then the spatial reach of LFPs should not be directionally different. Studies by Goto et al report that horizontal conductivity is half of the vertical direction [159]. Some studies have reported a vertical volume conduction of layer IV LFPs reaching the cortical surface [111, 112]. This observation satisfies the evidence for anisotropy at a micro-meso scale. Yet still, the common practice of forward modeling is based on the assumption of isotropic conductivity. Recent advances in studies of connectomics or synaptomics [160, 161], will certainly provide an opportunity to not only have a better understanding of the cerebral microcircuitry [162], but also to have a better formulation of the micro-meso scale volume conductor.

At the meso-macro scale, evidence of strong anisotropy of the brain tissue has been put forward by number of studies [147, 156, 163, 164]. A recent technically demanding study has provided very orderly anisotropic rules of the white matter [165]. These anisotropies, depending on their location, would cause different levels of perturbation on the electrical field. For example, in the case of skull anisotropy, a severe smearing effect has been observed. However, these types of anisotropy do not affect the MEG [147, 150].

Anisotropy of the white matter forces the return currents to flow in parallel to the white matter fiber tracts. Naturally, superficial sources are not much affected by this factor before reaching the extracranial sensors. In contrast, deeper source being surrounded by more of such anisotropies will affect both MEG and EEG cases [77]. It is possible to non-invasively estimate the white matter anisotropy based on the Diffusion tensor imaging (DTI) [154, 156, 166]. In comparison to isotropic models, such anisotropic model shows an improved performance in the calculation of intracranial EEG forward solution [166].

2.9 State-dependent characteristics

Nonlinear influences of dynamic changes in ionic conductance states [167], the leaky conductance in rest versus high conductance in up state [31] along with the common features of ”up state” and slow-wave sleep [168, 169], enforce a complex state-dependent nonlinear local dynamics that is not accounted for in these experimental/computational studies. The computational consequences of high conductance state, i.e. ”enhanced responsiveness and gain modulation” [170], ”modulation of intrinsic neuronal properties” [171, 172], ”increased temporal resolution” [173] and the resultant randomness in synaptic activity, lead to the emergence of stochasticity in neural dynamics. Therefore, as it has been shown, that the spatial correlation of

LFPs changes according the state of the cortical dynamics [174].

Chapter 3

Neural avalanche dynamics

In physics we have dealt hitherto only with periodic crystals.

Erwin Schrodinger

3.1 Self-organized criticality

The dynamics evolution of many natural complex systems happens close to a phase transition point. Systems which maintain themselves at (or close to) a phase transition point, are called self-organized critical (SOC) systems. The so-called ”critical configuration” keeps such dissipative dynamical systems with many degrees of freedom to operate near the phase transition. This critical configuration internally fine tunes the evolution the system [128, 175]. After perturbation by external stimuli, such systems return back to equilibrium. This behavioral dynamic leads to the emergence of punctuated equilibrium [175].

The family of SOC systems was introduced by Bak, Tang and Wiesenfeld [127]. SOC systems have been observed in many different natural phenomena, from sandpiles, to rice piles, in forest fires and earthquakes [128, 175–178]. Scale-invariance is a fundamental characteristic of SOC systems. The power-law distribution of characteristics of the system's dynamics, such as event size or the waiting time between events, is usually considered as the evidence for scale-invariance. Therefore, the temporal fingerprint of SOC systems is often described by $1/f$ or $1/f^2$ noise and their spatial signature is manifested as a scale-invariant fractal [128, 175]. These features indicate a tendency toward long-lasting temporal or long-range spatial correlations in the system.

Non-critical systems' response to perturbations relies on their characteristic response time and spatial tuning [128]. In contrast, critical systems may respond with different magnitudes in perturbations each time they are pushed by a given stimulus. This property is preserved to achieve punctuated equilibrium. This characteristic of SOC systems, brings them to the spotlight as a candidate for neural information processing. Specifically, if an SOC state were to be responsible for neural processing, then the recruitment of "avalanches" would substitute oscillations or waves as the pillar for neural coding.

The dynamics of SOC systems are structured as "avalanches" of activity, separated by silent periods. Avalanche sizes are typically distributed as a power law, which is particularly interesting for the scale invariance it presents[1]. Power-laws are ubiquitous features in many physical phenomena such as phase transitions. In these cases, the exponent is called the critical exponent. Diverse natural systems, as they evolve toward criticality, show the same critical exponent. This may indicate some unifying underlying dynamics for such systems of such nature.

3.2 Neural avalanches

As mentioned above, it is of crucial interest to evaluate whether neural avalanche recruitments follow a power-law distribution. In such a case, the power-law could be a signature for the underlying critical dynamics in the neural network. If neural networks were to operate near criticality, rather than the usual wave-type, oscillatory or stochastic dynamics, it would then rely on long-lasting and long-range correlations.

Evidence of SOC in the spontaneous activity of neural network was first shown by Beggs and Plenz *in vitro* [135]. The distribution of neural events (or "neuronal avalanches") was reported to follow the power-law distribution. This feature was interpreted as evidence for self-organized criticality in the nervous system (see also [179] for retinal spontaneous activity). Microscale scale-invariant dynamics were originally reported in spontaneous cortical activity of *in vitro* preparations, i.e. slice cultures and acute slices, and later in the anesthetized rat (in vivo) [135, 180]. In all these studies, nLFPs, i.e. local maximas of negative deflections in LFPs above some threshold, was the reference for creating the avalanche data. Later, studies of spike avalanche in dissociated cultures also suggested that the avalanches follow a power-law regime and therefore cortical dynamics are of a self-organizing nature. [181].

The presence of avalanches is however controversial *in vivo*. Often with no real "pause" in the firing activity of a large network, it becomes difficult to properly define the "avalanche" in the awake in vivo state. [30, 134]. In an early study on awake cats, it was shown that the spectrum of local field potential (LFP) scales as 1/f. However, spike recordings did not follow

[1] firstTo be precise, if the probability of observing value x for a given variable is a power-law, $p(x) = ax^{-\alpha}$, then scaling x by a constant factor yields to a proportional law: $p(cx) = ac^{-\alpha}x^{-\alpha}$.

a power-law distribution. [134]. It was suggested that the observed power-law in discretized LFPs of prior studies could be attributed to the filtering of the propagated electrical field in the extracellular medium [134, 136].

In contrast, later studies report that in anesthetized cats [182] and awake monkeys [183], power-law distributed avalanches are present in the negative peaks of the local field potentials (LFP). Based on the assumption that LFP negative peaks are statistically related to neuronal firing, this scale-invariant behavior was taken as evidence for self-organized criticality. These observed power-laws in the negative LFP peak were then criticized in a later report showing that even purely stochastic processes can display power-law scaling when subjected to similar thresholding procedures [184]. It has to be emphasized that stochastic mechanisms, other than SOC, are perfectly capable of manifesting power-law statistics [184–186]. There are many different scenarios that lead to the emergence of spurious power-law. For example, sudden termination of exponentially growing processes will lead to heavy tail power-like distribution [187]. This case would be similar to a non-stationary Poisson processes, or combining Poisson processes at different rates, a situation that is likely to happen in the nervous system. Such scenarios can give rise to spurious power laws.

These contrasting results correspond to different preparations and recording techniques, single units or LFPs, or different species, so that it is difficult to compare them. In Chapter 7, we attempt to overcome these shortcomings by providing a systematic analysis of both units and LFPs for different species and different brain states.

Part II

Studies

Chapter 4

Overview

If biologists have ignored self-organization, it is not because self-ordering is not pervasive and profound. It is because we biologists have yet to understand how to think about systems governed simultaneously by two sources of order, Yet who seeing the snowflake, who seeing simple lipid molecules cast adrift in water forming themselves into cell-like hollow lipid vesicles, who seeing the potential for the crystallization of life in swarms of reacting molecules, who seeing the stunning order for free in networks linking tens upon tens of thousands of variables, can fail to entertain a central thought: if ever we are to attain a final theory in biology, we will surely, surely have to understand the commingling of self-organization and selection. We will have to see that we are the natural expressions of a deeper order. Ultimately, we will discover in our creation myth that we are expected after all.

Stuart Kauffman

4.1 Electromagnetic properties of the extracellular medium

The electromagnetic nature of the extracellular medium is an essential component of the field potentials modeling in neural tissue. In the chapter 2, we provided extensive details on the characteristics of the medium. Here, we briefly re-sketch those concepts and formulate our approach to study this issue in the case of large scale non-invasive recordings (i.e. EEG and MEG).

In general, the extracellular space around neurons is considered as a purely resistive medium [75]. A resistive (or Ohmic) medium simply replaces the extracellular space with a simple resistance. This approach turns the Maxwell equations into quasi-static ones and significantly simplifies the computations of the field potentials. The outcome of such an assumption is that everything adds up linearly and the extracellular potentials can be estimated from the joint activity of all the existent elements within the studied volume [75, 188]. This approach is also routinely practiced in electromagnetic source localization. In forward/inverse solution, in macroscopic modeling of the medium, the assumption of resistivity is the cornerstone of forward predictor calculations. Thus, any inverse solution based on such forward models also treats the medium as a simple linearly resistive one [76, 189, 190]. However, if we formulate the medium in a non-resistive fashion, the assumption of a quasi-static approximation of Maxwell equations is no longer valid and the equations become significantly more complex [122]. In such a case, the generators within the volume no longer add up in a simple linear fashion and the sum will be greater than its parts.

As mentioned in the chapter 2, the experimental evidence about the non-resistive characteristics of the medium are contradictory. Some experiments report pure resistivity to be the case [138] while others present it to be of a non-resistive nature [139–141, 191].This issue is still subject for debate as none of these studies followed an experimental setup that would allow the use of currents at the level of physiological perturbations in the medium. Using high current intensities masks the filtering properties of the tissue by preventing phenomena such as ionic diffusion [192]. Details of the potential pitfalls in these experiments are discussed elsewhere [63]. In summary, these studies are inconclusive and further work is needed to test this issue experimentally.

In chapter 2, we also presented the case for different characteristics of EEG and MEG. Their rather complex comparative features in terms of lead fields and synchrony, as well as differential sensitivity to tissue conductance is the bases for the formulation of our study. In Chapter 5, we propose an indirect method to estimate whether or not extracellular space can be considered a purely resistive medium. Like others, we base our assumptions on a non-capacitive medium. We then show theoretically that in such cases, the frequency-scaling of the EEG and MEG should behave similarly. We then test the spectral scaling of simultaneous EEG and MEG measurements in humans. In doing so, we adapt noise corrections for MEG. This comparative characterization of frequency scaling provides a window to address the question of

the non-resistivity of the medium.

4.2 State-dependent spatiotemporal dynamics of cortical microcircuitry

In chapter 2, we reviewed the state-dependent modulation of LFP correlations. We also discussed the case for LFP-spike relationship and how their features can help us discern the nature of the generators in invasive recordings. In humans, intracranial recordings are routinely used as a means to localize epileptogenic foci prior to surgical treatment of epileptic foci. Recent advances in these extracellular recordings have provided a chance to record from an ensemble of neurons using microwires [193] or 2D multielectrode arrays [60]. Such recording systems have been shown to provide excellent recordings of single-neuron activity in human cerebral cortex (for recent reports, see [194–196]). In our experiments, we used the so-called Neuroport electrodes based on Utah electrode arrays. A methodological count of the properties of these high density multielectrode arrays is provided in chapter 6.

Using these electrodes, we were able to tackle the state-dependent spatiotemporal dynamics in the human cortex. Such dynamics manifest rich characteristics of excitation/inhibition interaction. As the local dynamics are shaped by these two different populations, studying their functional relationship is crucial in our understanding of microcircuitry of the cortex. In animal experiments, it is possible to separate units between “regular-spiking” (RS) and “fast-spiking” (FS). In rat hippocampus, RS and FS cells can be reliably separated based on spike waveform, duration and mean firing rate [40]. This type of separation was validated using intracellular and juxtacellular recordings simultaneous with extracellular recordings from the same neurons in vivo [197–199]. A similar approach was also used to successfully separate units into RS and FS cells in human hippocampus [41].

To date, such validation experiments are not available for human cerebral cortex. Nonetheless, it was previously shown that separation between RS and FS cells is possible and reliable using high-density recordings in rat cerebral cortex [39, 200]. As for hippocampal recordings, this separation results in different waveforms, rates and autocorrelations. In addition, occasional monosynaptic connections confirmed the excitatory nature of RS cells, and similarly that FS cells are inhibitory.

We follow the same approach using high-density microelectrode arrays in human cerebral cortex as described in Chapter 1. We attempt to separate extracellularly-recorded units into RS and FS cells, and to investigate their excitatory or inhibitory nature based on monosynaptic connections. Using this morpho-functional approach, we divide the cells into two clusters of putative inhibitory (FS) and putative excitatory (RS). We then evaluated their network interaction in different states of consciousness. In chapter 6 and 8, we present an extension of this

study where we test the balance of excitation and inhibition in different states and quantify the dynamic multiscale correlation within the microcircuitry of the human neocortex.

4.3 Neural avalanche dynamics

In chapter 3, we briefly overviewed self-organized critical (SOC) systems. We discussed their discoveries [127], dynamical properties [128, 175] and their spatiotemporal signatures. We also briefly discussed why SOC systems are appealing to the eye of neuroscientists from an information coding point of view. A stark contrast between a neural network operating in SOC mode with one that relies on oscillatory and stochastic properties is in long-range and long-time correlation within the system. In an SOC system, the recruitment of avalanches is the defining characteristic of its dynamic.

One of the fundamental the characteristics of SOC systems is the occurrence of "avalanches" of activity, separated by quiescent periods. The probability of occurrence $p(x)$ of a given avalanche size x typically follows a power-law:

$$p(x) \sim x^{-\alpha} ,$$

where α is the scaling exponent of the distribution.

As discussed previously, if a system manifests power-law, then it is likely that it is of an SOC nature. A number of in vitro studies (slices/cultures) provide evidence of a power-law distribution and thus verify the assumption of neural avalanches. However, the existence of power-law in an intact brain in vivo is a subject for debate. Some prior studies have shown evidence of criticality in invasive recordings from the cortex [135, 182, 183]. In parallel, there are also some large-scale non-invasive recordings that have reported the presence of spectral 1/f in MEG and EEG recordings [130, 131]. In contrast, some reports have shown that the spiking activity in awake in cats does not scale as power-law [134] and that stochastic processes subjected to the arbitrary thresholding of LFP could also show spurious power-laws [184] and that the observed 1/f scaling in LFP could be described based on the filtering properties of the extracellular medium [136]. Footnote: (For a comprehensive review of criticality research in nervous system, see [186]).

To overcome these controversies, in our investigations, we studied the system at both ends of the scale. The spectral frequency scaling of MEG and EEG was accomplished with detailed attentions to the MEG noise as well considering the SNR and topographical distribution of the sensors with different lead fields (chapter 2). In studying spike/LFP avalanches, we approached the system at multiple conscious states of wakefulness, slow-wave sleep (SWS) and rapid-eye movement (REM). To avoid species-specific findings, we used multielectrode recordings from cats, monkeys and humans, sometimes from two cortical locations recorded simultaneously. In

all these preparations, we used the data from Utah electrode arrays (see chapter 1 for instrumentation details). In addition to studying avalanches in spiking activity, we also studied LFP avalanches. In our examination, we investigated both the negative LFP (nLFP) peaks (which is related to spiking of neurons) as well as the positive LFP (pLFP) peaks, which are not related to neuronal firing. To analyze this extensive set of data, from multi-states, multi-species, multiple cortical areas and multiple scales, we used rigorous methods that are proposed to be capable of discerning true power-laws from spurious observations [201]. These studies are presented in chapter 7.

Chapter 5

MEG/EEG Spectra

It is the harmony of the diverse parts, their symmetry, their happy balance; in a word it is all that introduces order, all that gives unity, that permits us to see clearly and to comprehend at once both the ensemble and the details.

Henri Poincaré

Comparative power spectral analysis of simultaneous elecroencephalographic and magnetoencephalographic recordings in humans suggests non-resistive extracellular media

Nima Dehghani[1,*], Claude Bédard[1,*], Sydney S. Cash[2], Eric Halgren[3], Alain Destexhe[1]

1 Laboratory of Computational Neuroscience. Unité de Neurosciences, Information et Complexité (UNIC). CNRS. Gif-sur-Yvette, France.
2 Department of Neurology, Massachusetts General Hospital and Harvard Med. School, Boston, MA, USA.
3 Multimodal Imaging Laboratory, Departments of Neurosciences and Radiology, University of California San Diego, La Jolla, CA, USA.
∗ co-first authors. [1]

[1]Author contributions: N.D., C.B. and A.D. designed research; N.D., E.H., and S.S.C. performed research; N.D. designed the theoretical aspects of analyses and analyzed the data; C.B designed the theoretical comparison; and N.D., C.B., E.H., S.S.C., and A.D. wrote the paper.

5.1 Summary

The resistive or non-resistive nature of the extracellular space in the brain is still debated, and is an important issue for correctly modeling extracellular potentials. Here, we first show theoretically that if the medium is resistive, the frequency scaling should be the same for electroencephalogram (EEG) and magnetoencephalogram (MEG) signals at low frequencies ($<$10 Hz). To test this prediction, we analyzed the spectrum of simultaneous EEG and MEG measurements in four human subjects. The frequency scaling of EEG displays coherent variations across the brain, in general between $1/f$ and $1/f^2$, and tends to be smaller in parietal/temporal regions. In a given region, although the variability of the frequency scaling exponent was higher for MEG compared to EEG, both signals consistently scale with a different exponent. In some cases, the scaling was similar, but only when the signal-to-noise ratio of the MEG was low. Several methods of noise correction for environmental and instrumental noise were tested, and they all increased the difference between EEG and MEG scaling. In conclusion, there is a significant difference in frequency scaling between EEG and MEG, which can be explained if the extracellular medium (including other layers such as dura matter and skull) is globally non-resistive.

Reference:
J Comput Neurosci. 2010 Dec;29(3):405-21. Epub 2010 Aug 10. "Special issue on modeling extracellular potentials"

Keywords:
EEG , MEG; Local Field Potentials , Extracellular resistivity , Maxwell Equations , Power-law

5.2 Résumé

La nature résistive ou non-résistive du milieu extracellulaire est toujours débattue, mais elle constitue un élément important pour la modélisation des potentiels extracellulaires. Nous montrons d'abord théoriquement, que si le milieu est résistif, le comportement d'echelle en fréquence doit être le même pour les signaux d'électroencéphalogramme (EEG) et magnétoencéphalogramme (MEG) à basse fréquence ($<$10 Hz). Afin de tester cette prédiction, nous avons analysé le spectre d'enregistrements EEG et MEG simultanés de quatre sujets humains. Le comportement d'échelle en fréquence de l'EEG montre des variations cohérentes sur la surface du cerveau, avec des exposants en général compris entre $1/f$ et $1/f^2$; ces exposants tendent à être plus faibles dans les régions temporales et pariétales. Dans une région donnée, les exposants de la MEG ont une variabilité plus grande que pour l'EEG, mais les deux signaux ont systématiquement un exposant différent. Dans certains cas, les exposants sont proches, mais ces cas correspondent à un mauvais rapport signal/bruit pour la MEG. Plusieurs méthodes de corrections du bruit instrumental et environmental ont été testées, et dans tous les cas, ces méthodes augmentent la différence de comportement spectral entre l'EEG et la MEG. En conclusion, il y a une différence significative de comportement déchelle en fréquence entre EEG et MEG, ce qui peut être expliqué si le milieu extracellulaire (incluant d'autres couches telles que la dure-mère et le crâne) est globalement non-résistif.

5.3 Introduction

An issue central to modeling local field potentials is whether the extracellular space around neurons can be considered as a resistive medium. A resistive medium is equivalent to replacing the medium by a simple resistance, which considerably simplifies the computation of local field potentials, as the equations to calculate extracellular fields are very simple and based on Coulomb's law [75, 188]. Forward models of the EEG and inverse solution/source localization methods also assume that the medium is resistive [76, 189, 190]. However, if the medium is non-resistive, the equations governing the extracellular potential can be considerably more complex because the quasi-static approximation of Maxwell equations cannot be made [122].

Experimental characterizations of extracellular resistivity are contradictory. Some experiments reported that the conductivity is strongly frequency dependent, and thus that the medium is non-resistive ([139–141, 191]. Other experiments reported that the medium was essentially resistive [138]. However, both types of measurements used current intensities far larger than physiological currents, which can mask the filtering properties of the tissue by preventing phenomena such as ionic diffusion [192]. Unfortunately, the issue is still open because there exists no measurements to date using (weak) current intensities that would be more compatible with biological current sources.

In the present paper, we propose an indirect method to estimate if extracellular space can be considered as a purely resistive medium. We start from Maxwell equations and show that if the medium was resistive, the frequency-scaling of electroencephalogram (EEG) and magnetoencephalogram (MEG) recordings should be the same. We then test this scaling on simultaneous EEG and MEG measurements in humans.

5.4 Methods

5.4.1 Participants and MEG/EEG recordings

We recorded the electromagnetic field of the brain during quiet wakefulness (with alpha rhythm occasionally present) from four healthy adults (4 males ages 20-35). Participants had no neurological problems including sleep disorders, epilepsy, or substance dependence, were taking no medications and did not consume caffeine or alcohol on the day of the recording. We used a whole-head MEG scanner (Neuromag Elekta) within a magnetically shielded room (IMEDCO, Hagendorf, Switzerland) and recorded simultaneously with 60 channels of EEG and 306 MEG channels [202]. MEG SQUID (super conducting quantum interference device) sensors are arranged as triplets at 102 locations; each location contains one "magnetometer" and two orthogonal planar "gradiometers" (GRAD1, GRAD2). Unless otherwise noted, MEG will be used

here to refer to the magnetometer recordings. Locations of the EEG electrodes on the scalp of individual subjects were recorded using a 3D digitizer (Polhemus FastTrack). HPI (head position index) coils were used to measure the spatial relationship between the head and scanner. Electrode arrangements were constructed from the projection of 3D position of electrodes to a 2D plane in order to map the frequency scaling exponent in a topographical manner. All EEG recordings were monopolar with a common reference. Sampling rate was 1000 Hz.

For all subjects, four types of consecutive recordings were obtained, in the following order: (1) Empty-room recording; (2) Awake "idle" recording where subjects were asked to stay comfortable, without movements in the scanner, and not to focus on anything specific; (3) a visual task; (4) sleep recordings. All idle recordings used here were made in awake subjects with eyes open, where the EEG was desynchronized. A few minutes of such idle time was recorded in the scanner. For each subject, 3 awake segments with duration of 60 seconds were selected from the idle recordings (see example signals in Fig. 5.1).

As electrocardiogram (ECG) noise often contaminates MEG recordings, Independent component analysis (ICA) algorithm was used to remove such contamination; either Infomax ([25] or the "Jade algorithm" from the EEGLAB toolbox [203] was used to achieve proper decontamination. In all recordings, the ECG component stood out very robustly. In order not to impose any change in the frequency content of the signal, we did not use the ICA to filter the data on any prominent independent oscillatory component and it was solely used to decontaminate the ECG noise. We verified that the removal of ECG did not change the scaling exponent (not shown).

In each recording session, just prior to brain recordings, we recorded a few minutes of the electromagnetic field present within the dewar in the magnetic shielded room. Similar to wake epochs, 3 segments of 60 seconds duration were selected for each of the four recordings. This will be referred to "empty room" recordings and will be used in noise correction of the awake recordings.

In each subject, the power spectral density (PSD) was calculated by first computing the Fast Fourier transform (FFT) of 3 awake epochs, then averaging their respective PSDs (square modulus of the FFT). This averaged PSD was computed for all EEG and MEG channels in order to reduce the effects of spurious peaks due to random fluctuations. The same procedure was also followed for empty-room signals.

5.4.2 Noise correction methods

Because the environmental and instrumental sources of noise are potentially high in MEG recordings, we took advantage of the availability of empty-room recordings to correct for the presence of noise in the signal. We used five different methods for noise correction, based on

different assumptions about the nature of the noise. We describe below these different correction methods, while all the details are given in *Supplementary Methods*.

A first procedure for noise correction, exponent subtraction (ES), assumes that the noise is intrinsic to the SQUID sensors. This is justified by the fact that the frequency scaling of some of the channels is identical to that of the corresponding empty-room recording (see Results). In such a case, the scaling is assumed to entirely result from the "filtering" of the sensor, and thus the correction amounts to subtract the scaling exponents.

A second class of noise subtraction methods assume that the noise is of ambient nature and is uncorrelated with the signal. This chatacteristics, warrants the use of spectral subtraction (where one subtracts the PSD of the empty-room from that of the MEG recordings), prior to the calculation of the scaling exponent. The simplest form of spectral subtraction, linear multiband spectral subtraction (LMSS), treats the sensors individually and does not use any spatial/frequency-based statistics in its methodology [204]. An improved version, nonlinear multiband spectral subtraction (NMSS), takes into account the signal-to-noise ratio (SNR) and its spatial and frequency characteristics [205, 206]. A third type, Wiener filtering (WF), uses a similar approach as the latter, but obtain an estimate of the noiseless signal from that of the noisy measurement through minimizing the Mean Square Error (MSE) between the desired and the measured signal [207, 208].

A third type of noise subtraction, partial least squares (PLS) regression, combines Principal component analysis (PCA) methods with multiple linear regression [209, 210]. This methods finds the spectral patterns that are common in the MEG and the empty-room noise, and removes these patterns from the PSD.

5.4.3 Frequency scaling exponent estimation

The method to estimate the frequency scaling exponent was composed of steps: First, applying a spline to obtain a smooth FFT without losing the resolution (as can happen by using other spectral estimation methods); Second, using a simple polynomial fit to obtain the scaling exponent. To improve the slope estimation, we approximated the PSD data points using a spline, which is a series of piecewise polynomials with smooth transitions and where the break points ("knots") are specified. We used the so-called "B-spline" (see details in [211].

The knots were first defined as linearly related to logarithm of the frequency, which naturally gives more resolution to low frequencies, to which our theory applies. Next, in each frequency window (between consecutive knots), we find the closest PSD value to the mean PSD of that window. Then we use the corresponding frequency as the optimized knot in that frequency range, leading the final values of the knots. The resulting knots stay close to the initial distribution of frequency knots but are modified based on each sensor's PSD data to provide the

optimal knot points for that given sensor (Fig. 5.2A). We also use additional knots at the outer edges of the signal to avoid boundary effects [212]. The applied method provides a reliable and automated approach that uses our enforced initial frequency segments with a high emphasis in low frequency and it optimizes itself based on the data. After obtaining a smooth B-spline curve, a simple 1st degree polynomial fit was used to estimate the slope of the curve between 0.1-10 Hz (the fit was limited to this frequency band in order to avoid the possible effects of the visible peak at 10 Hz on the estimated exponent).Using this method provides a reliable and robust estimate of the slope of the PSD in logarithmic scale, as shown in Fig. 5.2B. For more details on the issue of automatic non-parametric fitting, and the rationale behind combining the polynomial with spline basis functions, we refer the reader to [213] as well as [214] and [215].

This procedure was realized on all channels automatically (102 channels for MEG, 60 channels for EEG, for each patient). Every single fit was further visually confirmed. In the case of MEG, noise correction is essential to validate the results. For doing so, we used different methods (as described above) to reduce the noise. Next, all the mentioned steps of frequency scaling exponents were carried out on the corrected PSD. Results are shown in Fig. 5.4.

5.4.4 Region of Interest (ROI)

Three ROIs were selected for statistical comparisons of the topographic plots. As shown in Figure 5.4 (panel F), FR (Frontal) ROI refers to the frontal ellipsoid, VX (Vertex) ROI refers to the central disk located on vertex and PT (Parietotemporal) refers to the horseshoe ROI.

5.5 Theory

We start from first principles (Maxwell equations) and derive equations to describe EEG and MEG signals. Note that the formalism we present here is different than the one usually given (as in [216,217], because the linking equations are here considered in their most general expression (convolution integrals), in the case of a linear medium (see Eq. 77.4 in [218]. This generality is essential for the problem we treat here, because our aim is to compare EEG and MEG signals with the predictions from the theory, and thus the theory must be as general as possible.

5.5.1 General formalism

Maxwell equations can be written as

$$\begin{aligned} \nabla \cdot \vec{D} &= \rho^{free} & \nabla \cdot \vec{B} &= 0 \\ \nabla \times \vec{E} &= -\frac{\partial \vec{B}}{\partial t} & \nabla \times \vec{H} &= \vec{j} + \frac{\partial \vec{D}}{\partial t} \end{aligned} \tag{5.1}$$

If we suppose that the brain is linear in the electromagnetic sense (which is most likely), then we have the two following linking equations. The first equation links the electric displacement with the electric field:

$$\vec{D} = \int_{-\infty}^{+\infty} \varepsilon(\tau)\vec{E}(t-\tau)d\tau \tag{5.2}$$

where ε is a symmetric second-order tensor.

A second equation links magnetic induction and the magnetic field:

$$\vec{B} = \int_{-\infty}^{+\infty} \mu(\tau)\vec{H}(t-\tau)d\tau \tag{5.3}$$

where μ is a symmetric second-order tensor.

If we neglect non-resistive effects such as diffusion (Bédard and Destexhe, 2009), as well as any other nonlinear effects[2], then we can assume that the medium is linear. In this case, we can write:

$$\vec{j} = \int_{-\infty}^{+\infty} \sigma(\tau)\vec{E}(t-\tau)d\tau \tag{5.4}$$

where σ is a symmetric second-order tensor [3]. Because the effect of electric induction (Faraday's law) is negligible, we can write:

$$\begin{array}{rclcrcl} \nabla\cdot\vec{D} & = & \rho^{free} & & \nabla\cdot\vec{B} & = & 0 \\ \nabla\times\vec{E} & = & 0 & & \nabla\times\vec{H} & = & \vec{j}+\frac{\partial\vec{D}}{\partial t} \end{array} \tag{5.5}$$

This system is much simpler compared to above, because electric field and magnetic induction are decoupled.

By taking the Fourier transform of Maxwell equations (Eqs. 5.1) and of the linking equations (Eqs. 5.2,5.3,5.4), we obtain:

$$\begin{array}{rclcrcl} \nabla\cdot\vec{D}_f & = & \rho_f^{free} & & \nabla\cdot\vec{B}_f & = & 0 \\ \nabla\times\vec{E}_f & = & 0 & & \nabla\times\vec{H}_f & = & \vec{j}_f+i\omega\vec{D}_f \end{array} \tag{5.6}$$

where $\omega = 2\pi f$ and

$$\begin{array}{rcl} \vec{D}_f & = & \varepsilon_f\vec{E}_f \\ \vec{B}_f & = & \mu_f\vec{H}_f \\ \vec{j}_f & = & \vec{j}_f^{\,p}+\sigma_f\vec{E}_f \end{array} \tag{5.7}$$

[2]Examples of nonlinear effects are variations of the macroscopic conductivity σ_f with the magnitude of electric field $\vec{E}$. Such variations could appear due to ephaptic (electric-field) interactions for example. In addition, any type of linear reactivity of the medium to the electric field or magnetic induction can lead to frequency-dependent electric parameters σ, ε, μ (for a detailed discussion of such effects, see [192].

[3]Note that in textbooks, these linking equations (Eqs. 5.2–5.4) are often algebraic and independent of time (for example, see Eqs. 5.2-6, 5.2-7 and 5.2-8 in [217]. The present formulation is more general, more in the line of Landau and Lifchitz [218].

where the relation $\sigma_f \vec{E}_f$ in Eq. 5.7 is the current density produced by the (primary) current sources in the extracellular medium. Note that in this formulation, the electromagnetic parameters ε_f, μ_f and σ_f depend on frequency[4]. This generalization is essential if we want the formalism to be valid for media that are linear but non-resistive, which can expressed with frequency-dependent electric parameters. It is also consistent with the Kramers-Kronig relations (see [218, 219]).

$\vec{j}_f^p$ is the current density of these sources in Fourier frequency space. This current density is composed of the axial current in dendrites and axons, as well as the transmembrane current. Of course, this expression is such that at any given point, there is only one of these two terms which is non-zero. This is a way of preserving the linearity of Maxwell equations. Such a procedure is legitimate because the sources are not affected by the field they produce[5].

5.5.2 Expression for the electric field

From Eq. 5.6 (Faraday's law in Fourier space), we can write:

$$\vec{E}_f = -\nabla V_f \ . \tag{5.8}$$

From Eq. 5.6 (Ampère-Maxwell's law in Fourier space), we can write:

$$\begin{aligned} \nabla \cdot (\nabla \times \vec{H}_f) &= \nabla \cdot \vec{j}_f + i\omega \nabla \cdot (\varepsilon_f \vec{E}_f) \\ &= \nabla \cdot \vec{j}_f^p - \nabla \cdot ((\sigma_f + i\omega\varepsilon_f)\nabla V_f) = 0 \end{aligned} \tag{5.9}$$

Setting $\gamma_f = \sigma_f + i\omega\varepsilon_f$, one obtains:

$$\nabla \cdot (\gamma_f \nabla V_f) = \nabla \cdot \vec{j}_f^p \tag{5.10}$$

where $\nabla \cdot \vec{j}_f^p$ is a source term and γ_f is a symmetric second-order tensor (3×3). Note that this tensor depends on position and frequency in general, and cannot be factorized. We will call this expression (Eq. 5.10) the "first fundamental equation" of the problem.

5.5.3 Expression for magnetic induction

From the mathematical identity

$$\nabla \times \nabla \times \vec{X} = -\nabla^2 \vec{X} + \nabla(\nabla \cdot \vec{X}) \tag{5.11}$$

[4] In textbooks, the electric parameters are sometimes considered as complex numbers, for example with the notion of phasor (see Section 5.3 in Gulrajani, [217], but they are usually considered frequency independent.

[5] If it was not the case, then the source terms would be a function of the produced field, which would result in more complicated equations

it is clear that this is sufficient to know the divergence and the curl of a field $\vec{X}$, because the solution of $\nabla^2 X$ is unique with adequate boundary conditions.

As in the case of magnetic induction, the divergence is necessarily zero, it is sufficient to give an explicit expression of the curl as a function of the sources.

Supposing that $\mu = \mu_o \delta(t)$ is a scalar (tensor where all directions are eigenvectors), and taking the curl of Eq. 5.6 (D), multiplied by the inverse of γ_f, we obtain the following equality:

$$\nabla \times (\gamma_f^{inv} \nabla \times \vec{B}_f) = \mu_o \nabla \times (\gamma_f^{inv} \vec{j}_f^{p}) \tag{5.12}$$

because $\nabla \times \vec{E}_f = 0$. This expression (Eq. 5.12) will be named the "second fundamental equation".

5.5.4 Boundary conditions

We consider the following boundary conditions:

1 - on the skull, we assume that $V_f(\vec{r})$ is differentiable in space, which is equivalent to assume that the electric field is finite.

2 - on the skull, we assume that $\hat{n} \cdot \gamma_f \nabla V_f$ is also continuous, which is equivalent to assume that the flow of current is continuous. Thus, we are interested in solutions where the electric field is continuous.

3 - because the current is zero outside of the head, the current perpendicular to the surface of cortex must be zero as well. Thus, the projection of the current on the vector $\hat{n}$ normal to the skull's surface, must also be zero.

$$\hat{n}(\vec{x}) \cdot \gamma_f \nabla V_f(\vec{x}) = 0 \tag{5.13}$$

The latter expression can be proven by calculating the total current and apply the divergence theorem (not shown).

5.5.5 Quasi-static approximation to calculate magnetic induction

The "second fundamental equation" above implies inverting γ_f, which is not possible in general, because it would require prior knowledge of both conductivity and permittivity in each point outside of the sources. If the medium is purely resistive ($\gamma_f = \gamma$ where γ is independent of space and frequency), one can evaluate the electric field first, and next integrate $\vec{B}_f$ using the

quasi-static approximation (Ampère-Maxwell's law). Because for low frequencies, we have necessarily $\vec{j}_f >> i\omega\vec{D}_f$, we obtain

$$\nabla \times \vec{B}_f = \mu_o \vec{j}_f \ ,$$

which is also known as Ampère's law in Fourier space.

Thus, for low frequencies, one can skip the second fundamental equation. Note that in case this quasi-static approximation cannot be made (such as for high frequencies), then one needs to solve the full system using both fundamental equations. Such high frequencies are, however, well beyond the physiological range, so for EEG and MEG signals, the quasi-static approximation holds if the extracellular medium is resistive, or more generally if the medium satisfies $\nabla \times \vec{E}_f = -i\omega\vec{B}_f \backsimeq 0$ (see Eqs. 5.5 and 5.6).

According to the quasi-static approximation, and using the linking equation between current density and the electric field (Eq. 5.7), we can write:

$$\nabla \times \vec{B}_f = \mu_o(\vec{j}_f^{\,p} - \gamma \nabla V_f) \tag{5.14}$$

Because the divergence of magnetic induction is zero, we have from Eq. 5.11:

$$\nabla \times \nabla \times \vec{B}_f = -\nabla^2 \vec{B}_f = -\mu_o \nabla \times (\vec{j}_f^{\,p} - \gamma \nabla V_f) \tag{5.15}$$

This equation can be easily integrated using Poisson integral ("Poisson equation" for each component in Cartesian coordinates) In Fourier space, this integral is given by the following expression

$$\vec{B}_f(\vec{r}) = \frac{\mu_o}{4\pi} \iiint_{head} \frac{\nabla \times (\vec{j}_f^{\,p}(\vec{r'}) - \gamma \nabla V_f(\vec{r'}))}{\|\vec{r} - \vec{r'}\|} dv' \tag{5.16}$$

5.5.6 Consequences

If the medium is purely resistive ("ohmic"), then γ does not depend on the spatial position (see [122, 192]) nor on frequency, so that the solution for the magnetic induction is given by:

$$\vec{B}_f(\vec{r}) = \frac{\mu_o}{4\pi} \iiint_{head} \frac{\nabla \times \vec{j}_f^{\,p}(\vec{r})}{\|\vec{r} - \vec{r'}\|} dv' \tag{5.17}$$

and does not depend on the nature of the medium.

For the electric potential, from Eq. 5.10, we obtain the solution:

$$V_f(\vec{x}) = -\frac{1}{4\pi\gamma}\iiint_{head}\frac{\nabla\cdot\vec{j}_f^{\,p}}{|\vec{x}-\vec{x}'|}dv' \tag{5.18}$$

Thus, when the two source terms $\nabla\times\vec{j}_f^{\,p}$ and $\nabla\cdot\vec{j}_f^{\,p}$ are white noise, the magnetic induction and electric field must have the same frequency dependence. Moreover, because the spatial dimensions of the sources are very small (see appendices), we can suppose that the current density $\vec{j}_f^{\,p}(\vec{x})$ is given by a function of the form:

$$\vec{j}_f^{\,p}(\vec{x}) = \vec{j}^{\,pe}(\vec{x})F(f) \tag{5.19}$$

such that $\nabla\times\vec{j}_f^{\,p}$ and $\nabla\cdot\vec{j}_f^{\,p}$ have the same frequency dependence for low frequencies. Eq. 5.19 constitutes the main assumption of this formalism.

In Appendix A, we provide a more detailed justification of this assumption, based on the differential expressions of the electric field and magnetic induction in a dendritic cable. Note that this assumption is most likely valid for states with low correlation such as desynchronized-EEG states or high-conductance states, and for low-frequencies, as we analyze here (see details in the appendices).

Thus, the main prediction of this formalism is that if the extracellular medium is resistive, then the PSD of the magnetic induction and of the electric potential must have the same frequency dependence. In the next section, we will examine if this is the case for simultaneously recorded MEG and EEG signals.

5.6 Test on experimental data

A total of 4 subjects were used for the analysis. Figure 5.1 shows sample MEG and EEG channels from one of the subjects, during quiet wakefulness. Although the subjects had eyes open, a low-amplitude alpha rhythm was occasionally present (as visible in Fig. 5.1). There were also oscillations present in the empty-room signal, but these oscillations are evidently different from the alpha rhythm because of their low amplitude and the fact that they do not appear in gradiometers (see Suppl. Fig. S1).

In the next sections, we start by briefly presenting the method that was used to estimate the frequency scaling of the PSDs. Then we report the scaling exponents for 0.1-10 Hz frequency bands and their differences in EEG and MEG recordings.

5.6.1 Frequency scaling exponent estimation

Because of the large number of signals in the EEG and MEG recordings, we used an automatic non-parametric procedure to estimate the frequency scaling (see Methods). We used a B-spline approximation by interpolation with boundary conditions to find a curve which best represents the data(see Methods). A high density of knots was given to the low-frequency band (0.1-10 Hz), to have an accurate representation of the PSD in this band, and calculate the frequency scaling. An example of optimized knots to an individual sensor is shown in Figure 5.2A; note that this distribution of knots is specific to this particular sensor. The resulting B-spline curves were used to estimate the frequency scaling exponent using a 1st degree polynomial fit. Figure 5.2B shows the result of the B-spline analysis with optimized knots (in green) capturing the essence of the data better than the usual approximation of the slope using polynomials (in red). The goodness of fit showed a robust estimation of the slope using B-spline method. Residuals were -0.01 $\pm$ 0.6 for empty-room, 0.2 $\pm$ 0.65 for MEG awake, 0.05 $\pm$ 0.6 for LMSS, 0.005 $\pm$ 0.64 for NMSS, 0.08 $\pm$ 0.5 for WF,0.001 $\pm$ 0.02 for PLS, and -0.02 $\pm$ 0.28 for EEG B-spline (all numbers to be multiplied by 10^{-14}).

5.6.2 MEG and EEG have different frequency scaling exponents

Figure 5.3 shows the results of the B-spline curve fits to the log-log PSD vs frequency for all sensors of all subjects. In this figure, and only for the ease of visual comparison, these curves were normalized to the value of the log(PSD) of the highest frequency. As can be appreciated, all MEG sensors (in red) show a different slope than that of the EEG sensors (in blue). The frequency scaling exponent of the EEG is close to 1 ($1/f$ scaling), while MEG seems to scale differently. Thus, this representation already shows clear differences of scaling between EEG and MEG signals.

However, MEG signals may be affected by ambient or instrumental noise. To check for this, we have analyzed the empty-room signals using the same representation and techniques as for MEG, amd the results are represented in Fig. 5.3 (insets). Empty-room recordings always scale very closely to the MEG signal, and thus the scaling observed in MEG may be due in part to environmental noise or noise intrinsic to the detectors. This emphasizes that it is essential to use empty-room recordings made during the same experiment to correct the frequency scaling exponent of MEG recordings.

To correct for this bias, we have used five different procedures (see Methods). The first class of procedure (ES) considers that the scaling of the MEG is entirely due to filtering by the sensors, which would explain the similar scaling between MEG and empty-room recordings. In this case, however, nearly all the scaling would be abolished, and the corrected MEG signal would be similar to white noise (scaling exponent close to zero). Because the similar scaling

may be coincidental, we have used two other classes of noise correction procedures to comply with different assumptions about the nature of the noise. The second class, is composed of spectral subtraction (LMSS and NMSS) or Wiener filtering (see Methods). These methods are well-established in other fields such as acoustics. The third class, uses statistical patterns of noise to enhance PSD (PLS method, for details see Methods).

5.6.3 Spatial variability of the frequency scaling exponent

We applied the above methods to all channels and represented the scaling exponents in topographic plots in Fig. 5.4. This figure portrays that both MEG and EEG do not show a homogenous pattern of the scaling exponent, confirming the differences of scaling seen in Fig. 5.3. The EEG (Figure 5.4A) shows that areas in the midline have values closer to 1, while those at the margin can deviate from $1/f$ scaling. MEG on the other hand shows higher values of the exponent in the frontal area and a horseshoe pattern of low value exponents in parietotemporal regions (Figure 5.4B). As anticipated above, empty-room recordings scale more or less uniformly with values close to $1/f$ (Figure 5.4C), thus necessitating the correction for this phenomena to estimate the correct MEG frequency scaling exponent. Different methods for noise reduction are shown in Figure 5.4: spectral subtraction methods, such as LMSS (Figure 5.4D), NMSS (Figure 5.4E), WF enhancement (Figure 5.4F). These corrections preserve the pattern seen in Figure 5.4B, but tend to increase the difference with EEG scaling: one method (LMSS) yields minimal correction while the other two (NMSS and WF) use band-specific SNR information in order to cancel the effects of background colored-noise (see Suppl. Fig. S2), and achieve higher degree of correction (see Supplementary Methods for details). Figure 5.4G portrays the use of PLS to obtain a noiseless signal based on the noise measurements. The degree of correction achieved by this method is higher than what is achieved by spectral subtraction and WF methods. Exponent subtraction is shown in Figure 5.4H. This correction supposes that the scaling is due to the frequency response of the sensors, and nearly abolishes all the frequency scaling (see also Suppl. Fig. S3 for a comparison of different methods of noise subtraction).

5.6.4 Statistical comparison of EEG and MEG frequency scaling

Based on the patterns in Fig. 5.4, we created three ROIs covering Vertex (FR), Vertex (VX) and the horseshoe pattern (PT). These masks are shown in Fig. 5.4I.

Figure 5.5A represents the overall pattern providing evidence on the general difference and the wider variability in MEG recordings. The next three panels relate to the individual ROIs. Of the spectral subtraction methods, NMSS achieves a higher degree of correction in comparison with LMSS (see Figure 5.4C, Figure 5.4D as well as Suppl. Fig. S3). Because NMSS takes into account the effects of the background colored-noise (Suppl. Fig. S2), it is certainly more rele-

vant to the type of signals analyzed here. The results of NMSS and WF are almost identical and confirm one another (see Figure 5.4E, as well as Suppl. Fig. S3). Therefore, of this family of noise correction, only NMSS is portrayed here. Of the methods dealing with different assumptions about the nature of the noise, the "Exponent subtraction" almost abolishes the frequency scaling (Also see in Figure 5.4H, as well as Suppl. Fig. S3). Applying PLS yields values in between "Exponent subtraction" and that of NMSS and is portrayed in Figure 5.5.

In the Frontal region (Figure 5.5B), the EEG scaling exponents show higher variance by comparison to MEG. Also, EEG shows some overlaps with the distribution curve of non-corrected MEG; this overlap becomes limited to the tail end of the NMSS correction and is abolished in the case of PLS correction. As can be appreciated, VX (Figure 5.5C) shows both similar values and similar distribution for EEG and non-corrected MEG. These similarities, in terms of regional overall values and distribution curve, are further enhanced after NMSS correction. It is to be noted that, in contrast to these similarities, the one-to-one correlation of NMSS and EEG at VX ROI are very low (see below, Table 1B-C). The values of PLS noise correction are very different from that of EEG and have a similar, but narrower, distribution curve shape. Two other ROIs show distinctively different values and distribution in comparing EEG and MEG. Both NMSS and PLS agree on this with PLS showing more extreme cases. Figure 5.5D reveals a bimodal distribution of MEG exponents in the parietotemporal region (PT ROI). This region has also the highest variance (in MEG scaling exponents) compared to other ROIS. The distinction between EEG and MEG is enhanced in PLS estimates; however, the variance of PT is reduced in comparison to NMSS while the bimodality is still preserved but weakened. The values of mean and standard deviation for these ROIs' exponents are provided in Table 1A (mean $\pm$ standard deviation).

The box-plots of Fig. 5.5-plots further show the difference between the medians, lower/upper quartile and interquartile range. The overall difference is that the uncorrected MEG has much wider variance compared to EEG and corrected MEG (in case of PLS correction); the absolute value of the median of MEG (uncorrected, or corrected with either NMSS or PLS) is always smaller than that of EEG. The VX region is an exception to the above rules; interestingly, the one-to-one correlation of VX happens to be the lowest of all (see below). In the case of NMSS-corrected MEG, the shape of the pdf is preserved. However, PLS narrows the distribution curve of MEG but further enhances the differences between MEG and EEG. Therefore, median and lower/upper quartiles will have different value than that of EEG.

Correlation values (Table 1B-C) show that, although VX ROI has the closest similarity in terms of its central tendency and probability distribution, it provides the lowest correlation in a pairwise fashion. P-values (for testing the hypothesis of no correlation against the alternative that there is a nonzero correlation) for Pearson's correlation were calculated using a Student's t-distribution for a transformation of the correlation and they were all significant (less than 10^{-15} for $\alpha = 0.05$). Similarly, a non-parametric statistic Kendall tau rank correlation was used to measure the degree of correspondence between two rankings and assessing the significance of this

correspondence between MEG and EEG in the selected ROIs (Table 1C). P-values for Kendall's tau and Spearman's rho calculate using the exact permutation distributions were all significant (less than 10^{-15} for $\alpha = 0.05$). Kendall tau shows that the rank correlation for all areas considered together as well as for PT, show a lesser correlation than that is shown by Pearson linear correlation. Furthermore, we carried out a Kruskal-Wallis nonparametric version of one-way analysis of variance. We used this test to avoid bias in ANOVA (KruskalWallis assumes that the measurements come from a continuous distribution, but not necessarily a normal distribution as is assumed in ANOVA). KruskalWallis uses analysis of variance on the ranks of the data values, not the data values themselves and therefore is an appropriate test for comparison of the homogeneity of pattern between ROIs of two image as well as their statistical median. As shown in Table 1D, all p-values were significant emphasizing the difference between the spatial aspect of the spectral nature of MEG and EEG. Note that the difference of scaling exponent of EEG and MEG was also confirmed by nonlinear spatial kendall correlation analysis, independently of the ROIs classification (not shown).

5.6.5 Relation of scaling exponent to signal-to-noise ratio

Noise correction does not affect all the sensors in a same fashion. As presented in Suppl. Fig. S3, the simple linear spectral subtraction (LMSS) may lead to an increment or decrement of the scaling exponent. In any case, the correction achieved by this method is minimal. This is due to the fact that LMSS ignores the complex non-linear patterns of the SNR in different channels (Suppl. Fig. S2). We show that for all subjects, as the frequency goes up, the SNR goes down. It is also noticable that in each defined frequency band, i.e. 0-10 Hz (Slow, Delta and Theta), 11-30 Hz (Beta), 30-80 Hz (Gamma), 80-200 Hz (Fast oscillation), 200-500 Hz (Ultra-fast oscillation), there is an observable sensor-to-sensor SNR variability. This variability is at its maximum in the band with the highest SNR (i.e. 1-10 Hz). All together, the non-linear nature of MEG SNR shows that a linear spectral subtraction could behave non-optimally, leading to minimal correction. This also conveys that the optimal spectral correction can be achieved only by non-linear methods that explicitly take into account the SNR information of the data. Therefore the correction achieved by NMSS and WF have higher validity, in agreement with the fact that both methods yield similar results in terms of values and spatial distribution (Fig. 5.4E, Fig. 5.4F).

5.7 Discussion

In this paper, we have used a combination of theoretical and experimental analyses to investigate the spectral structure of EEG and MEG signals. In the first part of the paper, we presented a theoretical investigation showing that if the extracellular medium is purely resistive, the equa-

tions of the frequency dependence of electric field and magnetic induction take a simple form, because the admittance tensor does not depend on spatial coordinates. Thus, the macroscopic magnetic induction does not depend on the electric field outside the neuronal sources, but only depends on currents inside neurons. In this case, the frequency scaling of the PSD should be the same for EEG and MEG signals. This conclusion is only valid in the linear regime, and for low frequencies.

An assumption behind this formalism is that the spatial and frequency dependence of the current density factorize (Eq. 5.19). We have shown in the appendices that this is equivalent to consider the different current sources as independent. Thus, the formalism will best apply to states where the activity of synapses is intense and of very low correlation. This is the case for desynchronized-EEG states or more generally "high-conductance states", in which the activity of neurons is intense, of low correlation, and the neuronal membrane is dominated by synaptic conductances [31]. In such conditions, the dendrites are bombarded by intense synaptic inputs which are essentially uncorrelated, and one can consider the current sources as independent [123]. In the present paper, we analyzed EEG and MEG recordings in such desynchronized states, where this formalism best applies.

Note that the above reasoning neglects the possible effect of abrupt variations of impedances between different media (e.g., between dura matter and cerebrospinal fluid). However, there is evidence that this may not be influential. First, our previous modeling work [122] showed that abrupt variations of impedance have a negligible effect on low frequencies, suggesting that even in the presence of such abrupt variations should not play a role at low frequencies. Second, in the frequency range considered here, the skull and the skin are very close to be resistive at low frequencies [140], so it is very unlikely that they play a role in the frequency scaling in EEG and MEG power spectra even at high frequencies.

In the second part of the paper, we have analyzed simultaneous EEG and MEG signals recorded in four healthy human subjects while awake and eyes open (with desynchronized EEG). Because of the large number of channels involved, we used an automatic procedure (B-splines analysis) to calculate the frequency scaling. As found in previous studies [129,134,220], we confirm here that the EEG displays frequency scaling close to $1/f$ at low frequencies[6]. However, this $1/f$ scaling was most typical of the midline channels, while temporal and frontal leads tended to scale with slightly larger exponents, up to $1/f^2$ (see Fig. 5.4A). The same pattern was observed in all four patients.

This approach differs from previous studies in two aspects. First, in contrast to prior studies (such as [130, 131]), we calculated the frequency scaling of all the sensors and did not confine our analysis to a specific region. Second, unlike other investigators (such as [221, 222]), we

[6]Note that to compare scaling exponents between studies one must take into account that the electrode montage may influence the scaling. For example, in bipolar (differential) EEG recordings, if two leads are scaling as $1/(A+f)$ and $1/(B+f)$, the difference will have regions scaling as $1/f^2$.

did not limit our evaluations to either EEG or MEG alone, but rather analyzed the scaling of both type of signals simultaneously. Such a strategy enables us to provide an extended spatial analysis of the frequency scaling. It also provides a chance to compare the scaling properties of these signals in relation to their physical differences.

For the MEG recordings, the frequency scaling at low frequencies was significantly lower compared to the EEG (see Fig. 5.3). This difference in frequency scaling was also accompanied by spatial variability patterns (see Fig. 5.4) showing three distinct regions: 1) a frontal area where the exponents had their highest values in the case of MEG; 2) a central area where the values of exponents of EEG and MEG get closer to each other and 3) a parietotemporal horseshoe region showing the lowest exponents for MEG with bimodal characteristics (Fig. 5.5). In some cases, the scaling of the uncorrected and corrected MEG signal was also close to $1/f$, as reported previously (Novikov et al., 1997). In the frontal area (FR mask), the scaling exponent of the EEG was generally larger. At Vertex (VX mask), EEG and MEG had similar values and at the Parietotemporal region (PT mask), MEG showed a bimodal property with a much broader range of scaling exponent in comparison to EEG (see Fig. 5.4). Note that to avoid the effect of spurious peaks, Novikov et al. used the spectrum of signal differences and argued for the existence of a local similarity regime in brain activity [131]. This approach fundamentally changes the spectral characteristics of Magnetometers (which measure the absolute magnitude of the magnetic induction) into a measure that only for the neighboring sensors approximates the behavior of the gradiometers (which measures the gradient of the magnetic induction). So it is not clear how to relate their values to the ones obtained here.

To make sure that the differences of frequency scaling between EEG and MEG were not due to environmental or instrumental noise, we have used five different methods to remove the effect of noise. These methods are based on different assumptions about the nature and effect of the noise. A first possibility is to correct for the noise induced by the MEG sensors. It is known that the SQUID detectors used in MEG recordings are very sensitive to environmental noise and they can produce $1/f$ noise [8]. Under this assumption, part of the scaling of the MEG could be due to "filtering" by the sensors themselves, which justifies a simple subtraction of scaling exponents to remove the effects of this filtering. Note that such empty-room recordings were not possible for the EEG, although the noise from the recording setup could be estimated (see [133] for example). Because in some cases both MEG and emptyroom signals have similar scaling, a simple correction by subtracting the exponents would almost entirely abolish the frequency scaling while in other cases it may even revert the sign of the scaling exponent (see Fig. 5.4H , Suppl. Fig. S3).

However, if noise is not due to the sensors but is of additive uncorrelated nature, then another method for noise correction must be used. For this reason, we have used a second class of well-established methods consisting of spectral subtraction [204, 223]. Using three of such methods (LMSS, NMSS and WF) changed the scaling exponent, without fundamentally changing its spatial pattern (Fig. 5.4D-F). The largest correction was obtained by non-linear methods

which take into account the SNR information in the MEG signal. We also applied another class of method which uses the collective characteristics of all frequencies in noise correction (PLS). Similar to exponent subtraction, this method nearly abolished all the scaling of the MEG (Fig. 5.4G). In conclusion, although different methods for noise subtraction give rise to different predictions about frequency scaling, all of the used methods enhanced the difference between EEG and MEG scaling. Thus, we conclude that the difference of EEG and MEG scaling cannot be attributed to noise, but is significant, therefore reinforcing the conclusion that the medium must be non-resistive.

An alternative method to investigate this is the "Detrended Fluctuation Analysis" (DFA; see [130, 221, 222, 224]). Like many nonlinear approaches, DFA results are very vulnerable to the selection of certain parameters. Different filters severely affect the scaling properties of the electromagnetic signals to different extents, and therefore the parameters estimated through the DFA analysis could be false or lead to distorted interpretations of real phenomena [225], and these effects are especially prominent for lower frequencies, which are precisely our focus of investigation here. One of the fields for which DFA can provide robust results is to analyze surrogate data with known characteristics. Although the use of DFA to evaluate the scaling exponents of EEG was vigorously criticized [225], a previous analysis [221, 222] reported two different regions, a central and a more frontal, which somehow correlate with the FR and VX regions identified in our analysis. Similarly, a study by [226] using DFA provided evidence for topographical differences in scaling exponents of EEG recordings. They report that scaling exponents were homogeneous over the posterior half of the scalp and became more pronounced toward the frontal areas. In contrast to Linkenkaer-Hansen et al., [130] (where envelope of alpha oscillations was used for DFA estimation), this study uses the raw signal in its DFA analysis and yields values closer to those reported here.

Both uncorrected signals and empty-room correction show that there is a fundamentally different frequency scaling between EEG and MEG signals, with near-$1/f$ scaling in EEG, while MEG shows a wider range at low frequencies. Although it is possible that non-neuronal sources affect the lower end ($<$1Hz) of the evaluated frequency domain [227], the solution to avoid these possible effects remain limited to invasive methods such as inserting the electrode into the scalp [228] or using intracranial EEG recordings (similar to [133]. This approach would render wide range spatial recording as well as simultaneous invasive EEG and MEG recordings technically demanding or impractical. However, if technically feasible, such methods could provide a way to bypass non-neuronal effects at very low frequency. It could also provide a chance to evaluate the effects of spatial correlation on spectral structure at a multiscale level.

The power spectral structure we observe here is consistent with a scenario proposed previously [134]: the $1/f$ structure of the EEG and LFP signals is essentially due to a frequency-filtering effect of the signal through extracellular space; this type of scaling can be explained by ionic diffusion and its associated Warburg impedance[7] (see Bédard and Destexhe, 2009).

[7] Ionic diffusion can create an impedance known as the "Warburg impedance", which scales as $1/\sqrt{\omega}$, giving

It is also consistent with the matching of LFPs with multi-unit extracellular recordings, which can be reconciled only assuming a $1/f$ filter [134]. Finally, it is also consistent with the recent evidence from the transfer function calculated from intracellular and LFP recordings, which also showed that the extracellular medium is well described by a Warburg impedance [123]. If this non-resistive aspect of extracellular media is confirmed, it may influence the results of models of source localization, which may need to be reformulated by including more realistic extracellular impedances.

In conclusion, the present theoretical and experimental analysis suggests that the scaling of EEG and MEG signals cannot be reconciled using a resistive extracellular medium. The $1/f$ structure of EEG with smaller scaling exponents for MEG is consistent with non-resistive extracellular impedances, such as capacitive media or diffusion (Warburg) impedances. Including such impedances in the formalism is non trivial because these impedances are strongly frequency dependent. The Poisson integral (the solution of Poisson's law $\nabla \cdot \vec{D} = -\nabla \cdot \varepsilon \nabla V = \rho$) would not apply anymore (see [122, 192]). Work is under way to generalize the formalism and include frequency-dependent impedances.

Finally, it is arguable that the scaling could also be influenced by the cancellation and the extent of spatial averaging of microscopic signals, which are different in EEG and MEG (for more details on cancellation see [115]; for details on spatial sensitivity profile see [114]). Such a possible role of the complex geometrical arrangement of underlying current sources should be investigated by 3D models which could test specific assumptions about the geometry of the current sources and dipoles, and their possible effect on frequency scaling. Such a scenario constitutes another possible extension of the present study.

5.8 Appendices

5.8.1 A: Theoretical

5.8.1.1 Frequency dependence of electric field and magnetic induction

To compare the frequency dependence of magnetic induction and electric field, we evaluate them in a dendritic cable, expressed differentially. For a differential element of dendrite, in Fourier space, the current produced by a magnetic field (Ampère-Laplace law) is given by the following expression (see Appendix B):

$$\delta \vec{B}_f(\vec{r}) = \frac{\mu_o}{4\pi} \vec{j}_f^{\,p}(\vec{r'}) \times \frac{\vec{r} - \vec{r'}}{\|\vec{r} - \vec{r'}\|^3} \, \delta v' \tag{5.20}$$

$1/f$ scaling in the power spectra [229, 230].

when the extracellular medium is resistive. Note that the source of magnetic induction is essentially given by the component of $\vec{j}_f^p$ along the axial direction (j_f^i) within each differential element of dendrite because the perpendicular (membrane) current does not participate to producing the magnetic induction if we assume a cylindrical symmetry.

For the electric potential, we have the following differential expression for a resistive medium (see Appendix C):

$$\delta\vec{V}_f(\vec{r}) = \frac{1}{4\pi\gamma}\frac{\delta I_f^{\perp}(\vec{r}')}{\|\vec{r}-\vec{r}'\|} = \frac{1}{4\pi\gamma}\frac{j_f^m(\vec{r}')}{\|\vec{r}-\vec{r}'\|}\delta S' \tag{5.21}$$

where j_f^m is the transmembrane current per unit of surface.

If we consider the differential expressions for the magnetic induction (Eq. 5.20) and electric potential (Eq. 5.21), one can see that the frequency dependence of the ratio of their modulus is completely determined by the frequency dependence of the ratio of current density j_f^m and j_f^i. In Appendix D, we show that this ratio is quasi-independent of frequency for a resistive medium, for low frequencies (smaller that $\sim$10 Hz), and if the current sources are of very low correlation.

Thus, magnetic induction and electric potential can be very well approximated by:

$$\begin{aligned} V_f(\vec{r}) &= N < V >= N < \sum_{l=1}^{N} \delta V_f^l > \\ \vec{B}_f(\vec{r}) &= N < \vec{B} >= N < \sum_{l=1}^{N} \delta \vec{B}_f^l > \end{aligned} \tag{5.22}$$

for sufficiently small differential dendritic elements (N/l large).

Because the functions of spatial and frequency are statistically independent, we can write the following expressions for the square modulus of the fields (see Eqs. 5.20 and 5.21):

$$\begin{aligned} |V_f(\vec{r})|^2 &= N^2| < \sum_{l=1}^{N} V^l(\vec{r}) G_l^m(f) > |^2 = |V(\vec{r})|^2 |G(f)|^2 \\ \|\vec{B}_f(\vec{r})\|^2 &= N^2\| < \sum_{i=1}^{N} \vec{B}^i(\vec{r}) G_l^m(f) > \|^2 = \|\vec{W}(\vec{r})\|^2 |G(f)|^2 \end{aligned} \tag{5.23}$$

where $G(f) =< G_l^m(f) >$, $V^l(\vec{r}) =< V^l(\vec{r}) >$ and $\vec{W}(\vec{r}) =< \vec{B}^l(\vec{r}) >$. Thus, the scaling of the PSDs of the electric potential and magnetic induction must be the same for low frequencies (smaller than $\sim$10 Hz) if the medium is resistive and when the current sources have very low correlation.

5.8.1.2 Differential expression for the magnetic induction

According to Maxwell equations, the magnetic induction is given by:

$$\vec{B}_f(\vec{r}) = \frac{\mu_o}{4\pi} \iiint_{head} \frac{\nabla' \times \vec{j}_f^p(\vec{r'})}{\|\vec{r} - \vec{r'}\|} \, dv' \tag{5.24}$$

where $dv' = dx'^1 dx'^2 dx'^3$ and

$$\nabla'(\frac{1}{\|\vec{r} - \vec{r'}\|}) = \frac{\vec{r} - \vec{r'}}{\|\vec{r} - \vec{r'}\|^3}$$

for a perfectly resistive medium.

We now show that this expression is equivalent to Ampere-Laplace law.

From the identity $\nabla' \times (g\vec{A}) = g(\nabla' \times \vec{A}) + \nabla' g \times \vec{A}$, where $\nabla' = \hat{e}_x \frac{\partial}{\partial x'} + \hat{e}_y \frac{\partial}{\partial y'} + \hat{e}_z \frac{\partial}{\partial z'}$, we can write:

$$\vec{B}_f(\vec{r}) = \frac{\mu_o}{4\pi} \iiint_{head} [\nabla' \times (\frac{\vec{j}_f^p(\vec{r'})}{\|\vec{r} - \vec{r'}\|}) + \frac{\mu}{4\pi} \vec{j}_f^p(\vec{r'}) \times \nabla' \frac{1}{\|\vec{r} - \vec{r'}\|}] \, dv' \tag{5.25}$$

Moreover, we also have the following identity

$$\iiint_{head} \nabla' \times (\frac{\vec{j}_f^p(\vec{r'})}{\|\vec{r} - \vec{r'}\|}) \, dv' = - \iint_{\partial head} \frac{\vec{j}_f^p(\vec{r'})}{\|\vec{r} - \vec{r'}\|} \times \hat{n} \, dS' \tag{5.26}$$

where $\hat{n}$ is a unitary vector perpendicular to the integration surface and going outwards from that surface. Extending the volume integral outside the head, the surface integral is certainly zero because the current is zero outside of the head. It follows that:

$$\vec{B}_f(\vec{r}) = \frac{\mu_o}{4\pi} \iiint_{head} \vec{j}_f^p(\vec{r'}) \times \frac{\vec{r} - \vec{r'}}{\|\vec{r} - \vec{r'}\|^3} \, dv' \tag{5.27}$$

where $dv' = dx'^1 dx'^2 dx'^3$ because

$$\nabla'(\frac{1}{\|\vec{r} - \vec{r'}\|}) = \frac{\vec{r} - \vec{r'}}{\|\vec{r} - \vec{r'}\|^3}$$

Eq. 5.27 is called the Ampère-Laplace law (see Eq. 13 in Hämäläinen et al., 1993). It is important to note that this expression for the magnetic induction is not valid when the medium is not resistive.

Finally, from the last expression, the magnetic induction for a differential element of dendrite can be written as:

$$\delta\vec{B}_f(\vec{r}) = \frac{\mu_o}{4\pi} \vec{j}_f^p(\vec{r'}) \times \frac{\vec{r} - \vec{r'}}{\|\vec{r} - \vec{r'}\|^3} \, \delta v' \tag{5.28}$$

5.8.1.3 Differential expression of the electric field and electric potential

In this appendix, we derive the differential expression for the electric field. Starting from Eq. 5.10, we obtain the solution for the electric potential:

$$V_f(\vec{r}) = -\frac{1}{4\pi\gamma_f} \iiint_{head} \frac{\nabla \cdot \vec{j}_f^p(\vec{r}')}{\|\vec{r}-\vec{r}'\|}\, dv' \tag{5.29}$$

It follows that the electric field produced by the ensemble of sources can be expressed as:

$$\vec{E}_f(\vec{r}) = -\nabla V_f(\vec{r}) = \frac{1}{4\pi\gamma_f} \iiint_{head} \nabla \cdot \vec{j}_f^p(\vec{r}') \cdot \frac{\vec{r}-\vec{r}'}{\|\vec{r}-\vec{r}'\|^3}\, dv' \tag{5.30}$$

such that every differential element of dendrite produces the following electric field:

$$\delta\vec{E}_f(\vec{r}) = \frac{\nabla \cdot \vec{j}_f^p(\vec{r}')}{4\pi\gamma_f} \cdot \frac{\vec{r}-\vec{r}'}{\|\vec{r}-\vec{r}'\|^3}\, \delta v' \tag{5.31}$$

The transmembrane current $\delta I_f^{\perp}$ obeys $\delta I_f^{\perp} = i\omega\rho_f(\vec{r}')\delta v'$ because we are in a quasi-stationary regime in a differential dendritic element. Taking into account the differential law of charge conservation $\nabla \cdot \vec{j}_f(\vec{r}') = -i\omega\rho_f(\vec{r}')$, we have:

$$\delta\vec{E}_f(\vec{r}) = \frac{\delta I_f^{\perp}(\vec{r}')}{4\pi\gamma_f} \frac{\vec{r}-\vec{r}'}{\|\vec{r}-\vec{r}'\|^3} = \frac{j_f^m(\vec{r}')}{4\pi\gamma_f} \frac{\vec{r}-\vec{r}'}{\|\vec{r}-\vec{r}'\|^3} \delta S' \tag{5.32}$$

where j_f^m is the density of transmembrane current per unit surface and $\delta S'$ is the surface area of a differential dendritic element. This approximation is certainly valid for frequencies lower than 1000 Hz because the Maxwell-Wagner time (see Bedard et al., 2006b) of the cytoplasm ($\tau_{mw}^{cyto} = \varepsilon/\sigma \sim 10^{-10}\ s.$) is much smaller than the typical membrane time constant of a neuron ($\tau_m \sim 5-20\ ms$).

Finally the contribution of a differential element of dendrite to the electric potential at position $\vec{r}$ is given by

$$\delta\vec{V}_f(\vec{r}) = \frac{1}{4\pi\gamma_f} \frac{\delta I_f^{\perp}(\vec{r}')}{\|\vec{r}-\vec{r}'\|} = \frac{1}{4\pi\gamma_f} \frac{j_f^m(\vec{r}')}{\|\vec{r}-\vec{r}'\|} \delta S' \tag{5.33}$$

We note that the expressions for the electric field and potential produced by each differential element of dendrite have the same frequency dependence because it is directly proportional to $\frac{j_f^m}{\gamma_f}$ for the two expressions. Also note that if the medium is resistive, then $\gamma_f = \gamma$ and the frequency dependence of the electric field and potential are solely determined by that of the transmembrane current j_f^m.

5.8.1.4 Frequency dependence of the ratio $j_f^i(\vec{x})/j_f^m(\vec{x})$.

For each differential element of dendrite, we consider the standard cable model, in which the impedance of the medium is usually neglected (it is usually considered negligible compared to the membrane impedance). In this case, we have:

$$\begin{cases} j_f^m &= \frac{V_f^m}{r_m} + i\omega c_m V_f^m \\ j_f^i &= -\sigma \frac{\partial V_f^m}{\partial x} = -\frac{1}{r_i}\frac{\partial V_f^m}{\partial x} \end{cases} \tag{5.34}$$

where V_f^m, j_f^i, j_f^m, c_m, r_m et r_i are respectively the membrane potential, the current density in the axial direction, the transmembrane current density, the specific capacitance (F/m^2), the specific membrane resistance ($\Omega.m^2$) and the cytoplasm resistivity ($\Omega.m$).

It follows that

$$\frac{j_f^i(\vec{x})}{j_f^m(\vec{x})} = \frac{r_m}{r_i(1+i\omega\tau_m)} \cdot \frac{\partial}{\partial x}[ln(V_f^m(\vec{x})] \tag{5.35}$$

where $\tau_m = r_m c_m$.

Under *in vivo*–like conditions, the activity of neurons is intense and of very low correlation. This is the case for desynchronized-EEG states, such as awake eyes-open conditions, where the activity of neurons is characterized by very low levels of correlations. There is also evidence that in such conditions, neurons are in "high-conductance states" [31], in which the synaptic activity dominates the conductance of the membrane and primes over intrinsic currents. In such conditions, we can assume that the synaptic current sources are essentially uncorrelated and dominant, such that the deterministic link between current sources will be small and can be neglected (see [123]). Further assuming that the electric properties of extracellular medium are homogeneous, then each differential element of dendrite can be considered as independent and the voltages V_m have similar power spectra.

In such conditions, we have:

$$V_f^m(\vec{x}) = F^m(\vec{x})G^m(f) \tag{5.36}$$

Note that this expression implies that we have in general for each differential element of dendrite:

$$\begin{cases} j_f^m(\vec{x}) &= F^m(\vec{x})(\frac{1+i\omega\tau_m}{r_m})G^m(f) \\ j_f^i(\vec{x}) &= -\frac{1}{r_i}\frac{\partial F^m(\vec{x})}{\partial x}G^m(f) = F^i(\vec{x})G^m(f) \end{cases} \tag{5.37}$$

according to Eq. 5.34.

It follows that

$$\frac{j_f^i(\vec{x})}{j_f^m(\vec{x})} = \frac{r_m}{r_i(1+i\omega\tau_m)} \cdot \frac{\partial}{\partial x}[ln(F(\vec{x}))] \approx \frac{r_m}{r_i} \cdot \frac{\partial}{\partial x}[ln(F(\vec{x}))] \tag{5.38}$$

Thus, for frequencies smaller than $1/(\omega\tau_m)$ (about 10 to 30 Hz for τ_m of 5-20 ms), the ratio $\frac{j_f^i(\vec{x})}{j_f^m(\vec{x})}$ will be frequency independent, and for each differential element of dendrite, we have:

$$\begin{cases} j_f^m(\vec{x}) &= F^m(\vec{x})G^m(f) \\ j_f^i(\vec{x}) &= F^i(\vec{x})G^m(f) \end{cases} \tag{5.39}$$

for frequencies smaller than $\sim$10 Hz.

5.8.2 B: Methodological

5.8.2.1 SNR

Two of the used methods for noise-correction are based on band-specific signal-to-noise ratio (SNR) in order to cancel the effects of background colored-noise in the spectra of interest. In each subject, average PSD was used to calculate signal-to-noise ratio (SNR). For SNR calculation, few frequency bands were defined based on the categorization in Buzsaki & Draguhn [231]: 0-10 Hz (Slow, Delta and Theta), 11-30 Hz (Beta), 30-80 Hz (Gamma), 80-200 Hz (Fast oscillation), 200-500 Hz (Ultra-fast oscillation). SNR was calculated as:

$$SNR_{bi} = \frac{\sum 10 * log10(\frac{PSDsignal_{bi}}{PSDnoise_{bi}})}{n} \tag{5.40}$$

for a given band "b" and sensor "i", "n" is the frequency resolution of that band. This method was applied on individual average PSD as well as shape preserving spline of each average PSD where each PSD was fist smoothed in log10 scale using a shape preserving spline, i.e, Piecewise Cubic Hermite Interpolating Polynomial (PCHIP).

5.8.2.2 Multiband spectral subtraction

Assuming the additive noise to be stationary and uncorrelated with the clean signal, nearly most spectral subtraction methods can be formulated using a parametric equation:

$$|\widehat{S(k)}|^\alpha = a_k|Y(k)|^\alpha - b_k|\widehat{D(k)}|^\alpha \tag{5.41}$$

where $|\widehat{S_k}|$, $|Y_k|$ and $|\widehat{D_k}|$ refer to enhanced magnitude spectrum estimate (corrected signal), the noisy magnitude spectrum (original signal) and noise magnitude spectrum estimate ("noise"), respectively. k is the frequency index, while a_k and b_k are linear coefficient parameters of the summation. Spectral subtraction methods fall into three main categories (Sim et al., 1998). The simplest of all, a linear method where $a_k = b_k = 1$, α=2, following [204] was used here. This linear multiband spectral subtraction (LMSS) method is well-established for noise subtraction (see [206] for a comparative study of noise subtraction methods).

An improved method, with $a_k = 1$ and b_k = v, where "v" is the oversubtraction factor. This method uses oversubtraction and introduces a spectral flooring to minimize residual noise and musical noise [232]. A second category of spectral subtraction is based on $a_k = b_k = f(k)$. Third and the most robust methods are based on a non-linear multiband subtraction (NMSS) where $a_k = 1$ and $b_k = v(k)$; i.e., the oversubtraction factor is adjusted based on a specfic band's SNR. These methods proposed by [205, 206] are suitable for dealing with colored noise [223, 233], a case similar to MEG recordings. The spectrum is divided into N non-overlapping bands, and spectral subtraction is performed independently in each band. The Eqs. 5.41 is simply reduced to:

$$|\widehat{S_i(k)}|^2 = |Y_i(k)|^2 - \alpha_i \delta_i |\widehat{D_i(k)}|^2, b_i \leq k \leq e_i \tag{5.42}$$

where b_i and e_i are the beginning and ending frequency bins of the ith frequency band, α_i is the overall oversubtraction factor of the ith band and δ_i is a tweaking factor. The band specific oversubtraction factor α_i is a function of the segmental SNR_i of the ith frequency band. After calculating bandspecific SNR (Eqs. 5.40), we used the product of lower 10 percent of crosssubject average SNR and standard deviation of SNR_i to estimate the α_i δ_i subtraction coefficient. Next, simply by multiplying the noise PSD by this coefficient and subtracting it from the measured PSD, the enhanced PSD was achieved.

5.8.2.3 Wiener filter (WF) spectral enhancement

The principle of the Wiener filter is to obtain an estimate of the clean signal from that of the noisy measurement through minimizing the Mean Square Error (MSE) between the desired and the measured signal [207, 208]. In the frequency domain, this relation is formulated as filtering transfer function:

$$WF(k) = \frac{P_s(k)}{P_s(k) + P_n(k)} \tag{5.43}$$

where, as before, $P_s(k)$ and $P_n(k)$ refer to enhanced power spectrum estimate and noise power spectrum estimate respectively for a signal frame and k is the frequency index. Based on the definition of SNR as, the ratio of these two elements, one can formulate the WF as:

$$WF_K = [1 + \frac{1}{SNR_k}]^{-1} \tag{5.44}$$

After calculation of bandspecific WF, the noisy signal is simply muliplied by the WF to obtain the enhanced signal.

5.8.2.4 Partial least square (PLS) approximation of non-noisy spectrum

Partial least squares (PLS) regression, combines “Principal component analysis” (PCA) and “Multiple linear regression” [209, 234]. While PCA finds hyperplanes of maximum variance between the response and independent variables, PLS projects the predicted variables and the observable variables to a new space. Then from this new space, it finds a linear regression model for the projected data. Next, using this model, PLS finds the multidimensional direction in the X space that explains the maximum multidimensional variance direction in the Y space [210,234]. If X is the PSD of noise measurement and Y is the PSD of the measured signal contaminated with background noise, one can use PLS to ”clean” one matrix (Y) by predicting Y from X and then using the residual of the prediction of Y by X as the estimate of pure PSD. The patterns of the awake spectrum that statistically resembles the patterns of emptyroom spectral noise are those that should be removed. As during PLS algorithm, the data is mean subtracted and z-normalized, the predection of Y from X is an approximate of the zscored PSD. Therefore, the reseidual Y, which is taken as the spectral features that can not be predicted by noise, also has zscored values. It has too be emphasized that this approach of denoising only works in the spectral but not the time domain.

5.9 Figures & Tables

5.9.1 Figures

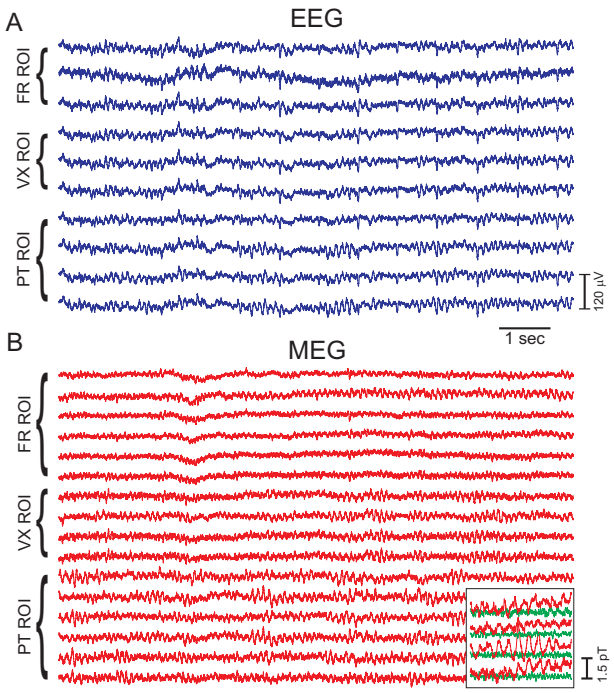

Figure 5.1. Simultaneous EEG and MEG recordings in an awake human subject. This example shows a sample of channels from MEG/EEG after ECG noise removal. Labels refer to ROIs as defined in methods (also see Figure 5.4). FR: Frontal, VX:Vertex and PT: Parietotemporal. These sample channels were selected to represent both right and left hemispheres in a symmetrical fashion. Inset: magnification of the MEG (red) and "empty-room" (green) signals superimposed from 4 sample channels. All traces are before any noise correction, but after ECG decontamination.

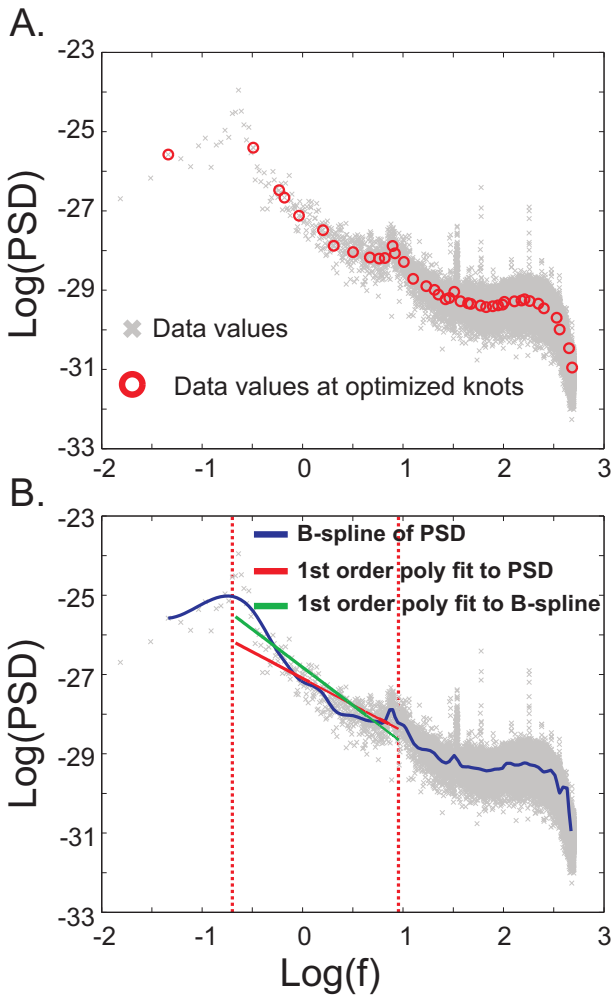

Figure 5.2. A.log-log scale of the PSD vs frequency of a sample MEG sensor along with the corresponding log(PSD) values (shown as circles) at optimized knots in log-scale. B. 1st degree Polynomial fit on B-spline curve effectively captures properties of the signal better than simple polynomial fit and avoids the 10 Hz peak. The fit was limited between 0.1 to 10 Hz excluding the boundaries. This limits the fit approximation to the next limiting optimized knots (between 0.1 and 0.2 to between 9 and 10 Hz) to avoid the peaks at alpha and low frquencies (shown by vertical dotted lines).

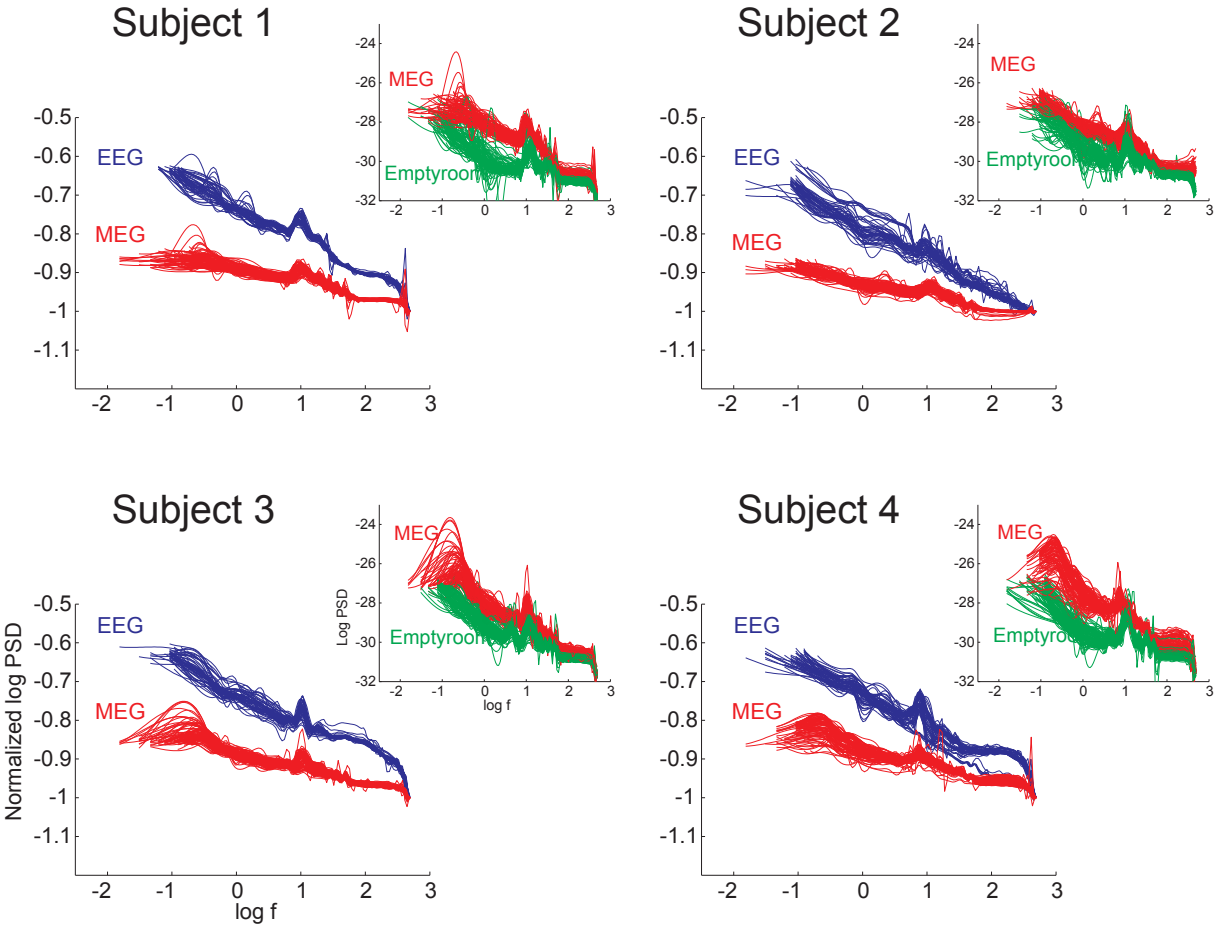

Figure 5.3. B-spline fits of EEG awake and MEG awake (prior to noise correction) recordings from all four subjects. Each line refers to the fit of one sensor in log(PSD)-log(frequency) scale. For the ease of visual comparison of the frequency scaling exponent, log(PSD) values are normalized to their value at the maximum frequency. Each panel represents the data related to one of our four subjects. These plots show a clear distinction between the frequency scaling of EEG and MEG. Insets show the comparison between MEG awake (prior to noise correction) and MEG empty-room recordings (not normalized). Note that the empty-room scales the same as the MEG signal, but in general EEG and MEG scale differently.

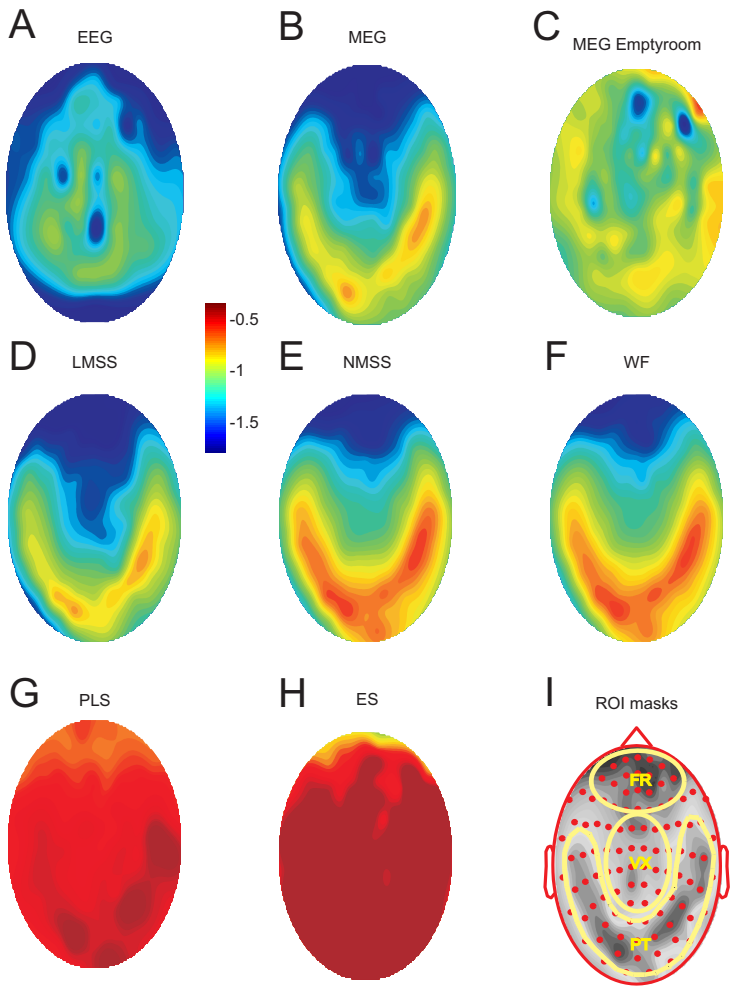

Figure 5.4. Topographical representation of frequency scaling exponent averaged across four subjects. A. EEG awake. B. MEG awake. C. MEG empty-room. D, E. MEG after spectral subtraction of the empty-room noise using linear (LMSS) and non-linear (NMSS) methods respectively. F. MEG spectral enhancement using Wiener filtering (WF). G. MEG, partial least square (PLS) approximation of non-noisy spectrum. H. Exponent subtraction (the exponent represented is the value of the frequency scaling exponent calculated for MEG signals, subtracted from the scaling exponent calculated from the corresponding emptyroom signals). I. Spatial location of ROI masks (shown in yellow). FR covers the Frontal, VX covers Vertex and PT spans Parietotemporal. Dots show spatial arrangement of 102 MEG SQUID sensor triplets. The background gray-scale figure is same as the one in panel B. Note that panels A through H use the same color scaling.

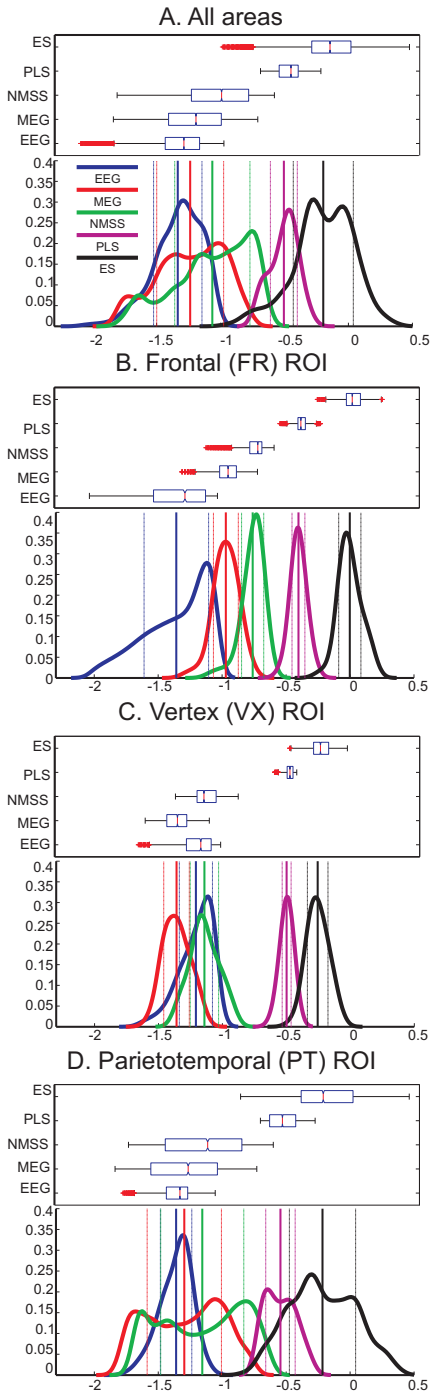

Figure 5.5. Statistical comparison of EEG vs. MEG frequency scaling exponent for all regions (A) and different ROI masks (B,C & D). In each panel, a box-plot on top is accompanied by a non-parametric distribution function in the bottom. In the top graph, the box has lines at the lower quartile, median (red), and upper quartile values. Smallest and biggest non-outlier observations (1.5 times the interquartile range IRQ) are shown as whiskers. Outliers are data with values beyond the ends of the whiskers and are displayed with a red + sign. In the bottom graph, a Non-parametric density function shows the distribution of EEG, MEG and empty-room-corrected MEG frequency scaling exponents (note that LMSS and WF are not shown here; see the text for description.). Thick and thin vertical lines show the mean and mean $\pm$ std for each probability density function (pdf).

5.9.2 Tables

A. Mean and standard deviation

	EEG	MEG (awake)	NMSS
All	-1.33 $\pm$ 0.19	-1.24 $\pm$ 0.26	-1.06 $\pm$ 0.29
FR ROI	-1.36 $\pm$ 0.25	-0.97 $\pm$ 0.10	-0.76 $\pm$ 0.09
VX ROI	-1.21 $\pm$ 0.13	-1.36 $\pm$ 0.10	-1.14 $\pm$ 0.11
PT ROI	-1.36 $\pm$ 0.12	-1.30 $\pm$ 0.29	-1.16 $\pm$ 0.32

B. Pearson correlation

	EEG vs. MEG	EEG vs. Corrected MEG (NMSS)
All	0.29	0.32
FR ROI	0.41	0.32
VX ROI	-0.17	-0.15
PT ROI	0.35	0.38

C. Kendall Rank Corr

	EEG vs. MEG	EEG vs Corrected MEG (NMSS)
All	0.21	0.24
FR ROI	0.29	0.21
VX ROI	-0.03	-0.04
PT ROI	0.23	0.26

D. KruskalWallis

	p value	Chi-square	df Error
All	$< 10^{-15}$	1.53 10^3	34838
All noise-corrected	$< 10^{-15}$	8.03 10^3	34838
FR ROI	$< 10^{-15}$	3.30 10^3	5008
FR ROI noise-corrected	$< 10^{-15}$	3.72 10^3	5008
VX ROI	$< 10^{-15}$	1.72 10^3	5452
VX ROI noise-corrected	$< 10^{-15}$	0.23 10^3	5452
PT ROI	$< 10^{-15}$	0.21 10^3	13010
PT ROI noise-corrected	$< 10^{-15}$	1.18 10^3	13010

Table 5.1. ROI statistical comparison. A. mean and std of frequency scale exponent for all regions and individual ROI. B. numerical values of linear Pearson correlation. C. rank-based Kendall correlation. D. non-parametric test of analysis of variance (KruskalWallis). Corrected MEG refers to spectral subtraction using NMSS. The full table is provided in Supplementary information.

5.10 Suplplementart Tables & Figures

5.10.1 Supplementary table

A. Mean and standard deviation

	EEG	MEG (awake)	MEG(empty)	LMSS
All	-1.33 ± 0.19	-1.24 ± 0.26	-1.04 ± 0.13	-1.24 ± 0.28
FR ROI	-1.36 ± 0.25	-0.97 ± 0.10	-0.97 ± 0.06	-0.96 ± 0.11
VX ROI	-1.21 ± 0.13	-1.36 ± 0.10	-1.10 ± 0.09	-1.36 ± 0.10
PT ROI	-1.36 ± 0.12	-1.30 ± 0.29	-1.08 ± 0.15	-1.31 ± 0.32

	NMSS	WF	PLS	ES
All	-1.06 ± 0.29	-1.05 ± 0.27	-0.50 ± 0.11	-0.20 ± 0.23
FR ROI	-0.76 ± 0.09	-0.76 ± 0.08	-0.40 ± 0.05	-0.00 ± 0.09
VX ROI	-1.14 ± 0.11	-1.12 ± 0.11	-0.50 ± 0.04	-0.26 ± 0.08
PT ROI	-1.16 ± 0.32	-1.14 ± 0.30	-0.54 ± 0.11	-0.22 ± 0.26

B. Pearson correlation of EEG vs.

	MEG	LMSS	NMSS	WF	PLS	ES
All	0.29	0.29	0.32	0.33	0.37	0.35
FR ROI	0.41	0.39	0.32	0.37	0.01	0.17
VX ROI	-0.17	-0.10	-0.15	-0.13	0.01	-0.28
PT ROI	0.35	0.34	0.38	0.39	0.46	0.41

C. Kendall Rank Corr of EEG vs.

	MEG	LMSS	NMSS	WF	PLS	ES
All	0.21	0.21	0.24	0.25	0.29	0.23
FR ROI	0.29	0.23	0.21	0.27	-0.06	0.12
VX ROI	-0.03	0.04	-0.04	-0.03	0.07	-0.09
PT ROI	0.23	0.23	0.26	0.26	0.30	0.27

Table 5.2. ROI statistical comparison for different noise correction methods. A. mean and std of frequency scale exponent for all regions and individual ROI. B. numerical values of linear Pearson correlation. C. rank-based Kendall correlation.

5.10.2 Supplementary figures

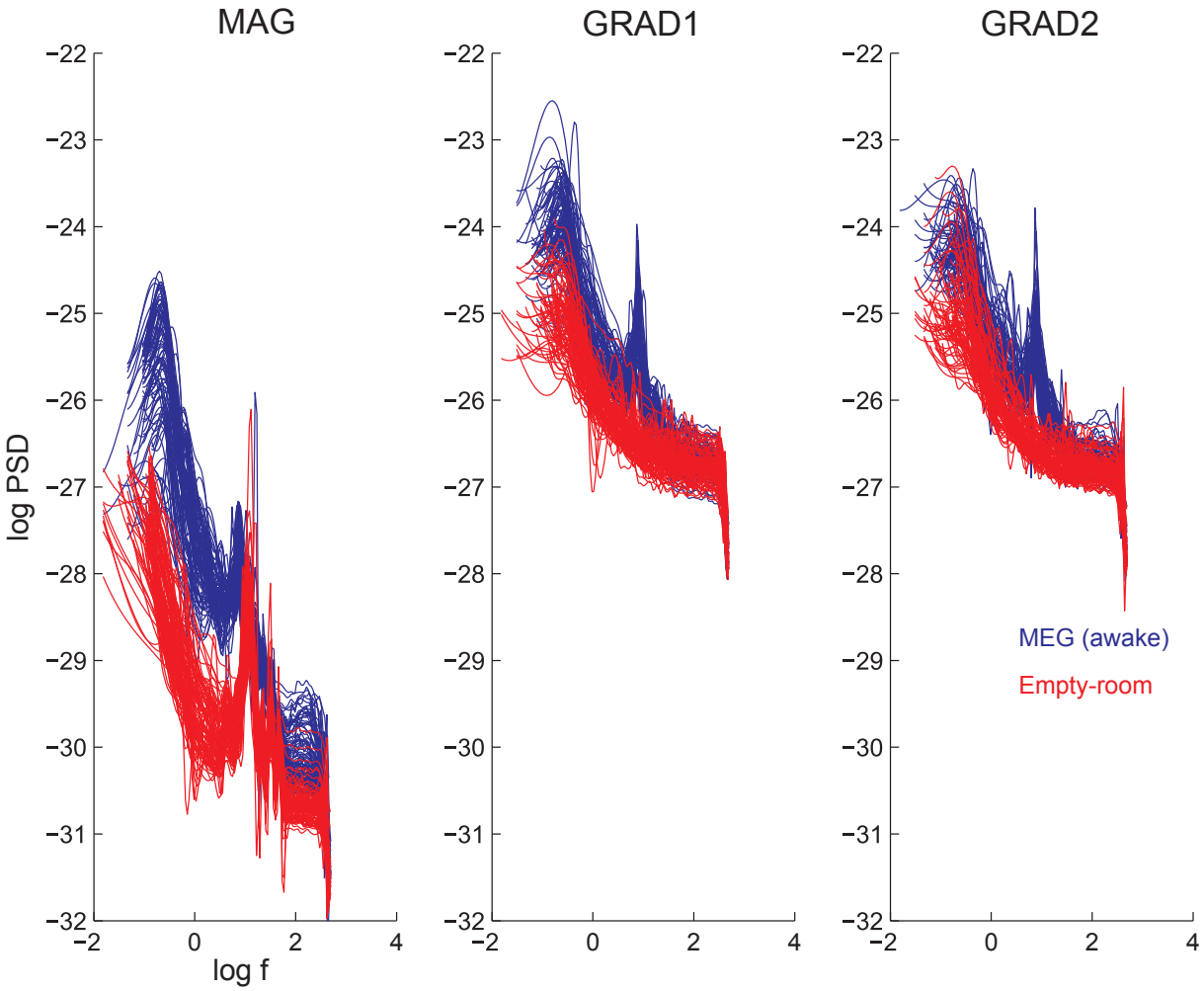

Figure 5.6. Figure S1: Frequency spectra of magnetometers and gradiometers. Comparison of awake (blue) vs empty-room (red) recordings between Magnetometers (MAG) and Gradiometers (GRAD1, GRAD2) in a sample subject. As for the EEG, the MEG signal is characterized by a peak at around 10 Hz, which is presumably due to residual alpha rhythm (although the subject had eyes open). This is also visible from the MEG signals (Fig. 5.1) as well as from their PSD (Fig. 5.3 and MAG panel here). The power spectrum from the empty-room signals also show a peak at around 10 Hz, but this peak disappears from the gradiometer empty-room signals, while the 10 Hz peak of MEG still persists for gradiometers awake recordings. This suggests that these two 10 Hz peaks are different oscillation phenomena. All other subjects showed a similar pattern.

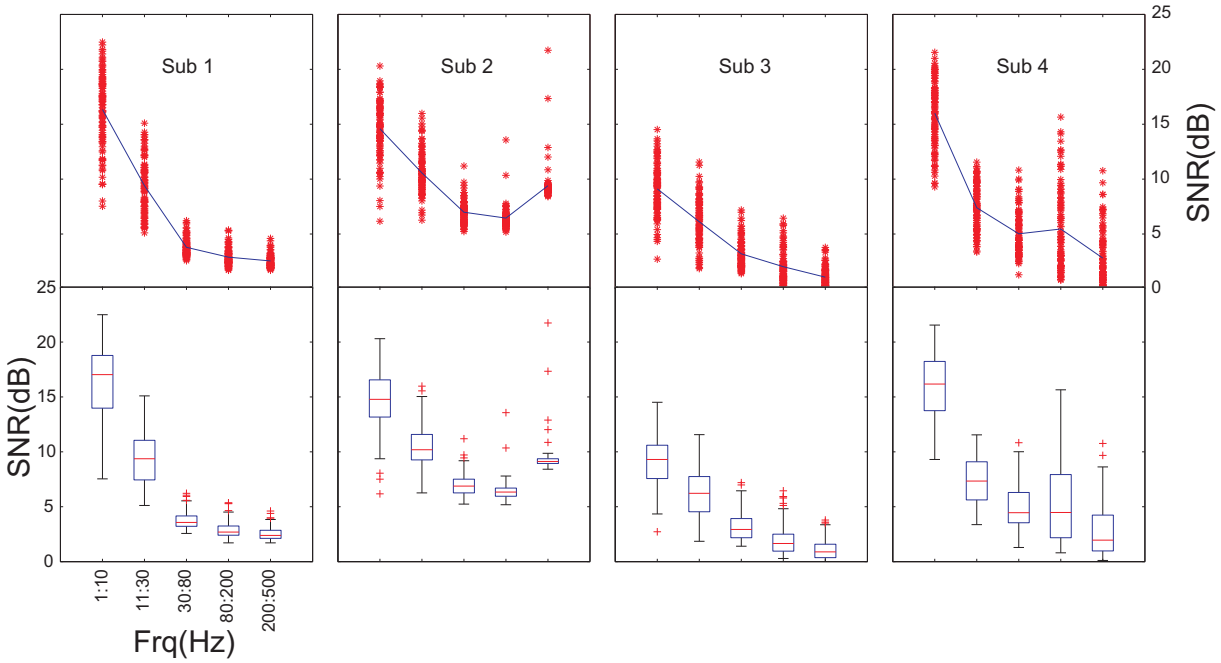

Figure 5.7. Figure S2: Signal-to-noise ratio (SNR) of Magnetometers (MAG) for multiple frequency bands: 0-10 Hz (Slow, Delta and Theta), 11-30 Hz (Beta), 30-80 Hz (Gamma), 80-200 Hz (Fast oscillation), 200-500 Hz (Ultra-fast oscillation). In the scatterplots, red astrisks relate to individual sensors and the blue line is the band-specific mean across the sensors. In boxplots, the box has lines at the lower quartile, median (red), and upper quartile values. Smallest and biggest non-outlier observations (1.5 times the interquartile range IRQ) are shown as whiskers. Outliers are data with values beyond the ends of the whiskers and are displayed with a red + sign. In all subjects, the SNR shows a band-specific trend and has the highest value for lower frequencies and gradually drops down as band frequency goes up. As the frequency drops, the variability of SNR (among sensors) rises; therefore, the SNR of the lowest band (1-10 Hz) shows the highest sensors-to-sensor variability and the highest SNR in comparison to other frequency bands.

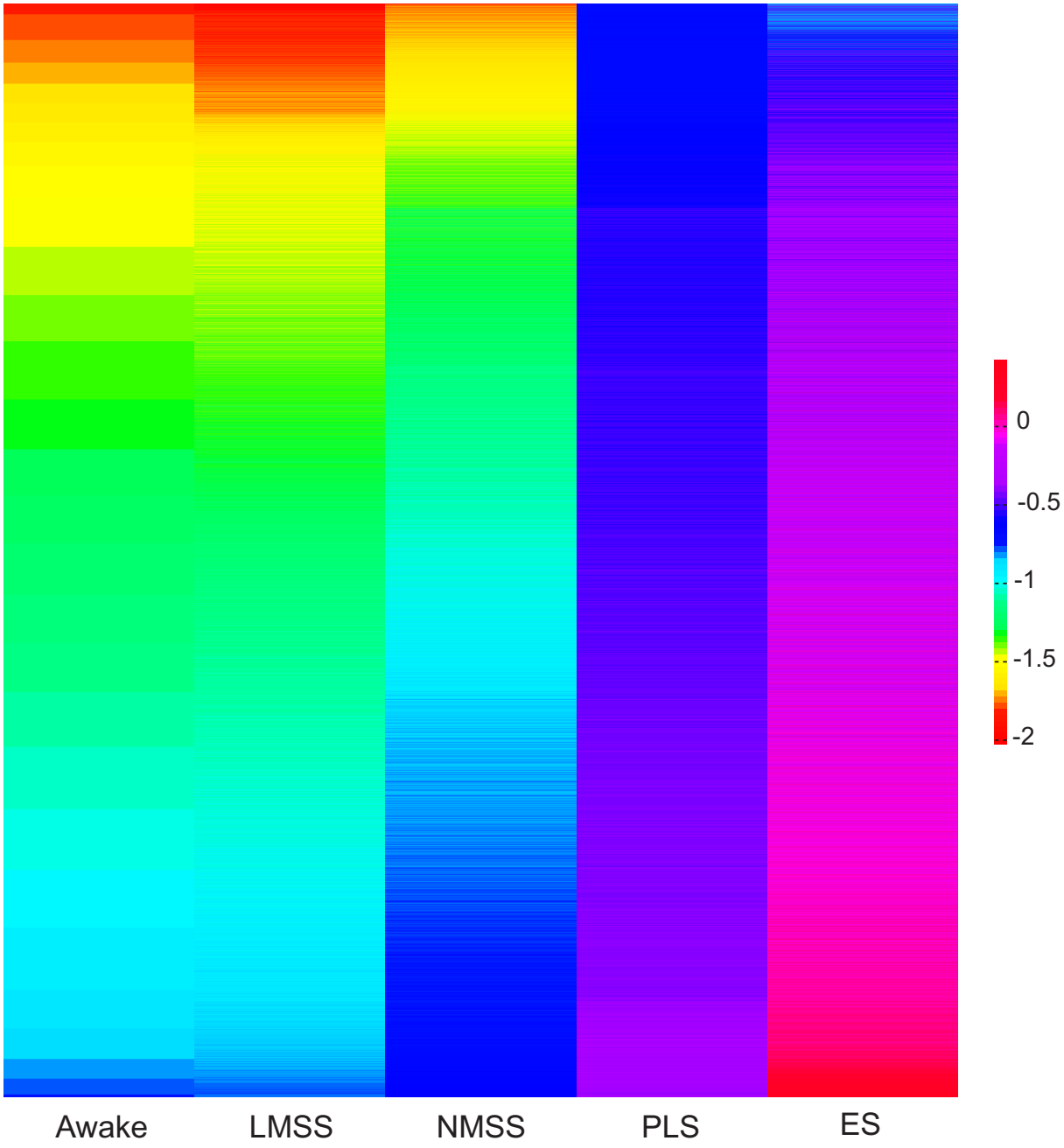

Figure 5.8. Figure S3: Noise correction comparison. Every horizontal line showes a voxel of the topographical maps shown in Fig. 5.4 sorted based on the scaling exponent values of awake MEG (left stripe). Using a continuous color spectrum, these stripes show that minimal correction is achived by LMSS. As indicated in the text, the performance of this method is not reliable due to the nonlinear nature of SNR (see Suppl. Fig. S2). NMSS yields higher degree of correction. WF performs almost identical to NMSS (not shown here). Exponent subtraction almost abolishes the sacling all together (far right stripe). PLS results in values between NMSS and ”Exponent subtraction”. For details of each of these correction procedures, see Methods. LMSS, NMSS and WF rely on additive uncorrelated nature of noise. “Exponent subtraction” assumes that the noise is intrinsic to SQUID. PLS ascertains the characteristics of noise to the collective obeserved pattern of spectral domain across all frequencies. See text for more details.

Chapter 6

Human neocortical excitation and inhibition

There is a fundamental error in separating the parts from the whole, the mistake of atomizing what should not be atomized. Unity and complementarity constitute reality.

Werner Karl Heisenberg

Spatiotemporal dynamics of neocortical excitation and inhibition during human sleep

Adrien Peyrache[1,2], Nima Dehghani[1], Emad N. Eskandar[3,4], Joseph R. Madsene[5,6], William S. Anderson[6], Jacob A. Donoghue[7], Leigh R. Hochberg[7,8,9,10], Eric Halgren[11], Sydney S. Cash [7,*], Alain Destexhe[1,*]

1 Laboratory of Computational Neuroscience. Unité de Neurosciences, Information et Complexité (UNIC). CNRS, France.
2 Center for Molecular and Behavioral Neuroscience, Rutgers University, USA.
3 Department of Neurosurgery, Massachusetts General Hospital, USA.
4 Nayef Al-Rodhan Laboratories for Cellular Neurosurgery and Neurosurgical Technology, Massachusetts General, USA.
5 Department of Neurosurgery, Children's Hospital and Harvard Medical School, USA.
6 Department of Neurosurgery, Brigham and Women's Hospital and Harvard Medical School, USA.
7 Department of of Neurology, Massachusetts General Hospital and Harvard Medical School, USA.
8 Institute for Brain Science, Brown University, USA.
9 Rehabilitation Research and Development Service, Department of Veterans Affairs, RI, USA.
10 School of Engineering, Brown University, USA.
11 kDepartments of Radiology, Neurosciences, and Psychiatry, University of California at San Diego, USA.

∗ **co-corresponding authors** [1]

[1]Author contributions: A.P., N.D., S.S.C., and A.D. designed research; A.P., N.D., E.N.E., J.R.M., W.S.A., J.A.D., L.R.H., E.H., S.S.C., and A.D. performed research; A.P., N.D., and A.D. analyzed data; and A.P., N.D., E.H., S.S.C., and A.D. wrote the paper.

6.1 Summary

Intracranial recording is an important diagnostic method routinely used in a number of neurological monitoring scenarios. In recent years, advancements in such recordings were extended to include unit activity of an ensemble of neurons. However, a detailed functional characterization of excitatory and inhibitory cells has not been attempted in human neocortex particularly during the sleep state. Here, we report that such feature discrimination is possible from high-density recordings in the neocortex using 2-dimensional multielectrode arrays. Successful separation between RS neurons (regular or bursting cells) from fast-spiking (FS) cells resulted in well-defined clusters where each showed unique intrinsic firing properties. The high density of the array allowing recording from large number of cells (up to 90) helped us to identify apparent monosynaptic connections, which confirmed the excitatory and inhibitory nature of RS and FS cells, thus categorized as putative pyramidal and interneurons, respectively. Finally, we investigated the dynamics of correlations within each class. A marked exponential decay with distance was observed in the case of excitatory but not for inhibitory cells. While the amplitude of that decline was dependent on the timescale at which the correlations were computed, the spatial constant was not. Furthermore, this spatial constant is compatible with the typical size of human columnar organization. These findings provide a detailed characterization of neuronal activity, functional connectivity at the micro-circuit level and the interplay of excitation and inhibition in the human neocortex.

Reference: *Proc Natl Acad Sci U S A. 2012 Jan 31;109(5):1731-6*

Keywords: *spontaneous activity , ensemble recordings , single unit , functional dynamics*

6.2 Résumé

Les enregistrements intra-crâniens constituent une méthode importante de diagnostic ultilisée de façon routinière dans plusieurs scenarios de monitoring en neurologie. Ces dernières années, les avancées de ces méthodes ont permis l'enregistrement de signaux unitaires multiples. Cependant, une caractérisation fonctionnelle détaillée de neurones excitateurs et inhibiteurs n'a pas encore été réalisée dans le neocortex humain, et en particulier pendant le sommeil. Dans cette étude, nous montrons qu'une telle discrimination entre neurones excitateurs et inhibiteurs est possible à partir d'enregistrements à haute densité au moyen de peignes d'électrodes en 2D. Une séparation efficace entre cellules "regular spiking" (RS) et "fast spiking" (FS) est possible et résulte en deux ensembles bien séparés, avec des propriétés distinctes. La haute densité des électrodes permet d'obtenir des connections apparemment mono-synaptiques, et de corroborer cette séparation RS-FS avec la nature excitatrice ou inhibitrice de la connection. Cette procédure confirme que les cellules classifiées comme FS sont toujours inhibitrices, alors que les RS sont toujours excitatrices, et donc peuvent être classifiées respectivement comme cellules pyramidales ou interneurones inhibiteurs. Finalement, nous investiguons la dynamique des corrélations au sein de chaque classe de neurone. Les corrélations entre excitateurs montrent une décroissance exponentielle avec la distance, tandis que les cellules inhibitrices restent corrélées à plus grande distance. L'amplitude des corrélations dépend de l'échelle temporelle du calcul de corrélation, mais pas la constante spatiale. Cette constante est compatible avec la taille typique des collonnes corticales chez l'homme. Ces résultats permettent une caractérisation détaillée de l'activité neuronale, de la connectivité fonctionnelle au niveau de microcircuits, et de l'interaction entre excitation et inhibition dans le neocortex humain.

From columnar microcircuits [235–237] to higher-order neuronal functional units, neocortical dynamics are characterized by a large range of spatial and temporal scales [231,238]. Recent technical improvements have allowed the nature of these dynamics in the human brain to be directly explored: Single-neuron activity in conjunction with local field potentials (LFPs) can be detected from the cerebral cortex and hippocampus in the course of intense monitoring of brain activity before surgical treatment of epileptic foci [239]. Modern electrode systems provide the possibility of extracellular recordings of neuronal ensembles by using either microwires [193] or high-density microelectrode arrays [60, 240]. Prior efforts have demonstrated excellent recordings of single-neuron activity in human cerebral cortex [194–196]. Separation of units between "regular-spiking" (RS) and "fast-spiking" (FS) neurons, presumably excitatory (pyramidal) and inhibitory (interneuron) cells, respectively, is commonly practiced in animal experiments. In the neocortex of various mammalian species, RS and FS cells can be reliably separated based on spike waveform, duration, and firing rates [39, 241]. Similar criteria were also used to successfully separate units into putative pyramidal (Pyr) cells and inhibitory interneurons (Int) in human hippocampus [41]. Two recent studies have used morphological features to distinguish between these two classes of neurons [55, 56]. However, the network interaction between these types of morphofunctional discriminated units has still largely not been investigated. Neuronal correlations have been shown to decay with space in primary visual cortex, possibly caused by the highly structured nature of inputs [242]. In parallel, it has been shown that, in the rodent hippocampus, at the top of cortical processing, such an effect of distance on neuronal correlations was also present and was different for excitatory and inhibitory cells [243]. The 2D high-density recordings of human neuronal activity offer a unique opportunity to study the spatiotemporal dynamics of excitation and inhibition in the neocortical network [55, 56, 244]. In the present paper, we successfully categorize the extracellularly recorded units into RS and FS during sleep and show their putative excitatory or inhibitory nature based on monosynaptic connections. We also provide evidence for distinctive network dynamics for each category of these neurons during drowsiness and sleep spontaneous activity.

6.3 Results

6.3.1 Separation of RS and FS Cells

A sample recording of intracranial EEG, LFP, and unit recordings from the microelectrode array is shown in Figure 6.1. The firing of excitatory and inhibitory cells was strongly correlated (Figure 6.1C). By using standard methods [39, 241], those two cell types were discriminated on the basis of their action potential waveforms (SI Materials and Methods). The waveform half-widths and valley-to-peak distributions exhibited two automatically detected well-defined clusters (Figure 6.2 A and B). Other waveform features can be used and yielded the same separation (Figure 6.6B and C). Each cluster showed a distinct spike waveform (Figure 6.2C):

A short, fast-decaying action potential represents putative FS and GABAergic cells; a large and slower one depicts putative RS and glutamatergic neurons. A total of 190 RS and 46 FS cells were discriminated from three patients (four recording sessions). This ratio amounts to an 80% excitatory and 20% inhibitory distribution of cells. This morphological clustering was validated by distinctive cell intrinsic properties. The average firing rates showed remarkable separation between the two groups, with FS firing at higher rates (Figure 6.2D, P $< 10^{-10}$, one-way ANOVA). Both firing-rate distributions had a Gaussian-like shape in logarithmic x coordinates (Figure 6.2D); therefore, firing rates can be estimated as being drawn from log-normal distribution for both cell types. FS firing rate was on average five times higher than RS cell firing rate was, which, interestingly, is comparable to the ratio of discriminated FS and RS cells in the whole dataset. Coefficients of variation [the ratio of the SD to the mean of the interspike interval (ISI) distribution] were also significantly different for the two cell groups (Figure 6.2E, P < 0.01, one-way ANOVA). Furthermore, cells could be also segregated based on their autocorrelogram (Figure 6.2F): Int are known to have long refractory periods and show a slow rising autocorrelation. On the other hand, RS cells show sharp autocorrelograms, reflecting their shorter refractory period and their tendency to fire in bursts. The distributions of the modes (i.e., time of maximal values in the autocorrelogram) were highly distinct (Figure 6.2G). Finally, isolated neurons were tested for their burstiness. The histograms of the ISIs were sometimes characterized by a clear bimodality, especially when the logarithm of the ISI was considered (Figure 6.2H, Left and Center). Cells were classified as bursty when they passed the significance level of a bootstrap-based test for bimodality [245]. As displayed in Figure 6.2H, of the population that did not have FS morphological characteristics, 64% expressed bursting behavior. Only 2% of FS (that is only one cell in the whole dataset) showed such properties.

6.3.2 Putative Monosynaptic Connections

Analysis of cross-correlograms between pairs of units allows the characterization of putative monosynaptic connections [39]: Positive, short-latency peaks (<4ms) are the sign of a biased tendency of the reference cell A firing just before the other cell (B) at above chance level, which would thus be the functional signature of an excitatory monosynaptic connection from cell A to cell B. Conversely, a gap in the crosscorrelograms indicates an inhibitorymonosynaptic connection. The expected cross-correlogram for two unrelated cells was obtained by jittering each pair of spike trains and by computing the 99% confidence interval (SI Materials and Methods). Cell pairs showing an excess of biased spikes occurring above this threshold were categorized as monosynaptically connected. Figure 6.3A shows an example of a reciprocally connected putative Pyr/Int pair. Occasionally, some Pyr cells excited another target cells without any significant reciprocal connection (Figure 6.3B). The excitatory or inhibitory nature of the postsynaptic effect from the efferent cells was remarkably matched to their spike waveform characteristics (Figure 6.3C). This association of synaptic effects with action potential waveforms significantly differed from chance ($\chi^2 = 33.6, df = 2, P$¡0.0001) and provides converging evidence for the

validity of the morphofunctional dichotomy within the network. The monosynaptic connectivity matrix was typically sparse. In the dataset, only 0.17% of the possible connections (28 of 16,932) showed a significant monosynaptic effect in the cross-correlograms. This result was not different for postsynaptic excitation and inhibition (respectively, 0.16% and 0.19% of the total numbers of possible postsynaptic contacts from Pyr or Int cells; $P > 0.05$, binomial test). Monosynaptic contacts were almost entirely local, 76% (16 of 21) of excitatory effects, and the totality of inhibitory ones was confined to pairs recorded on the same electrode (Fig. 3D); 5.65% of the possible contacts on pairs from same electrode showed a significant bias in the cross-correlograms. Based on this functional categorization, throughout the rest of the paper, we interchangeably use FS, inhibitory, and Int. Similarly, we do the same for RS, excitatory, and Pyr.

6.3.3 Spatiotemporal Dynamics of Cell Interaction

To investigate the interaction at the maximum possible spatial scale (i.e., 4 mm), we correlated the binned spike trains at various timescales. This approach provides a spatiotemporal view of cell-cell interaction, mono- or polysynaptically. Figure 6.4, Center Upper and Right shows the strength of the absolute correlation between one example Pyr cell and all other Pyr cells: The strength of the correlation between Pyr cells seems to decrease with distance. The absolute Pearson's correlation coefficients were directly related to peak or trough in the cell's cross-correlograms for different randomly chosen Pyr cells (Figure 6.4, Right) in reference to the spike trains of the example cell from Figure 6.4, Center Upper. Conversely, for Int (Figure 6.4, Center Lower and Left), the correlation between cell pairs appeared to be independent of the distance separating the two cells. Also, unlike for Pyr cells, the degree of modulation of the cross-correlograms did not appear to be related to the size of Pearson's correlation, possibly because of the dependence of correlation coefficients on cell-intrinsic firing rates [246].

To further analyze the relationship between correlation and spatial arrangement of the cells, all of the cell pairs from the datasets were pooled together, and the absolute coefficients of correlation, computed with 50-ms time bins, were plotted as a function of interelectrode distance (Figure 6.5A). To remove bias caused by firing-rate inhomogeneity in correlation values and to render Pyr-Pyr correlation coefficients comparable to those of Int pairs, correlations were then normalized by the geometric mean of each cell pair's average firing rates [246]. Furthermore, to avoid experiment-dependent spurious covariation, which may, for example, arise from electrode drift, a local version of correlation was used (SI Materials and Methods). This analysis revealed that, first, the correlation between cell pairs recorded from the same electrode depended on their connectivity: As expected, putative monosynaptically connected pairs–whatever the nature of the synapse(s)–showed significantly higher absolute correlation than did nonconnected pairs (Figure 6.72), revealing fine-scale structure in local microcircuits. Second, at the level of the whole recording matrix, the cell pairs were divided in two categories: putative inhibitory Int

pairs (designated as the I-I group) and excitatory Pyr pairs (E-E group). Because of the improbability of an equal sampling ratio of the recorded Int and Pyr cells to the existent cells in the examined tissue, the E-I comparison does not hold the same validity as do E-E and II comparisons of correlation and therefore is not reported here. The linear regression between absolute correlations and distance between recording sites showed a negative slope for both groups but was significant only for the E-E group. Furthermore, when the same analysis was carried out for different time bin sizes (Figure 6.5B and Figure 6.83), the negative slope of the linear regression was significant ($P < 0.05$, Pearson's correlation test) across all timescales for the E-E group, but not for the I-I group. To ensure that the oversampling of Pyr cells compared with Int did not yield the difference in the significance levels, the number of Pyr pairs was down-sampled to match the number of Int pairs and bootstrapped. The correlation between neuronal pairwise correlation and distance remained significantly lower than 0 for time bins smaller than 200 ms (Figure 6.9).

Next, the correlation values were averaged in equally spaced 0.8-mm intervals of interelectrode distance (Figure 6.5C). The relationship between correlation and spatial distance was approximately flat in the I-I group, thus confirming the lack of a significant relationship. The E-E correlations decayed with distance and were well fit with a three-parameter exponential (Figure 6.5D). The fitting parameters can be reduced to two meaningful values: the spatial extent of the exponential λ and the relative (dimensionless) amplitude modulation κ/β that quantifies the amplitude of the decay relatively to the baseline. κ/β decreased monotonically with time bin widths, whereas the spatial constant λ was more or less constant, with an average value of 1 mm. Notice that such decay did not sustain for time bins longer than 2 s (the two far right points in Figure 6.5D). This decay resulted from a monotonic increase in the baseline correlation β and from a decrease of the exponential amplitude κ (Figure 6.5D, Inset; values diverged for time bins longer than 2 s). Similar results were yielded for non-normalized coefficients of correlation (Figure 6.105).

6.3.4 State-Dependent Long-Range Correlation

Finally, we investigated the difference in spatial correlation between different states (Figure 6.5E). Clear periods of light and deep non-rapid eye movement (NREM) sleep were detected in addition to wake/drowsiness epochs in two of the three patients (three recording sessions, representing 87% of the total discriminated cells in the analysis). The rapid eye movement (REM) episodes were brief, if detectable at all. For Int pairs, the linear regression between neuronal pairwise correlation and distance was never different from 0. For Pyr pairs, this correlation was highly significant for wake/drowsiness and light NREM over almost all tested time bin sizes. During deep NREM, the correlation was smaller for the different time bins but was still significant, or very close to significance, for most comparisons.

6.4 Discussion

The present paper reports a detailed quantitative analysis of the dynamics of excitation and inhibition in the human neocortex during overnight sleep. In particular, using massive cell recordings we have shown (i) robust morphological (extracellular waveform features) discrimination of putative cortical excitatory and inhibitory neurons; (ii) in vivo evidence of functional monosynaptic connections in the human neocortex; (iii) functional behavior of inhibitory and excitatory cells during human sleep; (iv) distinctive spatiotemporal patterns of Pyr-Pyr and Int-Int assembly interactions; and (v) detailed quantification of corticocortical correlations. Hence, this paper provides a unique insight to the dynamics of human neocortical microcircuits.

6.4.1 Separating Excitation from Inhibition

Different attempts were carried out recently to distinguish between putative Int and Pyr cells, for example, in the hippocampal formation [247]. In nonprimates, the separation between the two populations on the basis of extracellular features is now generally accepted [39, 241]. In this paper, human neocortical cell recordings were clustered on their extracellular waveforms. The two parameters describing waveform morphology formed well-defined clusters that were captured by standard algorithms (Figure 6.2 and Figure 6.6A). First, despite the a priori higher probability to detect the high-amplitude spikes from large Pyr cells, the overall proportion of cells in each group (80% Pyr and 20% Int) was consistent with the known ratio between Pyr and Int cells in the neocortex [143]. In other words, a random sampling with extracellular electrodes gives rise to the expected distribution of cell types, thus indicating that they are both detectable with sufficient reliability. Second, this segregation was consistent over several other cell-intrinsic parameters, such as firing rates (higher for FS Int) or the high tendency of the Pyr cells to burst (Figure 6.2). As supplementary evidence of separation between Int and Pyr cells, we analyzed the potential monosynaptic interactions between cell pairs and categorized them as excitatory or inhibitory. The distribution of cells' postsynaptic effects perfectly matched the clustering of excitatory and inhibitory cells based on their extracellular features (Figure 6.3). Overall firing rates were surprisingly low, < 0.5 Hz for the RS cells and ~ 2 Hz for the FS cells. However, using long-lasting recordings allowed us to reliably isolate the cells' spikes during cluster-cutting procedures, even if those were sometimes very rare, whereas those low firing-rate cells could have been disregarded in other situations. This low firing rate may relate to the recordings being in superficial layers because animal studies have demonstrated that many of these neurons have lower firing rates than in the deep layers [248]. It is also consistent with other recordings in human neocortex [195] and may reflect fundamental metabolic constraints in large brains [249]. Theoretical studies have emphasized that, in a sparsely connected network, the seemingly irregular firing of cells could be the consequence of the balance between excitation and inhibition [250–252] . Similarly, intracellular recordings have revealed a balance between

excitatory and inhibitory conductance both in vitro [172] and in vivo [253], they and even shown a possible excess of inhibition in vivo [254]. However, inhibitory cells are four to five times less common than excitatory cells, as are the number of synapses they form onto postsynaptic targets [143]. Although direct demonstration of balanced excitation and inhibition requires intracellular recordings, our extracellular analysis provides indirect evidence in favor of such a balance. First, the average firing rate of Int was five times higher than that of Pyr cells (Figure 6.2), which is the same ratio as the total number of cells from each type. Second, it has been shown theoretically that balanced networks exhibit a heavy-tailed, wide range of firing rates [250], which was found to be the case for the human neurons recorded here, where, for both Pyr and Int, the firing rates were log-normally distributed (Figure 6.2).

6.4.2 Spatiotemporal Extent of Neuronal Interrelationships

The interaction between neocortical neurons takes place at different spatiotemporal scales, and this paper sheds light on such interactions in human neocortex. We found that the short-latency monosynaptic effects from spike-train cross-correlograms were confined to the same or very proximal electrodes (Figure 6.3D), in agreement with the rapid decrement with distance of synaptic contact probability [143, 255]. The extent of monosynaptic contacts in local circuits is still a subject of debate [143, 235, 236, 255], and it is important to bear in mind that spike-train correlation analysis [255] is likely to underestimate the number of actual contacts because it is based only on suprathreshold activity from pre- and postsynaptic neurons. The connected cells showed higher long-timescale correlations than the cells recorded from the same electrodes without any detectable synaptic contact (Figure 6.7). This finding suggests that connected units tend to participate in the same cell assemblies [49] and echoes the recent findings that suggest that those units are more likely to receive common inputs within the cortical column [235]. We also found that the binned spike-train correlations showed spatial dependence only for excitatory cell pairs, whereas inhibitory cell pairs were as much correlated with both proximal and distal electrodes over the 4-mm extent of the array. For the Pyr cell pairs, the modulation of the spatial extent decreased with the timescale at which correlations were computed; however, the spatial constant of this decay (1 mm) was approximately the same, independent of the timescale (Figure 6.5 and Figure 6.8).

These results have strong implications for our understanding of cortical network dynamics. First, the neuronal activity of Pyr cells remains coherent on a scale corresponding to the spatial extent of the axonal arborization in superficial layers. This is also the same spatial extent of a typical “hyper-columnar” organization of human neocortex [143], robustly described in primary sensory cortices and less in higher-order areas such as the temporal neocortex. Second, the correlations tended to equalize, as measured by the spatial-modulation factor, for longer timescales. This is a known result from neocortical LFPs that shows high spatial correlation over a large proportion of the network during slow wave activity [238,256] (characterized by long-timescale

dynamics) compared with low spatial correlation during states dominated by short timescales exhibiting desynchronized, low-amplitude, and fast oscillations [174]. Accordingly, when the relationship between Pyr pairwise correlations and distance was investigated separately for the different wake/sleep states, the main difference was the decrease of this relationship during deep NREM sleep, although still significant (Figure 6.5E), presumably because of the widespread entrainment of neuronal activity by slow/δ oscillations. Conversely, the large spatial extent of interneuronal correlations could be caused by common subcortical inputs over large neocortical areas impinging directly onto GABAergic cells, as can be the case for thalamocortical [80, 97] projections. In addition, the highly complex distribution of interneuronal connectivity, with some cells contacting very distant areas, could produce large-scale synchronization of the inhibitory network [257]. It is important to keep in mind that these recordings were made in epileptic patients, and, although the present analyses were done in periods of activity devoid of seizures or activity on either the microelectrode array or any subdural electrode, we cannot eliminate the possibility that some of our results may reflect a pathological rearrangement of neuronal numbers and/or interconnections. The current results suggest that neocortical principal cells may be organized into coherent firing units, or cell assemblies, mainly on the basis of local excitatory interactions (1 mm). In parallel, the inhibitory network maintains coherent activity over much larger distances ($>$4 mm). The role of such large-scale synchronized inhibition should be investigated by future studies. These results constitute an initial step toward understanding the dynamic and functional microarchitecture of human neocortical circuits, characterized by spatiotemporal interactions spanning several orders of magnitude. Overall, this paper not only extends the prior work reported in animals to the human cortex but also tackles it with an exhaustive quantification that can be verified in future studies (in animals as well as in humans) and will prove useful in the interpretation of the many studies, published and underway, that explore the details of human single neurons during cognition, sleep, seizures, and a wide range of other situations.

6.5 Materials and Methods

Recordings were made from three patients (ages 21, 24, and 52 y; two women and one man). All patients had focal epilepsy arising from differing causes: a cortical dysplasia, a glioneural tumor, or postencephalitic cortical gliosis and hippocampal sclerosis as confirmed by postoperative histology. The NeuroPort electrode array, 1mmin length, was placed in layers II/III of the middle temporal gyrus in all three patients. This array is silicon-based, made up of 96 microelectrodes with 400-μm spacing, covering an area of 4 *x* 4 mm(40). A total of four nights of natural sleep were examined (one night for two of the patients, two nights for the other patient). Data were sampled at 30 kHz (Blackrock Microsystems). The implantation site was included in the therapeutic resection in all patients. Recordings were made in 40-min segments, which were concatenated over a given night for spike sorting. Single units were discriminated by using

standard clustering methods (SI Materials and Methods). On average, 57% (±12%) of the electrodes showed visible neuronal activity, including electrodes that were not possible to cluster: Individual cells were isolated from 75% (±14%) of these electrodes. On average, 1.39 (±0.26) neurons were discriminated from each electrode where at least one neuron was isolated. See SI Materials and Methods for further details.

6.6 Supporting Information

6.6.1 Unit Recording and Spike Sorting

For offline sorting, the first three principal components of spike waveforms were computed independently for recordings from each electrode. The spikes were then clustered automatically with an expectation-maximization (EM) algorithm (Klustakwik, http://klustakwik.sourceforge.net) and then manually processed with Klusters software (http://klusters. sourceforge.net/). Because the signal was sometimes not stable, great care was taken during spike cluster cutting. Some cells with drifting action potential amplitudes were considered only for a portion of the total recording during which they were unequivocally distinguishable from the background noise. In that case, the average firing rates were computed only over the period those cells were firing.

6.6.2 Discrimination of Pyramidal (Pyr) Cells and Fast-Spiking (FS) Interneurons (Int)

Average waveforms were computed for each isolated cell. As described previously, the half width of the extracellular positive deflection has, at the neuronal population level, a bimodal distribution [39, 241]. The separation is even more striking when the valley-to-peak parameter [39] is added for 2D clustering (Figure 6.2 A and B). Automatic clustering of these average waveforms from individual cells by using a k-means algorithm discriminated two groups of cells (Figure 6.2 A and B). The resultant clustering was further confirmed by an E-M clustering method (Figure 6.6).

6.6.3 Detecting Monosynaptic Connections from Cross-Correlograms

We used established methods [255] to detect statistically significant temporal bias in the cell pair relative spike timing indicative of putative monosynaptic connections. The spikes were jittered by adding a random value (froma normal distribution with a 10-msSD and 0 mean) to the spike times. For each cell pair, 1,000 jittered spike trains were created, and the expected

cross-correlogram (and 99% confidence interval) was estimated on 0.5-ms time bins under the null hypothesis of no monosynaptic effects between the two cells. For any given cell pair where at least two consecutive bins in the [1.5 ms, 4 ms] interval exceeded or were below the 99% confidence interval, the interaction was considered monosynaptic. A final and blind examination of the cell pair cross-correlograms was carried out to remove noisy pairs. The strength of the interaction was defined, at the time lag of maximal (or minimal) value in the actual cross-correlogram, as the ratio between the value of the actual cross-correlogram (from which was subtracted the average value expected for uncorrelated units) and the SD of the distribution from jittered spike trains.

6.6.4 Nonstationary Correlation

The firing rates of neurons may not be stationary over the long recordings performed in the present study. To avoid any potential bias that could result from such long-timescale fluctuations, we filtered the spike trains so that only local firing rates were taken into account [252]. The binned spike trains (in time bins of the indicated length) were filtered with a "Mexican hat"-shaped kernel, equal to the sum of a positive (width T) and a negative Gaussian function whose width is the quadratic mean of T and a value J. Throughout the present paper, we used $T = 3$ (expressed in number of time bins) and $J = 4T$. The covariance between two neurons' firing was obtained by computing the dot product of the resulting filtered and binned spike trains. The correlation was calculated by dividing the covariance by the product of the square roots of the two individual variances (the dot product of the filtered binned spike train with itself). Only cells with an average firing rate above 0.1 Hz were included in the correlation study unless stated otherwise.

6.6.5 Sleep Scoring

The postimplantation recordings were performed during clinical monitoring for seizures. We used a combination of video monitoring, scalp EEG, electrooculography (EOG), and clinical intracranial EEG to stage the sleep. The sleep staging was carried out in three of the four recording sessions (comprising 87% of the neural data).Rapid eye movement (REM) episodes were too brief; therefore, we did not include REM in our analysis. Nonetheless, all states-including clear episodes of quiet waking/ drowsiness, light non-rapid eye movement (NREM), and deep NREM were present during all recordings. In this paper, we focused on these states and excluded the rare REM episodes as well as periods when the patient was interacting with medical personnel. In addition, any seizure activity (one event in one patient) was removed from the data and not further analyzed.

6.6.6 Electrode Localization

The electrode-localization procedure was based on combining coregistration of high-resolution preoperative MRI with postoperative computed tomography (taking into account the parenchymal shift introduced by the implantation) and 3D rendering of each patient's cortical surface [these methods are described elsewhere [258]].

6.7 Figures & Tables

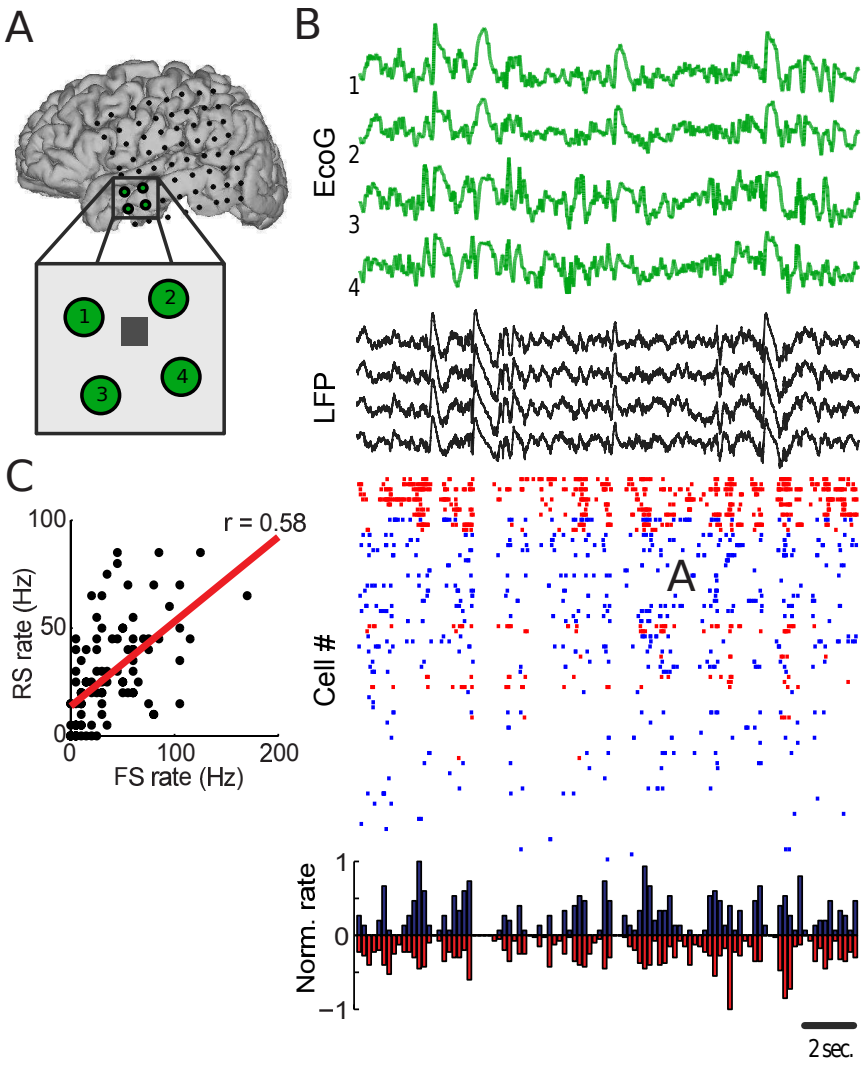

Figure 6.1. (A) Localization of subdural electrodes (SI Materials and Methods) and the NeuroPort electrode array (gray square in Inset). (B) Green traces show electrocorticogram (EcoG) of the four closest contacts to the microelectrode. LFP recorded from the NeuroPort is plotted in black. Raster plot shows the pooled firing of inhibitory (red) vs. excitatory (blue) cells for this period of slowwave sleep (note: the color is purly for visualization purposes. For morpho-functional discrimination of putative inhibitory and excitatory cells see Figure 6.2 and Figure 6.3 and the realted text). Histogram shows normalized neuronal firing rate for the two groups of cells in 200-ms time bins. (C) Total spikes by RS and FS cells in successive 200-ms bins, plotted against each-other (same epoch as in B).

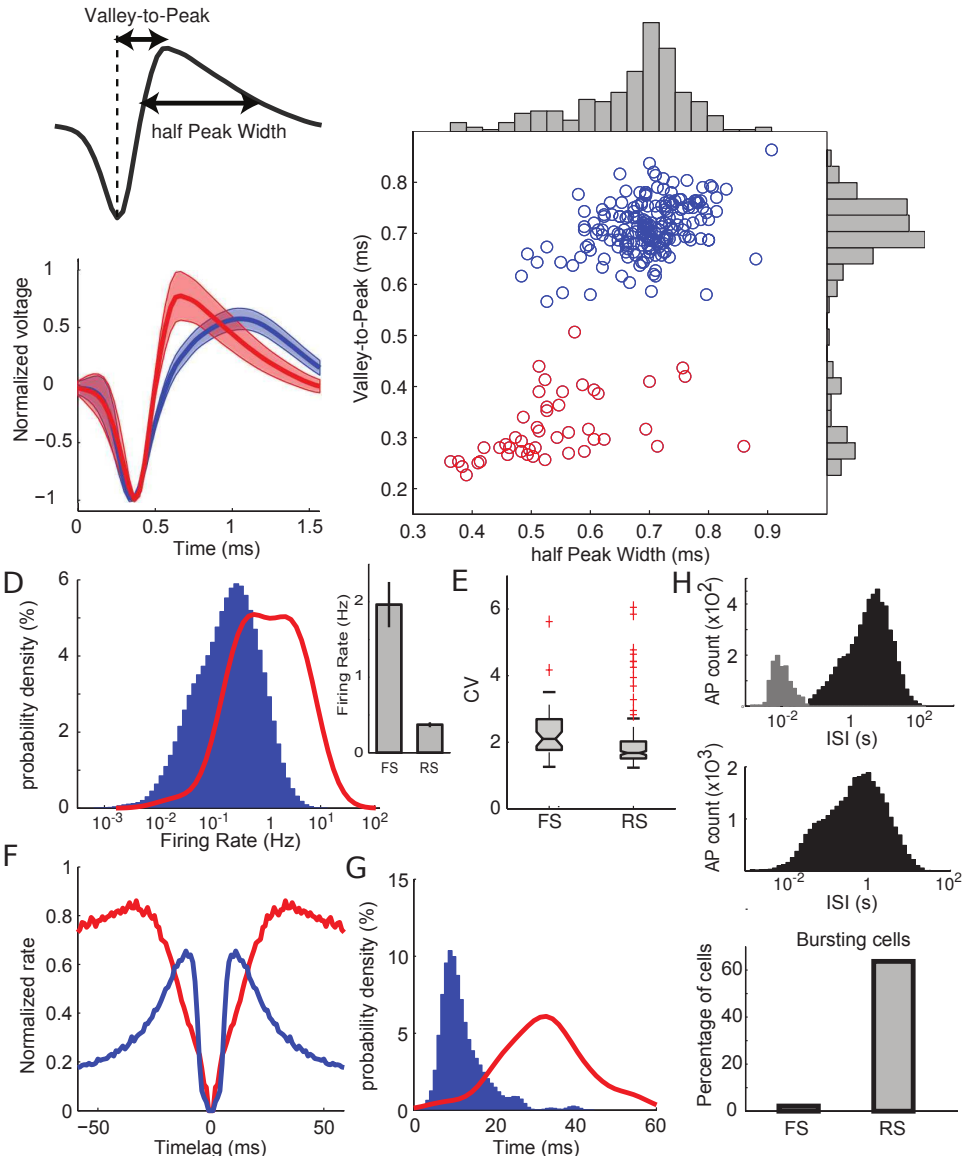

Figure 6.2. Separation of FS and RS cells based on spike waveform. (A) Valley-topeak and half-peak widths were the two parameters chosen to describe spike waveforms. (B) Each cell's average waveform is represented in the 2D space of the previous two parameters. The two clusters were identified with a k-means algorithm representing in red FS and in blue RS cells. (C) Average spike waveform for the two groups. Shading represents SD. (D) Probability density of firing rates for the two groups. (Inset) Average ± SEM. (E) Box plot indicating interquartile distribution of coefficients of variation (CV) of ISIs. (F) Average autocorrelogram normalized to maximum for each group. (G) Distribution of autocorrelogram modes (time of maximum peak) for each group. (H) Distribution of ISIs for an example RS cell (Left) and an FS cell (Center). The gray part of the distribution indicates the ISI categorized as bursts. (Right) Percentage of cells classified as bursty for each cell type. AP, action potentials. In D and G, the density probabilities were computed from kernel-smoothing density estimates of the actual data and displayed such that the sum over the whole displayed interval is equal to 100 for each group.

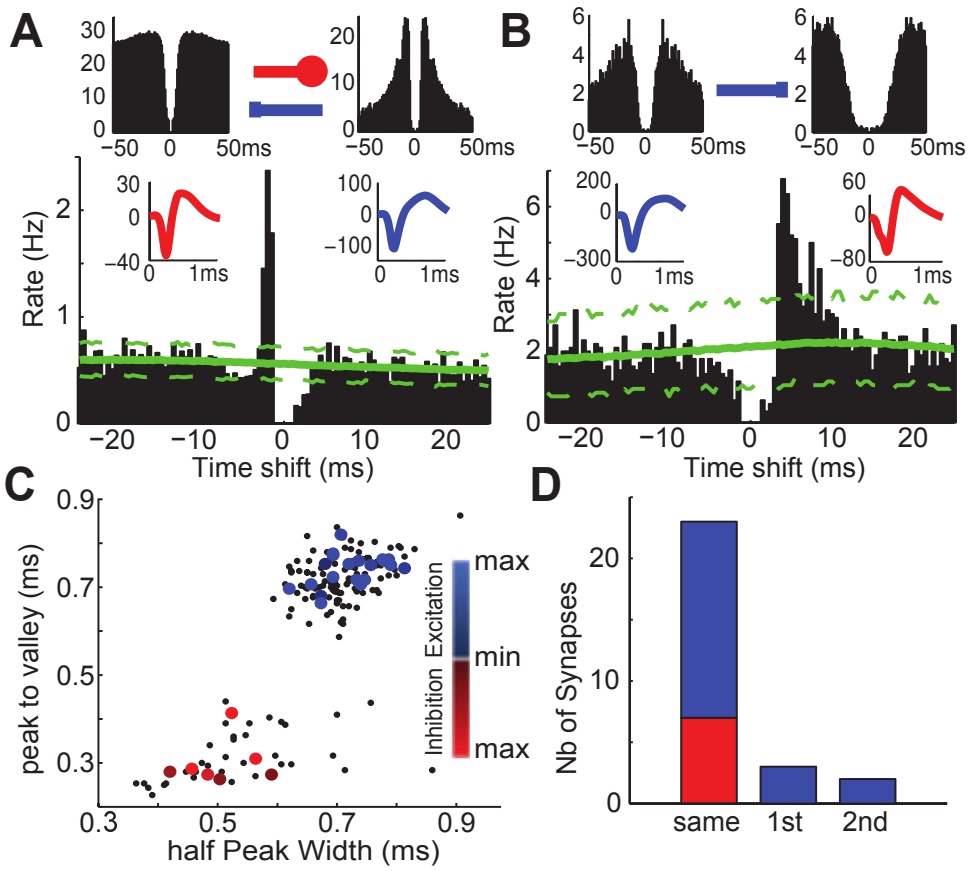

Figure 6.3. Putative monosynaptic connections reflect neuronal type. (A) Crosscorrelogram (Lower, referenced to firing by the putative Int) implies reciprocal monosynaptic interactions between an FS Int and an RS Pyr cell identified by their autocorrelograms (y-axis display rate in Hz) and spike waveforms (Upper Left and Upper Right, respectively). The large peak in the cross-correlogram indicates that the putative Pyr cell is systematically firing 2 ms before the putative FS Int. Conversely, the decreased firing for 4 ms after the putative Int firing suggests that it inhibits the putative Pyr cell. Dashed green lines show the 99% confidence interval from jittered spike trains. (B) In this example a putative Pyr cell (reference of the cross-correlogram) tended to excite a putative Int at a latency of 3 ms. In A and B, cells were recorded on the same electrodes; because of the nature of spike detection, the central values of the cross-correlograms are thus null. (C) The sign and strength of the putative monosynaptic connections were matched to the spike's average waveform. Small dots, all neurons; large dots, identified cell that appeared to monosynaptically affect another cell. Color code for sign (blue, excitation; red, inhibition) and strength (dark, weak; light, strong) of the connection. (D) Total number of synaptic connections between pairs of cells recorded by the same first- or second neighbor electrodes.

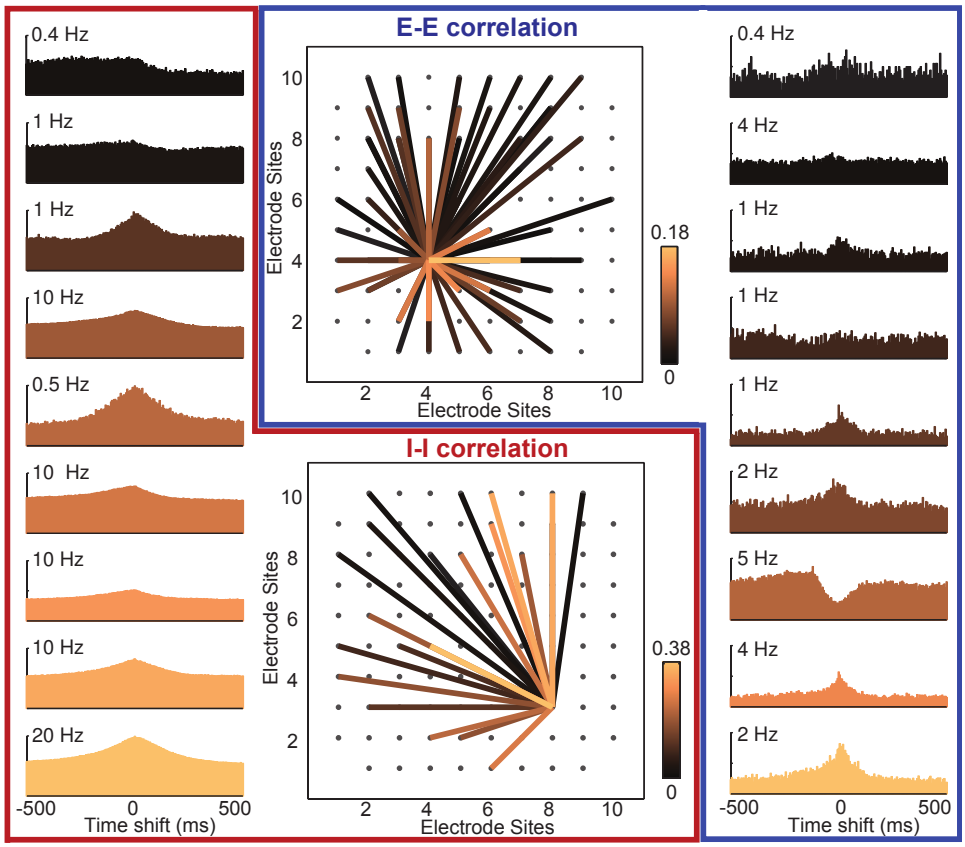

Figure 6.4. Spatial distribution of cell-cell interactions in an example 2D recording session. (Center Upper) Correlation values of one putative Pyr cell with all others. Color codes for the absolute value of Pearson's correlation (calculated for 50-ms bins), with black indicating low correlation and copper indicating high. (Right) Randomly chosen cross-correlograms between the reference cell and nine others sorted by correlation values. The y axis displays instantaneous rates of target cells. (Center Lower) Correlations between one putative Int and all others. (Left) Sample Int-Int cross-correlograms.

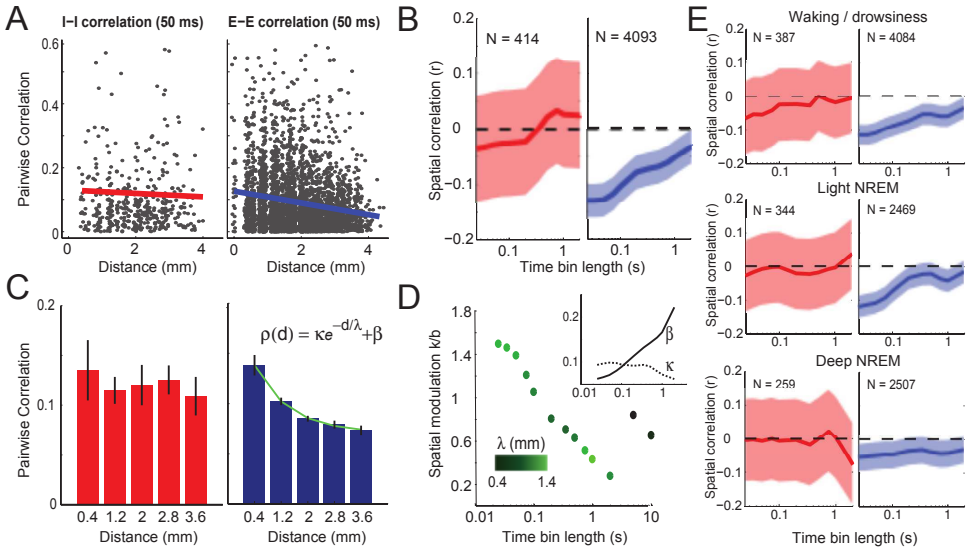

Figure 6.5. Relation of firing correlation to distance between cells. (A) Normalized coefficients of correlations were plotted against the distance between the two cells in each pair of putative Int (I-I correlations, Left) and putative Pyr (E-E correlations, Right) cells computed on time bins of 50 ms. Only the E-E group shows a significant linear regression (red and blue lines). (B) Correlation values of linear regressions for different time bins. Shaded areas indicate the 95% confidence interval (Fisher method). Numbers of cell pairs are indicated for the two populations. (C) Same as in A but normalized correlation coefficients were averaged over 0.8-mm spatial intervals. For E-E connections, the decay is well fitted with an exponential. (D) Strength and extent of spatial modulation of E-E correlations relative to the time bin width. Strength of spatial modulation is estimated with the dimensionless quantity kappa/beta. Green intensity codes for spatial extent of the modulation (lambda). (Inset) Values (y axis) of the fitting parameters beta (solid line) and kappa (dotted line) in function of time bin length (x axis). (E) Same as in B but in different wake/sleep states. Analyses were restricted to cells with mean firing rate $>$ 0.3 Hz in each particular state, resulting in the different numbers of cell pairs as indicated.

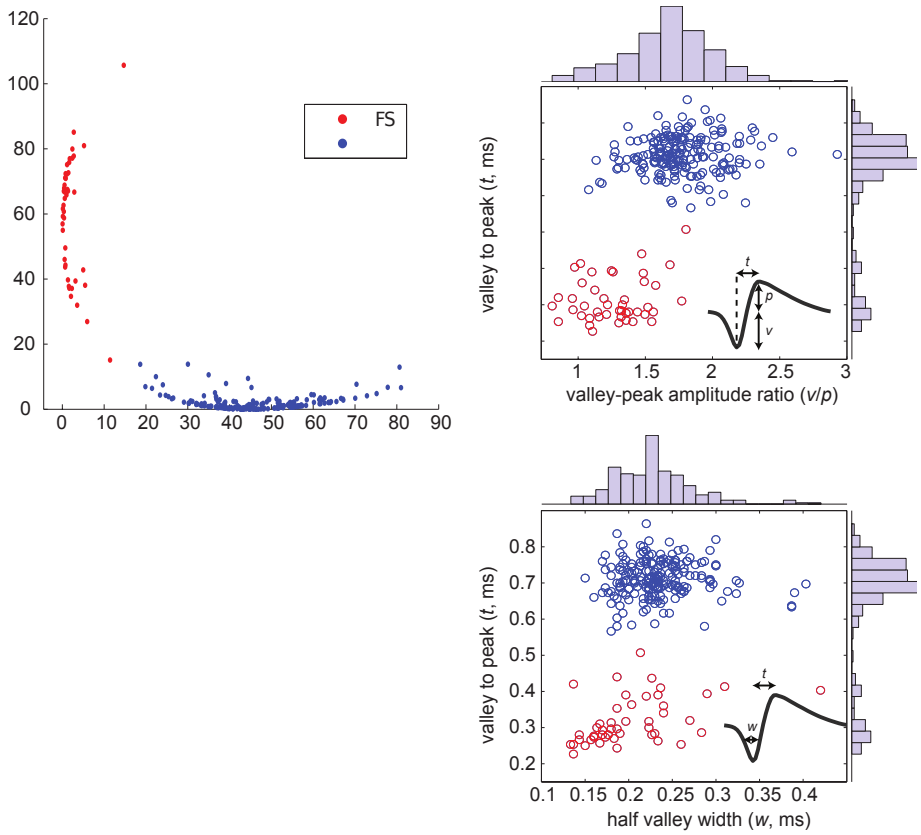

Figure 6.6. Separation of regular-spiking (RS) and FS cells with a Gaussian mixture model. The E-M algorithm was used to obtain maximum likelihood estimates of the parameters in a Gaussian mixture model with two components for an n-by-d data matrix, where n = 238 is the number of observations (individual cells pooled together from all subjects) and d = 2 is the dimension of the data (valley-to-peak and half-peak widths). The Mahalanobis distance (in squared units) of each observation to the mean of each of the two components of the Gaussian mixture distribution (described above) was computed. The plotted results form a curve in a non-Euclidean space where those above the diagonal represent FS and those below show RS characteristics. The asterisk indicates the only mismatching point between the two clustering procedures. (B) Spike waveform clustering using valley-to-peak amplitude ratio and valley-to-peak widths. Colors indicate clustering based on the features used in the main text (half-peak width and valley-to-peak distance). (C) Same as in B but using half-valley width and valley-to-peak distance.

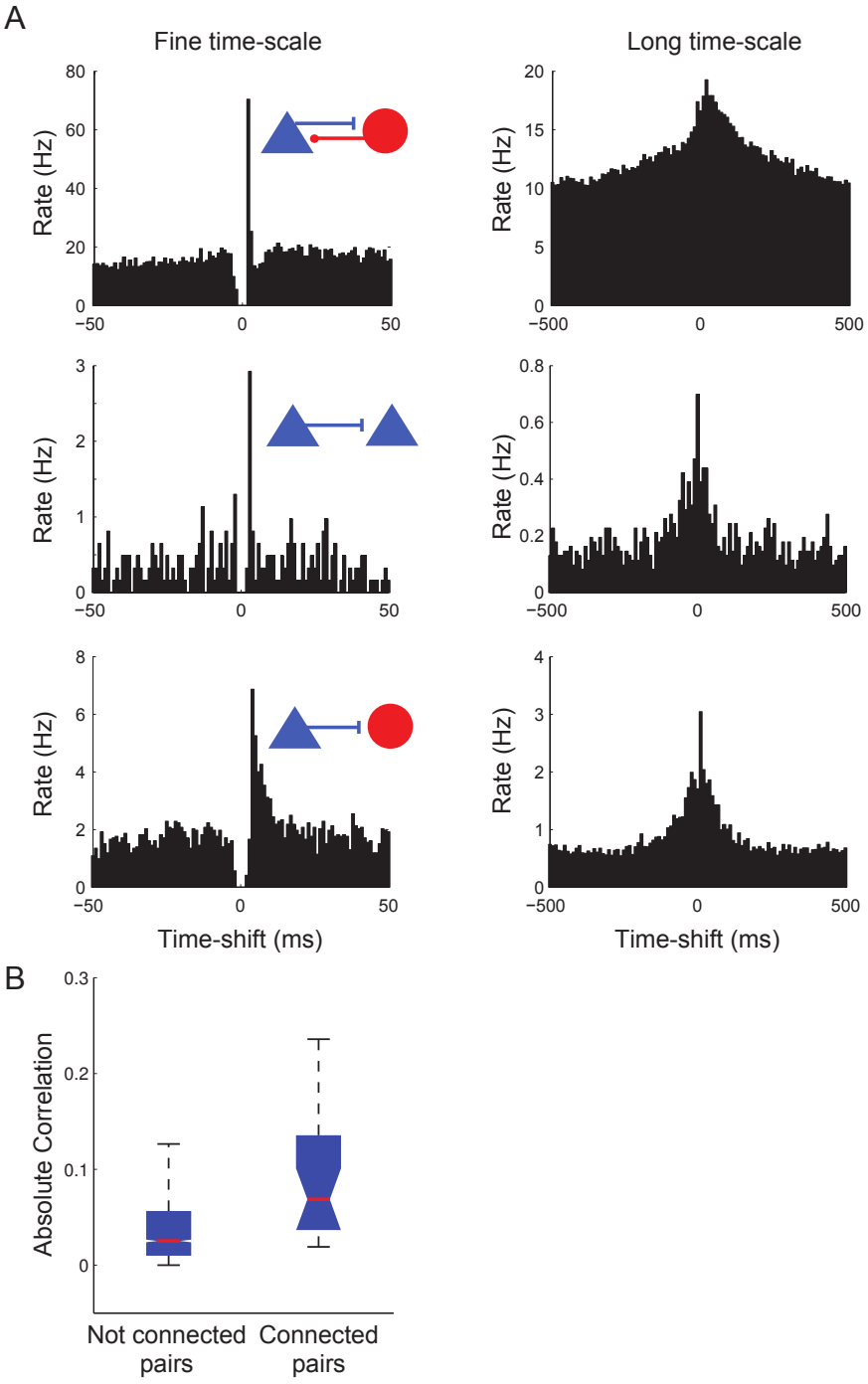

Figure 6.7. Correlation between pairs recorded on the same electrodes depended on their connectivity. (A) Examples of putative monosynaptically connected cells as revealed by the short-timescale cross-correlograms. At a longer timescale, the cross-correlograms tended to show positive peaks indicative of strong correlation. (B) Box plot of absolute correlation of binned spike trains (using 50-ms bins) depicting interquartile distribution. Correlations were significantly stronger for monosynaptically connected pairs ($P < 0.0001$, one-way ANOVA).

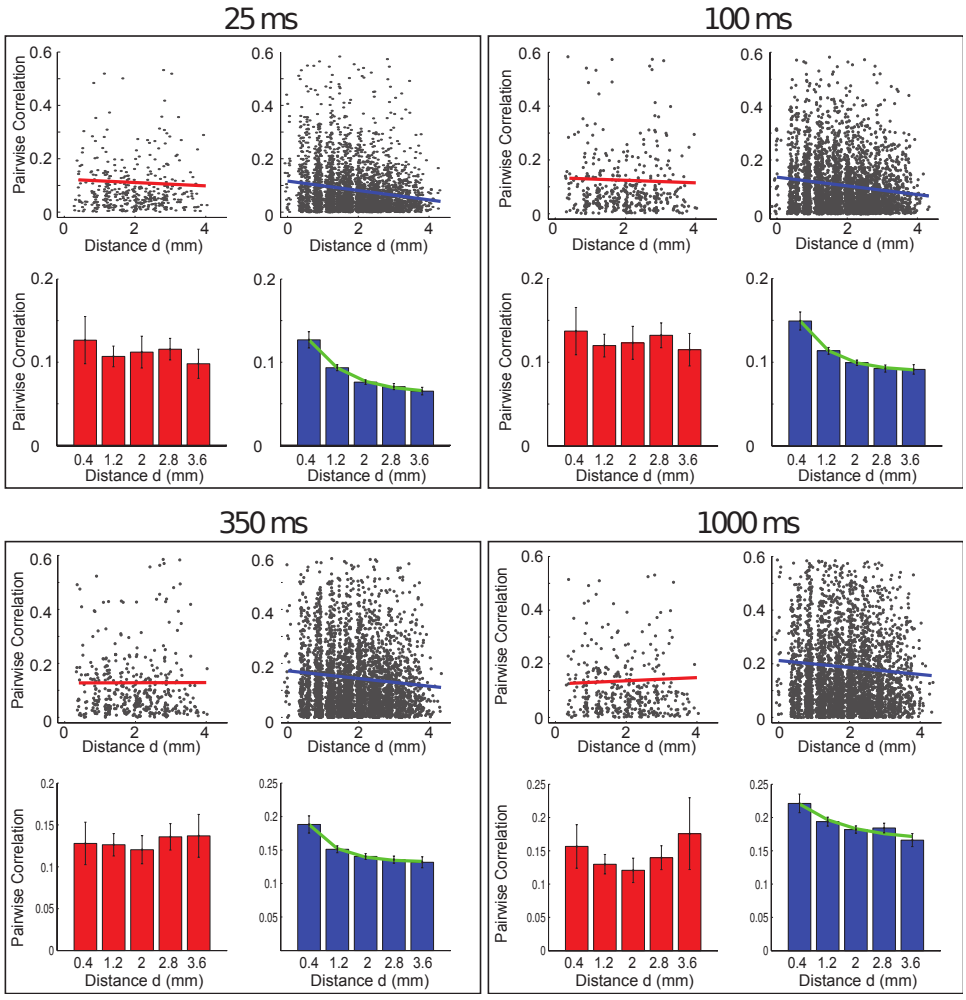

Figure 6.8. Correlations calculated for different time bins. The same plots are shown as in Fig. 5 A and C but for different time bins.

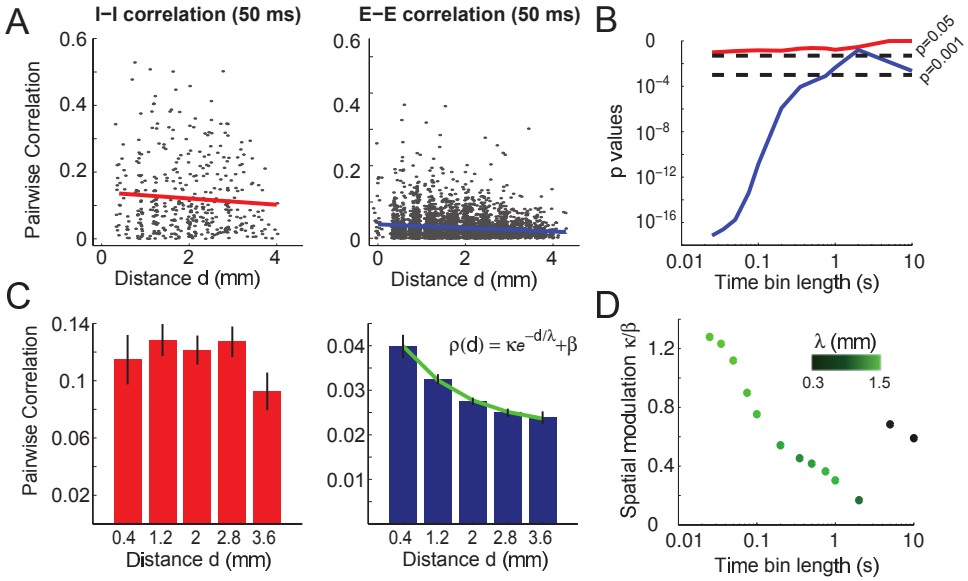

Figure 6.9. Same analysis as in Fig. 5B, correlation between neuronal pairwise correlations and relative distance. Here, the number of RS cell pairs (E-E, blue) was down-sampled so that it matched the number of FS cell pairs (I-I, red). Shaded areas of the E-E spatial correlation indicate the 95% confidence interval obtained by bootstrapping the down-sampled pairs (5,000 random samplings).

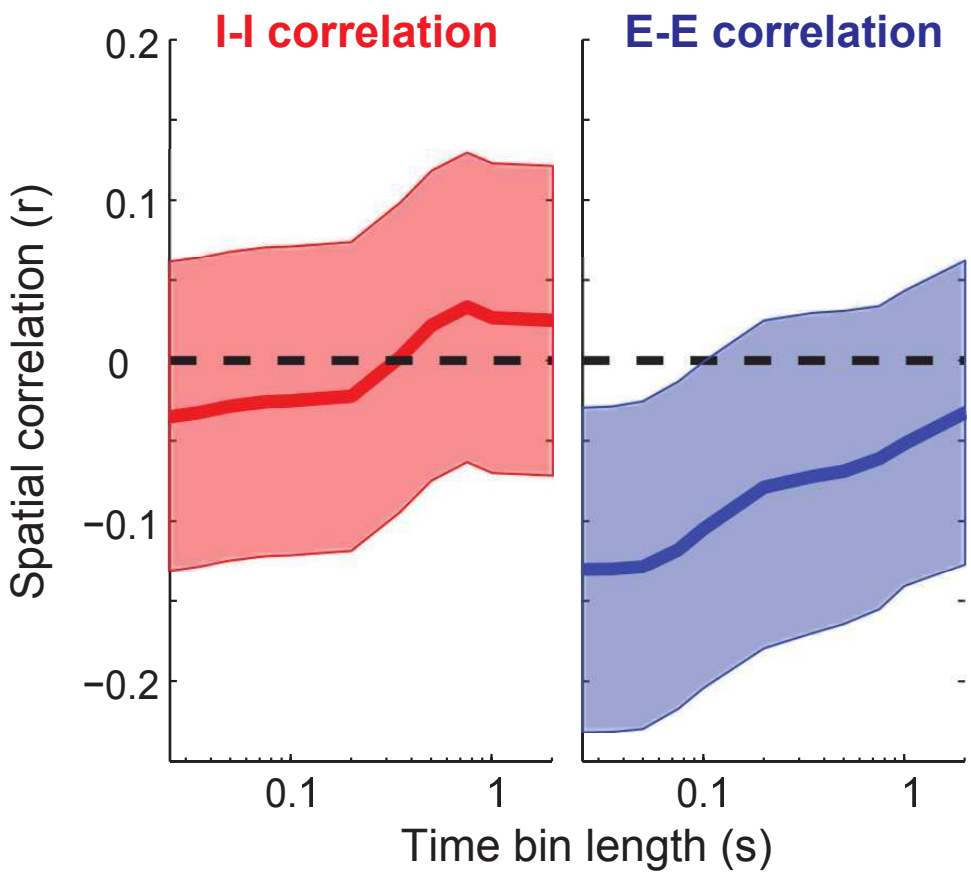

Figure 6.10. Same as in Fig. 5 but with non-normalized coefficients of correlation. In this case, correlation values were no longer comparable between the two groups of neurons. B shows the P values of linear regression.

Chapter 7

Avalanche dynamics

The irreversibility of time is the mechanism that brings order out of chaos.

Ilya Prigogine

Avalanche analysis from multi-electrode ensemble recordings in cat, monkey and human cerebral cortex during wakefulness and sleep

Nima Dehghani[1,*], Nicholas G. Hatsopoulos[2], Zach D. Haga[2], Rebecca A. Parker[3], Bradley Greger[4], Eric Halgren[5], Sydney S. Cash [6], Alain Destexhe[1,*]

1 Laboratory of Computational Neuroscience. Unité de Neurosciences, Information et Complexité (UNIC). CNRS. Gif-sur-Yvette, France.
2 Committee on Computational Neuroscience and Department of Organismal Biology and Anatomy, University of Chicago, Chicago, Illinois, USA.
3 Interdepartmental Program in Neuroscience, University of Utah, Salt Lake City, Utah, USA.
4 Department of Bioengineering, University of Utah, Salt Lake City, Utah, USA.
5 Multimodal Imaging Laboratory, Departments of Neurosciences and Radiology, University of California San Diego, La Jolla, CA, USA.
6 Department of Neurology, Massachusetts General Hospital and Harvard Med. School, Boston, MA, USA.
∗ co-corresponding authors. [1]

[1]Author contributions: N.D. and A.D. designed research; N.G.H., Z.D.H, R.A.P, B.G., E.H., and S.S.C. performed the experiments; N.D. designed the tests and analyzed data; and N.D., and A.D. wrote the paper.

7.1 Summary

Self-organized critical states are found in many natural systems, from earthquakes to forest fires, they have also been observed in neural systems, particularly, in neuronal cultures. However, the presence of critical states in the awake brain remains controversial. Here, we compared avalanche analyses performed on different *in vivo* preparations during wakefulness, slow-wave sleep and REM sleep, using high-density electrode arrays in cat motor cortex (96 electrodes), monkey motor cortex and premotor cortex and human temporal cortex (96 electrodes) in epileptic patients. In neuronal avalanches defined from units (up to 160 single units), the size of avalanches never clearly scaled as power-law, but rather scaled exponentially or displayed intermediate scaling. We also analyzed the dynamics of local field potentials (LFPs) and in particular LFP negative peaks (nLFPs) among the different electrodes (up to 96 sites in temporal cortex or up to 128 sites in adjacent motor and pre-motor cortices). In this case, the avalanches defined from nLFPs displayed power-law scaling in double logarithmic representations, as reported previously in monkey. However, avalanche defined as positive LFP (pLFP) peaks, which are less directly related to neuronal firing, also displayed apparent power-law scaling. Closer examination of this scaling using the more reliable cumulative distribution function (CDF) and other rigorous statistical measures, did not confirm power-law scaling. The same pattern was seen for cats, monkey and human, as well as for different brain states of wakefulness and sleep. We also tested other alternative distributions. Multiple exponential fitting yielded optimal fits of the avalanche dynamics with bi-exponential distributions. Collectively, these results show no clear evidence for power-law scaling or self-organized critical states in the awake and sleeping brain of mammals, from cat to man.

Reference:
Submitted to Frontiers in Physiology, 2012 Aug. 3:302. doi: 10.3389/fphys.2012.00302, special issue on "Critical Brain Dynamics"
(Edited by He BY, Daffertshofer A, Boonstra TW).

Keywords:
Criticality, Self-organization, Brain Dynamics, Scale invariance, Complexity, Power-law

7.2 Résumé

Les états auto-organisés critiques (SOC) ont été identifiés dans de nombreux systèmes naturels, des tremblement de terre aux feux de forêt, et ils ont également été observés dans le système nerveux, en particulier en culture. Cependant, la présence de tels états dans le cerveau éveillé reste encore controversée. Dans cette étude, nous comparons des analyses d'avalanche dans différentes préparations *in vivo* pendant l'éveil, le sommeil lent et le sommeil REM. Nous utilisons des enregistrements à haute densité dans le cortex moteur du chat (96 électrodes), le cortex moteur et prémoteur du singe et dans le cortex temporal humain (96 électrodes) de patients épileptiques. Lors d'avalanches définies à partir d'unités (jusqu'à 160 neurones), les distributions ne se comportent pas en loi de puissance, mais tendent a être exponentielles ou intermédiaires. Nous analysons également les potentiels de champ (LFPs), et en particulier les pics négatifs (nLFPs) au sein de l'ensemble délectrodes (de 96 a 128 sites, selon la configuration d'enregistrement). Dans ce cas, les avalanches définies à partir des nLFPs peuvent se comporter en loi d'échelle, comme observé précédemment chez le singe. Cependant, les avalanches définies à partir des pics positifs (pLFPs), qui ne sont pas directement reliées aux décharges des neurones, ont le même comportement. Une analyse plus détaillée en utilisant la représentation cumulée (CDF) ne confirme pas la présence de loi de puissance. Les mêmes résultats s'appliquent au chat, au singe et aux enregistrements humains, pendant différents états cérébraux d'éveil et de sommeil. Nous avons également testé des distributions alternatives, et des processus multi-exponentiels semblent expliquer les distributions obtenues, de façon optimale pour des distributions bi-exponentielles. L'ensemble de ces résultats ne montrent pas d'evidence de loi de puissance ou d'états SOC dans le cerveau éveillé ou en sommeil de différents mammifères, du chat à l'homme.

7.3 Introduction

Self-organized criticality (SOC) is a dynamical state of a system which maintains itself at (or close to) a phase transition point. This family of systems were initially described by Bak, Tang and Wiesenfeld [127], and have been found in many natural systems (reviewed in [128, 175]). SOC systems are characterized by scale invariance, which is usually identified as a power-law distribution of characteristics of the system's dynamics such as event size or the waiting time between events. The temporal fingerprint of SOC systems is often $1/f$ or $1/f^2$ noise. These features are interesting because they show the presence of long-lasting or long-range correlations in the system.

The dynamics of SOC systems are structured as "avalanches" of activity, separated by silent periods. Avalanche sizes are typically distributed as a power law, where the probability of occurrence $p(x)$ of a given avalanche size x scales as:

$$p(x) \sim x^{-\alpha} ,$$

where α is the scaling exponent of the distribution.

SOC systems have been observed in many different natural phenomena, from sandpiles, to rice piles, in forest fires and earthquakes [128, 175–178]. Evidence of SOC was also demonstrated in circuits of neurons *in vitro* [135], where network activity was found to alternate between active and quiescent periods, forming "neuronal avalanches". The presence of avalanches, although clear *in vitro*, is more controversial *in vivo*. Since power-laws fit neuronal avalanches better than other alternative probability distributions [259], their presence has been taken as evidence for neuronal avalanches *in vivo*. In anesthetized cats [182] and awake monkeys [183], power-law distributed avalanches have been found in the peaks of local field potentials (LFP). However, LFP peaks are only statistically related to neuronal firing. In a study on awake and naturally sleeping cats, no sign of avalanches were found in neuronal firing [134], and the apparent power-law scaling of LFP peaks could be explained as an artifact induced by the thresholding procedure used to detect LFP peaks. Previous studies have shown that even purely stochastic processes can display power-law scaling when subjected to similar thresholding procedures [184]. It was also stressed that power-law statistics can be generated by stochastic mechanisms other than SOC [184–186]. Similarly, if exponentially growing processes are suddenly killed (or "observed"), a power-law at the tail ends will emerge [187]. This case, would be similar to a non-stationary Poisson processes, or combining Poisson processes at different rates, a situation that is likely to happen in the nervous system. Such scenarios can give rise to spurious power laws.

These contrasting results correspond to different preparations and recording techniques, single units or LFPs, or different species, so that it is difficult to compare them. In the present paper, we attempt to overcome these shortcomings by providing a systematic analysis of both units and LFPs for different species and different brain states.

7.4 Materials and Methods

7.4.1 Recordings

7.4.1.1 Cat

Recordings of local field potentials (LFPs) and action potentials (APs) were obtained from motor cortex in 2 felines (M1 and approximately hindlimb region). Commercially obtained 96-electrode sputtered iridium oxide film arrays (Blackrock Microsystems, Inc., Salt Lake City UT) were chronically implanted and recordings were performed in the awake, unrestrained feline (as described in [59]). Electrodes on the array were arranged in a square with 400 micron spacing and 1 mm shank length. LFPs and APs were recorded using a Cerebus data acquisition system (Blackrock Microsystems). Spike sorting on AP data was performed using the t-dist EM algorithm built into Offline Sorter (Plexon, Inc.). All animal procedures were performed in accordance with University of Utah Institutional Animal Care and Use Committee guidelines.

We also compared these data with previously published multi-electrode data on cat parietal cortex ([174]. In this case, a linear array of 8 bipolar electrodes (separated by 1 mm) was chronically implanted in cortical area 5-7, together with myographic and oculographic recordings, to insure that brain states were correctly discriminated (quiet wakefulness with eyes-open, slow-wave sleep, REM sleep). Throughout the text, this cat will be referred to as “cat iii” LFP signals were digitized off-line at 250 Hz using the Igor software package (Wavemetrics, Oregon; A/D board from GW Instruments, Massachusetts; low pass filter of 100 Hz). Units were digitized off-line at 10 kHz, and spike sorting and discrimination was performed with the DataWave software package (DataWave Technologies, Colorado; filters were 300 Hz high-pass and 5 kHz low-pass).

7.4.1.2 Monkey

Recordings from three monkeys were used in this study. Each monkey was chronically implanted with 100-electrode Utah arrays (400microm inter-electrode separation, 1.0 mm electrode length; BlackRock Microsystems Inc., Salt Lake City UT). In two monkeys (i) and (ii), we used recordings made during the performance of motor tasks. The motor tasks involved moving a cursor to visually-presented targets in the horizontal plane by flexing and extending the shoulder and elbow of the arm contralateral to the cerebral hemisphere that was implanted. In monkey (iii), sleep recordings were used to test avalanche dynamics. Monkey i was implanted with one 96 electrode array in primary motor cortex (MI) and a second 96 electrode array in dorsal premotor cortex (PMd) from which recordings were made on 64 electrodes in each cortical area. Monkey ii had an array implanted in MI from which 96 electrodes were recorded.

and Monkey iii had two arrays in MI and PMd from which 96 electrodes were recorded in PMd cortex and 32 electrodes were recorded in MI area. During a recording session, local field potential (LFP) signals were amplified (gain, 5000), band-pass filtered (0.3 Hz to 250 Hz or 0.3 to 500 Hz), and recorded digitally (14-bit) at 1 kHz per channel To acquire extracellular action potentials, signals were amplified (gain, 5000), band-pass filtered (250 Hz to 7.5 kHz) and sampled at 30 kHz per channel. For each channel, a threshold was set above the noise band: if the signal crossed the threshold, a 1.6ms duration of the signal - as to yield 48 samples given a sampling frequency of 30 kHz - was sampled around the occurrence of the threshold crossing and spike-sorted using Offline Sorter (Plexon, Inc., Dallas, TX). All of the surgical and behavioral procedures performed on the non-human primates were approved by the University of Chicago's IACUC and conform to the principles outlined in the Guide for the Care and Use of Laboratory Animals (NIH publication no. 86-23, revised 1985).

7.4.1.3 Human

Recordings were obtained from two patients with medically intractable focal epilepsy using NeuroPort electrode array as discussed previously [54, 260]. The array, 1mm in length, was placed in layers II/III of the middle temporal gyrus with informed consent of the patient and with approval of the local Institutional Review Board in accordance with the ethical standards of the Declaration of Helsinki. This array is silicon-based, made up of 96 microelectrodes with 400-μm spacing, covering an area of 4×4 mm. Since the corners are omitted from the array, the furthest separated contacts are 4.6 mm apart. Data were sampled at 30 kHz (Blackrock Microsystems, Salt Lake City, Utah, USA). The continuous recording was downsampled to 1250 Hz to obtain LFPs. The dataset we analyzed was devoid of any form of identifiable epileptic activity (such as interictal spikes), and there was no seizure in the analyzed dataset. The implantation site was included in the therapeutic resection in both patients. For details on spike sorting, see [260].

7.4.2 Avalanche detection

Avalanches are defined by temporally contiguous clusters of activity among the different electrodes, separated by periods of silence. Either trains of neuronal action potentials (spikes) or LFP peaks can can be analyzed for the occurrence of avalanches. There are two empirical limits on bin duration. The smallest bin size is set by the duration of the action potential. The upper boundary, is limited by how many unique values of the aggregate ensemble activity occur in a window. When the number of unique values approaches 1, avalanche loses its definition, because there is no silent period left. In the cat data, where there are 160 cells, we reach this limit at a bin-width of 16 ms. So, we have stayed within the 1-15 ms regime in which an avalanche could be well defined.

7.4.2.1 Spike avalanche

In each set of recordings, regardless of the spatial location of a given electrode in the multi-electrode array, its spiking activity was put in the same pool with all other spikes recorded from other electrodes of the same array. This ensemble trace was then binned and coarse grained for different δt ranging from 1 ms to 16 ms in 2 ms steps. This created a series of bins containing the ensemble of activity across all neurons for that δt. The sum of spiking in that bin represents the total bin activity. The sum of all bin activities between two quiescent bins, represents the avalanche size, which was later used for statistical analyses. Notice that in the case of the minimum δt = 1, avalanche size would range between 0 and maximum number of neurons present as this bin approximates the size unity of spiking period. Figure 7.1A shows the definition of avalanche in spike series from human recordings.

7.4.2.2 LFP avalanche

Each LFP trace was first detrended through a least-squares fit of a straight line to the data and subsequent subtraction of the resulting function from all the sample points. After this detrending removed the mean value or linear trend from a LFP vector, it was then normalized (Z score) to have a common reference frame for discretization across channels, recordings, states and species. The z-scored LFP, was then discretized through a local maxima peak detection. An optimizing small running average filter was designed and 3 passes of the filter were applied to the data in order to remove small spurious peaks in each LFP deflection. Next, by comparing each element of data to its neighboring values, if that sample of data was larger than both of its adjacent ones, that element was considered as a local peak. Next, all the peaks were sorted in descending order, beginning with the largest peak, and all identified peaks not separated by more than minimum peak distance (of 3 samples) from the next local peak were discarded.

The threshold was fixed and defined as a multiple of the standard deviation (STD) of the LFP signal. Different thresholds were tested, starting at 1.25$\times$STD and increasing in 0.25 steps up to 5$\times$STD for both negative and positive maxima. This procedure was realized on each LFP channel, state, species (Fig. 8.1B). Such matrix of discrete events (for a given polarity and a given threshold), was then treated the same way the spike matrix was used to create avalanche vectors of quiescent and active periods.

7.4.3 LFP peak and spiking relationship

7.4.3.1 Wave-triggered-average (WTA)

We used wave-triggered averaging (WTA) to analyze the differences in the relationships of spikes to nLFP versus pLFP. In WTA, the individual negative LFP peaks (nLFP) were used to epoch the ensemble spike series. The epoched ensemble spike series were normalized by the number of epochs (triggered by nLFPs). This procedure was performed for the three different thresholds (low, medium and high) and the results were averaged across these thresholds to obtain cross-threshold WTA percentage firing to quantify the spike-nLFP relationship. An identical procedure was applied to pLFPs. The red and blue solid lines in Figure 7.6 refer to nLFP-spike and pLFP-spike WTA percentage firing, respectively.

7.4.3.2 Controls and Randomization Methods

We used 4 methods of surrogate/randomization in order to evaluate the statistical robustness of the comparative relation of spike-nLFP vs spike-pLFP. Each of the following 4 methods, was first performed on all 3 chosen thresholds and then the results were averaged to obtain the overall randomization effect.

7.4.3.2.0.1 *Poisson surrogate data* At the first step, we wanted to test whether the observed nLFP and pLFP differences could be reproduced by surrogate spike series. For this type of control, first, each individual channel's spike rate was calculated. Then, using a renewal process, a surrogate Poisson spike series for that channel was created (matching the firing rate and duration of the experimental data from that channel). Then, all Poisson spike series (across all channels) were aggregated together to create the ensemble spike series (similar to the experimental data). Next, for each pLFP (or nLFP), the WTA of this Poisson aggregate series was created. This procedure was repeated 1000 times and then averaged across the 1000 trials. The results were close to a constant WTA percent firing and did not fluctuate according to the timing of the peak LFP that was used to epoch each individual WTA event. This control test showed that the simple aggregate of surrogate Poisson spikes can not reproduce the observed relation between nLFP and spikes in the WTA or mimic the behavior of natural peak(positive or negative)-induced percentage firing. This procedure was also repeated with Poisson spikes without a refractory period and provided similar results.

7.4.3.2.0.2 *Random permutation* In a follow up test, we wanted to verify that randomizing the aggregate spike series by itself can not mimic the observed the LFP-spike relation. For this procedure, we performed a random permutation on the aggregate spike series and then

calculated the nLFP(and pLFP)-based WTA. This procedure was repeated 1000 times. The observations are similar to the Poisson randomization, verifying that the nLFP peak is not reproducible by randomization of spikes and the fluctuations of WTA percentage firing are not results of random events.

7.4.3.2.0.3 *Local jitter randomization of LFP peaks* Next, we wanted to evaluate the effects of randomization based on the statistics of the individual channel's LFP peak times (before aggregating them into the ensemble LFP peak train). First, each channel's nLFP IPI (inter-peak-interval) were calculated. Then these IPIs from all channels were put in the same pool and the, 0.25, 0.5 and 0.75 quantiles IPI for the aggregate nLFPs were extracted. Next, we created a normal distribution with 0.5 percentile as the mean, the interquartile range (0.75 quantile minus 0.25 quantile) as the standard deviation of the pdf, and N events matching the number of aggregate nLFPs. This set of values, were used to jitter nLFPs in the following manner. Each sample from the aggregates nLFP peak series was shifted according to one drawn sample (without replacement) from the nLFP jitter pool. The direction of the shift was to the right if the drawn jitter value was negative (and to the left for the positive value). The magnitude of the shift was defined by the value of the jitter itself. The same procedure was repeated for pLFPs. The results of this randomization are shown in Figure 7.6.A. As can be appreciated, with this tightly regulated data-driven local randomization, the structure of the WTA is preserved except for the peak curve around 0 for the nLFP case.

7.4.3.2.0.4 *Fixed-ISI circular shift of spikes* In this procedure, we kept the ISI (inter-spike interval) of the aggregate spike series as well as the IPI (inter-peak intervals) of the nLFP and pLFP intact but randomized the relation between the aggregate spike and aggregate peak series. In each of the 1000 trials, a circular shift with the magnitude chosen randomly between 1 and the range of the ISI, was performed. The results, shown in Figure 7.6.B, show that by destroying the relation between ensemble spikes and ensemble peaks while preserving their internal structure, the observed fluctuations and most importantly, the tightly bound relation of nLFP and spikes, is lost.

7.4.4 Testing power law distribution in empirical data

For testing the power-law behavior, usually a simple least square method is applied to fit a power-law on the data. If such fit in a log-log scale, follows a straight line, the slope of the probability density function (PDF) line is taken as the scaling exponent. Such method is widely practiced but is highly inaccurate in its estimation of true existence of power-law in a given dataset. It has been argued that, for obtaining statistically sound results in estimating power-law in empirical data, one has to rely on rigorous statistical methods. In a detailed analysis

of the problem [201, 261], it was proposed that the cumulative distribution function (CDF) is much more accurate to fit the power-law exponent, as well as to identify if the system obeys a power-law.

If the initial distribution of the PDF is power-law, i.e.,

$$p(x) = Cx^{-\alpha} ,$$

then CDF is defined as

$$Pr(X > x) = C\int_{x}^{\inf} x'^{-\alpha}dx' = \frac{C}{\alpha - 1}x^{-(\alpha-1)} .$$

Thus, the corresponding CDF also behaves as a power-law, but with a smaller exponent

$$\alpha - 1$$

being 1 unit smaller than the original exponent [261].

Generally, in fitting the power-law to the empirical data, all the initial values (left hand of the distribution histogram i.e, smallest sizes of avalanches) are included in the used decades to obtain the slope of the fit (scaling exponent α). The inclusion of these initial parts may cause significant errors, and should be removed [201, 262, 263]. Thus, before calculating the scaling exponent, it is essential to discard the values below the lower bound (X_{min}). It is only above this lower bound that, a linear PDF or CDF can be reliably used for estimation of the scaling exponent. There are different methods for proper estimation of the X_{min}. We used a Kolmogorov-Smirnov (KS test) optimization approach that searches for the minimum "distance" (D) between the power-law model and the empirical, where for Xi$\geqslant X_{min}$, "D" is defined as

$$D = max|S(x) - P(x)| ,$$

S(x) the CDF of the empirical data and P(x) the CDF of the best matching power-law model. The X_{min} value that yields the minimum D, is the optimal X_{min}. The X_{min} is used in a maximum likelihood estimate (MLE) of power-law fit to the CDF of the avalanches in order to obtain the scaling exponent. This fitting, however, does not provide any statistical significance on whether the power-law is a plausible fit to the data or not. After the estimation of X_{min} and the exponent, we generated N (N=1000) power-law distributed surrogate data with the exact same features of X_{min} and exponent. Each of these surrogate series are then fitted with power-law and KS statistics of distance D (to the surrogate power-law), is performed. The fraction of N that the resultant statistics was bigger than the one obtained from the empirical data, comprises the p-value. If p-value $\leqslant 0.1$, the power-law is ruled out. However, even if p-value is larger than this threshold, the data is not necessarily guaranteed to be generated by a power-law process unless no better distribution is found to estimate the properties of the data. For this, the alternative test was adapted as following.

7.4.4.1 Generating power-law distributed random numbers with high precision

It is essential to use high precision and reliable algorithms to generate random numbers from a given probability distribution; otherwise the statistical tests based on such distributions may be erroneous. For initializing the generator with an "Integer Seed", we adapted the reliable Mersenne Twister algorithm (known as MT19937AR) with full precision of Mersenne prime $(2^{19937}-1)$ [264]. . This algorithm provides a proper method for running Monte Carlo simulations. After initialization, "Transformation algorithm" was used to generate the desired distribution [201, 265]. All the random number generations and analyses were performed on a 16-core Intel 48 GB Linux platform equipped with 448 core Tesla C2050 GPU with double precision of 515 Gflop and single precision of 1.03 Tflops. The custom code was based on Matlab (Mathworks) and CUDA (NVIDIA) wrapper Jacket (Accelreyes) for parallel computing on GPU.

7.4.5 Alternative fits

The power-law fit was compared with alternative hypotheses to test which distribution best fits the data. The alternatives included exponential distribution (as predicted by a Poisson type stochastic process), "Discretized log-normal distribution" (which is represented as a linear fit in log-normal scale), as well as fit of "Discrete exponential distribution" nature. These fits had two general types of simple exponential, defined as: $f(x) = a\exp(bx)$ as well as sum of exponential set as: $f(x) = a\exp(bx) + c\exp(dx)$ In each case, residual analyses, goodness of fit as well as confidence and prediction bounds were used to evaluate the properties of each fit vs power-law. In case of a good fit model, Residual, defined as the difference between data and fit, should approximate random error and behave randomly.

7.4.5.1 Goodness of fit comparison of exponential models

A measure of "goodness of fit", R-square, is the ratio of the sum of squares of the regression (SSR) and the total sum of squares (SST). This measure, represents the square of the correlation between the observed and predicted response values, and indicates what percentage of the variance of the data is explained by the chosen fit (values of R-square range from 0, worst fit, to 1, the best possible fit). If we have SSR as: $SS_{\text{reg}} = \sum_i (\hat{y}_i - \bar{y})^2$, and SSE as: $SS_{\text{err}} = \sum_i (y_i - \hat{y})^2$, and SST as: $SS_{\text{tot}} = \sum_i (y_i - \bar{y})^2$, where, $y_i, \bar{y}, \hat{y}$ are the original data values, their mean and modeled values respectively. Then, it follows that:

$$R^2 = SS_{\text{reg}}/SS_{\text{tot}} = 1 - \frac{SS_{\text{err}}}{SS_{\text{tot}}}.$$

Correction by "total degree of freedom" and "error degree of freedom", defines adjusted R-

square:

$$\bar{R}^2 = 1 - (1 - R^2)\frac{N-1}{N-M-1} = 1 - \frac{SS_{\text{err}}}{SS_{\text{tot}}}\frac{df_t}{df_e}.$$

where "N" is the sample size, and "M" is the number of fitted coefficients (excluding constants). Usage of $\bar{R}^2$ in the comparison of "simple exponential" and "sum of exponential" is warranted by the fact that by an increase in the fitted number of the components, from one model to the other, the degrees of freedom changes. Both R^2 and $\bar{R}^2$ measures were estimated through nonlinear least square optimization of exponential curve fitting. In the optimization process for estimating the coefficients of the models, we adapted Levenberg-Marquardt algorithm with a tolerance of 10^-8 [266].

7.4.5.2 Test of linearity in log-normal scale

Linearity in log-normal scale, is a hallmark of an exponential family process. In order to test the linearity of the PDF in log-normal scaling, we used Root mean square error (RMSE), $\text{RMSE}(\hat{\theta}) = \sqrt{\text{MSE}(\hat{\theta})}$ where MSE is: $\frac{SS_{\text{err}}}{df_e}$. This measure ranges from 0 to 1, where closer value to 0 is an indicator of a better fit.
This test was performed by fitting $y = Log(P(x))$ with a linear least square first degree polynomial. As shown in Fig. 7.13C, sometimes, the initial values in the left tail may slightly deviate from a simple 1st degree polynomial. Therefore, we tested whether the linearity was improved or worsened when the data range was reduced to above some X_{min}. For doing so, we adapted a more stringent regression, bisquare robust 1st degree polynomial [266]. This method is an iteratively reweighted least-squares, based on $\bar{R}^2$, and assigns less weight to the values farther from the line. This procedure was repeated after excluding consequent single values from the left tail (up to 20 percent of the points). For each new shortened series, the RMSE (based on bisquare method) was re-calculated. The rational behind using RMSE for testing the linearity range in these datasets (with variable N) is that when a distinct point is removed from the dataset, 2 other reductions follow: a) the sum of squares and b) degrees of freedom. Thus, if after limiting the range, the error remains the same, SS_{err} would increase. Similarly, when the error is significantly reduced, SS_{err} would increase. Therefore, any change in the error, should only be considered significant if it is compensated by the amount of change in the degree of freedom. For quantifying this, we defined two measures for linearity improvement after limiting the data above X_{min}. The first measure, "overal RMSE change" (oRMSE), was defined as:

$$oRMSE_i = \frac{RMSE_n - RMSE_{n-i}}{RMSE_n} * 100.$$

In parallel, "relative RMSE change" (rRMSE), was defined as:

$$rRMSE_i = \frac{RMSE_{n-i+1} - RMSE_{n-i}}{RMSE_n} * 100.$$

, where $RMSE_n$ was the RMSE of the full length data. Next, these measures were normalized to their maximum (*noRMSE* and *nrRMSE*) and a 3rd dimension was created by the distance of each pair ($noRMSE_i$, $nrRMSE_i$), from the geometrical diagonal defined as

$$D = \frac{det[(Q2-Q1)\cdot(P-Q1)]}{\|(Q2-Q1)\|}$$

, where P was the coordinates of a point ($noRMSE_i$, $nrRMSE_i$) while Q1=[0 0] and Q2=[1 1] were the vertices of the geometrical diagonal of the RMSEs pair space. The point that had the maximum "$(1-D_i)$ + $noRMSE_i$ + $nrRMSE_i$" (this value can range between 0 to 3), was taken as the optimal linearizing shortening index (X_{min}) (Fig. 7.13D). Next, we fitted all data ranges (from N sample points to $N - X_{min}$) with the two exponential models as described above.

7.5 Results

In this study, we used data from multielectrode recordings in 3 species: cat motor cortex (cats i and ii with a 96 channel multielectrode array in primary motor cortex, hindlimb area), cat parietal cortex (cat iii, 8 bipolar electrodes), monkey motor cortex (three monkeys with a 64 or 96 recordings from 96 channel multielectrode arrays in motor and/or premotor cortex), and humans (2 patients with a 96 multielectrode array in middle temporal gyrus). In the following, we briefly address definition of avalanche, then describe the results of power-law analyses on spike avalanche, state-dependence, regional differences and polarity-dependence of LFP maxima avalanche. At the end, we briefly discuss alternative fits to the data.

7.5.1 Avalanche definition

Figure 7.1 illustrates the definition of avalanche for discrete (spike) and continuous (LFP) data, as they are used in this study. For both spikes and LFP, we used bins of 1 to 15 ms (in 2ms steps) for defining the quiescent vs active periods. Avalanches are defined by contiguous bins of non-zero activity, separated by periods of quiescence (empty bins). The size of the avalanche is defined as the sum of all activities (spikes or LFP peaks) within that active period. Thus, the avalanches depend on the bin size (as illustrated in Fig. 7.1A for spikes). For LFPs, we first discretized the continuous data based on its local maxima. Both positive and negative maxima were examined in our study. For each polarity, 17 levels of thresholds were chosen (see Methods for details). After discretization, the obtained matrix (Fig. 7.1B) was used for the same binning and avalanche definition as used for spike series.

7.5.2 Power-law fit

It has been shown that that CDF provides a a better measure than PDF as it avoids erroneous measures at the far end of the distribution tail of probability curve [201,261]. It is also necessary to exclude the values below the valid lower bound, or else the calculated coefficient could be highly biased [201]. In each of the following estimates of power-law distribution, based on the methods described previously, we adapted the following steps on analyzing the CDF of avalanches: Values above a given X_{min} are used in a maximum likelihood estimate (MLE) of the exponent α. For each CDF, the proper lower bound of X_{min} is selected using a KS test. We also used 1000 semi-parametric repetitions of the fitting procedure for obtaining estimates of uncertainty and goodness of fit.

7.5.3 Avalanche analysis from spikes

Next, we studied whether the spike avalanches follow power-law distributions.

7.5.3.1 Avalanche analysis in wakefulness

We first studied avalanche dynamics in awake resting recordings from cats and humans. As depicted in Fig. 7.2, neither of these species, showed a dominant power-law behavior in their spike avalanche size distribution. The average scaling exponent of awake recordings for the decades that could be considered to follow power-law (i.e. $>X_{min}$), was to high to be related to SOC systems (see Table. 7.1 and Table. 7.2 and Fig. 7.2.i,ii,iii). These values not only are distant from those of 1/f noise, but also only apply to partial parts of the CDF (cumulative distribution function) of avalanche sizes. These lack of clear power-law characteristics is shown with X_{min} lower boundary (green dotted lines in Fig. 7.2). Only values above X_{min} could "statistically" follow a power-law regime and as mentioned, even in those cases, the exponent values were too high to be considered a signature of SOC systems. It is important to note that the CDF representation is cumulative, and thus the left tail is not excluded from the data but its influence is shifted to the right (see details in [201]; see also Methods).

Interestingly, representing the size distributions in log-linear scale revealed a scaling very close to linear for all species (Fig. 7.3), indicating that avalanches defined from spikes scale close to an exponential, as would be predicted by a Poisson-type stochastic process. This conclusion was also reached previously by analyzing units and LFP recordings in cats [134]. Also, as can be seen in the inset of panel A of Fig. 7.2, the same analyses done on the awake recording from the parietal cortex (albeit spatially sampled at only 8 electrodes) shows similar scaling behavior.

In addition to wake resting recordings, we also considered recordings made while monkeys

engaged in cognitive motor tasks. Similar to awake resting recordings in cat and man, the lower bound was variable between different binning sizes, thus excluding parts of the ”invalid” initial avalanche sizes, which are usually used as evidence of existence of power-law [135, 183, 259]. The inclusion of these initial parts may cause errors, and were removed here; however, their cumulative effects are still present in the tested regimen above X_{min} of the analyzed “cumulative distribution function” [201,261–263]. Above the lower bound value, all the CDF curves showed significant high exponent values. Interestingly, the MI (in both monkeys A and B) had similar mean to PMd (Table. 7.1, Fig. 7.2D,E,F), suggesting similar dynamics in the two areas.

7.5.3.2 Avalanche analysis during natural sleep

It has been claimed that wakefulness may not be the best state to display SOC, and that avalanches may be more naturally related to brain states with oscillations, and slow-wave oscillations in particular [267]. In contrast to this, a previous study in cat found that like wakefulness, slow-wave sleep (SWS) did not display power-law scaling as defined from spike avalanches [134], but this latter study suffered from a limited spatial sampling. To further investigate the issue, we have examined SWS and Rapid Eye Movement (REM) sleep periods with more dense sampling of spike activity. Figures 7.4 and 7.5, show the analyses for cat, human i and ii as well as monkey iii (MI and PMd) for SWS and REM periods. In none of these cases we see clear sign of power-law scaling. In all cases (except human ii), the variability of lower bound between different bin sizes is robust. All the curves represent ”partiality of power-law” with high exponent values. During SWS, cat, human subjects and monkey iii (MI and PMd) all manifested either lack of significant power-law scaling, or had such higher exponent values that makes it highly unlikely for power-law to be the generating process of spike dynamics (Table. 7.1). Similarly, in REM periods, there was no evidence for power-law scaling in human i’s first and second REM episodes. Together, with Cat REMs’ high exponents values, power-law scaling appears to be an unlikely candidate to describe the statistics of neural firing (Table. 7.1). Taken together, these various tests all based on proper statistical inferences, show that spike avalanches do not follow power-law scaling, for any brain state or sampling density.

Detailed numerical values for spike avalanche CDF exponents and their goodness of fit are provided in Table. 7.1 and Table. 7.2.

7.5.4 Avalanche dynamics from local field potentials

Next, we investigated the occurrence of avalanche type of dynamics from the local field potentials, which were simultaneously recorded with unit activity, in all datasets.

7.5.4.1 Relation between LFP peaks and spiking activity

Calculation of neuronal avalanches from LFP data is based on the assumption that statistically speaking, in comparison with the positive LFPs (pLFP), the negative LFP (nLFP) peaks are more strongly related to neuronal activity (e.g., see [174] and references therein). Indeed, the 8-electrode cat LFP data analyzed here show such a relation [174, 184]. To further test this relation, we also examined the simultaneous LFP and unit recordings in the ensemble recordings in cat, man and monkey. We used a wave-triggered-average (WTA) procedure, where the ensemble of nLFPs were used to epoch the ensemble spike activity. Averaging across these WTAs across different thresholds, show that there is indeed a weak relationship between nLFP and spiking (Fig. 7.6A). However, repeating the same procedure for positive LFP (LFP) peaks, did not display any relation (Fig. 7.6B), in agreement with the same analysis in cats [184]. Through four different types of control and randomization, we show that the relation between nLFP and spike is robust and is not attributable to randomness of the spiking events or spurious fluctuations in the LFPs. For details of these control/randomization, see methods and Fig. 7.6. This fundamental difference between nLFP and pLFP peaks provides a very important test to infer if a given power-law observation from LFPs is related to the underlying neuronal activity, as we will see below.

7.5.4.2 nLFP avalanches

Similar to previous studies, we investigated the avalanche dynamics from nLFPs. The nLFPs were detected using a fixed threshold, defined as a multiple of the standard deviation (STD) of the LFP signal (see Methods), and several thresholds were tested. In the following, we use "high", "medium" and "low" thresholds, which correspond to 2.25, 1.75 and 1.25 multiples of the standard deviation, respectively. As shown in Figs. 7.7 and 7.8, the distributions defined for avalanches at different bin sizes and thresholds seem to display power-law scaling, both for human and monkey. This result seems to be in agreement with similar analyses done on awake monkey [183]. However, plotting the same data as CDF revealed that the scaling as power-law was very narrow (Fig. 7.9). While Monkey ii displayed apparent power-law over more than one decade, the other cases from cats and humans, did not display any convincing power-law scaling. For details of nLFP avalanches for an example subject, and its comparison with pLFP avalanches, see Table. 7.3. One can also note that in some of the CDFs (and their counterpart PDF), there is a possibility that the distribution can be segmented into two regions each covering certain decades of avalanche size. In such cases, relying on a single scaling exponent to describe the totality of the functional dynamics of the network does not seem adequate. This could be an indication that the space of the distributions is not uniform and the underlying mechanisms could be of metastability nature [268]. In such scenario, interaction with the external world could push the system from the "currently most stable state" to a new "most stable state". Such constant changes may lead to the formation of nonuniform distribution of the neural events at

different temporal scales. Therefore it is essential to emphasize that, in some cases, one scaling exponent may not be sufficient to describe the complexity of the spiking or oscillations.

7.5.4.3 pLFP avalanches

Next, we investigated the avalanche dynamics of positive LFP peaks, which, as we have seen above, is not statistically related to firing activity (Fig. 7.6). Similar to nLFP peaks, the pLFP avalanches defined for human wakefulness did not display power-law scaling (Fig. 7.10). Both nLFP and pLFP had similar CDF of avalanche size across different species and cortices. The example shown in Fig. 7.10 (awake human) shows that across different thresholds, both nLFP and pLFP had variable lower bounds and high scaling exponents for the region of the data that could statistically be considered for power-law properties. Moreover, the absence of any region with clear linear scaling in the logarithmic coordinates further confirms that there is no power-law scaling in this case. For details, see Table. 7.3.

7.5.4.4 Avalanches in different cortical regions

In the cases that we had simultaneous, dual array multielectrode recordings from PMd and MI, the analyses showed that these two cortical areas do not show signs of criticality but have slight differences in their exponent values for MI and for PMd (Table. 7.1 and Table. 7.2, Fig. 7.11). Such findings show that the fact that these two cortices directly interact with each other, and one acts as input and one as the output of motor processing unit, is reflected in their slightly different CDF features. Thus, two different cortical areas seem to display similar features, although no sign of power-law scaling.

7.5.5 Statistical analysis of the avalanche distributions

7.5.6 Goodness of fit

Given data x and given lower cutoff for the power-law behavior X_{min}, we computed the corresponding p-value for the Kolmogorov-Smirnov test, according to the method described in Clauset et al. [201]. See methods for details. The results are given in Tables 7.1, 7.2 and 7.3 (“gof” columns).

7.5.7 Avalanche size boundaries

Imposing lower or upper bounds when fitting avalanche distributions can greatly affect the outcome of the fit [201]. In many cases, the analyses have been limited to the lower boundary of avalanche size $= 1$ and X_{max} of N, where N is the number of channels. Using such bounds improves the fitting of the data by power-law compared to other distributions, as confirmed by KS-statistics [259]. The pitfalls of such an approach are two-fold: a) the lower boundary is set to 1, therefore the avalanches that are below the acceptable lower bound of X_{min} are erroneously fitted with the power-law, thus reducing the reliability of the fit while producing mis-estimated scaling exponents (see [201] for details of lower bound selection). b) X_{max} is set to the maximum active channels, and any return to a given channel is counted in the avalanche, but the maximum allowed avalanche size is limited to N, based on the argument that the large avalanches are infrequent and their inclusion implies misfit. This type of approach, limits the number of avalanches to an extreme degree and introduces a bias. Below we investigate this bias.

7.5.7.1 Avalanche size distribution and upper boundary limits

Fig. 7.12 tests the effect of enforcing an upper boundary to the avalanche analysis. The red color shows the excluded (saturated) avalanches enforced by limiting the X_{max} to N (number of independent measures), while cyan represents the acceptable avalanches below this upper threshold. This figure shows that setting the X_{max} to a cutoff value of N, produces variable biases based on the bin size. Importantly, in simultaneously recorded regions, the majority of avalanches will be included in one case (like in PMd as shown in panel A) but not in the other (like MI, as depicted in panel B). Such discrepancy emphasizes that setting a cutoff will necessarily introduce a bias and causes variable results from region to region and from bin size to bin size.

7.5.7.2 Comparison of exponential and power-law fit: Model Mis-specification and lower boundary problem

It has been argued whether neuronal avalanches are better fitted by an exponential or power-law distribution. Here we tested two aspects, exponential vs. power-law comparison, as well as the effect of setting a lower boundary to the fit. It has been shown that defining a proper lower boundary improves the maximum likelihood that the distribution could be fit by a power-law [201]. In agreement with this, Klaus et al. (2011) used a lower boundary of 1 and showed that using KS-statistics, the power-law indeed provides a better fit to the data in comparison to exponential distribution. Here, we systematically tested whether such practice would return erroneous results in avalanche analysis. The results shown in Fig. 7.13A,B, are from cat spikes

data. For each bin size, we first defined the optimal lower boundary after Clauset et al. ([201]; see Methods), called X_{min}. We started with a lower boundary set to 1, and reduced the distribution of avalanche data gradually up to X_{min}. For each newly produced set, we calculated the empirical CDF (ECDF) as well as the provisional fitted probability's CDF (based on direct maximum likelihood) for both exponential as well as power-law. The results for a sample bin size are shown in Fig. 7.13A. Power-law at the lower boundary of 1 provides a bad fit. However, overall, power-law outperforms the exponential fit, specially after limiting the range of the data by increasing the lower boundary. The best power-law fit is obtained when the lower boundary approaches X_{min}.

This finding matches the results of the KS test (based on [201]) as we report in this manuscript. However, from our analyses, we know that when we reach the best power-law fit, the estimated scaling exponents are too high for any known natural system to follow a self-organized criticality regime. Therefore, we have a situation where either one gets unreliable but desired scaling exponent by setting the lower boundary to 1, or one obtains reliable but undesired scaling exponent by setting the lower boundary to $X_{min} > 1$.

Next, we quantified the goodness of fit with a more rigorous approach than the simple KS test. If the parametric CDF is close to the probabilities from the ECDF, then the depicted line should approach the diagonal (1:1) line with minimal drift from it. For quantifying this, we measured the integral of the distance of each point on the p-p curves from the 1:1 diagonal line. This value should be zero in a perfect fit; its non-zero value shows departure from a perfect fit. Fig. 7.13B shows the results for all bin sizes. Similar to Klaus et al. [259], the power-law provides a better fit in comparison to exponential. However, there are two aspects that can not be ignored for this condition to be true: a) the distance improves only as we tighten the lower bound criteria to be close to X_{min}, but it does not mean that this is a proper fit.; b) there is no rule of thumb for such an improvement; in almost all of the cases, a linear relationship in the normal probability plot distribution of the distance was not found. This shows that power-law provides a better fit than the exponential distribution, but that both fits are not satisfactory. We consider alternative distributions below.

7.5.8 Alternative distributions for avalanche dynamics

Although previously, at the microcircuit scale, some studies have asserted the existence of criticality as a universal characteristic of neural dynamics in both spike and LFP avalanches [135, 269], other evidence suggest that same behavior can also be observed through stochastic processes [134, 184]. In this study, after rigorous testing, we showed that the avalanches do not follow power-law as a universal feature. Thus we also tested whether an alternative probability distribution could provide a better estimate for the experimental observations.

We first tested a simple exponential fitting of the spike avalanches, by fitting straight lines in

a log-linear plot. As seen from Fig. 7.13C, a linear fit ("exp1") can only fit part of the data, as the initial points (for small size) do not scale linearly. In detection of the lower bound of linearity, i.e. (X_{min}), the robust bi-square method is more stringent than simple least square fits and leaves behind more data points for exponential fitting (see different lines in Fig. 7.13C; errors based on bi-square are plotted in Fig. 7.13D; see Methods for details on linearity optimization).

Next, we tested a multiple exponential fitting of the data. The rationale is that two exponential processes may represent differences in two populations of cells, for example excitatory and inhibitory cells. The fit resulting from a "sum of exponential processes" was extremely good in minimum residual and reliable prediction bounds for the data (Fig. 7.13E). This "sum of exponential" model ("exp2") gave a very good performance in both full length (dark blue) and reduced above "X_{min}" (red). The "simple exponential" model (exp1) reaches a very good fit only for the reduced set (cyan) but not for the full length of the avalanches (light brown). For comparison of "exp1" and "exp2" on different spike avalanches, with and without "linearity improvement", see Fig. 7.13F. Overall, it seems that both exp1 and exp2 exhibit comparably high values of goodness of fit for the reduced sets. However, only the double exponential fit was able to fit the entire dataset.

7.6 Discussion

In the present paper, we have analyzed and compared the avalanche dynamics obtained from multielectrode recordings of spikes and LFPs, for three species, cat, monkey and human. In each case, we used recordings exclusively made in non-anesthetized brain states, including quiet and active wakefulness, SWS (slow-wave sleep) and REM (Rapid eye movement). The primary result of our analysis is that there is no power-law scaling of neuronal firing, in any of the examined recordings, including "desynchronized" EEG states (wakefulness), SWS, and REM sleep. All species consistently showed distributions which approached exponential distributions. This confirms previous findings of the absence of power-law distributions from spikes in cats [134], and extends these findings to monkeys and humans. An obvious criticism to that prior study is that a set of 8 electrodes is too low to properly cover the system, and the absence of power-law may be due to this subsampling. We show here that the same results are obtained when a significantly higher density of recording is used, confirming the absence of power-law.

In contrast, avalanche dynamics built from nLFPs displayed more nuanced results. In some cases, the avalanche size distributions appear to draw a straight line in log-log representations, but the more reliable CDF-based tests did not show clear evidence for power-law scaling. Indeed, statistical tests such as the KS test did not give convincing evidence that these data are universally distributed according to a power-law. More importantly, while nLFP are related to firing activity, we showed that a similar behavior was also observed for pLFP peaks. The avalanche analysis from positive peaks displayed similar results as for negative peaks, although

positive peaks displayed a weaker statistical relation to firing activity. Using 4 types of control/randomization we provide very robust evidence that the fundamental differences between nLFP and pLFP are not attributable to random behavior of spikes or LFP peaks. Yet still, the discretized thresholded LFPs, show strikingly similar behavior in their avalanche statistics. These findings render any conclusions about self-organized criticality based on simple power-laws of PDFs as phenomenological.

Together, these results suggest that the power-law behavior observed previously in awake monkey [183, 269] cannot be reproduced in awake humans' temporal cortex or cat and monkey motor cortex. This conclusion also extends to slow-wave sleep and REM sleep, which we found did not display power-law distributed avalanches, as defined from either spikes or LFPs. In searching for the linear domains in CDF based on the KS test, one can force the scaling exponent to fall within the range of the plausible values (comparable to those observed in known physical phenomena). Doing so, of course, yields more conservative values of scaling, but means that such scaling would be applicable to only a limited range of data. In fact, unless the system has universal scaling, there is always a tradeoff between the range to which a scaling exponent can be extended (i.e. the linear regime in the data) and the proximity of the scaling exponent value to those of a narrow range (in this case, values of the SOC systems are of interest). Our tests, did not force the scaling exponent to be limited to values between 1-2, therefore it had a more stringent emphasis on the linearity of more decades of the avalanche sizes. In some cases where the data showed statistically significant linearity, the obtained scaling exponents were an order of magnitude higher than what falls in the range of the critical regime of known physical phenomena. Conversely, these observations imply that, a single scaling exponent is not sufficient to explain the complex dynamics of ensemble activity.

A possibility worth exploring is that some form of power-law in LFPs is the result of volume conduction associated with LFPs recorded in high density arrays. When a peak is detected, it is often also present in many different channels. A possibility worth to explore is whether the same event could be volume-conducted across many channels in the array, which may lead to an artificial increase the large-size avalanches. This possibility should be examined by mathematical models of the volume conduction effect.

It must be noted that the evidence for self-organized criticality in neuronal cultures or in slices [135], as well as in anesthetized states [182] is not contradictory with the present findings. The wiring of *in vitro* preparations, as well as the network dynamics in anesthesia, are evidently different than in the intact brain. We find here that there is no evidence for SOC in wakefulness and natural sleep states, and for 3 different species. On the other hand, the report of power-law scaling of nLFPs avalanches in awake monkey [183] seems in contradiction with the present findings. Many possibilities exist to reconcile these observations, such as differences between brain region, recording method, cortical layer or volume conduction effects. These possibilities should be investigated in future studies. Moreover, in a recent report [270], it has been shown that data from high density recordings (up to 512 electrodes) from from neural culture show

elements of universality and that avalanches can be collapsed into a universal scaling function [271]. Such findings confirm that brain circuits *in vitro* operate near criticality. Further studies should examine how to reconcile such evidence with the present *in vivo* findings.

Due to the high dimensionality of neural data, it is crucial to separate the features of the inferred models that are induced solely by the inference scheme from those that reflect natural tendencies of the studied system [268]. In some cases, one could fit the data with different lines by limiting the range of the decades within which a fit is analyzed. While it is indeed possible, and highly likely, that neural data at this level follow a multi-scale regime, albeit such a property would push the system away from cohesively operating at self organized criticality because the relation between microscopic interaction of the (neural) elements and collective behavior (of the cortical network) no longer manifests in single valued features, like a single scaling exponent.

Finally, it is important to emphasize that the present results were obtained using statistical tests similar to previous statistical analyses [201, 261]. In particular, the use of the CDF distribution rather than simple log-log representations of the size distribution is a particularly severe test to identify if a system scales as a power-law. The use of statistical measures such as the Kolmogorov-Smirnov test (Table. 7.1, 7.2 and 7.3) also constitutes a good quantification of which distribution fits the data, and is largely superior to the least square fit in double logarithmic scale [201]. The uncertainty and goodness of fit were estimated by 1000 repetitions of each fitted distribution. We also showed that setting bounds to the fit can introduce biases in favor of power-law fits, as analyzed previously [201]. In agreement with this, it was found with bounded fits that power-law provides a better match to data compared to exponential distributions [259]. Our analysis shows that neither power-law nor exponential distributions provide acceptable fits to the datasets analyzed here. Multi-exponential fits suggest that bi-exponential processes provide a particularly good fit to the distributions, which suggests that the underlying neuronal dynamics is most compatible with two exponential processes, which could be for example excitation and inhibition, both scaling as exponential distributions. Such a possibility should be tested by further studies, and seem in agreement with the complementary excitatory and inhibitory dynamics found in the awake and sleeping brain [260].

7.7 Figures

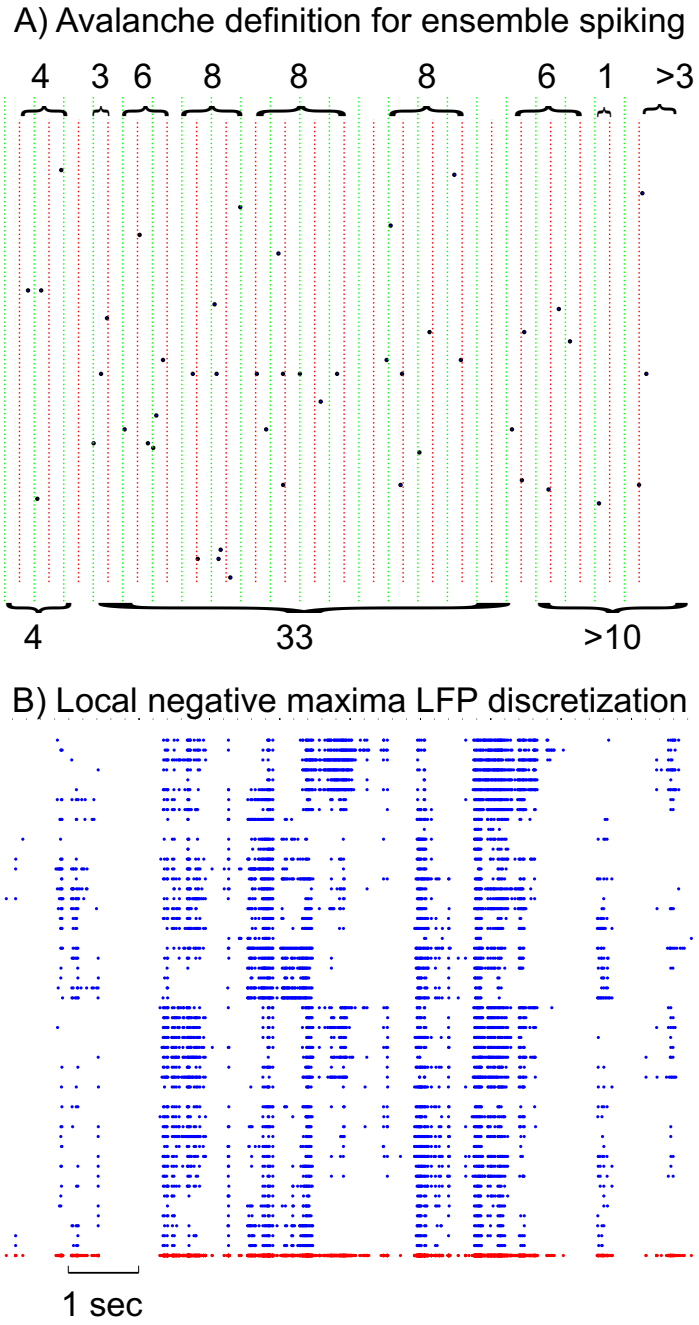

Figure 7.1. Definition of avalanches. (A) comparison of avalanche definition for 8ms vs 16 ms binning; green vertical lines define the boundaries of 16ms binning; naturally, each 16ms bin is composed of 2 independent 8ms bin (depicted with red dotted lines). Accolades point to the avalanches, separated by quiescent periods. Top, 8ms avalanches and their sizes, Bottom: 16ms avalanches and their corresponding size. Please note that last avalanche continues after of the limits in this figure. **(B)** negative local maxima obtained from the grid of electrodes for a period of 10 sec. Each row represents negative maxima of a single LFP channel of a selected threshold level $\geqslant 1.75 \times$STD of the normalized LFP. The red dots in the bottom refer to ensemble presence of nLFP maxima.

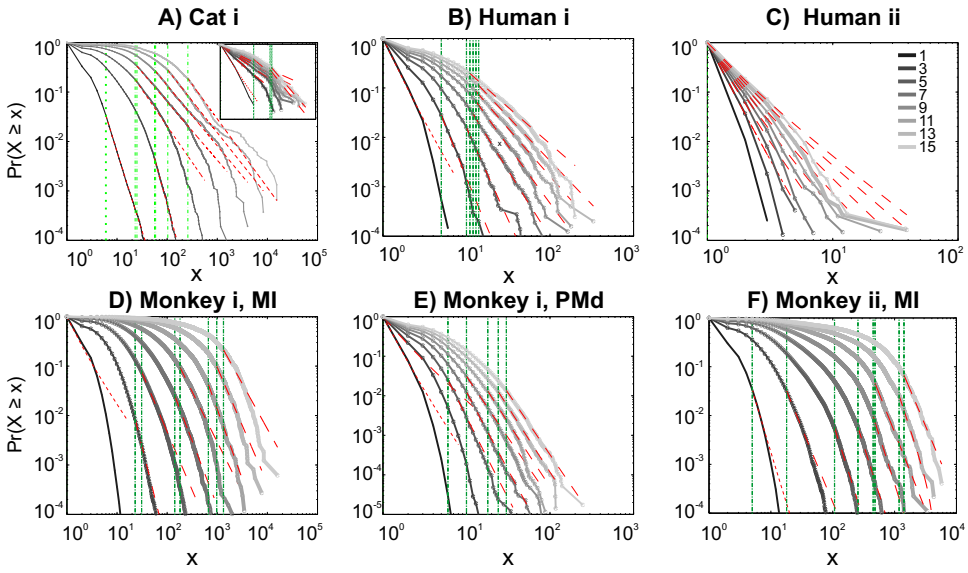

Figure 7.2. Avalanche analysis on spiking activity during wakefulness. In idle awake ,**(A)**. Cat i (96-electrode array) and Cat iii (inset, 8-electrode array), **(B)**. Human i (96-electrode array), **(C)**. Human ii (96-electrode array). Different line colors refer to different bin sizes as shown in the legend. The lower bound (X_{min}, shown in green dotted line), shows that the CDF of avalanche size, only partially, may follow power-law distribution. Even in such cases, the exponents had very high values, well above the criticality regime that is hypothesized for 1/f noise. Panels **(D)**,**(E)** and **(F)**, show the same type of curves for monkeys engaged in cognitive motor task (96-electrode array; augmented with a 64-electrode array). Same pattern is observed; it also seems MI has slightly higher values than PMd in the plausible power-law regime. For the mean/std exponent values, see Table. 7.1 and Table. 7.2.

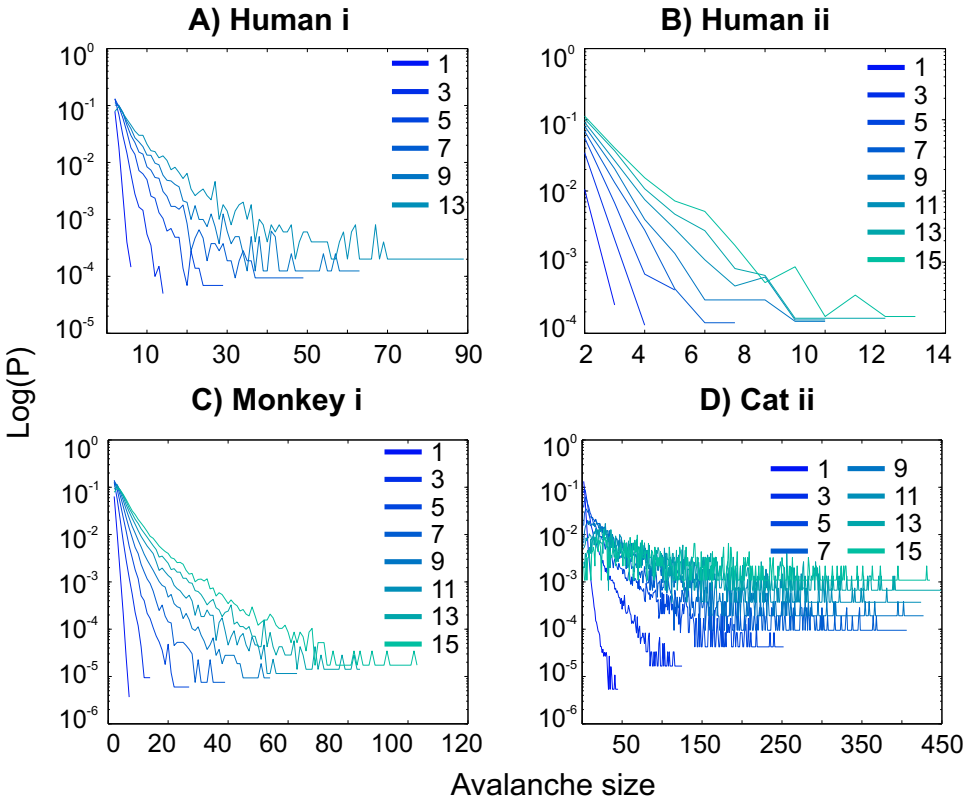

Figure 7.3. Spike avalanche distributions in log-linear representation. Different line colors refer to different bin sizes as shown in the legend. An exponential process has a linear trend in log-linear scale. Spike avalanches for all coarse graining levels, showed a linear trend. Please notice that bin sizes 11 and 15 are not shown because for the clarity in the line plot, but showed similar linear trend in this scale (not shown).

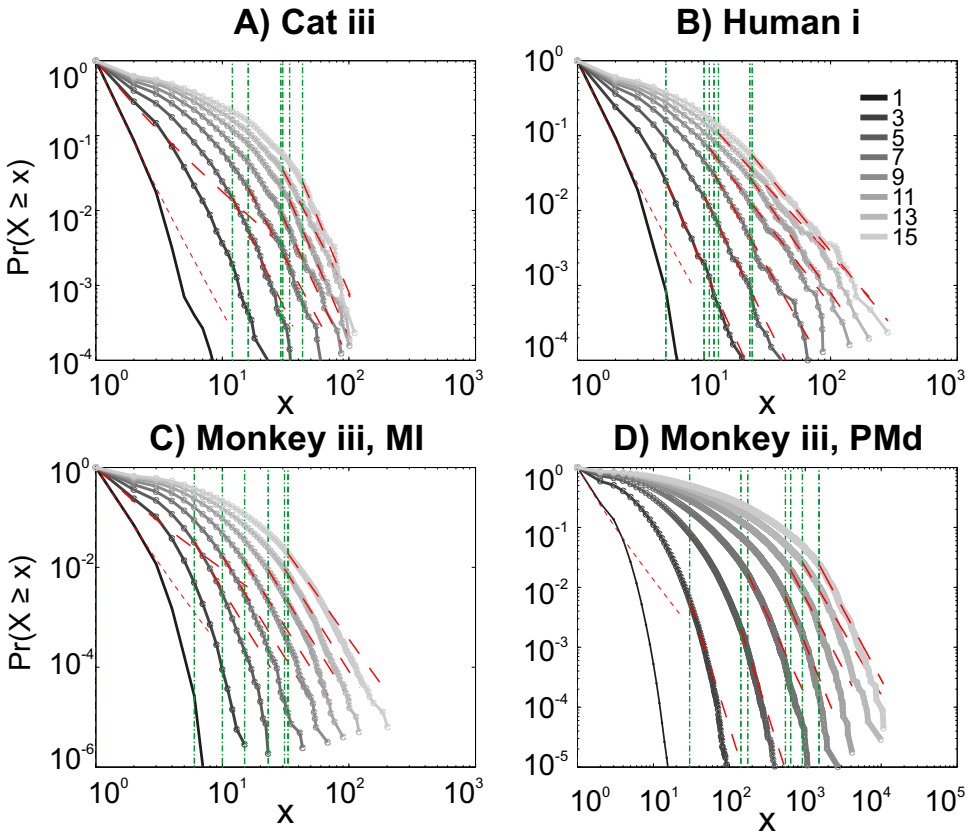

Figure 7.4. Avalanche analysis of spiking activity during slow-wave sleep. (A) Cat iii, **(B)** Human i, **(C)** monkey iii MI and **(D)** monkey iii PMd. Different line colors refer to different bin sizes as shown in the legend. In parallel to awake dynamics (Figure 2), there is no sign of criticality, the curves follow different partial power-law with high exponents and variable lower bound values. The avalanche dynamics do not show a state-dependent trend. For the mean/std exponent values, see Table. 7.1.

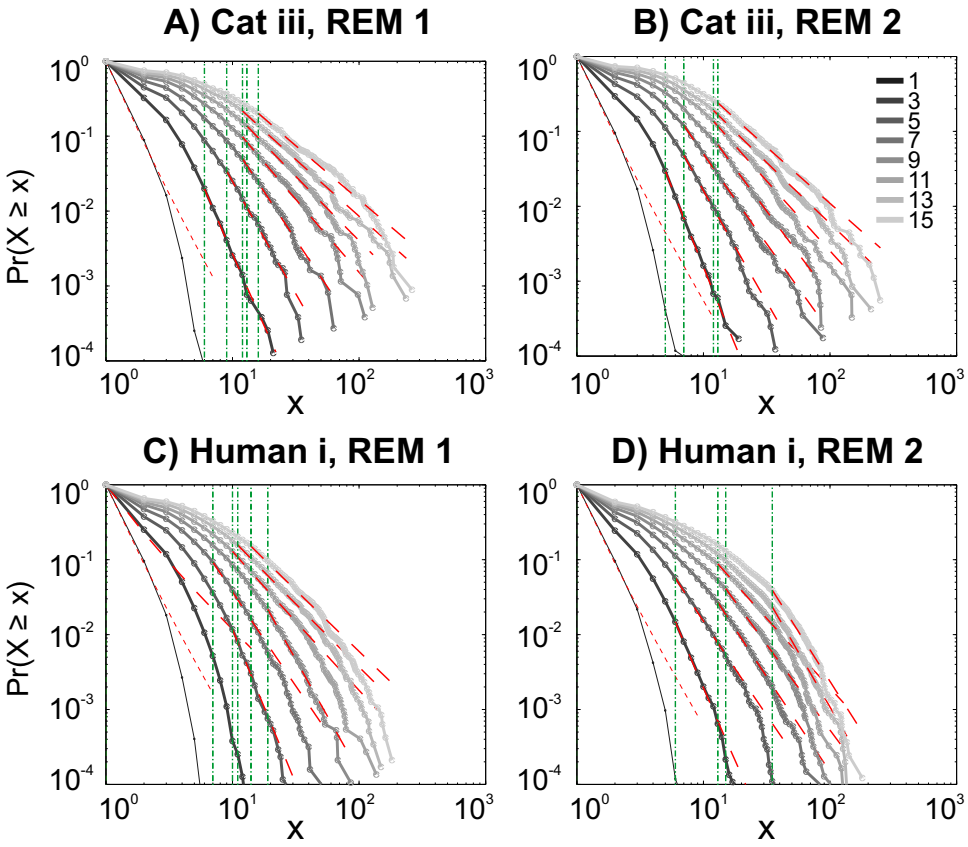

Figure 7.5. Avalanche analysis of spiking activity during REM sleep. (A) cat iii REM episode 1, **(B)** cat iii REM episode 2, **(C)** human i REM episode 1, **(D)** human i REM episode 2. Different line colors refer to different bin sizes as shown in the legend. Similar to awake and SWS, the lack of criticality, variability through different coarse graining thresholds and lower bounds is the universal finding. For the mean/std exponent values, see Table. 7.1.

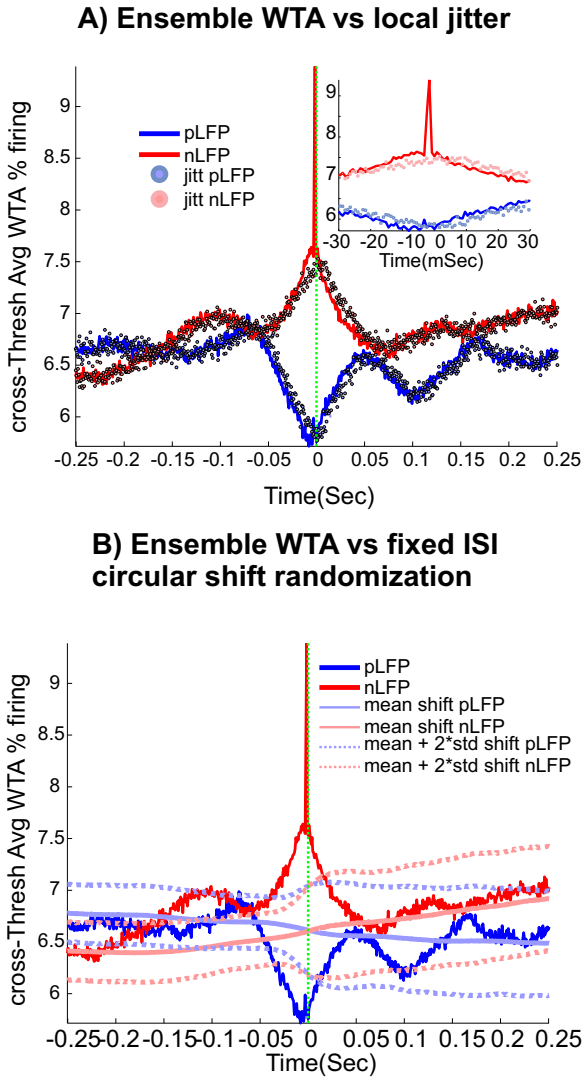

Figure 7.6. Relation between unit firing and LFP peaks in wakefulness. nLFP (red) and pLFP(blue)-based wave-triggered average (WTA) of percentage unit activity, showing that the negative peaks have closer association with an increase of neuronal firing. **(A)** Tightly regulated local jitter of nLFP peaks destroys the large nLFP peak. Inset shows the zoom around 0. **(B)** Preserving the internal structure of aggregate spike train and ensemble LFP peaks, but destroying the relation between the two leads to the disappearance of the nLFP peak. See text for details of randomization and controls. The WTA traces in this figure are from Human i, (based on 183127, 98520 and 47451 nLFP and 158737, 79225 and 36020 pLFP peaks for low, medium and high threshold respectively.)

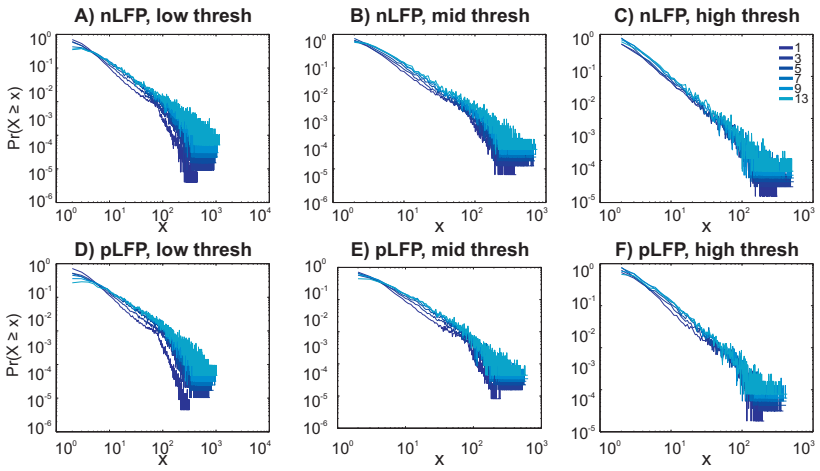

Figure 7.7. Avalanche analysis in awake monkey LFPs in logarithmic representation. A power-law process has a linear trend in log-log scale. LFP (negative or positive) maxima avalanches for all coarse graining levels, as well as all thresholds, showed a linear trend. Please notice that bin sizes 11 and 15 are not shown because for the clarity in the line plot; however, they too, also showed a very clear linear trend in this scale. Such trend is necessary but not sufficient for a process to be power-law. See text and Fig. 8.9

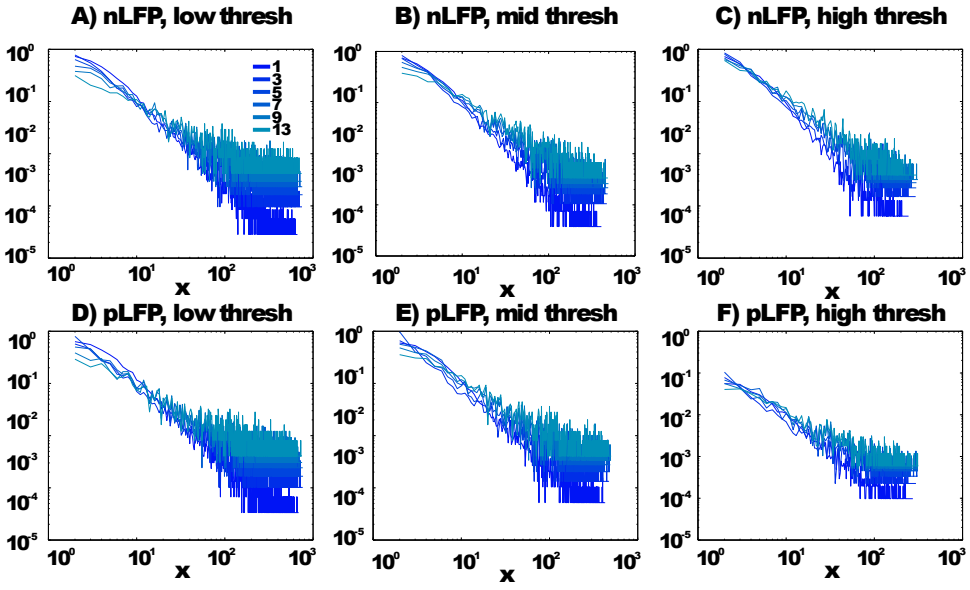

Figure 7.8. Avalanche analysis in awake human LFP in logarithmic representation. A power-law process has a linear trend in log-log scale. LFP (negative or positive) maxima avalanches for all coarse graining levels, as well as all thresholds, showed a linear trend. Please notice that bin sizes 11 and 15 are not shown because for the clarity in the line plot; however, they too, also showed a very clear linear trend in this scale. Such trend is necessary but not sufficient for a process to be power-law. See text and Fig. 8.9

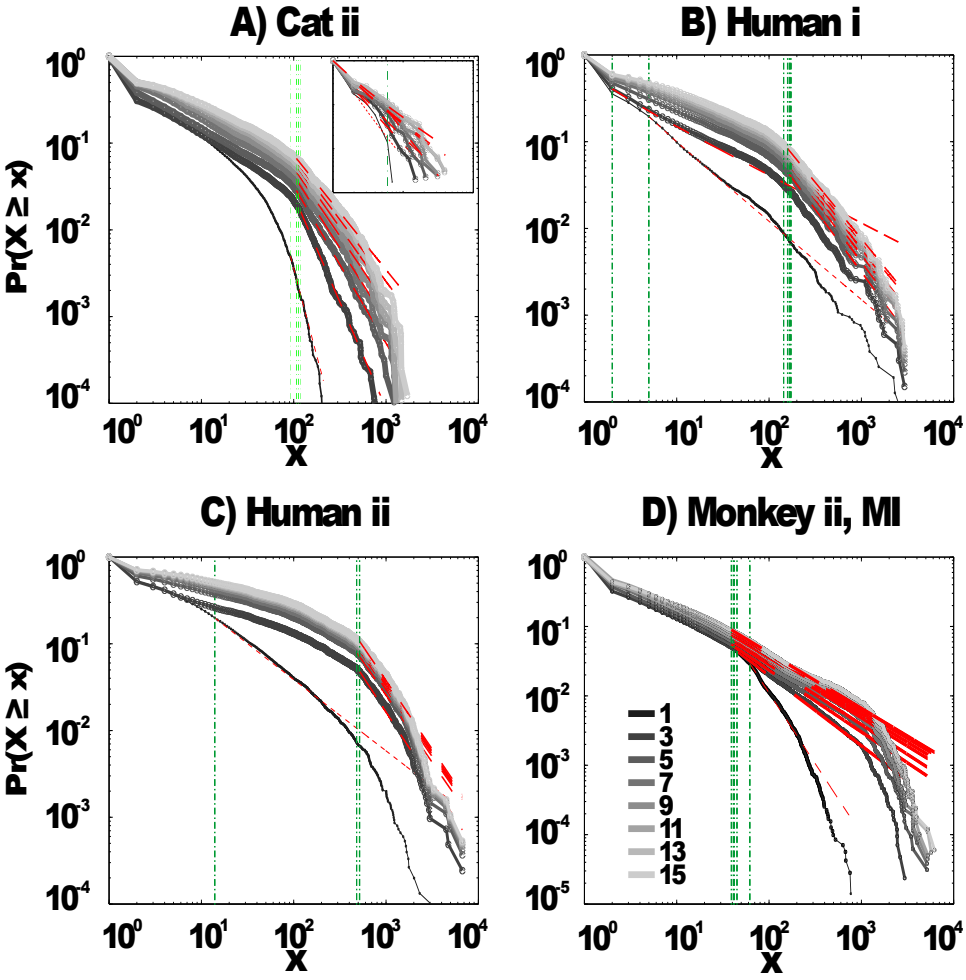

Figure 7.9. Avalanche analysis based on LFP negative peaks in wakefulness. (A) Cat ii (96 electrode array) and Cat iii (inset, 8 electrode array), **(B)** Human i, **(C)** Human ii , **(D)** Monkey ii MI. In all cases, different binnings lead to variable lower bound and scaling exponents. Lack of linear trend in CDF shows that the observed linear trend in log-log scale, as shown in Fig. 8.7 and Fig. 8.8, are not sufficient for showing that avalanche dynamics are power-law processes. For the mean/std exponent values, see Table. 7.3.

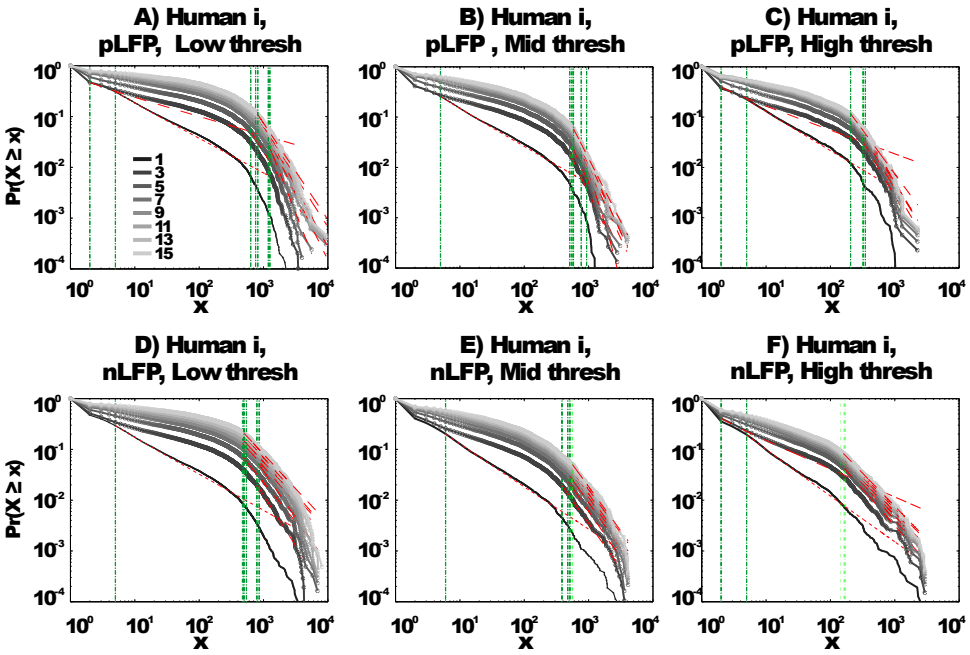

Figure 7.10. Comparison of Avalanche analysis based on negative and positive peaks. LFP (negative or positive) maxima avalanches for all coarse graining levels, as well as all thresholds did not show linear trend in CDF, therefore negate power-law as the generating process. These curves show while nLFP has a closer relation with spiking, the avalanche dynamics of nLFP and pLFP are strikingly similar in their lack of robust criticality when tested with rigorous statistical tests.

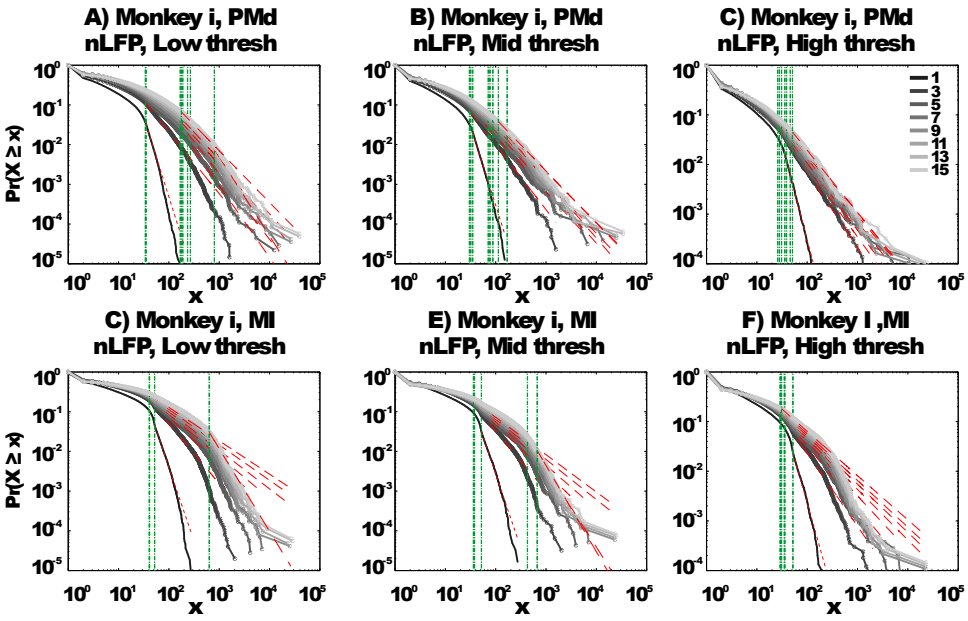

Figure 7.11. Avalanche analysis in different cortical areas recorded simultaneously. Avalanche dynamics in nLFP shows that the CDF of the input and output units of two interacting cortices have slightly different characteristics but neither follow criticality regime. **(A)** Monkey i, MI, low threshold **(B)** Monkey i, MI, medium threshold, **(C)** Monkey i, MI, high threshold, **(D)** Monkey i, PMd, low threshold **(E)** Monkey i, PMd, medium threshold, **(F)** Monkey i, PMd, high threshold.

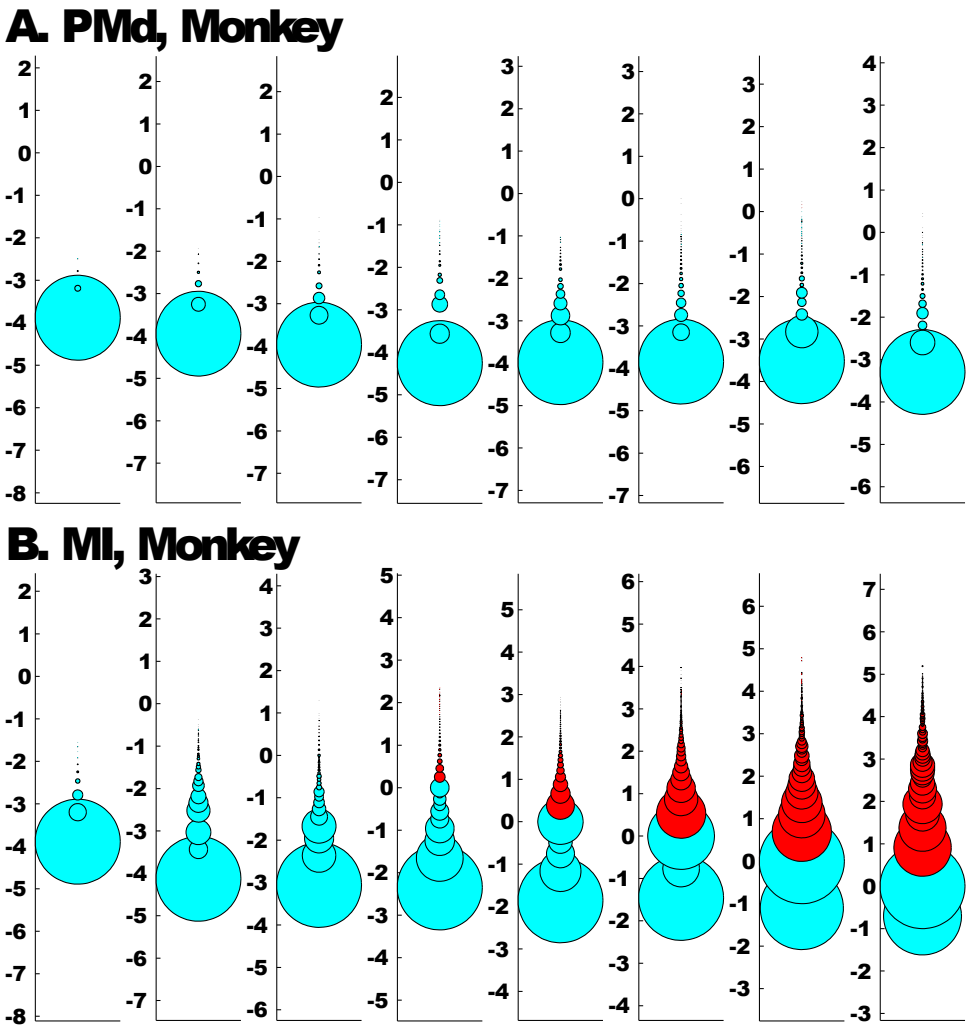

Figure 7.12. Effects of setting upper boundaries on avalanche size distribution. Each column shows avalanches of a different bin size (increasing from left to right).Panel **(A)** and **(B)**, show the results of spike avalanche size distribution of the PMd and MI (respectively). For each bin size, the distributions of different avalanche sizes are shown in circles; the avalanche size increases from the bottom to the top, while the size of each circle represents the ratio to the overall number of avalanches. Red color shows the excluded (saturated) avalanches enforced by limiting the Xmax to N (number of independent measures; i.e. units in the case of spike avalanches and electrodes in the case of LFP avalanches). Cyan color shows the included avalanches. Y axis is in logarithmic scale for better visualization and the values of Y represent the orders of magnitude of N for proper comparison between different bin sizes (i.e. a given circle at y=2, represents the avalanches that their size =2log(N), its diameter shows the number of avalanches that had that size and its color shows whether it is included or excluded according to the Xmax=N rule).

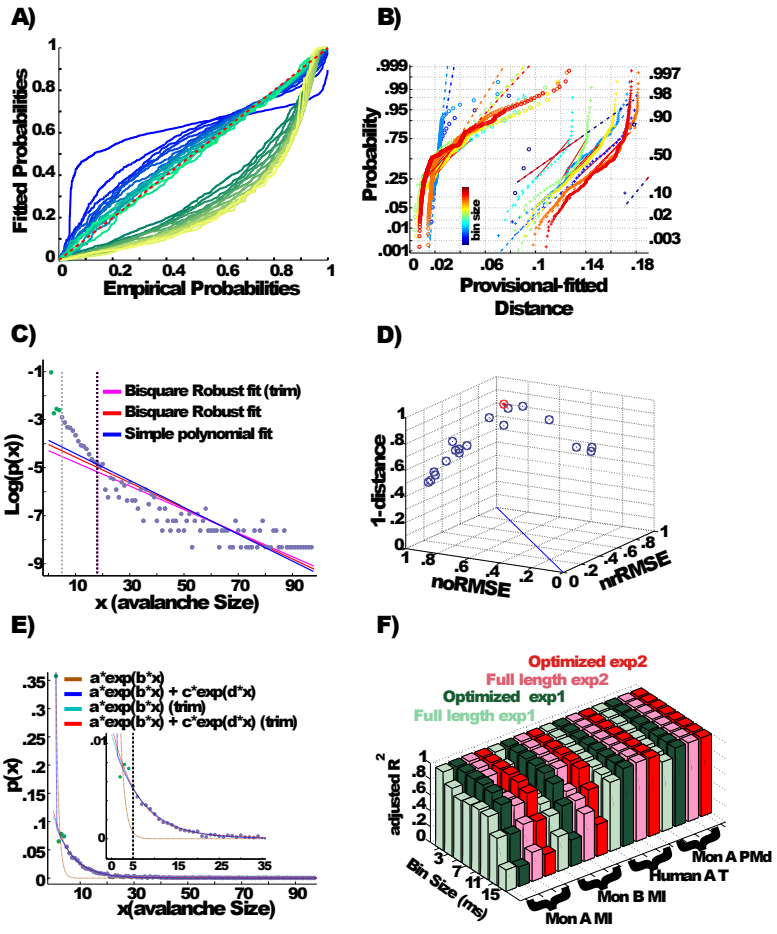

Figure 7.13. A-B: Fits comparison and lower boundary.C-F:Alternative fits for avalanche size distributions. (A) Probability-Probability plot (ECDF vs provisional CDF) for a sample bin-size (cat i spike avalanche). Green colors are p-p plot for ECDF vs exponential, and blue colors are for p-p plot for ECDF vs power-law. In each color family, as the lower boundary is increased (from 1 to Xmin), the color saturation fades; i.e. darkest color shows lower boundary of 1 and the lightest shows lower boundary of Xmin (where Xmin is based on the Clauset method for fitting power-law to empirical data). **(B)** Integral of p-p distance to the 1:1 diagonal (perfect match of the parametric CDF to ECDF). The colors (blue to red) are related to bin sizes (from smallest to biggest). Cross signs represents exponential distance and circles represents power law distance to the ECDF. **(C)** Simple exponential fitting of spike avalanche data. The data points (purple and green) are plotted in a log-linear representation, together with a simple polynomial fit (blue), a robust fit calculated on the full length data (red) and a robust fit on the reduced data (magenta). The two vertical lines indicate the lower bound of the region of linearity, i.e. "X_{min}", calculated based on the simple polynomial fit (black) and the bi-square method (grey). **(D)** Comparison of the goodness of fit of different exponential fits to different reductions of the same dataset. The 3 coordinates are "normalized overall improvement of RMSE" (noRMSE), "normalized relative improvement of RMSE" (nrRMSE) and distance of a point from the diagonal in (noRMSE,nrRMSE) plane. Each point in this 3D space, is the result of a bi-square robust fit after elimination of the first *i* elements of the data (best fit in red). **(E)** Bi-exponential fitting of the same data. The "sum of exponential" model (exp2) gave a very good performance in both full length (dark blue) and reduced above "X_{min}" (red). The "simple exponential" model (exp1) reaches a very good fit only for the reduced set

7.8 Tables

Table 7.1. Summary spike avalanche

Species	*Loc*	*State*	*CDF exponent*	*Pval*	*gof*
Monkey i	MI	Awake	3.4413 ± 0.7616	0.0419 ± 0.1152	0.0442 ± 0.0216
Monkey i	Pmd	Awake	4.1660 ± 0.6590	0.1130 ± 0.2140	0.0180 ± 0.0050
Monkey ii	MI	Awake	4.6250 ± 0.4730	0.4550 ± 0.3600	0.0330 ± 0.0120
Monkey iii	MI	SWS	4.5560 ± 0.7980	0.0030 ± 0.0100	0.0220 ± 0.0080
Monkey iii	Pmd	SWS	3.7760 ± 0.8660	0 ± 0	0.0430 ± 0.0170
Cat ii	MI	Awake	2.8412 ± 1.2184	0.3056 ± 0.3844	0.0599 ± 0.0368
Cat iii	Parietal	Awake	3.1410 ± 0.8720	0.2010 ± 0.3680	0.0270 ± 0.0180
Cat iii	Parietal	SWS	4.2110 ± 0.7930	0.3290 ± 0.3620	0.0350 ± 0.0140
Cat iii	Parietal	REM 1	3.3240 ± 0.8150	0.2990 ± 0.2170	0.0290 ± 0.0110
Cat iii	Parietal	REM 2	3.4050 ± 0.8250	0.4250 ± 0.4470	0.0230 ± 0.0140
Human i	Temporal	Awake	3.5490 ± 0.8790	0.3870 ± 0.3650	0.0210 ± 0.0080
Human i	Temporal	SWS 1	3.6340 ± 0.6410	0.3790 ± 0.3150	0.0250 ± 0.0100
Human i	Temporal	SWS 2	3.2550 ± 0.5770	0.1710 ± 0.2670	0.0330 ± 0.0150
Human i	Temporal	REM 1	3.3740 ± 0.8560	0.0930 ± 0.1720	0.0300 ± 0.0090
Human i	Temporal	REM 2	3.6430 ± 0.5540	0.0960 ± 0.1950	0.0320 ± 0.0170
Human i	Temporal	Awake	3.9200 ± 0.7970	0.0080 ± 0.0230	0.0090 ± 0.0070
Human i	Temporal	SWS	3.8950 ± 0.7630	0.0070 ± 0.0140	0.0100 ± 0.0070

Cross species summary of spike avalanche

Table 7.2. Detailed Awake spike Avalanche

Loc	*Bin size(ms)*	*CDF exponent*	*Pval*	*gof*
MI	1	2.5	0	0.036
MI	3	5	0.008	0.020
MI	5	3.36	0	0.029
MI	7	3.63	0	0.039
MI	9	3.03	0	0.047
MI	11	3.83	0.327	0.034
MI	13	3.35	0	0.060
MI	15	2.83	0	0.089
PMd	1	4.1	0	0.006
PMd	3	2.81	0	0.021
PMd	5	5	0	0.018
PMd	7	4.85	0.061	0.017
PMd	9	4.03	0	0.022
PMd	11	4.21	0.018	0.024
PMd	13	4.25	0.216	0.019
PMd	15	4.08	0.61	0.017

Monkey i detailed table.

Table 7.3. Detailed Awake LFP Avalanche

Bin size(ms)	*Polarity*	*Threshold*	*CDF exponent*	*Pval*	*gof*
1	neg	Low	1.71	0	0.019
3	neg	Low	2.99	0.056	0.051
5	neg	Low	2.55	0	0.052
7	neg	Low	2.84	0.074	0.052
9	neg	Low	2.42	0	0.053
11	neg	Low	2.37	0	0.059
13	neg	Low	2.43	0	0.054
15	neg	Low	2.36	0	0.052
1	neg	Mid	1.83	0.002	0.015
3	neg	Mid	2.79	0.425	0.040
5	neg	Mid	2.84	0.55	0.042
7	neg	Mid	2.81	0.376	0.048
9	neg	Mid	2.84	0.345	0.050
11	neg	Mid	2.84	0.435	0.048
13	neg	Mid	2.71	0.098	0.058
15	neg	Mid	2.74	0.204	0.056
1	neg	High	1.9	0	0.018
3	neg	High	1.55	0	0.029
5	neg	High	2.44	0.645	0.036
7	neg	High	2.43	0.201	0.046
9	neg	High	2.41	0.672	0.036
11	neg	High	2.39	0.67	0.035
13	neg	High	2.3	0.496	0.036
15	neg	High	2.3	0.36	0.040
1	pos	Low	1.68	0	0.020
3	pos	Low	1.37	0	0.073
5	pos	Low	3.03	0	0.066
7	pos	Low	4.21	0.762	0.051
9	pos	Low	3.59	0.585	0.048
11	pos	Low	3.39	0.43	0.047
13	pos	Low	2.98	0.079	0.046
15	pos	Low	2.9	0.032	0.052
1	pos	Mid	1.74	0	0.018
3	pos	Mid	3.67	0.128	0.062
5	pos	Mid	3.79	0.047	0.069
7	pos	Mid	5	0.827	0.061
9	pos	Mid	3.78	0.797	0.041
11	pos	Mid	3.68	0.926	0.036
13	pos	Mid	3.87	0.797	0.049
15	pos	Mid	3.51	0.553	0.046
1	pos	High	1.76	0.009	0.020
3	pos	High	1.47	0	0.061
5	pos	High	3.19	0.169	0.067
7	pos	High	3.17	0.063	0.066

Chapter 8

Appendix: Cell/LFP relations and E/I balance

al-gabr means "restoring", referring to the process of moving a subtracted quantity to the other side of an equation; al-muqabala is "comparing" and refers to subtracting equal quantities from both sides of an equation.
al-Kitab al-mukhtasar fi hisab al-jabr wal-muqabala ("The Compendious Book on Calculation by Completion and Balancing").

al-Khwarizmi

Appendix: Relations between excitatory and inhibitory cell activity and local field potentials during human brain states.

Nima Dehghani[1], Adrien Peyrache[2], Eric Halgren[3], Alain Destexhe[1,*] and Sydney S. Cash [4,*]

1 Laboratory of Computational Neuroscience. Unité de Neurosciences, Information et Complexité (UNIC). CNRS. Gif-sur-Yvette, France.

2 NYU Neuroscience Institute, New York University Medical Center , New York, NY, USA

3 Multimodal Imaging Laboratory, Departments of Neurosciences and Radiology, University of California San Diego, La Jolla, CA, USA.

4 Department of Neurology, Massachusetts General Hospital and Harvard Med. School, Boston, MA, USA.

∗ **co-corresponding authors.** [1]

Reference: *Dehghani, N., Peyrache, A., Eskandar, E.N., Madsen, J.R., Anderson, W.S., Donoghue, J.S., Hochberg, L.R., Halgren, E., Destexhe, A. and Cash, S.S. Relationship between excitatory and inhibitory neuronal activity and local field potentials during human sleep. Society for Neuroscience Abstracts* **37***: 451.05, 2011.*

Keywords: *Pyramidal, Interneuron, Fast spiking (FS), Regular spiking (RS), Human, cortex, sleeping*

[1] Author contributions: N.D. and A.D. designed research; N.D designed the tests and analyzed data.; N.D., A.P., E.H., S.S.C., and A.D. performed research.

8.1 Summary

High-density intracranial recordings (NeuroPort 96-electrode array) were obtained in the temporal cortex of humans under treatment for neurosurgery. We successfully separated regular-spiking (RS) and fast-spiking (FS) cells, as confirmed from monosynaptic connections (see Peyrache et al., SFN Abstract 2011). We report here the differential firing of RS and FS cells during different sleep stages, devoid of interictal activity. Up to 90 simultaneously recorded units (in Layer III), and 96 local field potential (LFP) recordings, provide a good basis to characterize the dynamics of excitation and inhibition during different brain states. During slow-wave sleep (SWS, Stage III or IV), dominated by delta-wave activity, all neurons fired according to Up and Down states, in relation to slow-waves complexes in the LFP, as described previously. Both RS and FS cells were silent during the Down-states. During REM sleep and wakefulness, both types of units fired according to very irregular patterns of discharge, while the LFP or ECoG were desynchronized. In all states, FS cells fired significantly more than RS cells (about 4 to 5 times on average). We next evaluated the characteristics of the different stages in more detail by using an automatic categorization of sleep stages combined with sequential multitaper spectral estimation. Dividing the recordings in episodes of light SWS, deep SWS, REM and wakefulness, we calculated and compared the spectral transfer function (LFP-Units) for each stage. We also estimated the correlated firing of the units, as well as the spatial and temporal correlation of LFPs and cells, which are significantly larger for SWS. In conclusion, these results show unit firing and spectral properties for human sleep, and are consistent with well-known electrophysiological characteristics in cats and rats.

8.2 Résumé

Des enregistrements intra-crâniens de haute-densité (NeuroPort, 96 électrodes) ont été obtenus dans le cortex temporal de patients traités pour la neuro-chirurgie. Nous avons pu séparer les cellules entre “regular-spiking” (RS) et “fast-spiking” (FS), ce qui a été confirmé par connections monosynaptiques (voir Peyrache et al., PNAS, 2012). Nous analysons ici la décharge spécifique des cellules RS et FS pendant différents états d’éveil et de sommeil, sélectionnés sans activité interictale. Jusqu’à 92 unités enregistrées simultanément, procurent une base solide pour la caractérisation de la dynamique de l’excitation et de l’inhibition pendant ces différents états. Pendant le sommeil lent (Stade III ou IV), dominé par les ondes lentes de type delta, tous les neurones déchargent selon des états “Up” ou “Down”, en relation avec les ondes lentes du LFP, comme décrit précédemment. Les cellules RS et FS sont toutes silencieuses pendant les états “Down”. Pendant le sommeil REM et pendant l’éveil, les neurones déchargent de façon irrégulière alors que le LFP ou l’ECoG sont désynchronisés. Dans tous les états les cellules FS déchargent plus que les cellules RS (4 ou 5 fois plus en moyenne). Ensuite, nous avons évalué les caractéristiques de chaque état en utilisant une procédure de classification automatique et analyse spectrale. En divisant les enregistrements en sommeil leger, sommeil profond, sommeil REM et éveil, nous calculons la fonction de transfert entre les neurones et le LFP pour chaque état. Nous estimons aussi le degré de corrélation des neurones, et l’étendue spatiale et temporelle de ces correlations, qui est la plus grande pour le sommeil profond. En conclusion, ces résultats démontrent que les relations entre unités et LFP dépendent de l’état cérébral, et sont consistantes avec les résultats publiés chez le chat et le rat.

8.3 Materials and Methods

Human intracranial recordings

Recordings were obtained from two patients with medically intractable focal epilepsy using NeuroPort electrode array as discussed previously [54, 260]. The array, 1mm in length, was placed in layers II/III of the middle temporal gyrus with informed consent of the patient and with approval of the local Institutional Review Board in accordance with the ethical standards of the Declaration of Helsinki. This array is silicon-based, made up of 96 microelectrodes with 400-μm spacing, covering an area of 4×4 mm. Since the corners are omitted from the array, the furthest separated contacts are 4.6 mm apart. Data were sampled at 30 kHz (Blackrock Microsystems, Salt Lake City, Utah, USA). The continuous recording was downsampled to 1250 Hz to obtain LFPs. The dataset we analyzed was devoid of any form of identifiable epileptic activity (such as interictal spikes), and there was no seizure in the analyzed dataset. The implantation site was included in the therapeutic resection in both patients. For details on spike sorting, see Peyrache et al. [260].

8.4 Figures

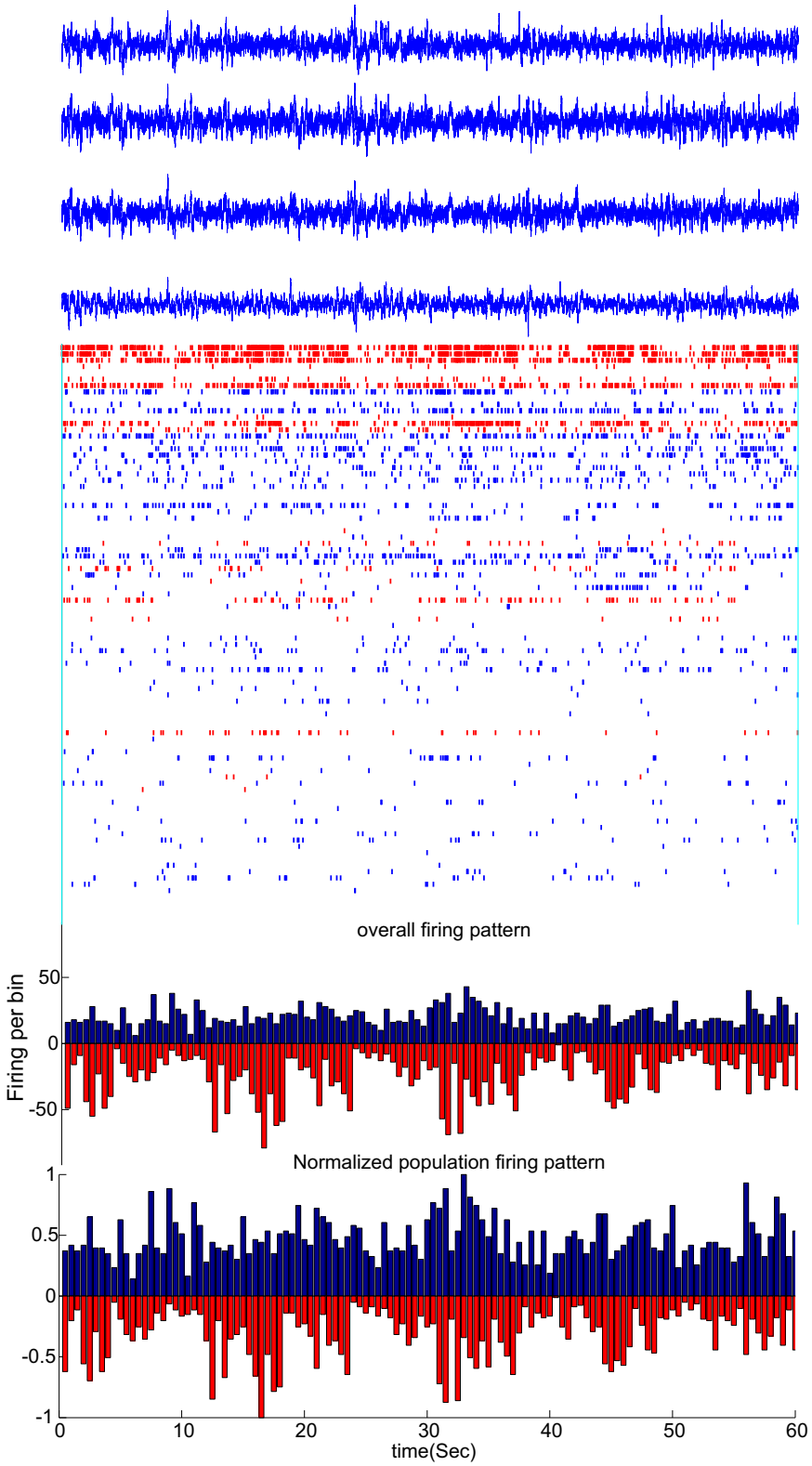

Figure 8.1. Relation between units and LFPs during wakefulness.

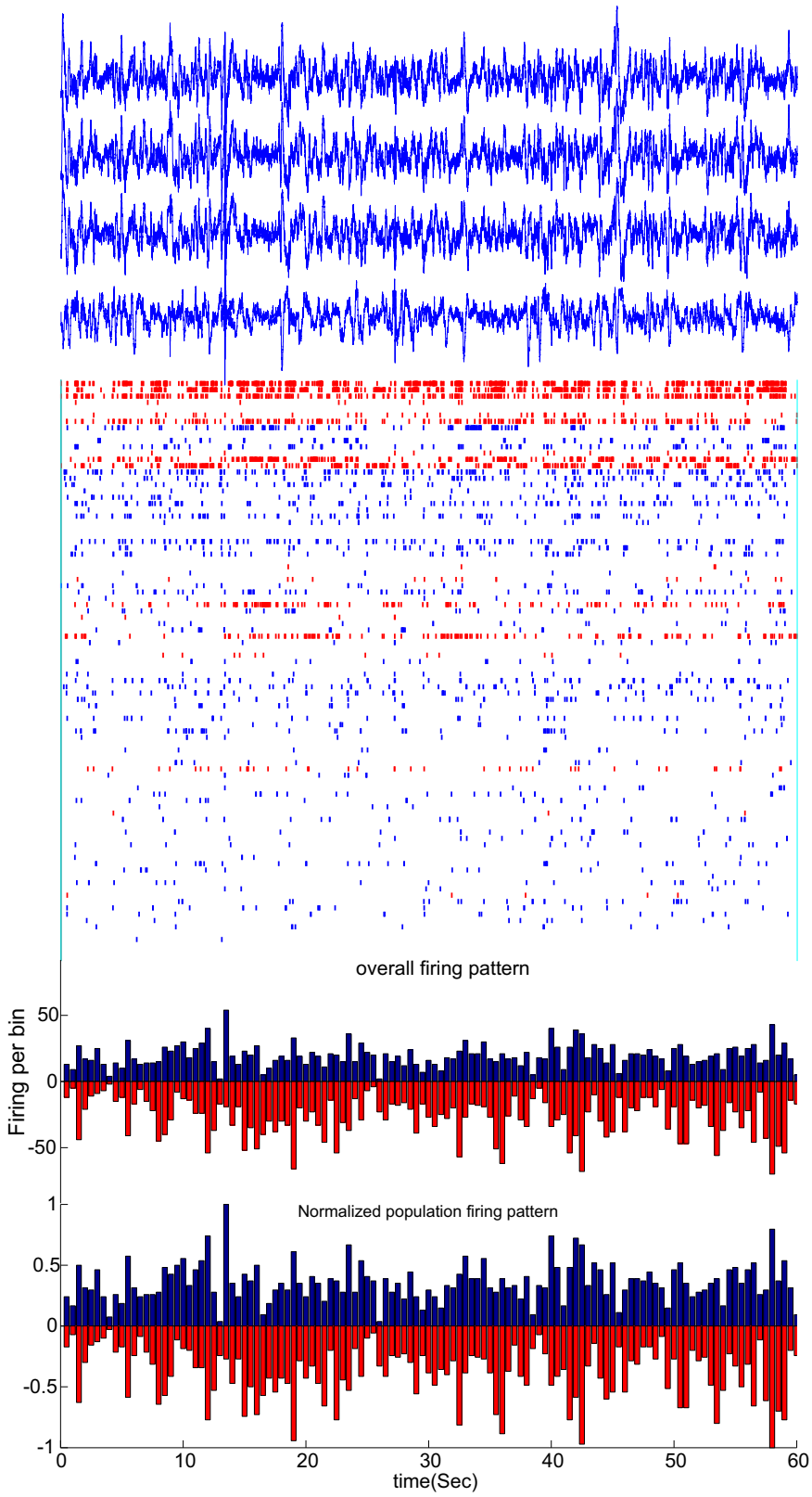

Figure 8.2. Relation between units and LFPs during light slow-wave sleep (Stage II).

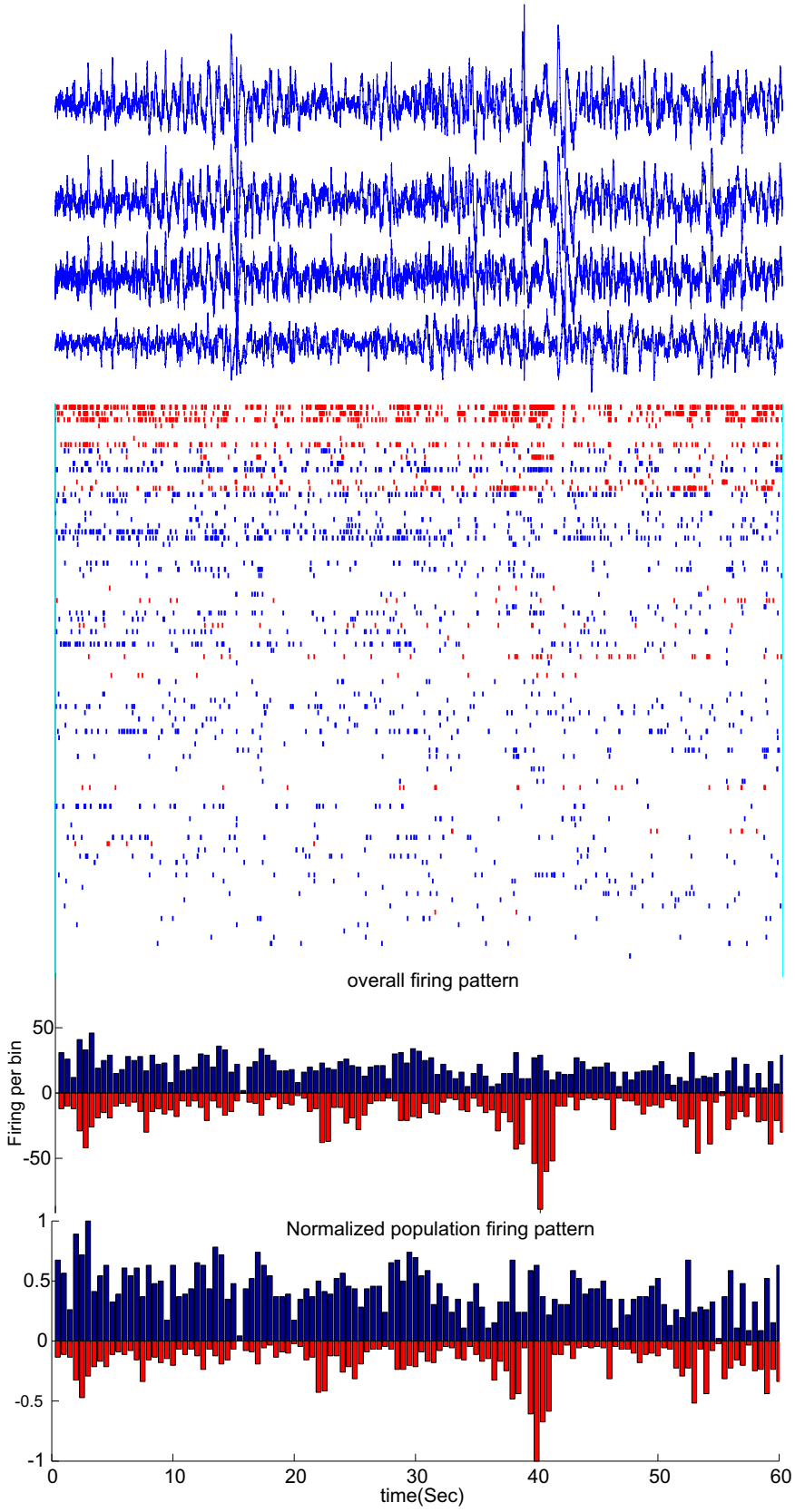

Figure 8.3. Relation between units and LFPs during deep slow-wave sleep (Stage IV).

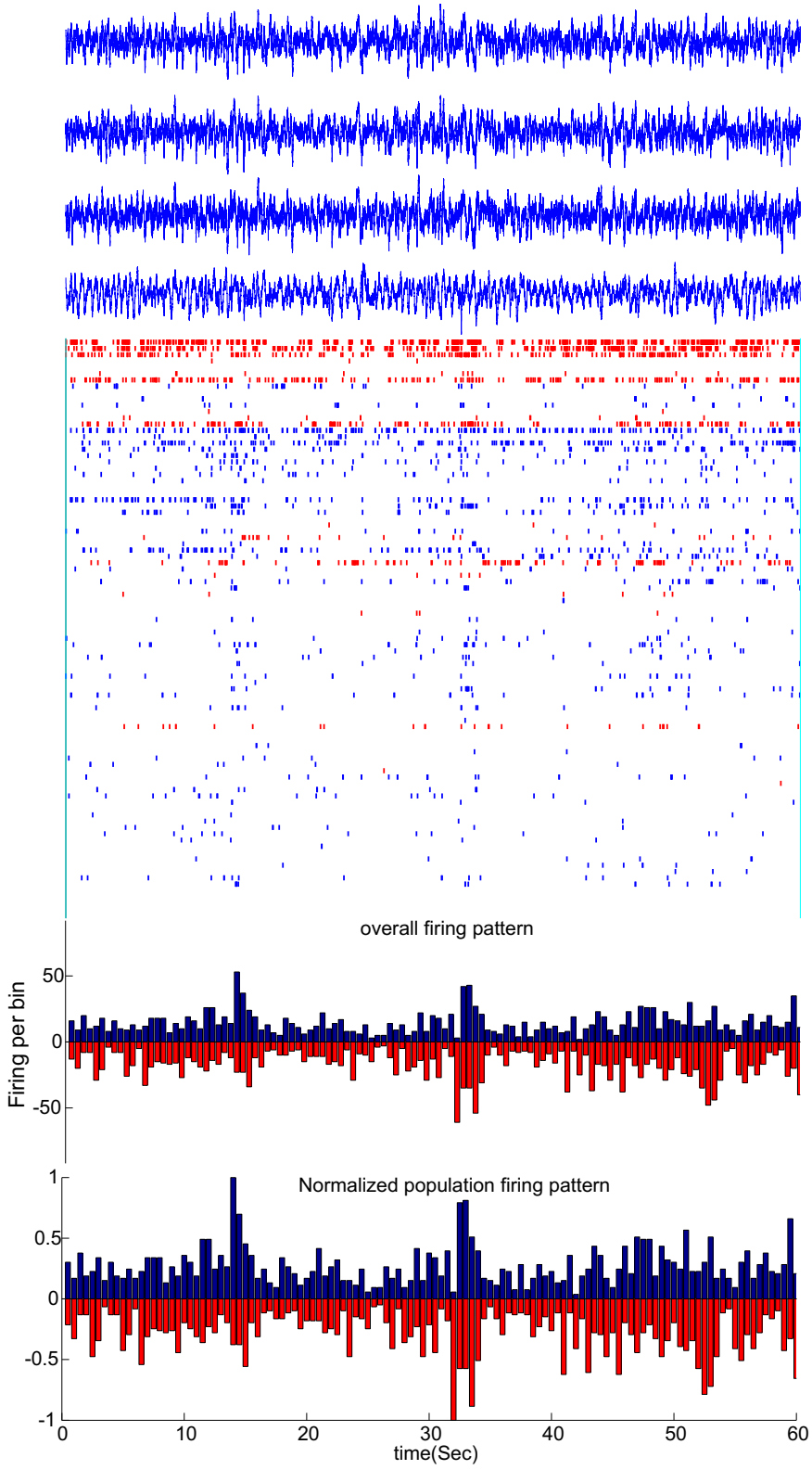

Figure 8.4. Relation between units and LFPs during REM sleep.

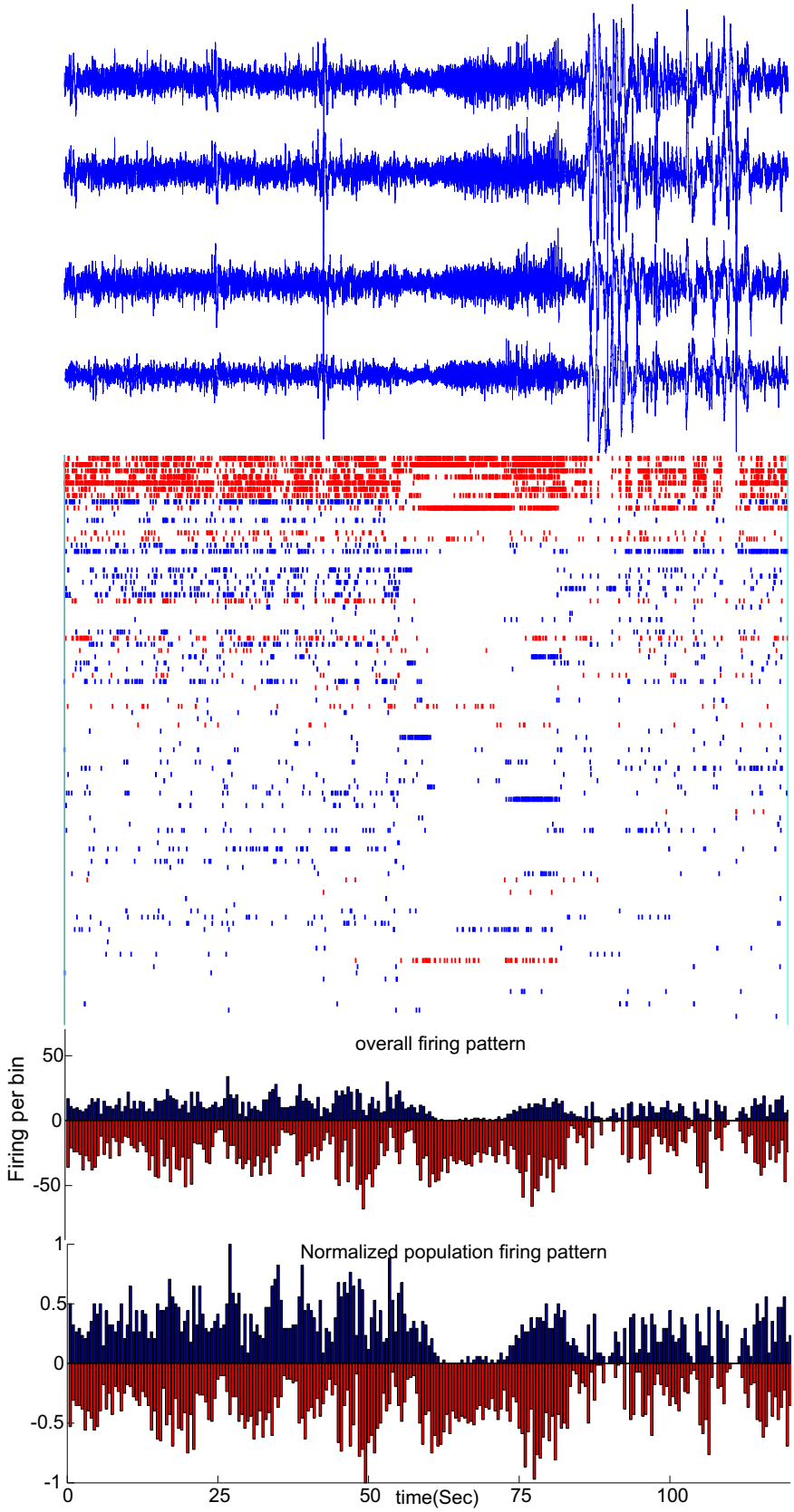

Figure 8.5. Relation between units and LFPs during a focal seizure.

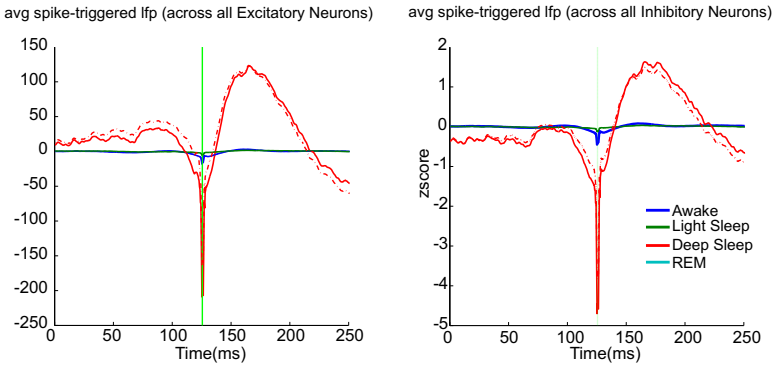

Figure 8.6. Relation between units and LFPs using spike-triggered averages (STA), during different brain states.

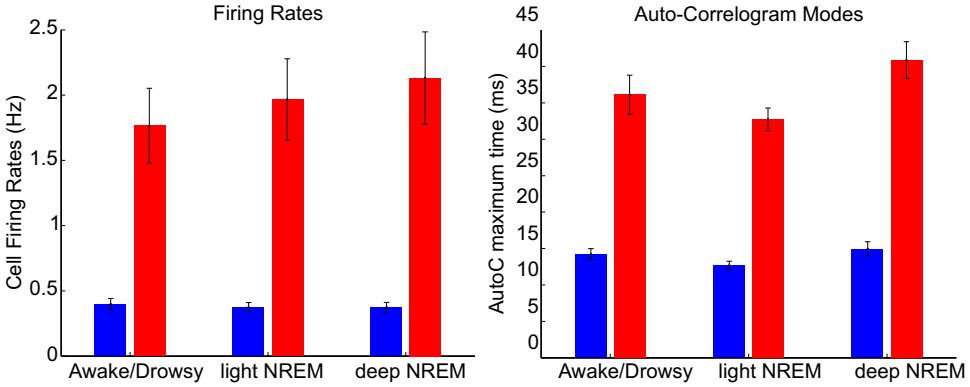

Figure 8.7. State-dependent descriptive statistics of FS vs. RS.

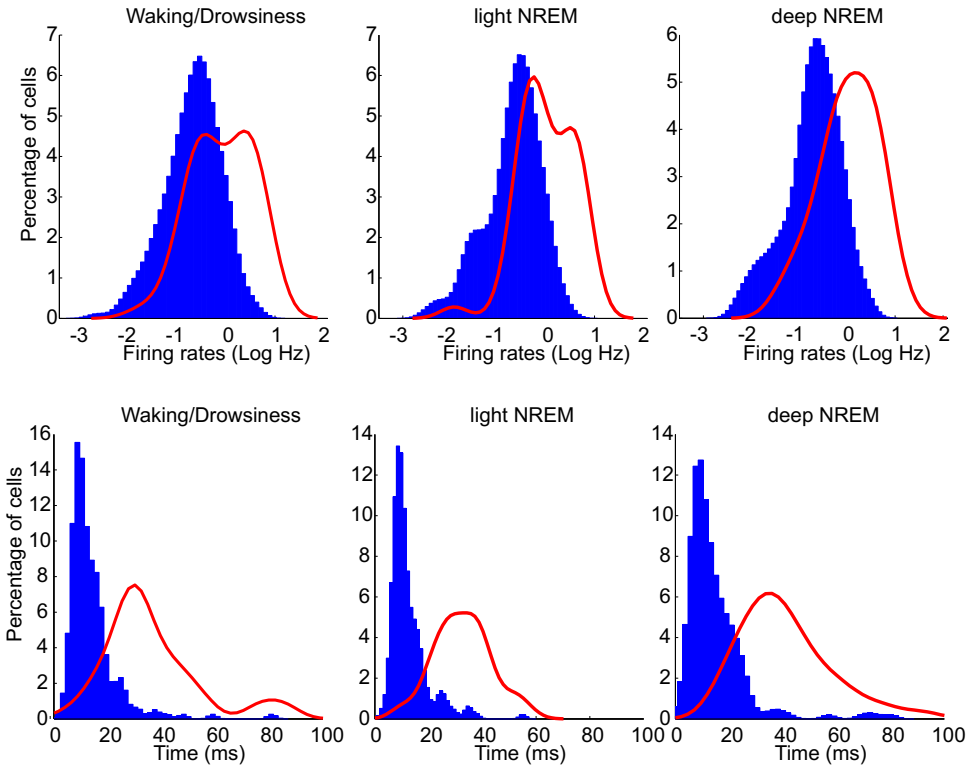

Figure 8.8. State-dependent firing probability. Density probabilities were computed from kernel smoothing density estimates of the actual data and displayed such that the sum over the whole displayed interval is equal to 100 for each group. Top row: in deep NREM, both firing rate distributions (FS in red and RS in blue) had a gaussian-like shape in logarithmic x-coordinates suggesting log-normal distribution for FS and RS cells. The FS cell distribution in Wake/drowsy as well as light NREM show possibility of bimodal characteristics. Bottom row: Distribution of auto-correlogram modes (time of maximum peak) for each group.

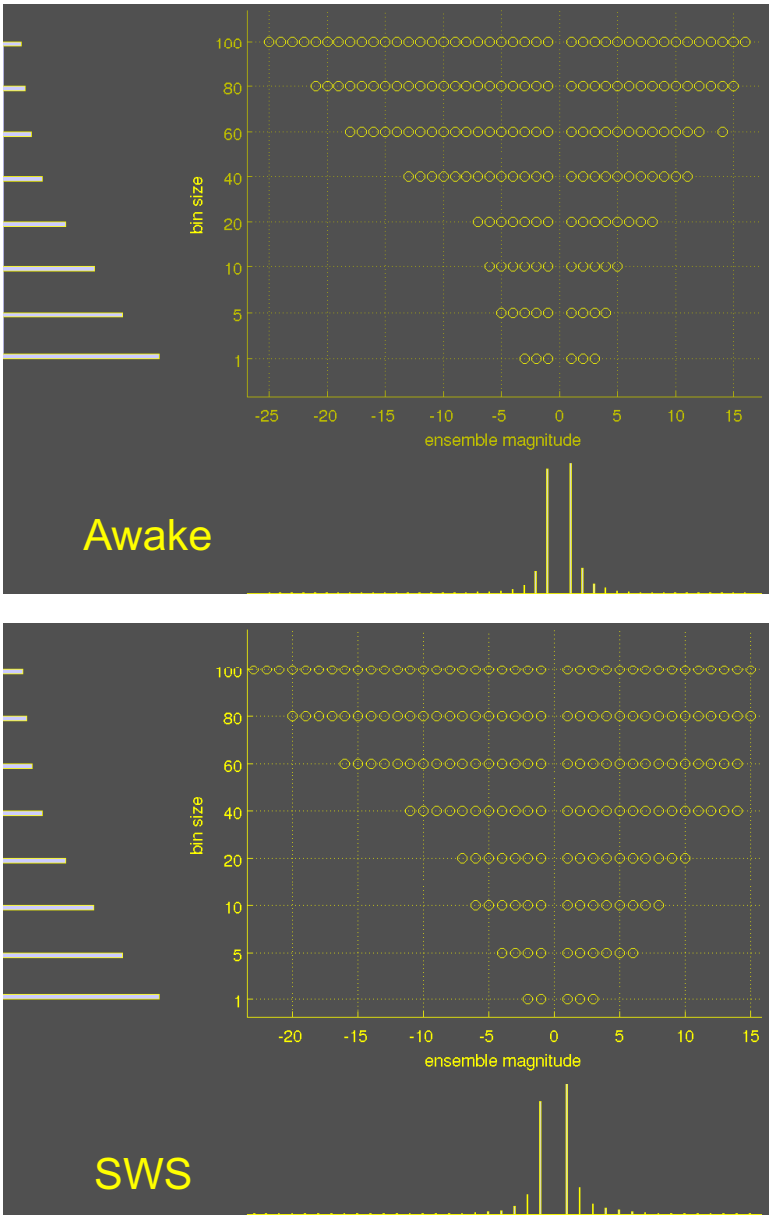

Figure 8.9. Multiscale dynamic excitation/inhibition balance: distribution of ensemble magnitude. Top:Awake, Bottom: SWS. Moving 30 sec windows, sliding in 1 sec steps, were used to characterize the dynamics of E/I balance. In each time step, the 30 sec window of the spike matrix was binned at multiple time-scales of 1, 5, 10, 20, 40, 80 and 100 ms. For each binned spike matrix, the ensemble magnitude of excitation and inhibition was calculated as the sum of all FS (or RS) spikes within that window. Scatter histograms, show how the magnitude range is distributed for FS (negative on x axis) and RS (positive on x axis). The range of the size of these ensemble magnitudes, seem to be in balance at all time scales. The L-R symmetry shows that ”distribution of ensemble magnitude” is similar for FS and RS for all scales. The pyramidal shape shows that as the scale increases, naturally, higher ensemble magnitudes are plausible and the range of possible magnitudes is wider. Similar pattern was observed for both awake and SWS.

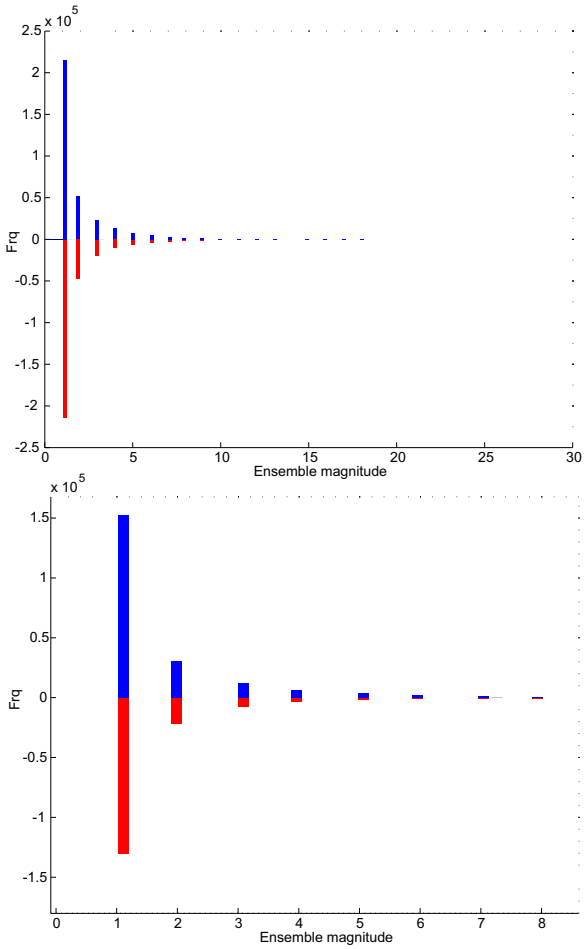

Figure 8.10. Multiscale dynamic excitation/inhibition balance: frequency of ensemble magnitude. Top:Awake, Bottom: SWS. The histogram count of different ensemble magnitudes (regardless of their time scale) is symmetrical for both FS (red) and RS (blue). Therefore the frequency of ensemble magnitude also seem to follow a balanced regime for both awake and SWS states.

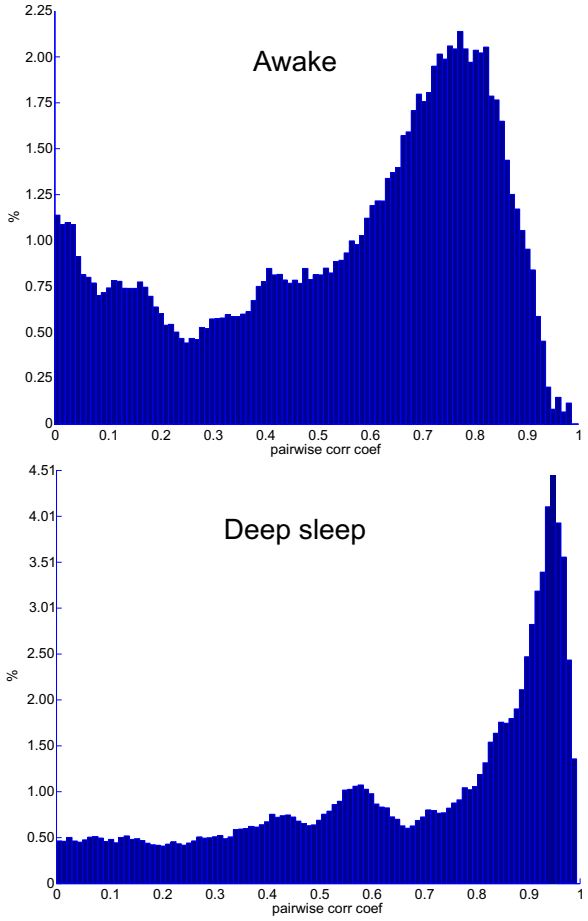

Figure 8.11. Dynamic pairwise-correlation of LFP. Top:Awake, Bottom: SWS. Moving 30 sec windows, sliding in 1 sec steps, were used to characterize the dynamics of LFP correlation. In each time step, pair-wise correlation coefficient among LFP channels was calculated. The values from all pairs, all time steps were pooled together to create the historgram distribution of dynamics LFP correlation. In case of SWS, the shift to the right of the histogram, shows an overall higher level of correlation within this 4mmx4mm patch of the cortex.

Part III

Discussion

Chapter 9

EEG/MEG Spectra

You can't say A is made of B or vice versa. All mass is interaction.

Richard Feynman

In Chapter 5, we have combined theoretical and experimental analyses to investigate the spectral structure of EEG and MEG signals.

9.1 Theoretical investigation of the frequency scaling of EEG and MEG signals

9.1.1 recount of biophysics

As discussed in chapter 2, in macroscopic modeling of MEG/EEG, the common practice is to assume that the cortex is composed of mini-columns or macro-columns [272]. In each of these elements, the vector sum of electrical activity is modeled as a current dipole [78]. It is hypothesized that such dipoles have the same biophysical roots. Given the structural organization of the cortex, when pyramidal cells in a given column are activated, the current passes through the apical dendritic structure toward the soma. This "impressed" current leaves the soma and "passively" returns to the superficial layers of the cortex [16, 76]. The magnetic induction caused by the impressed current is responsible for the MEG signal and the ohmic passive current is the source of EEG signal [8, 79]. If the activity within mesoscopic elements is synchronized, the approximated current dipole has a big enough amplitude that can be detected by distant electrodes.

The propagation of the electromagnetic source through the extracellular medium abides by the same principles that any electromagnetic wave would follow in its propagation through a volume conductor. By assuming that the extracellular is purely resistive, quasi-static Maxwell equations can be used to predict the propagation of the electromagnetic field generated by current dipoles. Given a set of sources, the precise prediction of their spatial spread, i.e. forward model, would rely on the volume conductor's geometry and conductivity. In defining the conductivity profile, the common practice is to neglect the capacitive effects, but leave room for possible inclusion of medium inhomogeneity and anisotropy if one decides to include more details in the model [77, 78]. In the numerical approach to the conductor modeling, whether one uses "Quasi-analytical solutions" [76, 89, 273], or relies on "Boundary element model (BEM)" [102, 157] or adapts "Finite element/volume model (FEM/FVM)" [166], the differences are only in piecewise details. In principle, by including more details, the computational cost adds up but the equations remain quasi-static. Based on these assumptions, the conductivity profile of the gray matter is similar for both MEG and EEG.

Other barriers, between the source and the sensor outside of the skull, include CSF, scalp and skull. It is known that electrical field is influenced by all these elements while the magnetic field is not [8, 16, 75, 77]. These barriers acting as spatial filters cause a smearing effect on EEG but not MEG. However, the spectral content of EEG and MEG should remain the same.

9.1.2 Theoretical assumptions

Our first study was formulated to explore these assumptions about the conductivity profile of gray matter and the negligible effect of other barriers on spectral content. In chapter 5, we start with theoretical formulation of the spectral density of MEG and EEG based on a purely resistive medium, and then follow with an experimental section testing the validity of such assumptions against the simultaneous measurements of EEG/MEG. Based on resistivity assumption, the frequency scaling of EEG and MEG signals should be similar. Based on our theoretical calculations, this conclusion is only valid in the linear regime, and for low frequencies. One of prerequisites of this phenomenon to be fully realized, is the assumptive independence of current densities at large scale. Therefore, the desynchronized state is the best matching experimental scenario to test this hypothesis. It has been shown that in such a state (a form of the high conductance in vivo) increased excitability of the neural membrane due to the synaptic bombardment is associated with the low correlation [31]. This situation results in focal activation, where at the micro-meso scale would lead to independence of the source [123].

9.2 Analysis of the frequency scaling of EEG and MEG signals

9.2.1 precisions and precautions

9.2.1.1 Optimal state

In the second part of the chapter, we have presented the scaling exponent analyses obtained from the PSD of simultaneously recorded EEG/MEG signals from four healthy subjects. In all cases, the recording were from the ”desynchronized EEG state”, awake with eyes open (which are the states at which our formalism best applies).

9.2.1.1.0.5 Data-driven optimized exponent estimation For automated and proper calculation of the frequency scaling exponent on large number of channels, we used a semi-parametric data-adapting ”B-spline” optimization method to obtain a smooth FFT without losing its frequency resolution. This method enforced criteria that would maximally improve the estimates from the low frequencies (which are the range at which our formalism best applies).

9.2.1.1.0.6 Multimodal topographical characterization of scaling exponent Due to the complex geometry of the volume conductor and differential sensitivity of MEG and EEG to orientation of the current dipoles, it is important to calculate the scaling exponent for all of the sensors (more is better) not a small group confined to a given region [as in studies such as [130, 131]. Naturally, the best case scenario is to compare the topographical maps of ”simultaneously” recorded MEG and EEG instead of limiting the analyses to only one modality (such as [221, 222]). Thus we relied on multimodal topographical characterization of scaling exponent to yield higher reliability.

9.2.1.1.0.7 Proper selection of the MEG sensor type Magnetometers measure the absolute magnitude of the magnetic induction and Gradiometers measure the gradient of the magnetic induction. Due to this property, a distant background source largely cancels at gradiometers. Therefore, these types of sensors are less noisy [8, 23]. This characteristic may prompt one to inadvertently estimate the scaling exponents from the spectral difference of magnetometers. This estimation is rationalized by the desire to mimic the higher SNR of the gradiometers and avoid spurious peaks [131]. Such a practice is improper because it fundamentally changes the spectral characteristics of the source and turns it into an approximated behavior of the gradiometers. Not only is this an uncontrolled approximation but also the gradiometers themselves are not the prime choice for the estimation of frequency scaling exponents. A better approach is

to use Magnetometers in a highly shielded room and apply ”spectrally” proper noise reduction methods to achieve reliability in the estimates. In the next section, we discuss such methods.

9.2.1.1.0.8 Noise correction As discussed in chapter 2, magnetic measurements are highly susceptible to the environmental and instrumental noise. While our data was recorded in a highly effective 6-layer magnetic shielded room [24], it is desirable to exclude the effects of the magnetic noise from the estimated scaling exponent. It is also shown that the MEG sensors may have different SNR characteristics depending on their relative location with respect to head [118]. In order to remove the noise effect, we developed a few measures of noise reduction based on the empty room recordings prior to the experimental session. As, a priori, the nature of noise was not known, each method was designed with a different source of noise in mind. In case of SQUID sensor noise induced $1/f$, a simple subtraction of scaling exponents was used to remove the effects of this filtering. In case of additive uncorrelated noise, spectral subtraction methods (linear, non-linear multi-band subtraction and Weiner Filter) based on the band-specific SNR information, would remove the frequency scaling imposed by the noise presence. To address general additive uncorrelated noise, partial least squares (PLS) was applied to help remove the noise based on its collective features.

9.2.1.2 Comparison with other studies

Prior studies have reported that, at low frequencies, EEG has a frequency scaling of $1/f$ [129, 134, 220]. Our findings showed that while (at low frequencies) EEG displays frequency scaling close to $1/f$, the spatial distribution of scaling exponents is not uniform. MEG showed significantly lower scaling exponents and it too had a non-uniform, but more complex, topographical map of scaling exponent. This variable topographical map could further be sequestered into 3 main regions: 1) a frontal area where the exponents had their highest values in the case of MEG 2) a central area where the values of exponents of EEG and MEG get closer to each other and 3) a parietotemporal horseshoe region showing the lowest exponents for MEG with bimodal characteristics.

Prior studies results each match with a subset of our observations [130, 131, 221, 222, 226]. However, as they were more methodologically limited, (as mentioned above and discussed in chapter 5) it is not clear how to relate their values to the ones obtained here. It is safe to say that the burden of the confirmation of our findings is upon future detailed and methodologically sound experiments. In summary, both uncorrected signals and empty-room correction show that there is a fundamentally different frequency scaling between EEG and MEG signals. Even in the light of different noise subtraction, the noise-corrected MEG showed a further distance from EEG in terms of frequency scaling exponent.

9.2.1.3 Mismatch of the quasi-static approximations with the experimental findings

The mismatch between the predictions of quasi-static approximations, and the complex variability of the measured scaling exponent of EEG vs MEG, shows that the original assumptions about the conductivity profile of gray matter and the negligible effect of other barriers on spectral content are improper. These findings are consistent with the hypothesis that the $1/f$ structure of the field potentials (EEG or LFP) is essentially due to a frequency-filtering effects of the extracellular medium due to the Warburg impedance caused by ionic diffusion [123, 134, 192].

9.3 concerns and future possibilities

9.3.1 Precise 3D geometric models

Complex spatial configuration of the sources and the differential sensitivity of the MEG and EEG signals to dipole orientation [114–116], remain as possible reasons for the different spectral behavior of EEG and MEG. The questions of whether the extent of spatial averaging of microscopic signals or the cancellation of sources of the walls of the sulcus due to their orientation disparity could affect the scaling of spectral density should be examined in the future studies adapting detailed 3D geometric models of the tissue.

9.3.2 Multiscale studies

Bypassing non-neuronal effects at very low frequency using invasive electromagnetic measurements is a possibility. Moreover, multiscale simultaneous recordings from an invasive method with a non-invasive one, like iEEG and MEG (as in [120]) could provide a chance to evaluate the effects of spatial correlation on spectral structure at a multiscale level.

9.4 Conclusion

These theoretical considerations and experimental analyses suggest that a purely resistive extracellular medium cannot explain the observed difference in frequency scaling of EEG. The $1/f$ structure of EEG with smaller scaling exponents for MEG is consistent with non-resistive extracellular impedances, such as capacitive media or diffusion (Warburg) impedances (see [63, 122, 192]) . If this non-resistive aspect of extracellular media is confirmed, it may influence the results of models of source localization, which may need to be reformulated to include more realistic extracellular impedances.

Chapter 10

Network dynamics

For it is the same whether you take it that the Earth is in motion or the Sky. For, in both the cases, it does not affect the Astronomical Science. It is just for the Physicist to see if it is possible to refute it. .

Abu-Rayhan Biruni

In Chapter 6, we used multielectrode array recording of cells from layer II/III of the of the middle temporal gyrus in epileptic patients. Details of the instrumentation are presented in Chapter 1. These high-density arrays, provide an opportunity to analyze the dynamics of the microcircuitry of a 4x4 mm patch of the cortex which is in the same order of magnitude as a cortical column. We used overnight sleep recordings to perform a detailed quantitative analysis of the spatiotemporal dynamics of excitation and inhibition in the human neocortex. The findings are categorically divided to: (i) robust morphological (based on the extracellular waveform features) discrimination of putative cortical excitatory and inhibitory neurons; (ii) in vivo evidence of functional monosynaptic connections in the human neocortex; (iii) functional behavior of inhibitory and excitatory cells during human sleep; (iv) distinctive spatiotemporal patterns of Pyr-Pyr and Int-Int assembly interactions; (v) detailed quantification of cortico-cortical correlations. Below, we provide an overview these findings.

10.0.1 Morpho-functional discrimination of putative inhibitory and putative excitatory units.

10.0.1.1 Morphological clustering of spike waveforms

It has been shown that the extracellular spike waveform may carry information about the functional characteristic of its generating cell. A short, fast-decaying action potential has been associated with Fast-spiking (FS) and GABAergic cells; therefore such characteristics are indicative of putative inhibitory neurons. A large and slower action potential depicts Regular-spiking (RS) and glutamatergic neurons, thus suggesting that the generator is a putative excitatory cell. The spike waveform features, along with firing rate characteristics, have therefore been used to discriminate FS and RS cells in various mammalian species, such as rats [39] and guinea pigs [241]. Using spike waveform features, later studies succeeded in separating FS and RS cells in human hippocampus [41, 247] as well as human neocortex [55, 56].

In our study, we computed the average waveform from each sorted cell. Then the waveform's ”half width” and ”valley-to-peak” were used in a K-means clustering algorithm to successfully separate the units into the two category of FS and RS. Selecting different pairs of waveform features, like ”valley-to-peak amplitude ratio” and ”valley-to-peak widths” or ”half-valley width” and ”valley-to-peak distance” also provided matching results. Moreover, a more sophisticated Expectation-Maximization (E-M) algorithm based on the Gaussian mixture models provided robust discrimination and confirmed the separation.

This segregation was consistent with several other cell intrinsic parameters of pyramidal and inhibitory neurons. For example, as anticipated, FS cells fire at much higher rates (five times higher than RS) while RS cells showed 64% bursting behavior (in comparison to the only 2% of FS). These two groups manifested different coefficients of variation (the ratio of the standard deviation to the mean of the interspike interval (ISI) distribution). Additionally, the autocorrelogram of putative inhibitory neurons showed a slow rising autocorrelation while putative excitatory cells had sharp autocorrelaograms. The two groups also had highly distinctive distributions of the mode (i.e., time of maximal values in the autocorrelogram). These characteristics match the known longer refractory period in the case of FS cells and shorter refractory period for the RS cells. Such properties may equip the inhibitory cells as members of an ensemble with longer memory of the immediate past events.

The ratio of the ”putative” excitatory (RS) to ”putative” inhibitory (FS) was 4 to 1 which is consistent with the known ratio between the pyramidal and inhibitory cells in the neocortex [143]. This finding is interesting because despite the assumption that larger pyramidal cells generate higher amplitude spikes (and thus are more easily detectable in the extracellular space), a random sampling within the dense multielectrode array's field of view detected both groups with sufficient reliability.

It has to be emphasized that not all excitatory cells have a narrow extracellular spike waveform signature. This issue seems to be especially clear in the motor cortex. In cats, in vitro [274], in vivo [275], and during anesthesia [276], it has been shown that pyramidal neuron exhibits a wide variety of spike durations and waveforms, including thin spikes. Similarly, evidence for thin spikes from a recent study in awake monkey secondary motor area [277] suggests that spike duration alone may not be a reliable tool property to discriminate interneurons and all types of pyramidal neurons in extracellular recordings. Perhaps the finding of these studies shows that the different functional cytoarchitecture of the motor cortex (morphology of cells, their density, modes of action and the composition of the extracellular tissue itself) and/or the specific layer of the cortex may play a role in how electrodes record the extracellular signature of action potentials.

10.0.1.2 Functional discrimination of units

Monosynaptic connectivity can be used as an evidence for the validity of the morphofunctional dichotomy within the network. Pairwise cross-correlograms can help characterizing putative monosynaptic connections [39]. Statistically significant temporal bias in the cell pair relative spike timing can be used as an indicator of putative monosynaptic connections [255]. For any given pair of units, excessive biased spikes occurring above/below a statistical thresholdwithin the short-latency ($<$4 ms) interval was the indicator of their monosynaptic functional connectivity. In the analyzed cross-correlograms, statistically significant peaks were considered as the functional signature of an excitatory monosynaptic connection from cell A to cell B. Conversely, statistically significant drops were interpreted as a sign for an inhibitory monosynaptic connection.

The distribution of the observed monosynaptic functional connectivity perfectly matched the morphological clustering of the two excitatory and inhibitory populations. The monosynaptic connectivity matrix was typically sparse (17%) and not different for excitatory or inhibitory units. Monosynaptic connections were almost entirely local (pairs recorded on the same electrode) for both populations. These observations have certain limitations based on the fact that the adapted method underestimates the number of actual functional connectivities based on its reliance on suprathreshold activity from pre- and post-synaptic neurons. The locality of the monosynaptic connectivity is in line with the fast distance-dependent decay of synaptic connections [143, 255]. The spatial extent of local monosynpatic connectivity is, however, still a subject of debate [235, 236]. Studying longer scale correlations showed that the units recorded from the same electrodes had higher functional connectivity with each other than with those recorded from other electrodes. This resonates with the hypothesis that connected units are more likely to form dynamic cell assemblies [49]. The observed morpho-functional dichotomy in our investigations enabled us to characterize the dynamic interaction of excitatory and inhibitory units, which is discussed next.

10.0.1.3 Functional balance of inhibition and excitation

Theoretically, it has been suggested that in a sparsely connected network, the seemingly irregular firing of cells could be the consequence of the excitation/inhibition (E-I) balance [250–252]. These theoretical predictions match with intracellular indications of a balance between excitatory and inhibitory conductance both in vitro [172] and in vivo [253]. Possible excess of inhibition in vivo has also been suggested [254]. Our extracellular analysis in chapters 6 and 8 represent indirect evidence in favor of E-I balance. The average firing rate for inhibitory neurons were five times higher than the excitatory neurons while the inhibitory cells were 4 to 5 times less common than excitatory cells. Thus it seems that total synaptic activity of the two populations are in an ongoing balance. Also, the lognormal distribution of the firing rates (for both populations), matches the theoretical prediction of heavy-tailed firing rate in sparsely connected networks [250].

10.1 Spatiotemporal dynamics of excitation and inhibition

Proponents of rate coding hypothesis have argued that the ample evidence for correlated cortical activity is not mirrored by a functional significance, and that the firing rate is sufficient for mediating perceptual binding [278]. In contrast, according to the temporal coding hypothesis, it has been suggested that the overall functional architecture along with coordinated spiking activity on a fine temporal scale is an essential property of the functioning brain [279]. What is neglected in the former claim is the detailed cytoarchitecture of the neocortex and the local spread of synaptic connectivity. What is missing from the later claim is the approximate balance of excitation-inhibition. Earlier studies have shown the existence of a distant-dependent pairwise correlation between MUAs. In addition, the spatial extend of the functional clusters was reported to match with the spatial organization of the sensory cortex contained by optical imaging [280]. The morpho-functional characterization of FS and RS units from the ensemble recordings gave us the opportunity to test the spatiotemporal extent of excitation and inhibition.

We found that the excitatory cells show a distant-dependent correlation whereas inhibitory cell pairs were equally correlated with both proximal and distal electrodes over spatial extent of the array. Our findings were later confirmed by an in vitro study reporting that, in contrast to RS neurons, FS interneurons correlation was not distant dependent [281]. We also noticed that in the case of excitatory cell pairs, as the timescale (bin size) increased, the modulation of the spatial extent decreased and the correlations tended to equalize irrespective of the distance between the units.

These results have strong implications for our understanding of cortical network dynamics, particularly with respect to the spatial extent of E-E correlation with the axonal arborization of the excitatory units of the human hypercolumn. Interestingly it is known that this spatial extent

of arborization is more evident in the primary sensory cortices than the higher order areas, like the examined temporal neocortex in our study [143]. In contrast, common subcortical inputs over large neocortical areas impinging directly onto GABAergic [80, 97] could be the result of the observed large spatial extent of inhibitory correlations. This finding shows that what is neglected in the rate coding hypothesis [278] is a major property of the cortical microcircuitry. The tendency of the correlations to equalize at longer timescales, along with the E-I balance measures (presented in Chapters 6 and 8) are reflective of the approximate balance of excitation-inhibition; this concept is missing from the temporal coding hypothesis [279].

In studying the spatiotemporal dynamics in different wake/sleep states, we also found that the distance-dependent E-E relationship decreased during deep NREM (non-REM) sleep. Although this distance-dependent property still remained statistically significant. From the mesoscopic or macroscopic field potentials, i.e. LFP and EEG, we know that during the slow-wave sleep, functional units orchestrate over large areas [238, 256], while during desynchronized state, neocortex manifests low spatial correlation [174]. The fact that SWS is matched with ”long time scale dynamics” and that desynchronized state show characteristics of ”short time scale dynamics” gives us a hint that functional units of the cortex are capable to operate in different modes. In addition, along with the intricate group-specific spatiotemporal connectivity of excitatory and inhibitory cells, some neurons are capable of reaching very distant areas and could produce large-scale synchronization of the inhibitory network [33]. Also, different thalamocortical (core and matrix) projections could recruit more focal or widespread cortical areas [26, 98, 102]. If cognition and feature binding is needed, perhaps the system tends to use a mode that rapidly but specifically recruits the proper excitatory cell. It is the task of the interneurons to balance the network in terms of the temporal and the spatial extent of excitation. In such a scenario, temporal and rate codes are two sides of the same coin, where one morphs into another depending on the required computation.

10.2 Limitations

Our study was based on recordings from epileptic patients. Although the selected segments were void of epileptic activities, there is a possibility that the studied tissue is not cytoarchitecturally and/or functionally normal. However, studying the E-I balance in the seizure and the preliminary findings of E-I disturbance during seizures (Chapter 8) may hint that the studies tissue may functionally behave normal except at the time of seizures when the whole network is pushed out of balance.

10.3 Conclusion & future directions

Our study not only extends some of the prior work in animal literature to the human cortex but also provides novel characterization of the dynamics of the neocortical microcircuitry. The observed large-scale synchronized inhibition, along with the more focal synchronized excitation and their variable characteristics at different time-scales and conscious states, serves as an initial step toward better understanding the intricate dynamics of the neural network computation. Extension of these findings to the study of cognition, sleep and seizures will help to better see the ever evolving spatiotemporal dynamics of the brain.

Chapter 11

Avalanche dynamics

A cloud is made of billows upon billows upon billows that look like clouds. As you come closer to a cloud you don't get something smooth, but irregularities at a smaller scale.

Benoit Mandelbrot

The dynamics of SOC systems are structured as "avalanches" of activity, separated by silent periods. Avalanche sizes are typically distributed as a power law, which is particularly interesting for the scale invariance it presents. In Chapter 7, we have analyzed and compared the avalanche dynamics obtained from multielectrode recordings of spikes and LFPs, for three species: cat, monkey and human. In each case, we used recordings exclusively made in non-anesthetized brain states, including quiet and active wakefulness, SWS (slow-wave sleep) and REM (Rapid eye movement). In monkeys, we had the opportunity to, simultaneously, record from two different patches of the cortex. In all cases, we used Utah-type multielectrode arrays. The details of the instrumentation are described in Chapter 1.

11.1 Avalanche dynamics from unit recordings

Previously, it had been shown that awake spike avalanche dynamics do not show power-law characteristics [134]. This study was criticized as having poor spatial sampling (only 8 electrodes, arranged linearly with contacts far from each other for properly characterizing avalanche dynamics). In our study, we used the significantly higher density two dimensional arrays.

Whether the recordings were from “desynchronized” EEG states (wakefulness), SWS, and REM sleep, we found no evidence for meaningful power-law scaling in the neural avalanches. This was the case for all three species.

11.2 Avalanche dynamics from LFP recordings

In evaluating LFP avalanche dynamics, we not only evaluated negative LFP (nLFP) peaks, but also analyzed positive LFP (pLFP) peaks. Additionally, for each of these polarities, we used numerous thresholds to discretize LFP in order to create an avalanche matrix. Our analyses for LFP avalanche dynamics was only done in awake state. In some cases, the subject was in idle wakefulness and in others they were engaged in a cognitive/motor task.

In contrast to spikes, analysis of nLFP avalanches displayed slightly variable results. In the log-log representation, some cases appeared not to follow a straight line and therefore could not be considered to have power-law distribution. Others, however, appeared to distribute close to a power-law in such representation. Albeit, when these cases were tested with stringent statistical tests (CDF-based evaluation of power-law in empirical datasets), they did not show clear evidence for meaningful power-law scaling. It is considered that nLFPs have a closer tie to cell spiking activity. This factor, along with the reported power-law scaling of nLFP in vitro, has been taken as evidence of self-organized criticality in the neural dynamics [135]. If that were the case, pLFPs (which are not as tightly related to neural firing) should not scale as a power-law. If pLFPs scale as a power-law as nLFPs do, then such scaling is a spurious one and is the result of something else rather than self-organized criticality. Based on the above argument, we also tested pLFPs from the three species at different thresholds and at different time scales. The results were similar to the findings drawn from the analyses of nLFP avalanches, in that in some cases pLFPs did not scale as power-law and other cases they did scale as power-law but with estimated exponents that were not meaningfully relevant to self-organized critical systems.

Given these findings, it is necessary to provide a comparative analyses of the relationship between spiking and the LFP peaks. Comparing nLFPs vs pLFPs showed that the former had a closer relationship with spike timing. We then used 4 methods of surrogate/randomization in order to evaluate the statistical robustness of the comparative relation of spike-nLFP vs spike-pLF. Each of these randomization methods tested a specific property of spike/LFP distribution : i) using Poisson surrogate data, we tested whether the observed nLFP and pLFP differences could be reproduced by surrogate spike series, ii) Random permutation was used to verify that randomizing the aggregate spike series by itself cannot mimic the observed the LFP-spike relation, iii) Local jitter randomization was used to evaluate the effects of randomization based on the statistics of the individual channel’s LFP peak times (before aggregating them into the ensemble LFP peak train) of LFP peaks, and iv) Fixed-ISI circular shift of spike was applied todestroy the relation between ensemble spikes and ensemble peaks while preserving their in-

ternal structure. All these test confirmed that the fundamental differences in the comparative nLFP-spsike and pLFP-spike relationships are not attainable from randomness of spikes or LFP peaks. Together, these findings show that basing self-organized criticality on the power-law scaling of pLFPs is not proper as it seems that such observations are phenomenological rather than depicting true nature of the underlying computation in the neural tissue.

While it is imperative that findings of some earlier studies be revisited and tested with more robust statistical methods, the evidence for power-law distribution (and the conclusion of self-organized criticality based on that) from in vitro [135] or anesthetized state [182] match our understandings about the natural differences of functional organization in comparison with in vivo non-anesthetized brain. Additionally, a recent report has shown that collapsing avalanches (from high density in vitro recordings) show elements of universality [270], a feature that is better tied to self-organized criticality. These observations do not contradict our results from in vivo non-anesthetized cortex in that the wiring of *in vitro* preparations are fundamentally different from the in vivo situation [30]. In addition, the network dynamics in anesthesia are much different from the high conductance state [31]. On the other hand, our results do contradict the report of power-law scaling of nLFPs avalanches in awake monkeys [183]. The scope of that study has been more limited in terms of i) the density of the electrodes and number of independent recordings of LFP and spike andii) the statistical rigor. Additionally, there are other possibilities that could reconcile these different observations, such as differences between the examined brain region, recording method, cortical layer or volume conduction effects.

11.3 Methodological considerations

In the search for the power-law in empirical data, using CDF distribution is statistically much more superior to the simple log-log representations of the size distribution [201, 261]. Additionally, the Kolmogorov-Smirnov test is also largely superior to the least square for fitting a distribution to an empirical data [201]. It is also important to note that in using CDF-based KS test, one can force the scaling exponent to fall within the range of the plausible values. After such practice, and if the scaling exponent passes statistical significance testing, naturally, the yielded scaling exponents will have values comparable to those in known self-organized natural systems. However, it is the range of the data that has to be sacrificed in order to achieve these ”acceptable” (from self-organized criticality point of view) exponent values. The only scenario that will not impose any trade-off between the range of the data and the plausible scaling exponent of SOC systems, is when the system universally scales across all the decades of its events.

In our analyses, we adapted the CDF-based KS testing of power-law. We opted to conserve more decades of the avalanche sizes in order to better understand the avalanche dynamics at the operating scales of the brain. Therefore, we did not force scaling the exponent range to be

limited to that of the known SOC systems (i.e 1-2). Therefore, in cases where the data was fit with a proper power-law, examining of the scaling exponent value becomes essential. In such situations, the obtained exponents were orders of magnitude higher than those of the SOC systems. Therefore, we claim that the power-law was non-existent or meaningless.

Conversely, some may opt to sacrifice the range in order to obtain desirable scaling exponents. This is exactly the approach that was adapted by Klaus et al [259]. In their approach, they limit the range of the data between 1 and maximum number of independent observations. Based on this range, they claimed that the power-law was performing better than exponentials in describing the avalanche distribution. Therefore, we tested our data in a similar fashion and found that setting such lower and upper bounds can introduce biases in favor of power-law fits. However, while power-law outperformed exponential, none were a proper fit for the avalanche data. We further showed that the avalanche data can be very well fit with a bi-exponential distribution. Of course this was done with statistical rigor to prove that the added coefficients are not the reason behind the fit improvement. This finding could be in line with the fact that the two populations of excitatory and inhibitory neurons, both could have their specific exponential distribution and therefore the conjoint ensemble reflects properties of the two system as one bi-exponential process. Moreover, our results show that there is a possibility that avalanche dynamics follow a multi-scale regime.

11.4 Future directions

One of the shortcomings of the LFP avalanche analysis is that it ignores the volume conduction and the spatial reach of the LFP altogether (for details on these biophyscial characteristics of extracellular recordings, see Chapter 2). In high density arrays, peak detection at a given recording site, is usually accompanied closely at different channels. Therefore, it is essential to theoretically and experimentally test the possibility of volume-conduction contribution to the avalanches. Additionally, it would be interesting to test whether the data can be collapsed into a universal scaling function [271].

Chapter 12

Grand conclusion

More is different.

Philip Anderson

The fundamental differences between the analysis of neurophysiological measurements and other non-biological or biological time-series are twofold, a) neurophysiological measurements contain information encoding dynamics and b) the dimensionality of neural data is many orders of magnitude larger than that of the other types of time-series. With the birth and rapid development of high throughput neural data, recorded by miniaturized devices, we are facing new challenges. There is an increased necessity to develop methods that are capable of unraveling the inherent complexity of biological systems as observed in multidimensional data. At the same time, this provides us the opportunity to adapt new methods and create algorithms that would help to detect the emergence of disorders of neural networks or evaluate the functional dynamics of their modification through the course of medical intervention.

In this thesis we have taken a multimodal approach to analyze the observed brain dynamics. Our multiscale experimental methods included large scale recordings including non-invasive methods at the macro-scale, i.e. EEG/MEG, at invasive large scale recordings at meso-scale, i.e. ECOG (electrocorticogram), and at micro-scale high density 2-D multielectrode arrays (for recording from a small patch of cortex). It is essential to use a multiscale approach to understand the system better and predict its behavior with higher accuracy. Whether we are interested in unraveling the mysteries behind cognition, or we wish to predict seizure or devise brain-computer interfaces, studying the system at its multitude modes of operation (ranging from desynchronized state to SWS and other states of consciousness) and at different levels of resolution is to the key to understanding and harnessing the complexity of the brain.

Brain shows a complexity unseen in other systems. Partly, this complexity is a reflection

of computation at multitude of levels. Other face of the brain complexity roots in the fact that as the registration and process of information happens at one scale, it transcends to the other scales. This creates an information processing system that is ever changing dynamically. ”How these system-wide changes happen across the different scales?”; this is one of the key questions in the daunting task of unraveling the mysteries behind the intricacy of neural computation. There is no doubt that only the simultaneous measurements across many scales can show us the right answer. However, technically, such task is still ahead of us. Surly, with the future advancements, it will be feasible to study the computation at many scales at once. At the time being, we can approach this problem through indirect ways. One way to find such links would be to investigate a certain type of information processing through parallel studies at multiple scales. For example, one can study facial recognition using macro-scale recordings (like EEG or MEG) and then, separately, he could repeat the same experiment while recording LFPs or spikes in the region of interest. Then, by combining the information, he could arrive at a detailed picture of that specific brain function. Such an approach is good for pinning down the properties of information processing behind a certain functionality of the brain. The other approach, which we adapted, is to find the links that reflect the nature of large-scale organization of neural computation. This body of work investigates the state-dependence of organization of computing characteristics of the brain.

It is now understood that the neural doctrine of Ramon y Cajal is not sufficient to tell us how the brain works. In the last decade, the nature of network computation at micro-scale and large-scale network interaction at macro-scale have became the subject of active research in neuroscience. By adapting a multi-scale multi-modal approach, we have a chance to combine details obtained from these different angles and construct theories that integrate microscopic models (that track the details of the system) with macroscopic ones (that track the global dynamics of the system). In parallel to dynamic assessment of multiscale neural complexity, it is essential to bind them together in a cohesive manner. The adapted modalities in our work are indeed complementary, each having a unique vantage point. The differential sensitivity between EEG and MEG to core and matrix thalamocortical projections provide valuable information about synchrony and recruitment vs asynchrony and fragmentation of neural networks. But how does the brain orchestrates its many scales of computation into one unique functional structure? Investigating the possibility of spectral self-organization, long-term state-dependent spatiotemporal dynamics at microscale and the avalanches at micro and meso level help to decipher how the system is governed. In this thesis, we have shown that the spectral characteristics of MEG and EEG have fundamental differences in their characteristics. In contrast to the prior belief, we show evidence to the contrary of self-organized criticality in large-scale spectra. The findings were suggestive of a highly complex pattern of spectral features (at the studied frequencies) that are reflective of the dynamics oscillatory aspects of cortex as well as the nature of the medium. It suggest that while the system may be communicating en-large through rhythmic activity, the controlling elements are not all summarized in near a phase transition. This temporal characteristic of self-organization at the spectral regime was mirrored by our investigation of the spatial

avalanches at the other end of the computing scale, i.e. spiking activity, and at the mediator stage, i.e. the avalanches constructed from the local field potentials. The studies of avalanche dynamics show us that neural networks of the brain may operate in a multi-scale regime rather than in punctuated equilibrium. In this study, we suggest that the dynamics are best predicted if one assumes that multiple processes interact with each other and form the future computational connectivity of the system rather than being pushed back to the phase transition zone each time a perturbation (here, information processing) occurs. Our study on microcircuitry is a step toward better prediction of the spatiotemporal dynamics of information flow within the neural networks. The rich dynamics of the two populations, i.e. excitatory and inhibitory neurons, and their distinctive spatiotemporal correlation characteristics show that the cortex, fine tunes its state-dependent activity through focal computing excitatory elements controlled by a more wide-spread inhibitory force. It is the constant interplay between these two systems that shapes an ongoing balance between the systems while providing the playground for instant response to the incoming stimuli and replay of information.

Bringing these findings under the same roof will enable us to better understand how the computation at a multitude of scales emerges from the interaction of the units with each other within their medium and how the medium affects the way the information is encoded within the network. In summary, we found no evidence for global features of self-organized critical dynamics at the levels that we have investigated. However, our results show that self-organization may emerge through other routes. It could be that large-scale rhythmical activities recruit the individual elements into a cohesive action. But it has to be emphasized that speaking of "individual elements" does not just simply translate to a semi-departure from the neuron doctrine by scaling up the size of functional units from the individual neurons to, for example, a hypercolumn. The observed rich spatiotemporal dynamics in our studies and the emerging evidence from other investigators guide us to a new doctrine in which the functional elements are not rigid and predefined. But perhaps, the state-dependent oscillatory and rhythmic activity recruit ensemble of neurons, tune them for the action that itself generates the forthcoming rhythmic activity. Self-organization happens within a dynamic environment where it is influenced by the medium's physical characteristics and limitations and influences the components of the system. But where are the switches for controlling this self-organization? We suggest that perhaps the interplay of excitatory and inhibitory elements (again we wish to emphasize that by element we mean a dynamic collection of individual neurons and their surrounding medium and perhaps glia) is they key element. It is through the interaction of multiple exponential processes that the inhibition and excitation mutually control each other and the fate of the neural network. We suggest that the coupled oscillator network models of interacting excitation and inhibition should reproduce these findings. To what degree such abstraction could reflect the dynamics of the system, is a challenge for future work.

Theories built upon multimodal, multi-scale investigations and computational studies, will help pave the way for quantitative medicine. By adapting a multi-scale multi-modal approach, one can create a dynamic algorithm that would search for patterns in multidimensional space

of high throughput neurophysiological data. Such algorithms would detect any perturbation that could lead to the abnormal behavior of the system as changes in its fractal dimensionality and complexity emerge. My expectation is that, in the near future, this work will be directly applicable to an anticipatory device. These types of anticipatory devices are critical because they will stand as one of the pillars of modern medicine and will prove to be inseparable from therapeutical control of biological networks. We are at the infancy of unraveling the mysteries of biological computation. The bits of a constantly morphing computing environment perhaps are not limited to a series of units that their dissociation or integrations would create a less or more sophisticated being. It is the emerging ascent of bits of interacting elements that truly defines the complexity of the system. Surly as Philip Anderson said, “more is different”; but in our case, it is the emerging information processing through multitude of scales that transcends us from being to becoming.

Part IV

Bibliography

Bibliography

1. M.A.B. Brazier. *A history of the electrical activity of the brain; the first half-century.* Macmillan, New York, 1961.

2. L.A. Geddes. Historical perspective Electroencephalography. In Joseph Bronzino, editor, *The Biomedical Engineering Handbook, Volume 2*, chapter 5, pages HP 5–1 to HP 5–7. CRC Press, Hartford, second edition, 2000.

3. T F Collura. History and evolution of electroencephalographic instruments and techniques. *Journal of clinical neurophysiology : official publication of the American Electroencephalographic Society*, 10(4):476–504, October 1993.

4. B E Swartz and E S Goldensohn. Timeline of the history of EEG and associated fields. *Electroencephalography and clinical neurophysiology*, 106(2):173–6, February 1998.

5. Hans Berger. Über das Elektrenkephalogramm des Menschen. *Archiv für Psychiatrie und Nervenkrankheiten*, 87(1):527–570, December 1929.

6. S. Finger. *Origins of Neuroscience: a history of explorations in brain function*. Oxford University Press, New York, 1994.

7. L F Haas. Hans Berger (1873-1941), Richard Caton (1842-1926), and electroencephalography. *Journal of Neurology, Neurosurgery & Psychiatry*, 74(1):9–9, January 2003.

8. Matti Hämäläinen, Riitta Hari, Risto J. Ilmoniemi, Jukka Knuutila, and Olli V. Lounasmaa. Magnetoencephalographytheory, instrumentation, and applications to noninvasive studies of the working human brain. *Reviews of Modern Physics*, 65(2):413–497, April 1993.

9. A.A. Ioannides. Magnetoencephalography (MEG). In Fahmeed Hyder, editor, *Dynamic Brain Imaging Multi-Modal Methods and In Vivo Applications*, chapter 8, pages 135–166. Humana Press, 2009.

10. A.A. Ioannides. Magnetoencephalography. In Marc Binder, Nobutaka Hirokawa, and Uwe Windhorst, editors, *Encylopedia of Neuroscience*, pages 2225–2229. Springer-Verlag, Berlin, 2009.

11. A.M. Ivanitsky, G.A. Ivanistky, A.R. Nikolaev, and O.V. Sysoeva. Electroencephalography. In M.D. Bider, N. Hirokawa, and U. Windhorst, editors, *Encyclopedia of Neuroscience*, pages 1067–1072. Springer-Verlog, Berlin, 2009.

12. Robert M. Chapman and Henry R. Bragdon. Evoked Responses to Numerical and Non-Numerical Visual Stimuli while Problem Solving. *Nature*, 203(4950):1155–1157, September 1964.

13. S. Sutton, M. Braren, J. Zubin, and E. R. John. Evoked-Potential Correlates of Stimulus Uncertainty. *Science*, 150(3700):1187–1188, November 1965.

14. John. Polich. Updating P300: an integrative theory of P3a and P3b. *Clinical neurophysiology : official journal of the International Federation of Clinical Neurophysiology*, 118(10):2128–48, October 2007.

15. M Kutas and S. Hillyard. Reading senseless sentences: brain potentials reflect semantic incongruity. *Science*, 207(4427):203–205, January 1980.

16. E. Niedermeyer and F.H. Lopes da Silva. *Electroencephalography. Basic Principals, Clinical Applications, and Related Fields.* Williams and Wilkins, fifth edition, 2005.

17. D Cohen. Magnetic fields around the torso: production by electrical activity of the human heart. *Science (New York, N.Y.)*, 156(3775):652–4, May 1967.

18. D Cohen. Magnetoencephalography: evidence of magnetic fields produced by alpha-rhythm currents. *Science (New York, N.Y.)*, 161(3843):784–6, August 1968.

19. J. E. Zimmerman. Design and Operation of Stable rf-Biased Superconducting Point-Contact Quantum Devices, and a Note on the Properties of Perfectly Clean Metal Contacts. *Journal of Applied Physics*, 41(4):1572, March 1970.

20. D Cohen. Magnetoencephalography: detection of the brain's electrical activity with a superconducting magnetometer. *Science (New York, N.Y.)*, 175(4022):664–6, February 1972.

21. J. Malmivuo and R. Plonsey. *Bioelectromagnetism - Principles and Applications of Bioelectric and Biomagnetic Fields*. Oxford Press, New York, 1995.

22. Myriam Pannetier, Claude Fermon, Gerald Le Goff, Juha Simola, and Emma Kerr. Femtotesla magnetic field measurement with magnetoresistive sensors. *Science (New York, N.Y.)*, 304(5677):1648–50, June 2004.

23. D. Cohen and E. Halgren. Magnetoencephalography. In LR Squire, editor, *Encyclopedia of Neuroscience, Vol. 5,*, pages 615–622. Academic Press, Oxford, 2009.

24. D Cohen, U Schlapfer, S Ahlfors, M Hamalainen, and E Halgren. New Six-Layer Magnetically Shielded Room For MEG. In H. Nowak, J. Haueisen, F. Giessler, and r. Huonker, editors, *Biomag 2002: Proceedings of the 13th International Conference on Biomagnetism,*, pages 919–921, Genna, 2002. VDE Verlag.

25. A J Bell and T J Sejnowski. An information-maximization approach to blind separation and blind deconvolution. *Neural computation*, 7(6):1129–59, November 1995.

26. Nima Dehghani, Sydney S Cash, Andrea O Rossetti, Chih Chuan Chen, and Eric Halgren. Magnetoencephalography demonstrates multiple asynchronous generators during human sleep spindles. *Journal of neurophysiology*, 104(1):179–88, July 2010.

27. Samu Taulu and Matti Kajola. Presentation of electromagnetic multichannel data: The signal space separation method. *Journal of Applied Physics*, 97(12):124905, June 2005.

28. Fahmeed Hyder. Dynamic imaging of brain function. In Fahmeed Hyder, editor, *Dynamic Brain Imaging Multi-Modal Methods and In Vivo Applications.*, chapter 1, pages 3–22. Humana Press, 2009.

29. P. Mitra and H. Bokil. *Observed Brain Dynamics*. Oxford University Press, New York, 2008.

30. Mircea Steriade. *The Intact and Sliced Brain*. MIT Press, Cambridge, October 2001.

31. Alain Destexhe, Michael Rudolph, and Denis Paré. The high-conductance state of neocortical neurons in vivo. *Nature reviews. Neuroscience*, 4(9):739–51, September 2003.

32. G L Gerstein and W A Clark. Simultaneous Studies of Firing Patterns in Several Neurons. *Science (New York, N.Y.)*, 143(3612):1325–7, March 1964.

33. György Buzsáki. Large-scale recording of neuronal ensembles. *Nature neuroscience*, 7(5):446–51, May 2004.

34. Carl Gold, Darrell a Henze, Christof Koch, and György Buzsáki. On the origin of the extracellular action potential waveform: A modeling study. *Journal of neurophysiology*, 95(5):3113–28, May 2006.

35. Ferenc Mechler and Jonathan D Victor. Dipole characterization of single neurons from their extracellular action potentials. *Journal of computational neuroscience*, 32(1):73–100, February 2012.

36. R Quian Quiroga, Z Nadasdy, and Y Ben-Shaul. Unsupervised spike detection and sorting with wavelets and superparamagnetic clustering. *Neural computation*, 16(8):1661–87, August 2004.

37. E M Schmidt. Computer separation of multi-unit neuroelectric data: a review. *Journal of neuroscience methods*, 12(2):95–111, December 1984.

38. M.S. Lewicki. A review of methods for spike sorting: the detection and classification of neural action potentials. *Network (Bristol, England)*, 9(4):R53–78, November 1998.

39. Peter Barthó, Hajime Hirase, Lenaïc Monconduit, Michael Zugaro, Kenneth D Harris, and György Buzsáki. Characterization of neocortical principal cells and interneurons by network interactions and extracellular features. *Journal of neurophysiology*, 92(1):600–8, July 2004.

40. J Csicsvari, H Hirase, A Czurkó, A Mamiya, and G Buzsáki. Oscillatory coupling of hippocampal pyramidal cells and interneurons in the behaving Rat. *The Journal of neuroscience : the official journal of the Society for Neuroscience*, 19(1):274–87, January 1999.

41. Michel. Le Van Quyen, Anatol. Bragin, Richard. Staba, Benoit. Crépon, Charles L. Wilson, and Jerome. Engel. Cell type-specific firing during ripple oscillations in the hippocampal formation of humans. *The Journal of neuroscience : the official journal of the Society for Neuroscience*, 28(24):6104–10, June 2008.

42. DJ Warren, RA Normann, and A Koulakov. Imaging Two-Dimensional Neural Activity Patterns in the Cat Visual Cortex using a Multielectrode Array. In TW Berger and GL Glanzman, editors, *Toward Replacement Parts for the Brain*, pages 43–66. MIT Press, Cambridge, 2005.

43. M A Nicolelis, R C Lin, D J Woodward, and J K Chapin. Dynamic and distributed properties of many-neuron ensembles in the ventral posterior medial thalamus of awake rats. *Proceedings of the National Academy of Sciences of the United States of America*, 90(6):2212–6, March 1993.

44. C M Gray, P E Maldonado, M Wilson, and B McNaughton. Tetrodes markedly improve the reliability and yield of multiple single-unit isolation from multi-unit recordings in cat striate cortex. *Journal of neuroscience methods*, 63(1-2):43–54, December 1995.

45. K D Wise and K Najafi. Microfabrication techniques for integrated sensors and microsystems. *Science (New York, N.Y.)*, 254(5036):1335–42, November 1991.

46. K E Jones, P K Campbell, and R A Normann. A glass/silicon composite intracortical electrode array. *Annals of biomedical engineering*, 20(4):423–37, January 1992.

47. Hideaki Shimazaki, Shun-ichi Amari, Emery N. Brown, and Sonja Grün. State-Space Analysis of Time-Varying Higher-Order Spike Correlation for Multiple Neural Spike Train Data. *PLoS Computational Biology*, 8(3):e1002385, March 2012.

48. Emery N Brown, Robert E Kass, and Partha P Mitra. Multiple neural spike train data analysis: state-of-the-art and future challenges. *Nature neuroscience*, 7(5):456–61, May 2004.

49. Kenneth D Harris. Neural signatures of cell assembly organization. *Nature reviews. Neuroscience*, 6(5):399–407, May 2005.

50. M Meister, J Pine, and D A Baylor. Multi-neuronal signals from the retina: acquisition and analysis. *Journal of neuroscience methods*, 51(1):95–106, January 1994.

51. Adrien Peyrache, Mehdi Khamassi, Karim Benchenane, Sidney I Wiener, and Francesco P Battaglia. Replay of rule-learning related neural patterns in the prefrontal cortex during sleep. *Nature neuroscience*, 12(7):919–26, July 2009.

52. A Riehle, S Grün, M Diesmann, and A Aertsen. Spike synchronization and rate modulation differentially involved in motor cortical function. *Science (New York, N.Y.)*, 278(5345):1950–3, December 1997.

53. R A Normann, D J Warren, J Ammermuller, E Fernandez, and S Guillory. High-resolution spatio-temporal mapping of visual pathways using multi-electrode arrays. *Vision research*, 41(10-11):1261–75, January 2001.

54. Wilson Truccolo, Leigh R Hochberg, and John P Donoghue. Collective dynamics in human and monkey sensorimotor cortex: predicting single neuron spikes. *Nature neuroscience*, 13(1):105–11, January 2010.

55. Corey J Keller, Wilson Truccolo, John T Gale, Emad Eskandar, Thomas Thesen, Chad Carlson, Orrin Devinsky, Ruben Kuzniecky, Werner K Doyle, Joseph R Madsen, Donald L Schomer, Ashesh D Mehta, Emery N Brown, Leigh R Hochberg, István Ulbert, Eric Halgren, and Sydney S Cash. Heterogeneous neuronal firing patterns during interictal epileptiform discharges in the human cortex. *Brain: A journal of neurology*, 133(Pt 6):1668–1681, 2010.

56. Wilson Truccolo, Jacob a Donoghue, Leigh R Hochberg, Emad N Eskandar, Joseph R Madsen, William S Anderson, Emery N Brown, Eric Halgren, and Sydney S Cash. Single-neuron dynamics in human focal epilepsy. *Nature neuroscience*, 14(5):635–41, May 2011.

57. Timothy A Fofonoff, Sylvain M Martel, Nicholas G Hatsopoulos, John P Donoghue, and Ian W Hunter. Microelectrode array fabrication by electrical discharge machining

and chemical etching. *IEEE transactions on bio-medical engineering*, 51(6):890–5, June 2004.

58. P J Rousche and R A Normann. Chronic intracortical microstimulation (ICMS) of cat sensory cortex using the Utah Intracortical Electrode Array. *IEEE transactions on rehabilitation engineering : a publication of the IEEE Engineering in Medicine and Biology Society*, 7(1):56–68, March 1999.

59. Rebecca A Parker, Tyler S Davis, Paul A House, Richard A Normann, and Bradley Greger. The functional consequences of chronic, physiologically effective intracortical microstimulation. *Progress in brain research*, 194:145–65, January 2011.

60. Allen Waziri, Catherine A Schevon, Joshua Cappell, Ronald G Emerson, Guy M McKhann, and Robert R Goodman. Initial surgical experience with a dense cortical microarray in epileptic patients undergoing craniotomy for subdural electrode implantation. *Neurosurgery*, 64(3):540–5; discussion 545, March 2009.

61. György Buzsáki, Costas A. Anastassiou, and Christof Koch. The origin of extracellular fields and currents EEG, ECoG, LFP and spikes. *Nature Reviews Neuroscience*, 13(6):407–420, May 2012.

62. KH Pettersen, H Lindén, AM Dale, and GT Einevoll. Extracellular spikes and CSD. In R Brette and A Destexhe, editors, *Handbook of Neural Activity Measurement*. Cambridge University Press, 2012.

63. Claude. Bédard and Alain. Destexhe. Local field potentials. In R Brette and A Destexhe, editors, *Handbook of Neural Activity Measurement*. Cambridge University Press, 2012.

64. JC Eccles. Interpretation of action potentials evoked in the cerebral cortex. *Electroencephalography and clinical neurophysiology*, 3(4):449–64, November 1951.

65. R Lorente de No. Analysis of the distribution of the action currents of nerve in volume conductors. *Studies from the Rockefeller institute for medical research. Reprints. Rockefeller Institute for Medical Research*, 132:384–477, January 1947.

66. U Mitzdorf. Current source-density method and application in cat cerebral cortex: investigation of evoked potentials and EEG phenomena. *Physiological reviews*, 65(1):37–100, January 1985.

67. Gaute T Einevoll, Klas H Pettersen, Anna Devor, Istvan Ulbert, Eric Halgren, and AM Dale. Laminar population analysis: estimating firing rates and evoked synaptic activity from multielectrode recordings in rat barrel cortex. *Journal of neurophysiology*, 97(3):2174–90, March 2007.

68. Henrik Lindén, Klas H Pettersen, and Gaute T Einevoll. Intrinsic dendritic filtering gives low-pass power spectra of local field potentials. *Journal of computational neuroscience*, 29(3):423–44, December 2010.

69. Shingo Murakami and Yoshio Okada. Contributions of principal neocortical neurons to magnetoencephalography and electroencephalography signals. *The Journal of physiology*, 575(Pt 3):925–36, September 2006.

70. F Varela, J P Lachaux, E Rodriguez, and J Martinerie. The brainweb: phase synchronization and large-scale integration. *Nature reviews. Neuroscience*, 2(4):229–39, April 2001.

71. E G Jones. Lamination and differential distribution of thalamic afferents within the sensory-motor cortex of the squirrel monkey. *The Journal of comparative neurology*, 160(2):167–203, March 1975.

72. E G Jones and S P Wise. Size, laminar and columnar distribution of efferent cells in the sensory-motor cortex of monkeys. *The Journal of comparative neurology*, 175(4):391–438, October 1977.

73. V B Mountcastle. The columnar organization of the neocortex. *Brain : a journal of neurology*, 120:701–22, April 1997.

74. Nelson Spruston. Pyramidal neurons: dendritic structure and synaptic integration. *Nature reviews. Neuroscience*, 9(3):206–21, March 2008.

75. PL Nunez and R Srinivasan. *Electric Fields of the Brain. The Neurophysics of EEG, Second Edition*. Oxford University Press, New York, 2006.

76. J Sarvas. Basic mathematical and electromagnetic concepts of the biomagnetic inverse problem. *Physics in medicine and biology*, 32(1):11–22, January 1987.

77. JC de Munck, CH Wolters, and M Clerc. EEG and MEG forward modelling. In R Brette and A Destexhe, editors, *Handbook of Neural Activity Measurement*. Cambridge University Press, 2012.

78. SP Ahlfors and MS Hämäläinen. EEG and MEG source estimation. In R Brette and A Destexhe, editors, *Handbook of Neural Activity Measurement*. Cambridge University Press, 2012.

79. Y C Okada, J Wu, and S Kyuhou. Genesis of MEG signals in a mammalian CNS structure. *Electroencephalography and clinical neurophysiology*, 103(4):474–85, October 1997.

80. Stephanie R Jones, Dominique L Pritchett, Steven M Stufflebeam, Matti Hämäläinen, and Christopher I Moore. Neural correlates of tactile detection: a combined magnetoencephalography and biophysically based computational modeling study. *The Journal of neuroscience : the official journal of the Society for Neuroscience*, 27(40):10751–64, October 2007.

81. Stephanie R Jones, Dominique L Pritchett, Michael A Sikora, Steven M Stufflebeam, Matti Hämäläinen, and Christopher I Moore. Quantitative analysis and biophysically realistic neural modeling of the MEG mu rhythm: rhythmogenesis and modulation of sensory-evoked responses. *Journal of neurophysiology*, 102(6):3554–72, December 2009.

82. K Jerbi, S Baillet, J C Mosher, G Nolte, L Garnero, and R M Leahy. Localization of realistic cortical activity in MEG using current multipoles. *NeuroImage*, 22(2):779–93, June 2004.

83. G. Nolte and G. Curio. Current multipole expansion to estimate lateral extent of neuronal activity: a theoretical analysis. *IEEE Transactions on Biomedical Engineering*, 47(10):1347–1355, 2000.

84. G Nolte and G Curio. On the calculation of magnetic fields based on multipole modeling of focal biological current sources. *Biophysical journal*, 73(3):1253–62, September 1997.

85. J. J. Riera, T. Ogawa, T. Goto, A. Sumiyoshi, H. Nonaka, A. Evans, H. Miyakawa, and R. Kawashima. Pitfalls in the dipolar model for the neocortical EEG sources. *Journal of Neurophysiology*, April 2012.

86. AM Dale and MI Sereno. Improved localization of cortical activity by combining EEG and MEG with MRI cortical surface reconstruction: A linear approach. *Journal of Cognitive Neuroscience*, (5):162–176, 1993.

87. AM Dale, A K Liu, B R Fischl, R L Buckner, J W Belliveau, J D Lewine, and E Halgren. Dynamic statistical parametric mapping: combining fMRI and MEG for high-resolution imaging of cortical activity. *Neuron*, 26(1):55–67, April 2000.

88. Ming-Xiong Huang, Tao Song, Donald J Hagler, Igor Podgorny, Veikko Jousmaki, Li Cui, Kathleen Gaa, Deborah L Harrington, AM Dale, Roland R Lee, Jeff Elman, and Eric Halgren. A novel integrated MEG and EEG analysis method for dipolar sources. *NeuroImage*, 37(3):731–48, September 2007.

89. J de Munck and BW van Dijk. Symmetry considerations in the quasi-static approximation of volume conductor theory. *Physics in Medicine and Biology*, 36(4):521–529, 1991.

90. James F A Poulet and Carl C H Petersen. Internal brain state regulates membrane potential synchrony in barrel cortex of behaving mice. *Nature*, 454(7206):881–5, August 2008.

91. Michael Okun, Amir Naim, and Ilan Lampl. The subthreshold relation between cortical local field potential and neuronal firing unveiled by intracellular recordings in awake rats. *The Journal of neuroscience : the official journal of the Society for Neuroscience*, 30(12):4440–8, March 2010.

92. Stavros Zanos, Theodoros P Zanos, Vasilis Marmarellis, George A Ojemann, and Eberhard E Fetz. Relationships between spike-free local field potentials and spike timing in human temporal cortex. *Journal of neurophysiology*, 107(7):1808–21, December 2011.

93. Michael Denker, Sébastien Roux, Henrik Lindén, Markus Diesmann, Alexa Riehle, and Sonja Grün. The local field potential reflects surplus spike synchrony. *Cerebral cortex (New York, N.Y. : 1991)*, 21(12):2681–95, December 2011.

94. J P Lachaux, E Rodriguez, J Martinerie, and F J Varela. Measuring phase synchrony in brain signals. *Human brain mapping*, 8(4):194–208, January 1999.

95. Michel Le Van Quyen and Anatol Bragin. Analysis of dynamic brain oscillations: methodological advances. *Trends in neurosciences*, 30(7):365–73, July 2007.

96. Henrik Lindén, Tom Tetzlaff, Tobias C Potjans, Klas H Pettersen, Sonja Grün, Markus Diesmann, and Gaute T Einevoll. Modeling the spatial reach of the LFP. *Neuron*, 72(5):859–72, December 2011.

97. D Contreras, A Destexhe, T J Sejnowski, and M Steriade. Spatiotemporal patterns of spindle oscillations in cortex and thalamus. *The Journal of neuroscience : the official journal of the Society for Neuroscience*, 17(3):1179–96, February 1997.

98. Nima. Dehghani, Eric. Halgren, and Syd. Cash. Possible differential sensitivity to the matrix vs core thalamocortical systems by MEG vs EEG. In *Front. Syst. Neurosci. Conference Abstract: Computational and systems neuroscience 2009*, 2009.

99. Nima Dehghani, Sydney S Cash, and Eric Halgren. Topographical frequency dynamics within EEG and MEG sleep spindles. *Clinical neurophysiology : official journal of the International Federation of Clinical Neurophysiology*, 122(2):229–35, March 2011.

100. E G Jones. Viewpoint: the core and matrix of thalamic organization. *Neuroscience*, 85(2):331–45, July 1998.

101. E G Jones. The thalamic matrix and thalamocortical synchrony. *Trends in neurosciences*, 24(10):595–601, October 2001.

102. Nima Dehghani, Sydney S Cash, Chih C Chen, Donald J Hagler, Mingxiong Huang, AM Dale, and Eric Halgren. Divergent cortical generators of MEG and EEG during human sleep spindles suggested by distributed source modeling. *PloS one*, 5(7):e11454, January 2010.

103. Thomas Andrillon, Yuval Nir, Richard J Staba, Fabio Ferrarelli, Chiara Cirelli, Giulio Tononi, and Itzhak Fried. Sleep spindles in humans: insights from intracranial EEG and unit recordings. *The Journal of neuroscience : the official journal of the Society for Neuroscience*, 31(49):17821–34, December 2011.

104. M. Bonjean, T. Baker, M. Bazhenov, S. Cash, E. Halgren, and T. Sejnowski. Interactions between Core and Matrix Thalamocortical Projections in Human Sleep Spindle Synchronization. *Journal of Neuroscience*, 32(15):5250–5263, April 2012.

105. Nima Dehghani, Sydney S Cash, and Eric Halgren. Emergence of synchronous EEG spindles from asynchronous MEG spindles. *Human brain mapping*, February 2011.

106. Steffen Katzner, Ian Nauhaus, Andrea Benucci, Vincent Bonin, Dario L Ringach, and Matteo Carandini. Local origin of field potentials in visual cortex. *Neuron*, 61(1):35–41, January 2009.

107. Dajun Xing, Chun-I Yeh, and Robert M Shapley. Spatial spread of the local field potential and its laminar variation in visual cortex. *The Journal of neuroscience : the official journal of the Society for Neuroscience*, 29(37):11540–9, September 2009.

108. Jing Liu and William T Newsome. Local field potential in cortical area MT: stimulus tuning and behavioral correlations. *The Journal of neuroscience : the official journal of the Society for Neuroscience*, 26(30):7779–90, July 2006.

109. C E Schroeder, C E Tenke, and S J Givre. Subcortical contributions to the surface-recorded flash-VEP in the awake macaque. *Electroencephalography and clinical neurophysiology*, 84(3):219–31, 1992.

110. Gabriel Kreiman, Chou P Hung, Alexander Kraskov, Rodrigo Quian Quiroga, Tomaso Poggio, and James J DiCarlo. Object selectivity of local field potentials and spikes in the macaque inferior temporal cortex. *Neuron*, 49(3):433–45, February 2006.

111. Chunmao Wang, Istvan Ulbert, Donald L Schomer, Ksenija Marinkovic, and Eric Halgren. Responses of human anterior cingulate cortex microdomains to error detection, conflict monitoring, stimulus-response mapping, familiarity, and orienting. *The Journal of neuroscience : the official journal of the Society for Neuroscience*, 25(3):604–13, January 2005.

112. Yoshinao Kajikawa and Charles E Schroeder. How local is the local field potential? *Neuron*, 72(5):847–58, December 2011.

113. F Grynszpan and D B Geselowitz. Model studies of the magnetocardiogram. *Biophysical journal*, 13(9):911–25, September 1973.

114. B N Cuffin and D Cohen. Comparison of the magnetoencephalogram and electroencephalogram. *Electroencephalography and clinical neurophysiology*, 47(2):132–46, August 1979.

115. Seppo P Ahlfors, Jooman Han, John W Belliveau, and Matti S Hämäläinen. Sensitivity of MEG and EEG to source orientation. *Brain topography*, 23(3):227–32, September 2010.

116. Andrei Irimia, John Darrell Van Horn, and Eric Halgren. Source cancellation profiles of electroencephalography and magnetoencephalography. *NeuroImage*, 59(3):2464–74, March 2012.

117. J R Melcher and D Cohen. Dependence of the MEG on dipole orientation in the rabbit head. *Electroencephalography and clinical neurophysiology*, 70(5):460–72, November 1988.

118. Daniel M Goldenholz, Seppo P Ahlfors, Matti S Hämäläinen, Dahlia Sharon, Mamiko Ishitobi, Lucia M Vaina, and Steven M Stufflebeam. Mapping the signal-to-noise-ratios of cortical sources in magnetoencephalography and electroencephalography. *Human brain mapping*, 30(4):1077–86, April 2009.

119. Seppo P Ahlfors, Jooman Han, Fa-Hsuan Lin, Thomas Witzel, John W Belliveau, Matti S Hämäläinen, and Eric Halgren. Cancellation of EEG and MEG signals generated by extended and distributed sources. *Human brain mapping*, 31(1):140–9, January 2010.

120. Sarang S Dalal, Sylvain Baillet, Claude Adam, Antoine Ducorps, Denis Schwartz, Karim Jerbi, Olivier Bertrand, Line Garnero, Jacques Martinerie, and Jean-Philippe Lachaux. Simultaneous MEG and intracranial EEG recordings during attentive reading. *NeuroImage*, 45(4):1289–304, May 2009.

121. Klas H Pettersen and Gaute T Einevoll. Amplitude variability and extracellular low-pass filtering of neuronal spikes. *Biophysical journal*, 94(3):784–802, February 2008.

122. C Bédard, Helmut Kröger, and Alain Destexhe. Modeling extracellular field potentials and the frequency-filtering properties of extracellular space. *Biophysical journal*, 86(3):1829–42, March 2004.

123. C Bédard, Serafim Rodrigues, Noah Roy, Diego Contreras, and Alain Destexhe. Evidence for frequency-dependent extracellular impedance from the transfer function between extracellular and intracellular potentials: intracellular-LFP transfer function. *Journal of computational neuroscience*, 29(3):389–403, December 2010.

124. C Koch. *Biophysics of Computation. Information Processing in Single Neurons*. Oxford University Press, 2004.

125. A R Martin. The effect of membrane capacitance on non-linear summation of synaptic potentials. *Journal of theoretical biology*, 59(1):179–87, June 1976.

126. J G Stinstra and M J Peters. The volume conductor may act as a temporal filter on the ECG and EEG. *Medical & biological engineering & computing*, 36(6):711–6, November 1998.

127. Per Bak, Chao Tang, and Kurt Wiesenfeld. Self-organized criticality: An explanation of the 1/f noise. *Physical review letters*, 59(4):381–384, July 1987.

128. HJ Jensen. *Self-Organized Criticality: Emergent Complex Behavior in Physical and Biological Systems*. Cambridge University Press, Cambridge, 1998.

129. W S Pritchard. The brain in fractal time: 1/f-like power spectrum scaling of the human electroencephalogram. *The International journal of neuroscience*, 66(1-2):119–29, September 1992.

130. K Linkenkaer-Hansen, V V Nikouline, J M Palva, and R J Ilmoniemi. Long-range temporal correlations and scaling behavior in human brain oscillations. *The Journal of neuroscience : the official journal of the Society for Neuroscience*, 21(4):1370–7, February 2001.

131. E Novikov, A Novikov, D Shannahoff-Khalsa, B Schwartz, and J Wright. Scale-similar activity in the brain. *Physical Review E*, (56):R2387–R2389, 1997.

132. Biyu J He, John M Zempel, Abraham Z Snyder, and Marcus E Raichle. The temporal structures and functional significance of scale-free brain activity. *Neuron*, 66(3):353–69, May 2010.

133. Kai J Miller, Larry B Sorensen, Jeffrey G Ojemann, Marcel Den Nijs, and Marcel den Nijs. Power-law scaling in the brain surface electric potential. *PLoS computational biology*, 5(12):e1000609, December 2009.

134. C Bédard, H Kröger, and A Destexhe. Does the 1/f frequency scaling of brain signals reflect self-organized critical states? *Physical Review letters*, 97(11):118102, September 2006.

135. John M Beggs and Dietmar Plenz. Neuronal avalanches in neocortical circuits. *The Journal of neuroscience : the official journal of the Society for Neuroscience*, 23(35):11167–77, December 2003.

136. C Bédard, H Kröger, and A Destexhe. Model of low-pass filtering of local field potentials in brain tissue. *Physical review. E, Statistical, nonlinear, and soft matter physics*, 73(5 Pt 1):051911, May 2006.

137. Christof. Koch and Idan. Segev. *Methods in Neuronal Modeling*. MIT Press, Cambridge, 2nd edition, 1998.

138. Nikos K Logothetis, Christoph Kayser, and Axel Oeltermann. In vivo measurement of cortical impedance spectrum in monkeys: implications for signal propagation. *Neuron*, 55(5):809–23, September 2007.

139. C Gabriel, S Gabriel, and E Corthout. The dielectric properties of biological tissues: I. Literature survey. *Physics in medicine and biology*, 41(11):2231–49, November 1996.

140. S Gabriel, R W Lau, and C Gabriel. The dielectric properties of biological tissues: II. Measurements in the frequency range 10 Hz to 20 GHz. *Physics in medicine and biology*, 41(11):2251–69, November 1996.

141. S Gabriel, R W Lau, and C Gabriel. The dielectric properties of biological tissues: III. Parametric models for the dielectric spectrum of tissues. *Physics in medicine and biology*, 41(11):2271–93, November 1996.

142. A Peters, SL Palay, and HF Webster. *The Fine Structure of the Nervous System*. Oxford University Press, Oxford, 1991.

143. V Braitenberg and A Schüz. *Cortex: Statistics and Geometry of Neuronal Connectivity*. Springer, Berlin, 2nd edition, 1998.

144. M.S. Hamalainen and J. Sarvas. Realistic conductivity geometry model of the human head for interpretation of neuromagnetic data. *IEEE Transactions on Biomedical Engineering*, 36(2):165–171, 1989.

145. Nevzat G Gençer and Can E Acar. Sensitivity of EEG and MEG measurements to tissue conductivity. *Physics in medicine and biology*, 49(5):701–17, March 2004.

146. S B Baumann, D R Wozny, S K Kelly, and F M Meno. The electrical conductivity of human cerebrospinal fluid at body temperature. *IEEE transactions on bio-medical engineering*, 44(3):220–3, March 1997.

147. C H Wolters, A Anwander, X Tricoche, D Weinstein, M A Koch, and R S MacLeod. Influence of tissue conductivity anisotropy on EEG/MEG field and return current computation in a realistic head model: a simulation and visualization study using high-resolution finite element modeling. *NeuroImage*, 30(3):813–26, April 2006.

148. K Wendel, N G Narra, M Hannula, P Kauppinen, and J Malmivuo. The influence of CSF on EEG sensitivity distributions of multilayered head models. *IEEE transactions on bio-medical engineering*, 55(4):1454–6, April 2008.

149. M Akhtari, H C Bryant, A N Mamelak, E R Flynn, L Heller, J J Shih, M Mandelkern, A Matlachov, D M Ranken, E D Best, M A DiMauro, R R Lee, and W W Sutherling. Conductivities of three-layer live human skull. *Brain topography*, 14(3):151–67, January 2002.

150. Moritz Dannhauer, Benjamin Lanfer, Carsten H Wolters, and Thomas R Knösche. Modeling of the human skull in EEG source analysis. *Human brain mapping*, 32(9):1383–99, September 2011.

151. S Gonçalves, J C de Munck, J P A Verbunt, R M Heethaar, and F H Lopes da Silva. In vivo measurement of the brain and skull resistivities using an EIT-based method and the combined analysis of SEF/SEP data. *IEEE transactions on bio-medical engineering*, 50(9):1124–8, September 2003.

152. P J Basser, J Mattiello, and D LeBihan. MR diffusion tensor spectroscopy and imaging. *Biophysical journal*, 66(1):259–67, January 1994.

153. S Vallaghé, M Clerc, and JM Badier. In vivo conductivity estimation using somatosensory evoked potentials and cortical constraints on the sources. In *Proceedings of 4th IEEE International Symposium on Biomedical Imaging: From Nano to Macro*, pages 1036–1039, 2007.

154. Kun Wang, Shanan Zhu, Bryon A Mueller, Kelvin O Lim, Zhongming Liu, and Bin He. A new method to derive white matter conductivity from diffusion tensor MRI. *IEEE transactions on bio-medical engineering*, 55(10):2481–6, October 2008.

155. Y Lai, W van Drongelen, L Ding, K E Hecox, V L Towle, D M Frim, and B He. Estimation of in vivo human brain-to-skull conductivity ratio from simultaneous extra- and intra-cranial electrical potential recordings. *Clinical neurophysiology : official journal of the International Federation of Clinical Neurophysiology*, 116(2):456–65, February 2005.

156. D S Tuch, V J Wedeen, A M Dale, J S George, and J W Belliveau. Conductivity tensor mapping of the human brain using diffusion tensor MRI. *Proceedings of the National Academy of Sciences of the United States of America*, 98(20):11697–701, September 2001.

157. M X Huang, J C Mosher, and R M Leahy. A sensor-weighted overlapping-sphere head model and exhaustive head model comparison for MEG. *Physics in medicine and biology*, 44(2):423–40, February 1999.

158. P B Hoeltzell and R W Dykes. Conductivity in the somatosensory cortex of the cat – evidence for cortical anisotropy. *Brain research*, 177(1):61–82, November 1979.

159. Takakuni Goto, Rieko Hatanaka, Takeshi Ogawa, Akira Sumiyoshi, Jorge Riera, and Ryuta Kawashima. An evaluation of the conductivity profile in the somatosensory barrel cortex of Wistar rats. *Journal of neurophysiology*, 104(6):3388–412, December 2010.

160. Jeff W. Lichtman, Jean Livet, and Joshua R. Sanes. A technicolour approach to the connectome. *Nature Reviews Neuroscience*, 9(6):417–422, April 2008.

161. Javier DeFelipe. From the connectome to the synaptome: an epic love story. *Science (New York, N.Y.)*, 330(6008):1198–201, November 2010.

162. Sydney Brenner and Terrence J Sejnowski. Understanding the human brain. *Science (New York, N.Y.)*, 334(6056):567, November 2011.

163. J Haueisen, D S Tuch, C Ramon, P H Schimpf, V J Wedeen, J S George, and J W Belliveau. The influence of brain tissue anisotropy on human EEG and MEG. *NeuroImage*, 15(1):159–66, January 2002.

164. Daniel Güllmar, Jens Haueisen, and Jürgen R Reichenbach. Influence of anisotropic electrical conductivity in white matter tissue on the EEG/MEG forward and inverse solution. A high-resolution whole head simulation study. *NeuroImage*, 51(1):145–63, May 2010.

165. V. J. Wedeen, D. L. Rosene, R. Wang, G. Dai, F. Mortazavi, P. Hagmann, J. H. Kaas, and W.-Y. I. Tseng. The Geometric Structure of the Brain Fiber Pathways. *Science*, 335(6076):1628–1634, March 2012.

166. Nitin B Bangera, Donald L Schomer, Nima Dehghani, Istvan Ulbert, Sydney Cash, Steve Papavasiliou, Solomon R Eisenberg, AM Dale, and Eric Halgren. Experimental validation of the influence of white matter anisotropy on the intracranial EEG forward solution. *Journal of computational neuroscience*, 29(3):371–87, December 2010.

167. L J Borg-Graham, C Monier, and Y Frégnac. Visual input evokes transient and strong shunting inhibition in visual cortical neurons. *Nature*, 393(6683):369–73, May 1998.

168. A Destexhe, Stuart W Hughes, Michelle Rudolph, and Vincenzo Crunelli. Are corticothalamic 'up' states fragments of wakefulness? *Trends in neurosciences*, 30(7):334–42, July 2007.

169. M Steriade. Impact of network activities on neuronal properties in corticothalamic systems. *Journal of neurophysiology*, 86(1):1–39, July 2001.

170. Jakob Wolfart, Damien Debay, Gwendal Le Masson, Alain Destexhe, and Thierry Bal. Synaptic background activity controls spike transfer from thalamus to cortex. *Nature neuroscience*, 8(12):1760–7, December 2005.

171. Frances S Chance, L F Abbott, and Alex D Reyes. Gain modulation from background synaptic input. *Neuron*, 35(4):773–82, August 2002.

172. Yousheng Shu, Andrea Hasenstaub, Mathilde Badoual, Thierry Bal, and David A McCormick. Barrages of synaptic activity control the gain and sensitivity of cortical neurons. *The Journal of neuroscience : the official journal of the Society for Neuroscience*, 23(32):10388–401, November 2003.

173. O Bernander, R J Douglas, K A Martin, and C Koch. Synaptic background activity influences spatiotemporal integration in single pyramidal cells. *Proceedings of the National Academy of Sciences of the United States of America*, 88(24):11569–73, December 1991.

174. Alain. Destexhe, Diego. Contreras, and Mircea. Steriade. Spatiotemporal analysis of local field potentials and unit discharges in cat cerebral cortex during natural wake and sleep states. *The Journal of neuroscience : the official journal of the Society for Neuroscience*, 19(11):4595–608, June 1999.

175. P Bak. *How Nature Works*. Springer-Verlag, New York, 1996.

176. V Frette, K Christensen, A Malthe-Sø renssen, J Feder, T Jø ssang, and P Meakin. Avalanche dynamics in a pile of rice. *Nature*, (379):49–52, 1996.

177. BD Malamud, G Morein, and DL Turcotte. Forest fires: An example of self-organized critical behavior. *Science (New York, N.Y.)*, 281(5384):1840–2, September 1998.

178. O Peters and D Neelin. Critical phenomena in atmospheric precipitation. *Nature Physics*, (2):293–396, 2006.

179. Matthias H Hennig, Christopher Adams, David Willshaw, and Evelyne Sernagor. Early-stage waves in the retinal network emerge close to a critical state transition between local and global functional connectivity. *The Journal of neuroscience : the official journal of the Society for Neuroscience*, 29(4):1077–86, January 2009.

180. Elakkat D Gireesh and Dietmar Plenz. Neuronal avalanches organize as nested theta- and beta/gamma-oscillations during development of cortical layer 2/3. *Proceedings of the National Academy of Sciences of the United States of America*, 105(21):7576–81, May 2008.

181. V Pasquale, P Massobrio, L L Bologna, M Chiappalone, and S Martinoia. Self-organization and neuronal avalanches in networks of dissociated cortical neurons. *Neuroscience*, 153(4):1354–69, June 2008.

182. Gerald Hahn, Thomas Petermann, Martha N Havenith, Shan Yu, Wolf Singer, Dietmar Plenz, and Danko Nikolic. Neuronal avalanches in spontaneous activity in vivo. *Journal of neurophysiology*, 104(6):3312–22, December 2010.

183. Thomas Petermann, Tara C Thiagarajan, Mikhail a Lebedev, Miguel a L Nicolelis, Dante R Chialvo, and Dietmar Plenz. Spontaneous cortical activity in awake monkeys composed of neuronal avalanches. *Proceedings of the National Academy of Sciences of the United States of America*, 106(37):15921–6, September 2009.

184. Jonathan Touboul and Alain Destexhe. Can power-law scaling and neuronal avalanches arise from stochastic dynamics? *PloS one*, 5(2):e8982, January 2010.

185. T Gisiger. Scale invariance in biology: coincidence or footprint of a universal mechanism? *Biological reviews of the Cambridge Philosophical Society*, 76(2):161–209, May 2001.

186. Dante R. Chialvo. Emergent complex neural dynamics. *Nature Physics*, 6(10):744–750, October 2010.

187. William Reed and Barry Hughes. From gene families and genera to incomes and internet file sizes: Why power laws are so common in nature. *Physical Review E*, 66(6):1–4, December 2002.

188. W Rall and G M Shepherd. Theoretical reconstruction of field potentials and dendrodendritic synaptic interactions in olfactory bulb. *Journal of neurophysiology*, 31(6):884–915, November 1968.

189. C Wolters and JC de Munck. Volume conduction. *Scholarpedia*, (2):1738, 2007.

190. RR Ramirez. Source localization. *Scholarpedia*, (3):1733, 2008.

191. J B. Ranck. Specific impedance of rabbit cerebral cortex. *Experimental neurology*, 7:144–52, February 1963.

192. C Bédard and A Destexhe. Macroscopic models of local field potentials and the apparent 1/f noise in brain activity. *Biophysical journal*, 96(7):2589–603, April 2009.

193. I Fried, C L Wilson, N T Maidment, J Engel, E Behnke, T A Fields, K A MacDonald, J W Morrow, and L Ackerson. Cerebral microdialysis combined with single-neuron and electroencephalographic recording in neurosurgical patients. Technical note. *Journal of neurosurgery*, 91(4):697–705, October 1999.

194. Sydney S Cash, Eric Halgren, Nima Dehghani, Andrea O Rossetti, Thomas Thesen, Chunmao Wang, Orrin Devinsky, Ruben Kuzniecky, Werner Doyle, Joseph R Madsen, Edward Bromfield, Loránd Eross, Péter Halász, George Karmos, Richárd Csercsa, Lucia Wittner, and István Ulbert. The human K-complex represents an isolated cortical down-state. *Science (New York, N.Y.)*, 324(5930):1084–7, May 2009.

195. Richárd Csercsa, Balázs Dombovári, Dániel Fabó, Lucia Wittner, Loránd Eross, László Entz, András Sólyom, György Rásonyi, Anna Szucs, Anna Kelemen, Rita Jakus, Vera Juhos, László Grand, Andor Magony, Péter Halász, Tamás F Freund, Zsófia Maglóczky, Sydney S Cash, László Papp, György Karmos, Eric Halgren, and István Ulbert. Laminar analysis of slow wave activity in humans. *Brain : a journal of neurology*, 133(9):2814–29, September 2010.

196. Michel Le Van Quyen, Richard Staba, Anatol Bragin, Clayton Dickson, Mario Valderrama, Itzhak Fried, and Jerome Engel. Large-scale microelectrode recordings of high-frequency gamma oscillations in human cortex during sleep. *The Journal of neuroscience : the official journal of the Society for Neuroscience*, 30(23):7770–82, June 2010.

197. D A Henze, Z Borhegyi, J Csicsvari, A Mamiya, K D Harris, and G Buzsáki. Intracellular features predicted by extracellular recordings in the hippocampus in vivo. *Journal of neurophysiology*, 84(1):390–400, July 2000.

198. Thomas Klausberger, Peter J Magill, László F Márton, J David B Roberts, Philip M Cobden, György Buzsáki, and Peter Somogyi. Brain-state- and cell-type-specific firing of hippocampal interneurons in vivo. *Nature*, 421(6925):844–8, February 2003.

199. A Sik, M Penttonen, A Ylinen, and G Buzsáki. Hippocampal CA1 interneurons: an in vivo intracellular labeling study. *The Journal of neuroscience : the official journal of the Society for Neuroscience*, 15(10):6651–65, October 1995.

200. Patrick L Tierney, Eric Dégenètais, Anne-Marie Thierry, Jacques Glowinski, and Yves Gioanni. Influence of the hippocampus on interneurons of the rat prefrontal cortex. *The European journal of neuroscience*, 20(2):514–24, July 2004.

201. Aaron. Clauset, Cosma Rohilla. Shalizi, and Mark. Newman. Power-Law Distributions in Empirical Data. *SIAM Review*, 51(4):661–703, 2009.

202. J Nenonen, M Kajola, J Simola, and A Ahonen. Total information of multichannel MEG sensor arrays. In E Halgren, A Ahlfors, M Hamalainen, and D Cohen, editors, *Proceedings of the 14th international conference on biomagnetism (Biomag2004)*, pages 630–631, Boston, 2004.

203. Arnaud Delorme and Scott Makeig. EEGLAB: an open source toolbox for analysis of single-trial EEG dynamics including independent component analysis. *Journal of neuroscience methods*, 134(1):9–21, March 2004.

204. SF Boll. Suppression of acoustic noise in speech using spectral subtraction. *IEEE Trans. Acoustic, Speech and Signal Processing*, 27:113–120, 1979.

205. S Kamath and P Loizou. A multi-band spectral subtraction method for enhancing speech corrupted by colored noise. In *Proceedings of ICASSP 2002*, pages 4160–4164, 2002.

206. PC Loizou. *Speech Enhancement: Theory and Practice*. CRC Press, Boca Raton, 2007.

207. JS Lim and AV Oppenheim. Enhancement and band width compression of noisy speech. In *Proc. of the IEEE*, pages 1586–1604, 1979.

208. MA. Abd El-Fattah, MI. Dessouky, SM. Diab, and FE. Abd El-samie. Speech enhancement using an adaptive Wiener filtering approach. *Prog. Electromagnetics Res.*, 4:167–184, 2008.

209. H Abdi and LJ Williams. Partial least square regression, projection on latent structure regression, PLS-Regression. *Wiley Interdisciplinary Reviews: Computational Statistics*, 2:97–106, 2010.

210. P Garthwaite. An interpretation of partial least squares. *J. Am. Stat. Assoc*, (89):122–127, 1994.

211. C de Boor. *A practical guide to splines (revised ed., 2001)*. Springer, New York, 2001.

212. PHC Eilers and BD Marx. Flexible smoothing with B-splines and penalties. *Statistical Science*, (11):89–121, 1996.

213. L Magee. Nonlocal behavior in polynomical regression. *The American Statistican*, (52):20–22, 1998.

214. P Royston and D Altman. Regression using fractional polynomials of continuous covariates: Parsimonious parametric modelling. *Applied Statistician*, (43):429–467, 1994.

215. V Katkovnik, K Egiazarian, and J Astola. *Local approximation in signal and image processing*. SPIE Publications, 2006.

216. R Plonsey. *Bioelectric phenomena*. McGraw Hill, New York, 1969.

217. RM Gulrajani. *Bioelectricity and biomagnetism*. Wiley, New York, 1998.

218. L Landau and E Lifchitz. *Electrodynamics of continuous media*. Pergamon Press, Moscow, 1984.

219. K R Foster and H P Schwan. Dielectric properties of tissues and biological materials: a critical review. *Critical reviews in biomedical engineering*, 17(1):25–104, January 1989.

220. W J Freeman, L J Rogers, M D Holmes, and D L Silbergeld. Spatial spectral analysis of human electrocorticograms including the alpha and gamma bands. *Journal of neuroscience methods*, 95(2):111–21, February 2000.

221. RC Hwa and TC Ferree. Fluctuation analysis of human electroencephalogram. *Nonlinear Phenomena in Complex Systems*, (5):302–307, 2002.

222. Rudolph C Hwa and Thomas C Ferree. Scaling properties of fluctuations in the human electroencephalogram. *Physical review. E, Statistical, nonlinear, and soft matter physics*, 66(2 Pt 1):021901, August 2002.

223. BL Sim, YC Tong, JC Chang, and CT Tan. A Parametric formulation of the generalized spectral subtraction method. *IEEE Trans. Speech and Audio Processing*, 6:328–337, 1998.

224. J Kantelhardt, E Koscielny-Bunde, H Rego, S Havlin, and A. Bunde. Detecting long-range correlations with detrended fluctuation analysis. *Physica A*, (295):441–445, 2001.

225. Miguel Valencia, Julio Artieda, Manuel Alegre, and Diego Maza. Influence of filters in the detrended fluctuation analysis of digital electroencephalographic data. *Journal of Neuroscience Methods*, 170(2):310–316, May 2008.

226. M Buiatti, D Papo, P-M Baudonnière, and C van Vreeswijk. Feedback modulates the temporal scale-free dynamics of brain electrical activity in a hypothesis testing task. *Neuroscience*, 146(3):1400–12, May 2007.

227. Juha Voipio, Pekka Tallgren, Erkki Heinonen, Sampsa Vanhatalo, and Kai Kaila. Millivolt-scale DC shifts in the human scalp EEG: evidence for a nonneuronal generator. *Journal of neurophysiology*, 89(4):2208–14, April 2003.

228. T C Ferree, P Luu, G S Russell, and D M Tucker. Scalp electrode impedance, infection risk, and EEG data quality. *Clinical neurophysiology : official journal of the International Federation of Clinical Neurophysiology*, 112(3):536–44, March 2001.

229. SR Taylor and E Gileadi. The physical interpretation of the Warburg impedance. *Corrosion*, (51):664–671, 1995.

230. JP Diard, B Le Gorrec, and C Montella. Linear diffusion impedance. General expression and applications. *Journal of Electroanalytical Chemistry*, (471):126–131, 1999.

231. György Buzsáki and Andreas Draguhn. Neuronal oscillations in cortical networks. *Science (New York, N.Y.)*, 304(5679):1926–9, June 2004.

232. M. Berouti, R. Schwartz, and J. Makhoul. Enhancement of speech corrupted by acoustic noise. In *Proc. ICASSP 1979*, pages 208–211, 1979.

233. C Boubakir, D Berkani, and F Grenez. A frequency-dependent speech enhancement method. *J. Mobile Communication*, 1:97–100, 2007.

234. H. Abdi and LJ. Williams. Principal component analysis. *Wiley Interdisciplinary Reviews: Computational Statistics*, 2:433–459, 2010.

235. Yumiko Yoshimura, Jami L M Dantzker, and Edward M Callaway. Excitatory cortical neurons form fine-scale functional networks. *Nature*, 433(7028):868–73, February 2005.

236. Sen Song, Per Jesper Sjöström, Markus Reigl, Sacha Nelson, and Dmitri B Chklovskii. Highly nonrandom features of synaptic connectivity in local cortical circuits. *PLoS biology*, 3(3):e68, March 2005.

237. Ifije E Ohiorhenuan, Ferenc Mechler, Keith P Purpura, Anita M Schmid, Qin Hu, and Jonathan D Victor. Sparse coding and high-order correlations in fine-scale cortical networks. *Nature*, 466(7306):617–21, July 2010.

238. M Steriade. *Neuronal Substrates of Sleep and Epilepsy* . Cambridge University Press, Cambridge, 2003.

239. S Wiebe, W T Blume, J P Girvin, and M Eliasziw. A randomized, controlled trial of surgery for temporal-lobe epilepsy. *The New England journal of medicine*, 345(5):311–8, August 2001.

240. William R Patterson, Yoon-Kyu Song, Christopher W Bull, Ilker Ozden, Andrew P Deangellis, Christopher Lay, J Lucas McKay, Arto V Nurmikko, John D Donoghue, and Barry W Connors. A microelectrode/microelectronic hybrid device for brain implantable neuroprosthesis applications. *IEEE transactions on bio-medical engineering*, 51(10):1845–53, October 2004.

241. D a McCormick, B W Connors, J W Lighthall, and D a Prince. Comparative electrophysiology of pyramidal and sparsely spiny stellate neurons of the neocortex. *Journal of neurophysiology*, 54(4):782–806, October 1985.

242. Matthew A Smith and Adam Kohn. Spatial and temporal scales of neuronal correlation in primary visual cortex. *The Journal of neuroscience : the official journal of the Society for Neuroscience*, 28(48):12591–603, November 2008.

243. H Hirase, X Leinekugel, J Csicsvari, A Czurkó, and G Buzsáki. Behavior-dependent states of the hippocampal network affect functional clustering of neurons. *The Journal of neuroscience : the official journal of the Society for Neuroscience*, 21(10):RC145, May 2001.

244. Catherine A Schevon, Sau K Ng, Joshua Cappell, Robert R Goodman, Guy McKhann, Allen Waziri, Almut Branner, Alexandre Sosunov, Charles E Schroeder, and Ronald G Emerson. Microphysiology of epileptiform activity in human neocortex. *Journal of clinical neurophysiology : official publication of the American Electroencephalographic Society*, 25(6):321–30, December 2008.

245. BW Silverman. Using kernel density estimates to investigate multimodality. *J R Stat Soc B*, (43):97–99, 1981.

246. Jaime de la Rocha, Brent Doiron, Eric Shea-Brown, Kresimir Josić, and Alex Reyes. Correlation between neural spike trains increases with firing rate. *Nature*, 448(7155):802–6, August 2007.

247. Indre V Viskontas, Arne D Ekstrom, Charles L Wilson, and Itzhak Fried. Characterizing interneuron and pyramidal cells in the human medial temporal lobe in vivo using extracellular recordings. *Hippocampus*, 17(1):49–57, January 2007.

248. Shuzo Sakata and Kenneth D Harris. Laminar structure of spontaneous and sensory-evoked population activity in auditory cortex. *Neuron*, 64(3):404–18, November 2009.

249. Peter Lennie. The cost of cortical computation. *Current biology : CB*, 13(6):493–7, March 2003.

250. C van Vreeswijk and H Sompolinsky. Chaos in neuronal networks with balanced excitatory and inhibitory activity. *Science (New York, N.Y.)*, 274(5293):1724–6, December 1996.

251. D J Amit and N Brunel. Model of global spontaneous activity and local structured activity during delay periods in the cerebral cortex. *Cerebral cortex*, 7(3):237–52, 1997.

252. Alfonso Renart, Jaime de la Rocha, Peter Bartho, Liad Hollender, Néstor Parga, Alex Reyes, and Kenneth D Harris. The asynchronous state in cortical circuits. *Science (New York, N.Y.)*, 327(5965):587–90, January 2010.

253. Bilal Haider, Alvaro Duque, Andrea R Hasenstaub, and David a McCormick. Neocortical network activity in vivo is generated through a dynamic balance of excitation and inhibition. *The Journal of neuroscience : the official journal of the Society for Neuroscience*, 26(17):4535–45, April 2006.

254. Michelle Rudolph, Martin Pospischil, Igor Timofeev, and Alain Destexhe. Inhibition determines membrane potential dynamics and controls action potential generation in awake and sleeping cat cortex. *The Journal of neuroscience : the official journal of the Society for Neuroscience*, 27(20):5280–90, May 2007.

255. Shigeyoshi Fujisawa, Asohan Amarasingham, Matthew T Harrison, and György Buzsáki. Behavior-dependent short-term assembly dynamics in the medial prefrontal cortex. *Nature neuroscience*, 11(7):823–33, July 2008.

256. P Achermann and A A Borbély. Coherence analysis of the human sleep electroencephalogram. *Neuroscience*, 85(4):1195–208, August 1998.

257. György Buzsáki, Caroline Geisler, Darrell A Henze, and Xiao-Jing Wang. Interneuron Diversity series: Circuit complexity and axon wiring economy of cortical interneurons. *Trends in neurosciences*, 27(4):186–93, April 2004.

258. Andrew R Dykstra, Alexander M Chan, Brian T Quinn, Rodrigo Zepeda, Corey J Keller, Justine Cormier, Joseph R Madsen, Emad N Eskandar, and Sydney S Cash. Individualized localization and cortical surface-based registration of intracranial electrodes. *NeuroImage*, 59(4):3563–70, February 2012.

259. Andreas Klaus, Shan Yu, and Dietmar Plenz. Statistical analyses support power law distributions found in neuronal avalanches. *PloS one*, 6(5):e19779, January 2011.

260. Adrien Peyrache, Nima Dehghani, Emad N Eskandar, Joseph R Madsen, William S Anderson, Jacob A Donoghue, Leigh R Hochberg, Eric Halgren, Sydney S Cash, and Alain Destexhe. Spatiotemporal dynamics of neocortical excitation and inhibition during human sleep. *Proceedings of the National Academy of Sciences of the United States of America*, 109(5):1731–6, January 2012.

261. Mark. Newman. Power laws, Pareto distributions and Zipf's law. *Contemporary Physics*, 46(5):323–351, September 2005.

262. H Bauke. Parameter estimation for power-law tail distributions by maximum likelihood methods. *Eur. Phys. J. B*, (58):167–173, 2007.

263. ML Goldstein, SA Morris, and GG Yen. Problems with fitting to the power-law distribution. *Eur. Phys. J. B*, (41):255–258, 2004.

264. M Matsumoto and T Nishimura. Mersenne twister: a 623-dimensionally equidistributed uniform pseudo-random number generator. *ACM Transactions on Modeling and Computer Simulation*, 8(1):3–330, 1998.

265. W. H. Press, B. P. Flannery, S. A. Teukolsky, and W.T. Vetterling. Random Numbers. In *in Numerical Recipes: The Art of Scientic Computing*, chapter 7, pages 340–418. Cambridge University Press, Cambridge, 3rd edition, 2007.

266. W. H. Press, B. P. Flannery, S. A. Teukolsky, and W.T. Vetterling. Nonlinear models. In *in Numerical Recipes: The Art of Scientic Computing*, chapter 15, pages 773–839. Cambridge University Press, Cambridge, 2007.

267. G. Hahn, C. Monier, and Y. Fregnac. Revisiting power law in vivo as a function of the global brain state, using multiple recordings in anesthetized cat. In *Soc. Neurosci. Abstracts*, Washington DC, 2011.

268. I Mastromatteo and M Marsili. On the Criticality of Inferred Models. *Journal of Statistical Mechanics: Theory and Experiment*, (10):P100102, 2011.

269. Tiago L Ribeiro, Mauro Copelli, Fábio Caixeta, Hindiael Belchior, Dante R Chialvo, Miguel a L Nicolelis, and Sidarta Ribeiro. Spike avalanches exhibit universal dynamics across the sleep-wake cycle. *PloS one*, 5(11):e14129, January 2010.

270. N Friedman, S Ito, BA Brinkman, M Shimono, RE Lee DeVille, KA Dahmen, JM Beggs, and TC Butler. Universal critical dynamics in high resolution neuronal avalanche data. . *Physical Review Letters*, 108(20):208102, 2012.

271. Stefanos. Papanikolaou, Felipe. Bohn, Rubem Luis. Sommer, Gianfranco. Durin, Stefano. Zapperi, and James P. Sethna. Universality Beyond Power laws and the average avalanche shape. *Nature Physics*, 7(4):316–320, January 2011.

272. Paul Nunez and Ramesh Srinivasan. Electroencephalogram. *Scholarpedia*, 2(2):1348, February 2007.

273. D B Geselowitz. On bioelectric potentials in an inhomogeneous volume conductor. *Biophysical journal*, 7(1):1–11, January 1967.

274. W Chen, J J Zhang, G Y Hu, and C P Wu. Electrophysiological and morphological properties of pyramidal and nonpyramidal neurons in the cat motor cortex in vitro. *Neuroscience*, 73(1):39–55, July 1996.

275. A. Baranyi, M B. Szente, and C D. Woody. Electrophysiological characterization of different types of neurons recorded in vivo in the motor cortex of the cat. II. Membrane parameters, action potentials, current-induced voltage responses and electrotonic structures. *Journal of neurophysiology*, 69(6):1865–79, June 1993.

276. W H Calvin and G W Sypert. Fast and slow pyramidal tract neurons: an intracellular analysis of their contrasting repetitive firing properties in the cat. *Journal of neurophysiology*, 39(2):420–34, March 1976.

277. Ganesh Vigneswaran, Alexander Kraskov, and Roger N Lemon. Large identified pyramidal cells in macaque motor and premotor cortex exhibit ”thin spikes”: implications for cell type classification. *The Journal of neuroscience : the official journal of the Society for Neuroscience*, 31(40):14235–42, October 2011.

278. M N Shadlen and J A Movshon. Synchrony unbound: a critical evaluation of the temporal binding hypothesis. *Neuron*, 24(1):67–77, 111–25, September 1999.

279. J I Nelson, P A Salin, M H Munk, M Arzi, and J Bullier. Spatial and temporal coherence in cortico-cortical connections: a cross-correlation study in areas 17 and 18 in the cat. *Visual neuroscience*, 9(1):21–37, July 1992.

280. Denise Berger, David Warren, Richard Normann, Amos Arieli, and Sonja Grün. Spatially organized spike correlation in cat visual cortex. *Neurocomputing*, 70(10-12):2112–2116, June 2007.

281. R. B. Levy and A. D. Reyes. Spatial Profile of Excitatory and Inhibitory Synaptic Connectivity in Mouse Primary Auditory Cortex. *Journal of Neuroscience*, 32(16):5609–5619, April 2012.

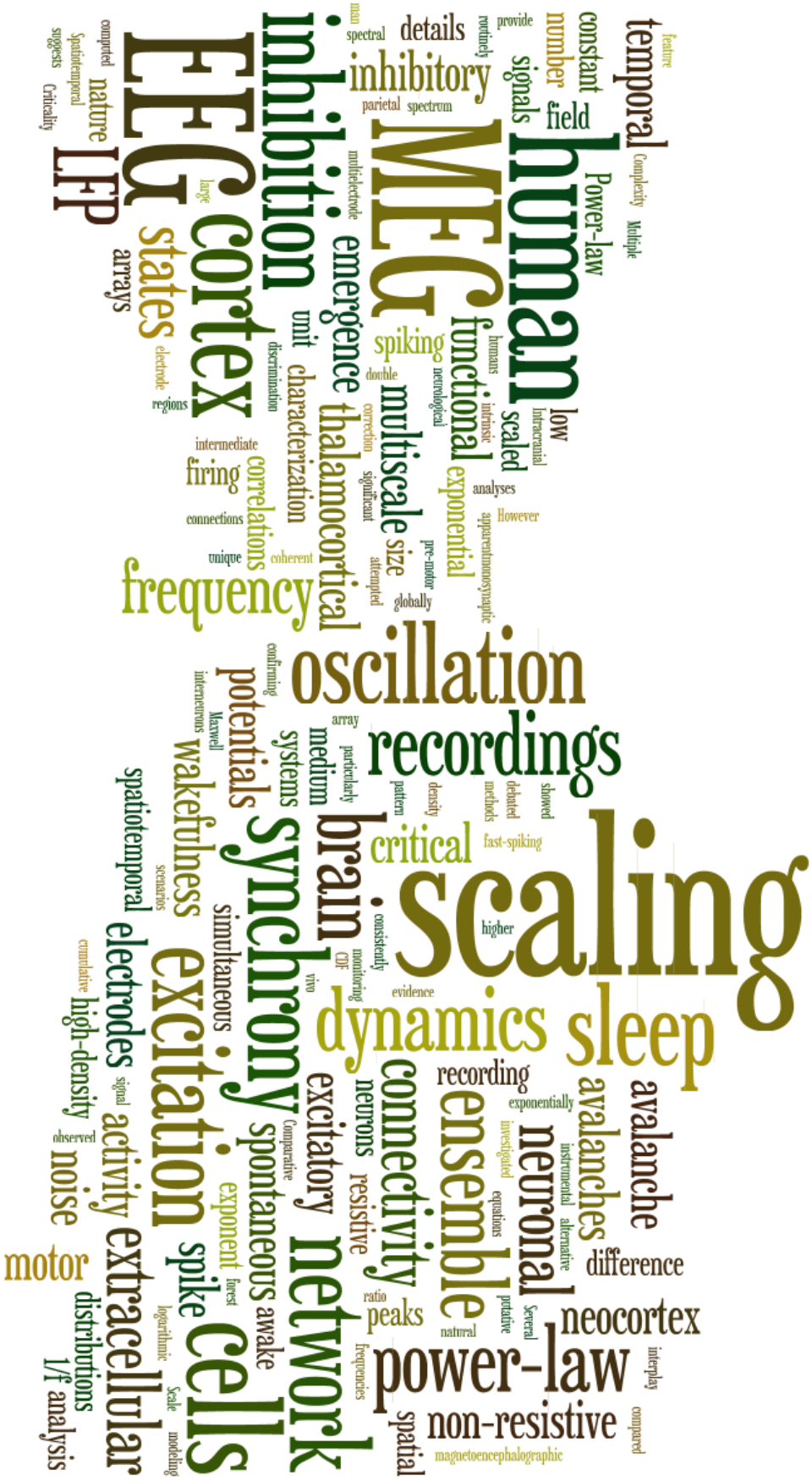
scaling
oscillation
frequency
recordings
dynamics
sleep
synchrony
network
excitation
cells
power-law
neocortex
MEG
human
EEG
cortex
inhibition
LFP
inhibitory
temporal
details
number
constant
field
signals
Power-law
states
arrays
emergence
thalamocortical
multiscale
spiking
functional
exponential
scaled
low
correlations
firing
characterization
unit
potentials
wakefulness
brain
critical
medium
systems
spatiotemporal
electrodes
high-density
noise
activity
motor
extracellular
spike
distributions
1/f
analysis
spontaneous
awake
exponent
peaks
ratio
natural
frequencies
spatial
non-resistive
magnetoencephalographic
compared
interplay
neuronal
avalanches
avalanche
ensemble
connectivity
recording
neurons
resistive
excitatory
difference
alternative
equations
instrumental
investigated
exponentially
simultaneous
evidence
consistently
higher
fast-spiking
showed
methods
debated
density
pattern
particularly
array
Maxwel
interneurons
confirming
pre-motor
globally
attempted
coherent
unique
connections
significant
correction
intermediate
regions
electrode
discrimination
double
humans
neurological
intrinsic
Intracranial
analyses
However
apparentmonosynaptic
Complexity
Multiple
feature
provide
routinely
spectral
parietal
spectrum
multielectrode
large
Criticality
Spatiotemporal
suggests
computed
nature
Several
putative
Comparative
CDF
vivo
monitoring
cumulative
signal
observed
scenarios
logarithmic
Scale
modeling